Exciton and Multiple Exciton Dynamics in Colloidal Semiconductor Nanocrystals

Vom Fachbereich Chemie der Rheinland-Pfälzischen Technischen
Universität Kaiserslautern-Landau zur Verleihung des
akademischen Grades „Doktor der Naturwissenschaften“
genehmigte Dissertation

DE - 386

Rheinland-Pfälzische
Technische Universität
Kaiserslautern
Landau

vorgelegt von

Raktim Baruah

geboren in Jorhat

Betreuer: Prof. Maria Wächtler

Kaiserslautern, 05.12.2024

This thesis was completed between October 2019 and October 2024 at Friedrich Schiller University Jena (until June 2023) and at the Department of Chemistry at RPTU Kaiserslautern-Landau (from July 2023) under the supervision of Prof. Dr. Maria Wächtler.

Date of the application for the opening of the doctoral procedure: 25.10.2024

Date of the scientific debate: 05.12.2024

Doctoral committee:

Chair: Prof. Dr. Wolfgang Kleist

1. Reviewer: Prof. Dr. Maria Wächtler

2. Reviewer: Jun.-Prof. Dr. Jennifer Meyer

3. Examiner: Prof. Dr. Georg Manolikakes

Declaration

Declaration of independent work

I, Raktim Baruah, hereby affirm that I have independently completed this thesis in accordance with the doctoral degree regulations of the Department of Chemistry of the RPTU Kaiserslautern-Landau and have not used any sources other than those indicated. Passages that are taken or verbatim from other sources are marked as such and are listed in the bibliography. The parts of the thesis which are published in other sources are specifically mentioned. A brief description of the co-authors in the published work has been provided.

Kaiserslautern, _____________ _____________

Raktim Baruah

Acknowledgements

Moving to a new country, completing four years of a PhD, and navigating through a global pandemic was far from a cakewalk. However, the people I encountered along the way transformed this experience into a saga of learning, togetherness, growth, and resilience. While words cannot fully express my gratitude, I feel toward everyone who helped me reach the finish line, I want to take this humble opportunity to appreciate each one. First and foremost, I would like to express my heartfelt gratitude to *Prof. Maria Wächtler*, who has not only welcomed me into her research group but also given me the incredible opportunity to work on a topic that has both challenged and fascinated me throughout this journey. Over the past five years, her unwavering support, patience, and keen insight have guided me through many obstacles. Her constant encouragement and deep interest in my work have made all the difference, shaping my growth as a researcher and as an individual. I am forever indebted to her for her mentorship and trust. I would also like to thank *Prof. Benjamin Dietzek-Ivanšić* who agreed to be my formal supervisor during the start of my PhD and made me a part of AG Dietzek-Ivanšić.

A special thanks to *Dr. Mathias Micheel* and *Dr. Alexander Schleusener* for providing the first hands-on training and ensuring that my start was both smooth and enriching. I will always appreciate their kindness and the confidence they placed in me during those early, uncertain days. I am equally grateful to *Dr. Krishan Kumar* for his invaluable discussions, constructive feedback, and detailed advice. Their guidance has always pushed me to think more deeply, challenged my assumptions, and strive for excellence in my research. Without their constant encouragement, I would not have reached this level of understanding and clarity. I also owe a deep sense of gratitude to *Yves* for always being so supportive in the lab, for his expertise in the instruments, and for his ability to solve all the technical setbacks. His constant kindness made the lab a warm place to work. I would like to thank *Avinash* for helping me find my footing in Jena and making my transition smoother. I am also incredibly grateful to *Qian*, *Hani*, *Jens*, *Luise*, and *Sarah*, for creating a vibrant and collaborative work environment at IAAC, where I always felt supported and surrounded by friends. I would also like to take this moment to thank everyone from *AG Dietzek.*

I have been fortunate enough to meet *Nina* and *Ratnadip* as my dearest friends in the lab. I am incredibly thankful for the countless hours we spent discussing science and life, sometimes blurring the lines between the two. Our friendship has been one of the most cherished parts of this journey, and I couldn't have asked for better companions along the way.

I must mention my students and offer my special thanks to *Louis*, *Munira*, and *Xhesi* for the enthusiasm they brought into the lab and for all the help and assistance in conducting my work. A special thanks to *Julia*, for all the great conversations and our friendship indeed means a lot to me.

I would also like to express my gratitude to *Julian* for his invaluable help with Raman spectroscopy, and to *Jan Dellith* and *Andrea Dellith* for their help with SEM, TEM, and AFM measurements. Thank you to *Marco* for your assistance with XRD.

Outside of work in Jena, I have been fortunate enough to meet some amazing and cheerful people who made post-work hours enjoyable and rejuvenating. I want to especially mention *Swarup*, *Tanvi*, and *Mahendra*, for being there as sounding boards, providing comfort and laughter when I needed it most. Along this way, meeting *Ankita* has brought an overwhelming sense of joy and gratitude. I am thankful for the brightened days with her presence, with an unique spirit, and an effortless connectivity with warmth and positivity. May it last for a life and a day!

After moving to RPTU, I was fortunate enough to meet incredible people like *Daniel*, *Kathi*, and *Subham*. A special thanks to *Daniel* and *Kathi*—their unwavering support and motivation lifted me during moments of doubt, and helped me a lot during my thesis writing days. My sincere gratitude to *Felix*, my student at RPTU, for his dedication and hard work.

I would like to express my deep sense of gratitude to মা, দেউতা, চাৰ and, বাইদেউ, and my family. This journey is equally theirs as much as mine. They have stood by me every step of the way, with unconditional love and encouragement with constant faith in me that instilled in me the strength to keep going even when the road seemed a little rocky.

I would like to acknowledge Deutsche Forschungsgemeinschaft (DFG), project no. 398816777–CRC 1375 NOA, C04, for the financial support in the first stage of my PhD.

Finally, to all the wonderful people I have met along this journey, who have contributed to my growth in ways big and small, this is my deepest expression of gratitude. Thank you for being part of this unforgettable chapter of my life.

List of Abbreviations

NC	Nanocrystal
LSPR	Localized surface plasmon resonance
UV	Ultraviolet
QD	Quantum dot
CdSe	Cadmium selenide
LED	Light emitting diode
TOPO	Tri-octylphosphine oxide
ODPA	Octadecylphosphonic acid
OA	Oleic acid
HDA	Hexadecylamine
MEG	Multiexciton generation
SILAR	Successive ionic layer adsorption and reaction
TOP	tri-octylphosphine
ODE	1-octadecene
MO	Molecular orbital
LCAO	Linear combination of atomic orbitals
2D	Two dimensions
1D	One dimensional
0D	Zero dimensional
DOS	Density of states
LA	Longitudinal acoustic
QX	Tetraexciton
BX	Biexciton
TX	Triexciton
TA	Transient absorption
tr-PL	Time-resolved photoluminescence
GSB	Ground state bleach
PIA	Photoinduced absorption
SE	Stimulated emission
MCMC	Markov Chain Monte Carlo
MPA	3-mercaptopropanoic acid
MUA	11-mercaptoundecanoic acid
NMF	N-methylformamide
FFT	Fast-fourier-transformation

TEM	Transmission electron microscopy
SEM	Scanning electron microscopy
FT-IR	Fourier transform infrared spectroscopy
TEM	Transmission electron microscopy
BE	Band edge
TS	Trap state

List of Figures

Figure 1: Colloidal CdSe QDs of different sizes under a UV lamp. 2

Figure 2: Graphical illustration of the thesis work divided into four chapters. The top left panel represents the Chapter 3, illustrating the influence of carrier trapping introduced by surface ligands on photoluminescence property. The top right panel represents the Chapter 4, illustrating the influence of carrier trapping on Auger recombination of multiexcitons observed by TA spectroscopy. Chapter 5 is represented in the bottom left panel, illustrating the effect of surface functionalization on exciton delocalization in QD thin film, and the impact on Auger recombination process probed by TA spectroscopy. The bottom right panel illustrates Chapter 6, with the methods to fabricate QD thin film by depositing it in a porous silica matrix. 7

Figure 3: Plot of Gibbs free energy vs. radius of nucleus. 10

Figure 4: LaMer model depicting the three phases of the NC formation. 11

Figure 5: Different surface ligands used for surface passivation of QD surface. 15

Figure 6: Effect of semiconductor nanocrystal size on band structure. 17

Figure 7: DOS for (a) 3D bulk, (b) 2D quantum well, (c) 1D quantum wire, and (d) 0D QD. 19

Figure 8: (a) Electronic level structure, and (b) an absorption spectrum of CdSe QDs with the three lowest energy transitions (1S, 2S, and 1P) marked by the three lines. 20

Figure 9: Schematic of exciton fine structure splitting the first excitonic state ($1S_{3/2}1S_e$) in CdSe QDs. G represents the ground state. 21

Figure 10: (a) Photoluminescence spectra of 2.6 nm QD upon 400 nm photoexcitation. (b) Schematics of exciton cooling, radiative recombination, non-radiative surface trapping, and an example of radiative recombination involving a trap state. 22

Figure 11: A schematic of electronic level diagram of BX, TX, and QX in CdSe QDs. 25

Figure 12: The three-carrier Auger recombination process in a (a) bulk material, and in a (b) semiconductor NC. (c) Multiexciton recombination process in CdSe QDs, via Auger recombination process. 26

Figure 13: Schematic of the femtosecond TA set-up used in this thesis work. 30

Figure 14: (a) 2D plot of TA data representing the evolution of ΔA as function of λ, and t. (b) electronic level diagram of CdSe QD showing the lowest three electronic transitions. (c) steady-state absorption and TA spectra (at 1900 ps) of CdSe QD representing the spectral features of the lowest three electronic transitions..........32

Figure 15: (a) Steady-state absorption and normalized photoluminescence spectra (λ_{ex} = 400 nm) of TOPO capped 2.4 nm, 4.0 nm, 4.8 nm, and 8.2 nm QDs. 38

Figure 16: (a) Gaussian fitting of the photoluminescence spectra of 2.4 nm QD. The band-edge peak (BE) is denoted by gauss 1 and the trap-state (TS) peak is denoted by gauss 2. (b) The relative contribution of band-edge (BE) and trap-state (TS) emission to the overall spectra of 2.4 nm, 4.0 nm, 4.8 nm, and 8.2 nm TOPO capped QDs..40

Figure 17: (a) Steady-state absorption spectra and (b) photoluminescence spectra (λ_{ex} = 400 nm) of 2.4 nm QD with TOPO, MPA, MUA, and S^{2-} ligands. The photoluminescence spectra are normalized to the respective absorbance at λ_{ex} (400 nm). (c) The relative contribution of band-edge (gauss 1) and trap-state (gauss 2) emissions obtained from the Gaussian fitting (as shown in Figure 16a) in the photoluminescence spectra of TOPO, MPA, MUA, and S^{2-} capped 2.4 nm QD. . 41

Figure 18: Photoluminescence spectra (λ_{ex} = 400 nm) of (a) 4.8 nm QD, and (b) 8.2 nm QD with TOPO, MPA, MUA, and S^{2-} ligands. The photoluminescence spectra are normalized to the respective absorbance at λ_{ex} (400 nm). The relative contribution of band-edge (gauss 1) and trap-state (gauss 2) emissions obtained from multi-gaussian fitting (as shown in Figure 16a) in the photoluminescence spectra of TOPO, MPA, MUA, and S^{2-} capped (c)4.8 nm, and (d) 8.2 nm QD....................43

Figure 19: (a) Raman spectra showing the LA modes of 2.4 nm, 4.0 nm, 4.8 nm, and 8.2 nm TOPO capped QDs deposited on CaF_2 substrates. (b) Representation of LA phonon frequency with QD size. The Raman spectra were cut between -10 cm^{-1} to 10 cm^{-1} to ignore the Rayleigh Scattering. 43

Figure 20: LA phonon modes of TOPO, MPA, MUA, and S^{2-} capped (a) 4.8 nm, and (b) 8.2 nm QDs. (c) The variation of LA phonon mode frequencies with respect to the molar mass of TOPO, MUA and MPA ligands in 4.8 nm and 8.2 nm QDs. (d) The LA phonon mode frequencies of TOPO, MUA, MPA and S^{2-} capped 4.8 nm and 8.2 nm QDs..45

Figure 21: (a) Steady-state absorption spectra of TOPO capped (solid lines) and S^{2-} capped (dashed lines) CdSe QDs of four different sizes. (b) steady-state absorption spectra (top panel) of the TOPO capped 4.8 nm QD with the marked 1S, 2S and 1P transitions, and the corresponding transitions are marked in the TA spectra (bottom panel) as B_1, B_2, and B_3. 50

Figure 22: Intensity-dependent TA spectra at 2 ps of (a) TOPO capped (b) S^{2-} capped CdSe QDs of four different sizes. Increasing intensity is indicated by the lines right to the panels. 52

Figure 23: Kinetics of B_1 and B_3 bleach of (a) & (b) TOPO capped, and (c) & (d) S^{2-} capped CdSe QDs of four different sizes. Increasing intensity is indicated by the lines right to the panels. B_1 position of TOPO capped 2.6 nm, 3.4 nm, 4 nm, and 4.8 nm QDs are at 530 nm, 576 nm, 590 nm, and 614 nm respectively. B_1 position of S^{2-} capped 2.6 nm, 3.4 nm, 4 nm, and 4.8 nm QDs are at 540 nm, 575 nm, 585 nm, and 610 nm respectively. 53

Figure 24: The energy level diagram (not scaled) of CdSe QDs, representing the conduction band and valence band population with increasing intensity (J) which lead to the formation of, e.g., exciton (X), BX, TX, and QX. 54

Figure 25: Absorption-cross section (α) (at 400 nm) determined from MCMC fit and absorption-cross section (α) (at 400 nm) determined from the extinction co-efficient (at 400 nm) of the four TOPO capped QDs. 58

Figure 26: (a) Multiexciton species spectra, and (b) initial concentration of multiexciton species over the pump intensities in TOPO capped QDs of four different sizes. (c) Multiexciton species spectra, and (d) initial concentration of multiexciton species over the pump intensities in S^{2-} capped QDs of four different sizes. X, BX, TX, and QX represent exciton, biexciton, triexciton, and tetraexciton respectively............ 59

Figure 27: (a) Radius dependency (multiexciton lifetime, $\tau MX \propto Rn$) of TX and BX lifetimes of TOPO and S^{2-} capped QDs. (b) Number of exciton dependencies (multiexciton lifetime, $\tau MX \propto Nn$) of TOPO and S^{2-} capped 4 nm and 4.8 nm QDs. (c) A schematic representing a TX, in a TOPO capped QD with the carrier density concentrated in the CdSe core and in a S^{2-} capped QD with a trapped hole on the surface site. 63

Figure 28: The A_1 and B_1 peak obtained from the multi-gaussian fitting of Eq. (30) of 4.8 nm (a) TOPO capped and (c) S^{2-} capped QD. The figures demonstrate the extent of A_1 and B_1 overlapping, which determines the BX binding energy (ΔBX). (b) A schematic of excitonic state diagram, representing the optical transitions corresponding to A_1 and B_1 in exciton (X). (d) Radius dependency ($\Delta MX \propto Rn$) of multiexciton binding energy (ΔMX) of BX, TX and QX obtained from the multi-gaussian fit of Eq. (30) – Eq. (33).. 68

Figure 29: SEM images of 4.0 nm QDs with surface ligands (a) TOPO, and (b) S^{2-}. The SEM images were collected by drop casting the QD solutions on silicon wafers. The insets in the SEM images represent the fast-fourier-transformed (FFT) images used to determine the distances between QDs. 72

Figure 30: (a) Steady-state absorption, and (b) photoluminescence spectra of TOPO capped 2.6 nm, 3.4 nm, 4.0 nm, and 4.8 nm QDs both in solution (sol), and thin films (film). (c) steady-state absorption, and (d) photoluminescence spectra of S^{2-} capped 2.6 nm, 3.4 nm, 4.0 nm, and 4.8 nm QDs both in solution (sol), and thin films (film). The left panels in (b) and (d) depict the normalized band-edge photoluminescence and in the right panels, the zoomed view of the trap-state emissions is shown. A background correction to remove the scattering contribution in the thin film absorption spectra was performed as described in Figure A 20.[133] 73

Figure 31: (a) Steady-state absorption spectra, and (b) photoluminescence spectra of thin films of TOPO and S^{2-} capped 2.6 nm, 3.4 nm, 4.0 nm, and 4.8 nm QDs. A background correction to remove the scattering contribution in the thin film absorption spectra was performed as described in Figure A 20.[133] (c) A schematic of localized excitons in well separated TOPO capped QD thin film, and delocalized excitons in closed-packed S^{2-}capped QD thin film. (d) Plot representing the red-shifts, observed in S^{2-}capped QD thin film with respect to the respective TOPO capped QDs, as a function of QD size. 74

Figure 32: Intensity-dependent TA spectra at 2 ps of TOPO capped 2.6 nm QD in (a) solution, and (b) film. Normalized (at B_1 bleach) intensity-dependent TA spectra at 1900 ps of TOPO capped 2.6 nm QD in (c) solution, and (d) film. The change of intensity is depicted by the arrow on the left with the highest and the lowest intensity used.. 76

Figure 33: Intensity-dependent TA spectra at 2 ps of S^{2-} capped 2.6 nm QD in (a) solution, and (b) film. Normalized (at B_1 bleach) intensity-dependent TA spectra at 1900 ps of TOPO capped 2.6 nm QD in (c) solution, and (d) film. The change of intensity is depicted by the arrow on the left with the highest and the lowest intensity used.. 77

Figure 34: Intensity-dependent B_1 kinetics of TOPO capped 2.6 nm QD in (a) solution, and (b) film. Intensity-dependent B_1 kinetics of S^{2-} capped 2.6 nm QD in (c) solution, and (d) film. Normalized Intensity dependent B_1 kinetics of (e) TOPO capped, and (f) S^{2-} capped 2.6 nm QD film. The change of intensity is depicted by the arrow on the left with the highest and the lowest intensity used. 80

Figure 35: Intensity-dependent A_1 kinetics of TOPO capped 2.6 nm QD in (a) solution, and (b) film. (c) Intensity-dependent A_1 kinetics of S^{2-} capped 2.6 nm QD film. The change of intensity is depicted by the arrow on left with the highest and the lowest intensity used. 82

Figure 36: Multiexciton species spectra obtained from MCMC fitting of (a) TOPO, and (b) S^{2-} capped 2.6 nm QD solution and thin film. Multiexciton species spectra obtained from MCMC fitting of (c) TOPO, and (d) S^{2-} capped 3.4 nm QD solution and thin film. The species spectra were normalized at the B_1 of TX spectra. Exciton (X) species spectra of (e) S^{2-} capped 2.6 nm QD solution and thin film, and (f) S^{2-} capped 3.4 nm QD solution and thin film. 83

Figure A 1: FT-IR spectra of 2.4 nm, 4.8 nm, and 8.2 nm QDs capped with (a) MPA, (b) MUA, and (c) S^{2-}. Along with the IR spectra of QDs, pure ligand spectra are also plotted. The P=O band vibration in pure TOPO spectra is specially marked in all the panels to indicate the efficient removal of TOPO ligands. 139

Figure A 2: Size distribution of the QDs obtained from TEM analysis. 140

Figure A 3: Photoluminescence spectra of (a) 2.6 nm, (b) 3.4 nm, (c) 4 nm and (d) 4.8 nm, TOPO capped and S^{2-} capped QDs. In each of the figures, the left panel represents the band-edge photoluminescence, and the right panel represents the trap-state photoluminescence. Band-edge photoluminescence spectra are corrected by the respective absorbance at excitation wavelength (λex 400 nm). Trap-state photoluminescence spectra are plotted while normalizing at the band-edge peak maxima. The photoluminescence spectra indicate strong surface hole trapping resulting in band-edge photoluminescence quenching and enhancement of trap-state emission (detailed description Section 3). 141

Figure A 4: Intensity-dependent TA spectra (normalized at B_1 bleach) of (a) TOPO capped and, (b) S^{2-} capped QDs at 1900 ps. (c) Kinetics of A_1 feature of TOPO capped QDs. The A_1 features are centered at 557 nm for 2.6 nm QD, 590 nm for 3.4 nm QD, 616 nm for 4.0 nm QD and 636 nm for 4.8 nm QD. 142

Figure A 5: TX model was used for MCMC fitting of 2.6 nm TOPO capped QD. (a) Contour plot representing the fit parameters obtained from MCMC. (b) Intensity dependent kinetics of B_1 bleach with the fit (grey lines). 143

Figure A 6: TX model was used for MCMC fitting of 2.6 nm S^{2-}capped QD. (a) Contour plot representing the fit parameters obtained from MCMC. (b) Intensity dependent kinetics of B_1 bleach with the fit (grey lines). 144

Figure A 7: TX model was used for MCMC fitting of 3.4 nm TOPO capped QD. (a) Contour plot representing the fit parameters obtained from MCMC. (b) Intensity dependent kinetics of B_1 bleach with the fit (grey lines). 145

Figure A 8: TX model was used for MCMC fitting of 3.4 nm S^{2-}capped QD. (a) Contour plot representing the fit parameters obtained from MCMC. (b) Intensity dependent kinetics of B_1 bleach with the fit (grey lines). 146

Figure A 9: QX model was used for MCMC fitting of 4.0 nm TOPO capped QD. (a) Contour plot representing the fit parameters obtained from MCMC. (b) Intensity dependent kinetics of B_1 bleach with the fit (grey lines). 147

Figure A 10: QX model was used for MCMC fitting of 4.0 nm S^{2-}capped QD. (a) Contour plot representing the fit parameters obtained from MCMC. (b) Intensity dependent kinetics of B_1 bleach with the fit (grey lines). 148

Figure A 11: QX model was used for MCMC fitting of 4.8 nm TOPO capped QD. (a) Contour plot representing the fit parameters obtained from MCMC. (b) Intensity dependent kinetics of B_1 bleach with the fit (grey lines). 149

Figure A 12: QX model was used for MCMC fitting of 4.8 nm S^{2-}capped QD. (a) Contour plot representing the fit parameters obtained from MCMC. (b) Intensity dependent kinetics of B_1 bleach with the fit (grey lines). 150

Figure A 13: TX, BX, and exciton spectra of TOPO capped 2.6 nm QD along with the respective gaussian fits. 151

Figure A 14: TX, BX, and exciton spectra of TOPO capped 3.4 nm QD along with the respective gaussian fits. 151

Figure A 15: QX, TX, BX, and exciton spectra of TOPO capped 4.0 nm QD along with the respective gaussian 152

Figure A 16: QX, TX, BX, and exciton spectra of TOPO capped 4.8 nm QD along with the respective gaussian fits. 152

Figure A 17: QX, TX, BX, and exciton spectra of S^{2-}capped 4.0 nm QD along with the respective gaussian fits. 153

Figure A 18: QX, TX, BX, and exciton spectra of S^{2-}capped 4.8 nm QD along with the respective gaussian fits. 153

Figure A 19: non-linear spectra derived from the multiexciton species spectra of (a) TOPO capped (b) S^{2-} capped 2.6 nm QD. 154

Figure A 20: Raw absorption spectra of QDs infiltrated porous silica layers, fitted scattering curve, and corrected absorption spectra. 155

Figure A 21: intensity-dependent TA spectra of TOPO capped 3.4 nm QD thin film at (a)2 ps, and at 1900 ps (normalized at B_1). (c) intensity-dependent B_1 kinetics of TOPO capped 3.4 nm QD thin film. 156

Figure A 22: intensity-dependent TA spectra of S^{2-} capped 3.4 nm QD thin film at (a)2 ps, and at 1900 ps (normalized at B_1). (c) intensity-dependent B_1 kinetics of S^{2-}capped 3.4 nm QD thin film.. 157

Figure A 23: TX model was used for MCMC fitting of 2.6 nm TOPO capped QD in thin film. (a) Contour plot representing the fit parameters obtained from MCMC. (b) Intensity dependent kinetics of B_1 bleach with the fit (grey lines).................................... 158

Figure A 24: TX model was used for MCMC fitting of 2.6 nm S^{2-} capped QD in thin film. (a) Contour plot representing the fit parameters obtained from MCMC. (b) Intensity dependent kinetics of B_1 bleach with the fit (grey lines).................................... 159

Figure A 25: TX model was used for MCMC fitting of 3.4 nm TOPO capped QD in thin film. (a) Contour plot representing the fit parameters obtained from MCMC. (b) Intensity dependent kinetics of B_1 bleach with the fit (grey lines).................................... 160

Figure A 26: TX model was used for MCMC fitting of 3.4 nm S^{2-} capped QD in thin film. (a) Contour plot representing the fit parameters obtained from MCMC. (b) Intensity dependent kinetics of B_1 bleach with the fit (grey lines).................................... 161

List of Tables

Table 1: Size determined from absorption spectra, TEM images, 1S peak position in absorption spectra, and band-edge photoluminescence peak positions of 2.4 nm, 4.0 nm, 4.8 nm, and 8.2 nm TOPO capped QDs..39

Table 2: LA phonon frequencies of 2.4 nm, 4.0 nm, 4.8 nm, and 8.2 nm TOPO capped QDs. 44

Table 3: LA phonon frequency of TOPO, MUA, MPA, and S^{2-} capped 4.8 nm, and 8.2 nm QDs. 45

Table 4: Table describing the three lowest optical transitions in the four TOPO capped QDs. 51

Table 5: Multiexciton lifetimes of TOPO and S^{2-} capped QDs of four different sizes determined by MCMC fitting. Parameters shown in the Table are fitted mean values and 99% confidence intervals obtained from MCMC sampling...........................61

Table 6: Bi- (ΔBX), tri- (ΔTX), tetra- (ΔQX), and penta- (ΔPX) exciton binding energies obtained from the fit of Eq. (30) – Eq. (33) in the multiexciton species spectra of TOPO and S^{2-} capped CdSe QDs...67

Table 7: Multiexciton lifetime and absorption cross-section (α) of TOPO and S^{2-} capped 2.6 nm and 3.4 nm QD solution and thin film determined by MCMC fit. Parameters shown in the Table are the mean values and 99% confidence intervals obtained from MCMC sampling. 85

Table A 1: Intensities used for MCMC fitting of TOPO capped 2.6 nm QD and $< N >$, σ and, α obtained from MCMC fitting. 143

Table A 2: Intensities used for MCMC fitting of S^{2-}capped 2.6 nm QD and $< N >$, σ and, α obtained from MCMC fitting...144

Table A 3: Intensities used for MCMC fitting of TOPO capped 3.4 nm QD and $< N >$, σ and, α obtained from MCMC fitting. 145

Table A 4: Intensities used for MCMC fitting of S^{2-}capped 3.4 nm QD and $< N >$, σ and, α obtained from MCMC fitting...146

Table A 5: Intensities used for MCMC fitting of TOPO capped 4.0 nm QD and $< N >$, σ and, α obtained from MCMC fitting. 147

Table A 6: Intensities used for MCMC fitting of S^{2-}capped 4.0 nm QD and $< N >$, σ and, α obtained from MCMC fitting...148

Table A 7: Intensities used for MCMC fitting of TOPO capped 4.8 nm QD and $< N >$, σ and, α obtained from MCMC fitting. 149

Table A 8: Intensities used for MCMC fitting of S^{2-} capped 4.8 nm QD and $< N >$, σ and, α obtained from MCMC fitting. 150

Table A 9: Intensities used for MCMC fitting of TOPO capped 2.6 nm QD thin film and $< N >$, σ and, α obtained from MCMC fitting. 158

Table A 10: Intensities used for MCMC fitting of S^{2-} capped 2.6 nm QD thin film and $< N >$, σ and, α obtained from MCMC fitting. 159

Table A 11: Intensities used for MCMC fitting of TOPO capped 3.4 nm QD thin film and $< N >$, σ and, α obtained from MCMC fitting. 160

Table A 12: Intensities used for MCMC fitting of S^{2-} capped 3.4 nm QD thin film and $< N >$, σ and, α obtained from MCMC fitting. 161

Table of Contents

Declaration ... iii
Acknowledgements ... v
List of Abbreviations ... vii
List of Figures ... ix
List of Tables ... xvii
Table of Contents ... xix

1. Introduction ... 1

1.1 Motivation and Goals of the Work ... 5

2. Scientific Background and Methodology ... 9

2.1 Colloidal Synthesis of Semiconductor NCs and Surface Modification ... 9
2.2 Confinement effect and electronic structure of CdSe QDs ... 16
2.3 Exciton and Multiexcitons in CdSe QDs ... 22
2.4 Transient Absorption Spectroscopy ... 30

3. Post-synthetic Modification of Colloidal CdSe QDs: Investigation of Photoluminescence and Phonon Properties ... 37

4. Determination of High-order Multiexciton Properties by Transient Absorption Spectroscopy ... 49

5. Observing High-order Multiexciton Dynamics under Weak and Strong Electronic Coupling in QD Thin Films ... 71

6. Deposition of CdSe NCs in Highly Porous SiO_2 Matrices – In-situ Growth vs. Infiltration Methods ... 87

7. Summary & Outlook ... 113

8. Zusammenfassung und Ausblick ... 117

Bibliography ... 123

Appendix A ... 133

Appendix B ... 139

Appendix C ... 141

Appendix D ... 155

List of Publications ... 163
List of Conference Contributions ... 165
Curriculum Vitae ... 167

1. Introduction

In the multifaceted regime of modern science, the study of nanocrystals (NCs) has emerged as an exciting field and has captivated the keen interest of chemists, physicists, engineers, and material scientists. The first chemical synthesis of NCs was done by Faraday in 1857.[1] Ever since the synthesis of Au NCs by Faraday, the unique properties of nano-sized crystals, particularly their tunable colours, have garnered significant attention. However, even before 1857, the colour tunability of crystals has long been utilized since medieval times to obtain vibrant stained glass as seen in church windows today. This was done by varying the baking time and duration of the glass with gold and silver salts.[2] Exploration of the properties of NCs later led to the attribution of the different colours of stained glass to localized surface plasmon resonance (LSPR) arising from the collective oscillation of conduction band electrons on the surface of gold and silver metal nanoparticles.[2] Later in the 1930s, Herbert Fröhlich first demonstrated the idea of material properties' dependency on particle size. The discovery of the quantum confinement effect was a breakthrough, particularly in the field of semiconductor NCs, which enabled precise control over their electronic and optical properties by variation of their size and shape.[1] When the size of a semiconductor material is reduced to the nanoscale, typically below the exciton Bohr radius, the quantum confinement effect becomes pronounced, leading to discrete energy levels with size-dependent energetic positions and hence electronic transitions.[3, 4] This effect allows tuning of the bandgap of the NCs by simply altering their size and shape, which in turn adjusts their colour and optical properties. A photograph of CdSe NCs of different sizes emitting different colours under an UV lamp is shown in Figure 1. Pioneering work in this area was conducted by A. Ekimov,[4] A. Efros,[5] T. Itoh,[6], and colleagues, who studied the size effects on the optical spectra of CuCl NCs embedded in alkali-halide matrices. Additionally, Brus and his team presented both experimental and theoretical evidence of the quantum size effect in CdS NCs.[7] Introduction of the hot-injection approach, for colloidal synthesis of semiconductor NCs by the Bawendi group in 1993 enabling precise control over the reaction offered even more boost to the rapidly growing research area.[8] This method allowed for the synthesis of monodisperse CdSe NCs at high reaction temperatures in high-boiling organic solvents. Since then, continuous research has expanded the horizons of this fascinating field. The rigorous efforts of many scientists working in this field of science received much-deserved recognition when the pioneers of the field, namely M. Bawendi, L. E. Brus, and A. Ekimov were awarded the Nobel Prize in Chemistry 2023. Today, the tunable optical properties of semiconductor NCs have been harvested in a wide range of applications, including optoelectronics, photovoltaics, and biomedical imaging, as it provides a customizable platform for designing materials with specific and desired properties.

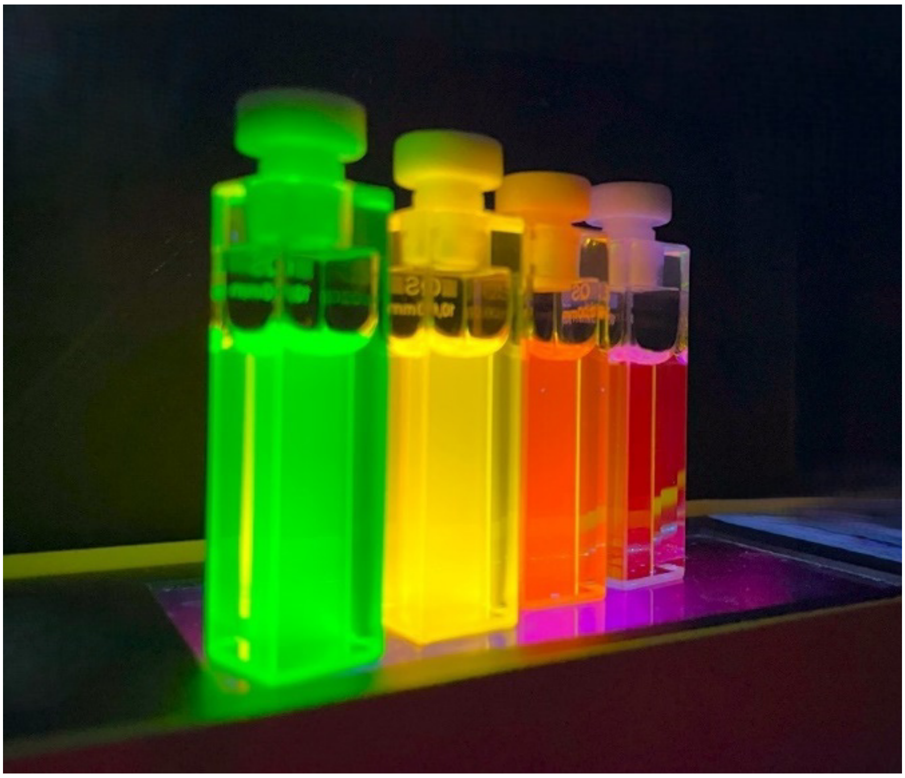

Figure 1: *Colloidal CdSe QDs of different sizes under a UV lamp.*

One of the most extensively studied NC systems are CdSe quantum dots (QDs). The CdSe QDs are particularly attractive for their exemplary optical properties that include a narrow photoluminescence band width and high photoluminescence quantum yields etc. These make CdSe QDs highly suitable for device applications such as light-emitting diodes (LEDs)[9-11] or in sensors.[12-16] The variation in the size of CdSe QDs allows for the tunability of the valence and conduction band levels, which in turn enables the optimization of band gaps. This facilitates the variation in emission colors and ensures the availability of sufficient driving force for energy and electron transfer processes. This has made CdSe QDs attractive light-absorbing candidates in photocatalytic reactions,[14, 16] LEDs,[9-11] and sensors.[12, 13] The synthesis of high quality (with respect to crystallinity and control over size distribution) CdSe QDs has been achieved via the well-established colloidal hot-injection method.[8, 17] Such colloidal CdSe QDs are usually capped with surface ligands with long aliphatic chains, e.g., trioctylphosphine oxide (TOPO), octadecylphosphonic acid (ODPA), oleic acid (OA), hexadecylamine (HDA) etc.[18] These surface ligands provide colloidal stability, stabilize the QD surface, and passivate dangling bonds. The dangling bonds are detrimental to the properties of QDs since they act as a source of surface trap states or introduce additional trapping states depending on the anchoring group of the surface ligand.[19-21] Surface functionalization can also alter the dispersibility of the QDs in different solvents, rendering them suitable for applications in various solvent environments, e.g., in aqueous environments for sensor applications in biological systems[12] or photocatalytic applications.[16, 22]

In such NC-based applications, the photophysical mechanism is governed by the properties of a photoexcited electron-hole pair, known as an exciton. The exciton generation, recombination, dissociation, and separation into free charge carriers play a pivotal role in determining the efficiency of NC-based applications, e.g., photocatalysis and photovoltaics.[14, 16, 23-25] One of the highly interesting phenomena exhibited by semiconductor NCs is the formation of multiple excitons or multiexcitons, coherent states involving multiple electron-hole pairs, formed upon high excitation density photoexcitation[26, 27] or via a process called multiexciton generation[27] (MEG), where a single photon (having atleast twice the higher energy than the band gap) absorption leads to the formation of multiple excitons. The formation of multiexciton states is facilitated by the high degree of degeneracy and large absorption-cross-section of NCs.[28, 29] Multiexcitons are of interest for potential applications of NCs in optical amplification[30] and could also be valuable for generating charge carriers in photovoltaics[27], as well as for photochemical and photocatalytic[31, 32] processes that involve multielectron mechanisms. The multiexciton lifetime is crucial in such applications because it directly influences the efficiency and effectiveness of the targeted processes. Longer multiexciton lifetimes allow the effective separation and utilization of charge carriers before they recombine, thus enhancing the overall efficiency of energy conversion and photochemical reactions.[33] Moreover, the formation of multiexcitons concurrently gives rise to population inversion in the NC ensemble, thereby enhancing the stimulated emission probability and rendering it eminently suitable for NC lasers. In NC lasers, longer multiexciton lifetimes increase the probability of achieving stimulated emission, thereby lowering the lasing threshold and improving optical gain.[34] However, the spatial confinement of charge carriers in NCs leads to stronger Coulombic interactions between electrons and holes, which results in enhanced non-radiative Auger processes, e.g., Auger recombination, compared to the bulk semiconductors.[35] Auger recombination involves multiexciton annihilation via promoting a third carrier to a higher energy level by the electron-hole exchange energy.[36] Hence, in NC-based applications, Auger recombination represents a dominant carrier-loss mechanism.[36] Unfortunately, the strong carrier wavefunction overlap in NCs results in fast Auger recombination of multiexciton states in the time range of 10s to 100s of ps.[26, 31, 35, 37] With rigorous research in the last several years, it has been demonstrated that both exciton and multiexciton lifetimes can be tuned via structural parameters like size, shape, and surface functionalization of NCs. To this end, CdSe QDs have been of the prime interest due to the established electronic structure which helps in a comprehensive understanding of excitonic properties.[38-40] Prolonged multiexciton lifetimes in CdSe QDs have been shown upon formation of CdS shells, either spherical or rod-shaped, which is attributed to the reduced carrier wavefunction overlap resulting in the suppression of Auger recombination due to the carrier delocalization to the CdS part.[41] Spectroscopic studies of multiexciton dynamics in CdSe QDs have been primarily focused on biexciton properties. However, higher order multiexciton states are equally important, offering valuable insights into underlying mechanisms and providing opportunities for material engineering. These high-order multiexciton states are particularly relevant for applications such as NC lasers and photovoltaics, where enhanced control over exciton interactions can lead to improved device performance and new functionalities. Moreover, thin films of colloidal QDs, can be produced via solution processing of colloidal QDs with controlled homogeneity and packing density, enabling fine-tuning of optoelectronic properties.[42, 43] Such assemblies of colloidal QDs are widely used in applications such as photovoltaics, NC laser etc. Therefore, the investigation of multiexciton properties is not only limited to QD solutions but also needs to be extended to QD thin films. Closely packed QD thin films are highly interesting for multiexciton dynamics. Unlike in the solution, the Auger processes can get more complex because of dominating inter-QD electronic coupling in thin film. In such films, close coupling between QDs facilitates rapid energy transfer and promotes the generation of multiple excitons from a single high-energy photon.[27] This process, known as MEG, can significantly boost the number of charge carriers available for electricity generation. By minimizing non-radiative recombination and enhancing exciton dissociation, strongly coupled QD thin films can lead to more efficient solar energy conversion, making them a promising material for advanced photovoltaic technologies.[27] This presents a scenario in which it becomes essential to unravel the complex dynamics of multiexciton within QD thin films, particularly under conditions of strong electronic interactions. In such films, exciton-exciton interactions and charge carrier behavior are significantly influenced by quantum confinement, inter-dot coupling, and surface ligand effects. These factors complicate the understanding of multiexciton dynamics, requiring detailed investigation to isolate and analyze the individual processes contributing to the overall excitonic behavior. Such insights are critical for optimizing QD thin films for advanced optoelectronic applications.

1.1 Motivation and Goals of the Work

Inspired by the potential of multiexcitons for the applications in photocatalysis, photovoltaics, NC lasers, and optoelectronic devices, this thesis work investigates the influence of size and surface functionalization on exciton and multiexciton properties in colloidal CdSe QDs. The objectives of this work are (i) to develop colloidal CdSe QDs of different sizes and to perform surface modification with surface ligands known to introduce surface traps, (ii) to determine exciton and multiexciton lifetime and spectral shape as a function of QD size and surface ligands, (iii) fabricate QD thin films and evaluate the influence of electronic interactions between nanocrystals in densely packed QDs on exciton and multiexciton properties, and finally (iv) to develop methods for fabricating QD thin films in templates such as porous silica matrix with the goal of achieving high-performance optoelectronic devices.

To address the objectives outlined, the work is divided into four chapters. Figure 2 illustrates a graphical representation of the overall thesis work. The Chapter 3 presents a discussion of the synthesis of colloidal TOPO capped CdSe QDs with varying sizes via the hot-injection method. Additionally, post-synthetic surface modification is performed via ligand exchange with mercaptopanoic acid (MPA), mercaptoundecanoic acid (MUA), and sulfide (S^{2-}) ligands, and their impact on optical properties are evaluated by absorption and photoluminescence spectroscopy. Different surface ligands with varying molar masses exert a pronounced effect on the acoustic phonon frequencies of QDs, which in turn affect properties, such as carrier trapping and photoluminescence linewidth. Therefore, Raman spectroscopy is additionally utilized to examine the influence of the surface ligands on the acoustic phonons of CdSe QDs. Subsequent to the QD synthesis and ligand exchange protocols established in Chapter 3, Chapter 4 demonstrates the implementation of intensity-dependent transient absorption spectroscopy (TA) to investigate the exciton and multiexciton properties of different sizes of colloidal CdSe QDs functionalized with TOPO and S^{2-} ligands. The evaluation and identification of the exciton and multiexciton species contributing to the intensity-dependent TA spectra, their lifetimes, and spectral shapes are simultaneously determined by a special global fitting routine based on Markov Chain Monte Carlo (MCMC) sampling. Further in Chapter 5, these investigations are extended to thin films of QDs, wherein the analysis of exciton and multiexciton properties in QD thin film is undertaken. This work is devoted to the fabrication of a QD thin film to examine the multiexciton properties under the conditions of strong and weak electronic coupling between QDs in thin films. Lastly, in Chapter 6, a strategy for immobilizing and embedding colloidal QDs in porous silica matrices is explored to prepare new luminescent materials. A comparative analysis of QD synthesis has been conducted using the successive ionic layer adsorption and reaction (SILAR) method in addition to the hot-injection method, dedicated to the fabrication of QD thin film using porous silica matrix as a template. This includes the fabrication of CdSe QD thin films embedded in porous layers, which serves to mitigate issues such as photooxidation and photodegradation.

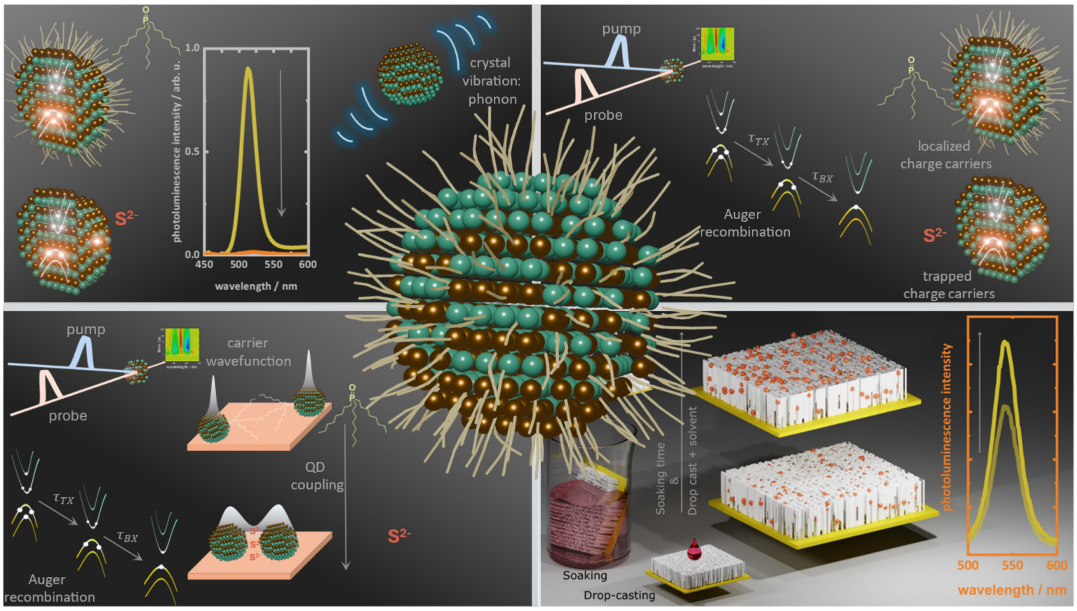
photoluminescence intensity / arb. u.
1.0
0.5
0.0
450
500
550
600
wavelength / nm
S2-
crystal
vibration:
phonon
pump
probe
τ_{TX}
τ_{BX}
Auger
recombination
localized
charge carriers
S2-
trapped
charge carriers
pump
probe
carrier
wavefunction
QD
coupling
S2-
τ_{TX}
τ_{BX}
Auger
recombination
Soaking time
&
Drop cast + solvent
Soaking
Drop-casting
photoluminescence intensity
500
550
600
wavelength / nm

Figure 2: *Graphical illustration of the thesis work divided into four chapters. The top left panel represents the Chapter 3, illustrating the influence of carrier trapping introduced by surface ligands on photoluminescence property. The top right panel represents the Chapter 4, illustrating the influence of carrier trapping on Auger recombination of multiexcitons observed by TA spectroscopy. Chapter 5 is represented in the bottom left panel, illustrating the effect of surface functionalization on exciton delocalization in QD thin film, and the impact on Auger recombination process probed by TA spectroscopy. The bottom right panel illustrates Chapter 6, with the methods to fabricate QD thin film by depositing it in a porous silica matrix.*

2. Scientific Background and Methodology

2.1 Colloidal Synthesis of Semiconductor NCs and Surface Modification

A plethora of methodologies have been developed for the synthesis of NCs, like chemical vapor deposition, molecular beam epitaxy, laser ablation, magnetron sputtering, etc.[44] Amongst the diverse synthetic approaches available, colloidal synthesis of semiconductor NCs has proven to be significantly advantageous.[8] In this approach, the NCs are grown in liquid phase yielding particles comprising an inorganic core and a shell of organic surface ligands, which can then be dispersed in different solvents depending on the nature of the surface ligands. Usually, colloidal synthesis employs high-boiling organic solvents that provide the scope for harvesting a wide temperature range for the growth of NCs resulting in the fine-tuning of their shape and size.[45] Colloidal synthesis has been exploited to synthesize different classes of materials including the III-V groups (e.g., InP, InAs),[46] metal chalcogenides of II-VI group (e.g., CdSe, CdS, ZnSe),[8, 17] IV-VI group (e.g., PbSe, PbS),[47] and perovskites, etc.

Understanding the formation mechanism of semiconductor NCs in colloidal synthesis necessitates a grasp over the concepts of nucleation and growth.[48] Nucleation is the first event during the formation of a crystal which essentially is the formation of a kinetically stable assembly of atoms that tends to minimize its Gibbs free energy by accumulating more monomers. For an isotropic spherical NC, the Gibbs free energy change upon nucleation can be expressed as the sum of the energetic gain due to bond formation and the total surface energy as described in Eq. (1).

$$\Delta G = \frac{4}{3}\pi r^3 |\Delta G_v| + 4\pi r^2 \gamma \tag{1}$$

Here, r is the radius of the nuclei formed, G_v is the Gibbs bulk free energy per unit volume and γ is the surface free energy per unit area. ΔG_c in Figure 3 corresponds to a maximum in the plot of Gibbs free energy change vs. radius of the nucleus, which depicts the activation energy needed to overcome for nucleation to occur.[48] r_c corresponding to ΔG_c in Figure 3 is the minimum critical radius above which the nucleus can proceed to the growth stage, while those smaller than r_c will redissolve into atoms.

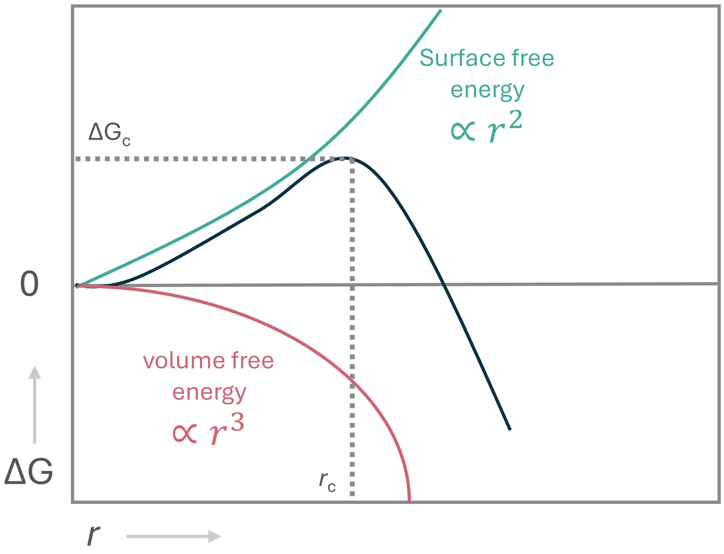

Figure 3: *Plot of Gibbs free energy vs. radius of nucleus.*

The growth phase proceeding nucleation is the actual deposition of monomers on the growing crystal. The aggregation of monomers is marked by two events, first is their transport to the NC surface and second is their reaction at the surface of the growing NC. The first event occurs via diffusion and thus the rate can be dominated by the diffusion coefficient D, whereas the rate of the second process can be defined as simply the rate of reaction between monomers and the NC surface. Generally, an excess of precursors is used to initiate growth and, therefore, the effect of diffusion can be neglected, and thus the rate entirely depends on the rate of the reaction between free monomers and the NC surface. In such a scenario, the growth regime is called a reaction-controlled growth rate.[17] In this time the growth rate is proportional to the surface area of the particle and a decrease in relative size distribution commences during this stage. The growth rate can be expressed as described in Eq. (2),

$$\frac{dr}{dt} = kV_m(S_b - S_r) \tag{2}$$

Here, k is the reaction rate constant, V_m is the molar volume of the solid, S_b is the bulk concentration of the monomer, and S_r is the solubility of the particle as a function of its radius r. However, as time progresses the concentration of monomers decreases, and subsequently the rate also becomes dependent on the diffusion of the monomers, and when this becomes the rate-limiting step then the growth rate is a 'diffusion-controlled growth rate'.[17] The growth rate according to Fick's law of diffusion is given as

$$\frac{dr}{dt} = DV_m\left(\frac{1}{r} + \frac{1}{\delta}\right)(S_b - S_r) \tag{3}$$

where D is the diffusion coefficient and δ is the thickness of the diffusion layer.

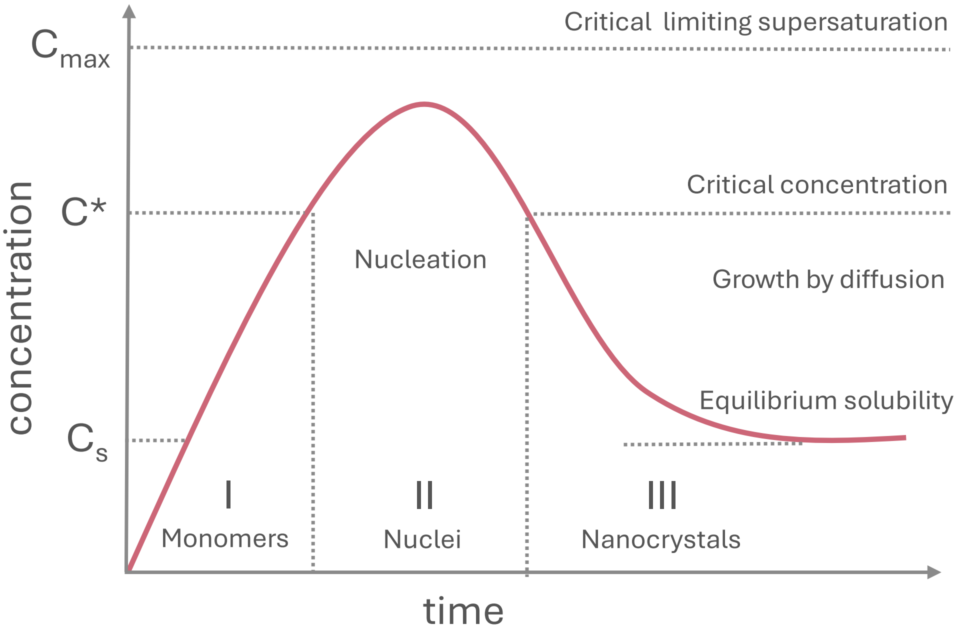

***Figure 4:** LaMer model depicting the three phases of the NC formation.*

The LaMer model[49] establishes a relation between nucleation and growth of colloidal NCs and is depicted in Figure 4. The model recognizes three phases in the formation of NCs. In the first phase, the concentration of monomers increases due to the availability of many precursors or changes in reaction parameters. Following this, the monomer concentration reaches the critical concentration (C^*), which marks the commencement of the second phase i.e., nucleation, wherein the addition of monomers forms nuclei. The termination of the nucleation process takes place when the concentration of monomers falls below C^*. Subsequently, the third growth phase of the NCs starts with monomer deposition on existing nuclei until the monomer concentration decreases below the critical level. The LaMer model describes three separate events, however, in a practical scenario, additional nuclei other than the ones undergoing the growth, can also be simultaneously formed. This often leads to a broad size distribution of NCs, a drawback of the LaMer model. Subsequently, Sugimoto proposed a relation between the size distribution and growth rate considering the particle solubility based on the Gibbs-Thomson equation for the diffusion-controlled growth rate.[50] This model suggests that when the size of the NCs is slightly larger than the critical radius then the smaller particles grow faster than the larger ones that facilitates focusing of the size distribution. With time, the concentration of monomers decreases, and the critical radius becomes larger than the average size. When this occurs, the smaller particles start shrinking and eventually redissolve into monomers, with the possibility of redepositing on larger particles. The dissolved monomers can deposit on smaller crystals resulting in larger particles. This defocusing of size distribution is known as 'Ostwald ripening', which is a common contributor to the broad size distribution. An experimental investigation of the relation of the size distribution of NCs with the growth rate for the synthesis of CdSe and InAs NCs was done by Alivisatos and coworkers.[51] During their study they found that during the initial event of injection, after a certain time, a narrow size distribution is observed (focusing), when the size of the particles is slightly larger than the critical radius. Upon monomer consumption the growth rate is predominantly diffusion controlled, resulting in low supersaturation of monomers, which in turn leads to defocusing of size distribution. They introduced a second event of injection of precursors after the broadening of the size distribution resulted in a second focusing regime. Therefore, it was shown that a high supersaturation of monomers is essential to keep the average size slightly larger than the critical radius which results in a narrow size distribution. This separation in the nucleation and growth phases has been obtained via hot injection and heat-up methods. Both these strategies have been shown to facilitate the growth of monodisperse NCs. In the first hot-injection approach, separation of nucleation and growth is achieved through a 'nucleation burst', wherein the concentration of the monomers rapidly increases above the nucleation threshold on rapid injection of precursors at a high temperature. Typically, these reactions are carried out in the presence of high-boiling organic solvents, like TOPO, tri-n-octylphosphine (TOP), 1-octadecene (ODE), alkane amines, alkanethiols, etc.[44] The hot-injection method was first carried out by Murray et al.[8] in 1993, which resulted in considerably monodisperse Cd chalcogenide NCs. The metal and chalcogenide precursors were prepared in high boiling solvents of TOP and TOPO. Rapid injection of Cd precursors into hot solvents at 300°C resulted in monodisperse CdSe and CdTe particles. This synthesis paved the way for the synthesis of monodisperse colloidal semiconductor NCs of the II-VI family and since then multiple reports with narrow size distribution have been published. Contrary to the hot-injection method, in the heat-up approach supersaturation of nucleation is achieved by in-situ formation of reactive species by increasing the temperature. Here, the precursors have lower reactivity at low temperatures and upon reaching a particular temperature, a nucleation burst is attained, since the reactivity of the precursors increases at this temperature. Monodisperse high-quality CdSe NCs synthesized via the heat-up method were reported by Cao et al.[52] In addition, the SILAR method is commonly employed for the synthesis of QDs.[53] In this technique, thin films of QDs are fabricated by alternately immersing a substrate into precursor solutions, where ionic adsorption and surface reactions occur sequentially. This stepwise deposition allows for layer-by-layer growth of QDs, with each cycle contributing to a uniform and controlled increase in QD size. Unlike the hot-injection method, room-temperature synthesis of QD is performed in the SILAR method. The synthesis of CdS NCs has been demonstrated by the SILAR method by successive growth of Cd^{2+} and S^{2-} ions .[53] Typically, the SILAR method is used to grow NCs on porous matrices, where the porous structure provides defined space for NC growth allowing precise control of NC size.[54] [55, 56]

In colloidal QDs, the surface ligands play a critical role both in the synthesis and applications, due to which surface engineering of QDs has been a highly interesting topic of research. The organic ligands usually contain a polar head (anchoring group), which binds to the NC surface, and a non-polar organic chain (functional group) which determines the colloidal stability.[22] A surface ligand in the context of colloidal synthesis serves several roles like stabilizing NCs in colloidal form through sufficient repulsive forces (steric or electrostatic), providing a medium for the reactants to form molecular precursors, and passivating the trap states on the core surface, which act as centers for non-radiative recombination.[19-21] Over the years various high boiling organic solvents have been tested as ligand sources for semiconductor NCs. Initial studies showed that the ligand and NC surface interacted with a dative bond between neutral electron donors with metal atoms, as in the case of the interaction of TOPO molecules with surface cadmium atoms of CdSe. However, as other molecules were investigated it was found that ligand species which act as neutral acceptors, bound ion pairs, and ionic species can be utilized as well. A classification of ligands was done by Owen which was based on the number of electrons involved in the bonding and the electron donating or accepting nature of ligands.[57] According to Owen's classification ligands that behave as neutral two-electron donors with a lone electron pair that coordinates surface metal atoms are termed as L-type ligands (e.g., phosphines, phosphine oxides, and amines). Ligands in a neutral form that have an odd number of valence-shell electrons, requiring one electron from the NC surface site to form a two-electron covalent bond were grouped as X-type. Its examples include carboxylates ($RCOO^-$), thiolates (RS^-), phosphonates ($RPO(OH)O^-$), and inorganic ions (such as S^{2-}, Cl^-, $InCl^{4-}$, $AsS_3{}^{3-}$), or bound ion pairs (e.g., $NEt^{4+}I^-$). Lastly, neutral electron acceptors with an unoccupied orbital that coordinates surface nonmetal atoms were classified as Z-type ligands (e.g., $Pb(OOCR)_2$ and $CdCl_2$). Apart from the type of bonding between the ligand and the surface, the affinity of a ligand to the NC surface is also governed by the well-known Pearson's hard and soft acid base theory (HSAB).[58] According to this theory, Lewis acids and bases can be classified into hard and soft ones, where soft-soft and hard-hard acid-base interactions are favoured over soft-hard acid-base interactions. Extending this theory to colloidal NCs, a soft ligand will have a higher affinity towards a soft metal cation residing on the surface of the NC due to the favoured soft-soft interaction. E.g., thiols being soft bases have stronger interaction with soft cations like Cd^{2+}, Pd^{2+}etc.

One of the key advantages of colloidal QDs is that the parent surface ligands (e.g., TOPO in CdSe QDs of hot-injection sythesis[8]) can be replaced via ligand exchange, a method that allows for the modification of the QD surface depending on the desired application and dispersion medium.[59-61] The selection of a stabilizing ligand generally depends on factors such as the solvent, the size of the QD, and its surface chemistry. Ligands that bind strongly to the QD surface form stable ligand layers, ensuring the stability of the nanoparticles in the solution. On the other hand, with the choice of functional groups, dispersion medium can be tuned. The long alkyl chains provide colloidal stability in non-polar solvents and aqueous dispersions, and polar or charged ligands facilitate effective solubility. In aqueous media, charged groups such as carboxylates or hydroxylates stabilize QDs effectively, depending on the pH and concentration of the solution. In addition to the alkyl chain surface ligands, inorganic surface ligands are also commonly employed to enhance the stability, functionality, and dispersibility of QDs in various media. These ligands typically consist of atoms or molecules that can form strong, covalent, or coordinate bonds with the QD surface, often improving the optical and electronic properties. Examples of inorganic ligands include metal chalcogenides, such as sulfide (S^{2-}), selenide (Se^{2-}), halides, and phosphonates, which can effectively passivate surface defects.[62] Using such ligands the distance between QDs can be tuned. For example, in photovoltaics high carrier mobility is achieved via small inorganic ligands or short organic ligands.

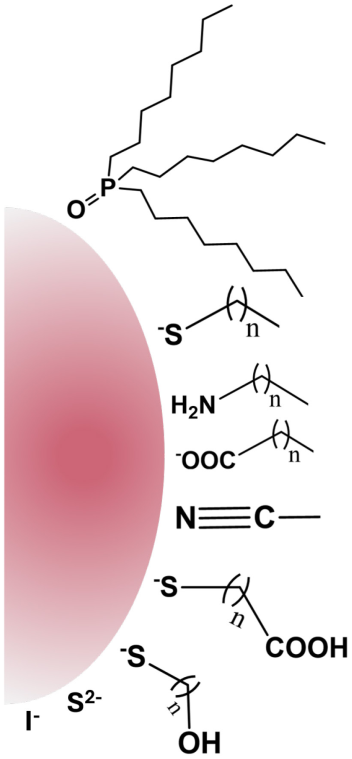

Figure 5: *Different surface ligands used for surface passivation of QD surface.*

Over the last several years, different ligand exchange procedures with different ligands have been reported.[12, 59] The most commonly used ligand exchange method is to stir the QD solution by mixing it with a highly concentrated solution of the new ligand. The efficiency of ligand exchange is highly dependent on the binding affinity of the new ligand compared to the parent ligand. Another ligand exchange method which is widely used is the biphasic ligand exchange.[61, 62] Biphasic ligand exchange with QDs involves a two-phase solvent system where QDs are transferred from one solvent to another, typically involving both a nonpolar and a polar phase. In this process, QDs initially stabilized in a nonpolar solvent are treated with a new ligand in a polar solvent phase, facilitating the replacement of the original ligands. This method leverages the different solubility characteristics of the QDs in the two phases to achieve efficient ligand exchange. This method is widely used to perform ligand exchange with inorganic ligands.[62]

In this thesis work, the synthesis of colloidal CdSe QDs with organic surface ligands via hot injection method and surface modification strategies are described for the materials used in the spectroscopic investigations. Exploiting the tunability of size via variation of injection temperature and growth time, different sizes of QDs are synthesized. Additionally, the SILAR method was also explored to perform in-situ growth of CdSe NCs in a porous silica matrix. The biphasic ligand exchange method is utilized to perform surface modification of the synthesized QDs.

2.2 Confinement effect and electronic structure of CdSe QDs

As opposed to bulk materials, semiconductor NCs are minute crystals that have dimensions in the nanoscale ranging from 1–100 nm.[44] The electronic structure of bulk semiconductors is described by energy bands that are made of a multitude of molecular orbitals (MO) formed from the linear combination of atomic orbitals (LCAO). The constituent MOs in a bulk semiconductor have very little energy difference thus creating a continuum. The low energy filled energy band is known as the valence band, and the high energy empty energy band is known as the conduction band, while the energy difference between these is known as the band gap (E_g).[63] Upon, nanostructuring the crystals undergo a phenomenon known as the quantum confinement effect[63] which increases the energy difference between the individual MOs and the band gap increases when the size decreases. Figure 6 depicts the evolution of band structures on moving from bulk-structured to nanostructured crystals.

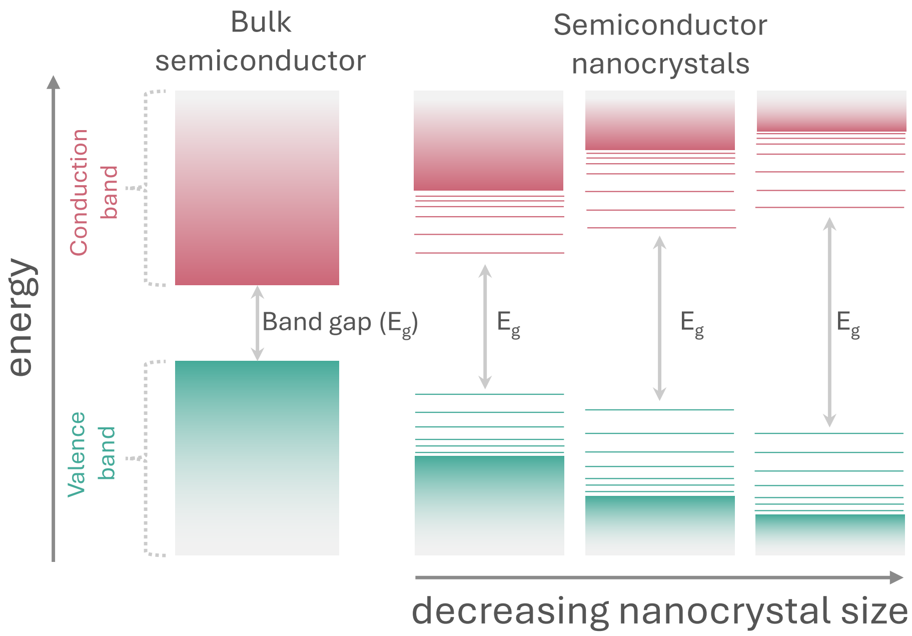

Figure 6: *Effect of semiconductor nanocrystal size on band structure.*

Absorption of a photon in a semiconductor can promote an electron from the valence band to the conduction band forming an electrostatically bound electron-hole pair called exciton. The exciton generated due to photoexcitation resides in a finite space within the crystal. The space occupied by the exciton varies with the material, and the radius of this allowed space is called the exciton Bohr radius (a_B). Eq. (4) is used to denote the exciton Bohr radius a_B.

$$a_B = \frac{\epsilon_0 \epsilon_r h^2}{\pi \mu e^2} \tag{4}$$

Here ϵ_0 *and* ϵ_r are the permittivity of free space and relative permittivity of the semiconductor, μ is the reduced mass of the electron and hole, and e is the charge of the electron. From Eq. (4) it can be inferred that the Bohr radius is dependent on the effective mass of the electron and hole and therefore is different for different materials. The quantum confinement effect described earlier becomes more pronounced when the size of a NC becomes closer to its corresponding Bohr radius. Brus equation[7] denoted in Eq. (5) is used to define the band gap ($E_g(R)$) for a spherical crystal with radius R, which also demonstrates the size effect of quantum confinement.

$$E_g(R) = E_g + \frac{h^2}{8R^2}\left(\frac{1}{m_e} + \frac{1}{m_h}\right) - \frac{1.8e^2}{4\pi\epsilon_0\epsilon_r R} \tag{5}$$

Here E_g is the bulk band gap, h is the Plank's constant, m_e and m_h are the effective masses of electron and hole, ϵ_r is the bulk optical dielectric constant or relative permittivity, and ϵ_0 is the permittivity of free space. The second term of the equation indicates that the E_g is inversely proportional to R^2, i.e., increases with a decrease in size. The opposite relation is shown in the third term, due to the increase in Coulombic interaction. However, when R is in the range of a few nanometers, the second term dominates, and the band gap increases as R or the size of the crystal decreases. This behavior is described by a particle in a box model, wherein the energy level spacing increases as the dimensions of the box decrease. The expression (Eq. (5)) stated earlier can be applied only to QDs (spherical NCs). Spherical NCs are spatially confined in all three dimensions and are known as 0D NCs. However, in practice different morphologies of NCs have been explored that have different spatial confinement. In the case of nanorods, nanotubes, and nanowires, confinement occurs within two dimensions (2D confinement) with unrestricted carrier motion along the length of the 1D NCs. Thirdly, quantization occurs within one dimension, e.g., in the case of nanoplatelets (NPLs), wherein the NCs are confined only in the thickness dimension (1D confinement). 2D materials like nanosheets and NPLs are included in this category.

In contrast, bulk materials are not confined, and free carrier motion is allowed in all dimensions and consequently, these are 3D materials. Dimensionality can also be explained in terms of density of states (DOS), as depicted in Figure 7. DOS describes the number of electronic states available per given energy. As shown in Figure 7a, for a bulk material, wherein excitons are free to move in all dimensions, a 3D DOS can be derived which is proportional to $\sqrt{E}$. In a 2D NC, free carrier motion is allowed in two dimensions while the exciton is confined in one dimension, resulting in a DOS that is independent of energy ($\propto E_0 = constant$). If there are several confined states within a 2D quantum well, then the DOS is a step function, as depicted in Figure 7b. In the case of 1D nanorods and wires the exciton is confined in two dimensions, with free motion along their length, resulting in 1D DOS with inverse square energy dependence. Figure 7c shows this dependence which reveals that the

DOS increases in fixed amounts and decreases between every step. Lastly, a 0D QD with excitons confined in all three dimensions exhibits 0D DOS with states allowed at only certain energy levels. Figure 7d shows a DOS for a 0D system which depicts a variation like that of a δ function.

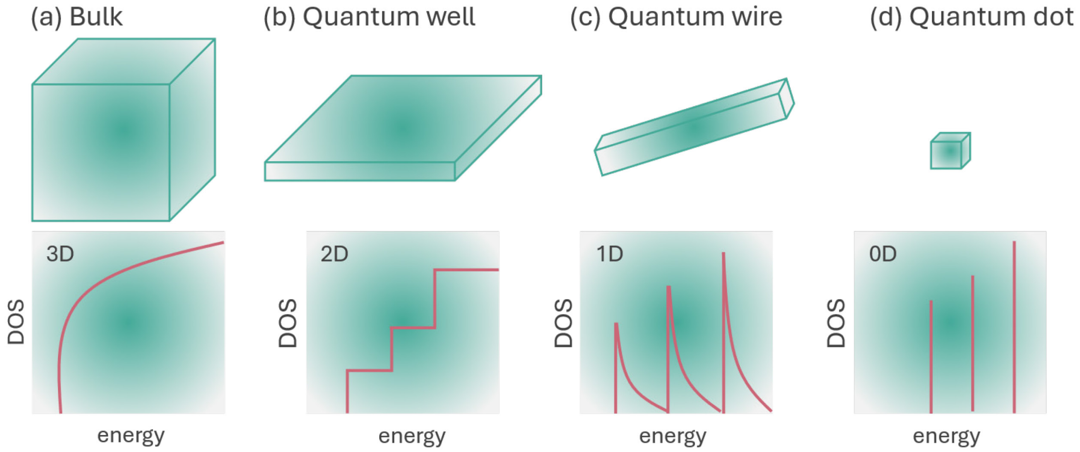

Figure 7: *DOS for (a) 3D bulk, (b) 2D quantum well, (c) 1D quantum wire, and (d) 0D QD.*

As a consequence of the quantum confinement effect, CdSe QDs exhibit discrete energy levels. To obtain the electronic structure of CdSe QDs, the confined electron-hole pair was described by the 'particle-in-a-sphere model'.[64] With this, the energy levels are defined by the typical atomic notation nL, with the principal quantum number, $n = 0, 1, 2 \ldots$, and the angular momentum quantum number, $L = 0, 1, 2 \ldots$labeled as S, P, D etc.[65] Therefore, the three lowest energy levels could be written as 1S, 1P, and 1D. However, this model provides a reasonable description for only the conduction band levels whereas the valence band levels with higher degeneracy cannot be explained with nL. The atomic origin of the conduction band levels is the 5s level of Cd with spin-degeneracy $J = {}^{1}/_{2}$. On the other hand, the valence band originates from the 4p orbitals of Se and exhibits 6-fold degeneracy. Due to the spin-orbit coupling, the 6-fold degeneracy is broken to form two upper and one lower level. The upper two levels with total angular momentum quantum number $J = {}^{3}/_{2}$, termed as heavy hole (HH, $J_m = \pm {}^{3}/_{2}$) and light hole (LH, $J_m = \pm {}^{1}/_{2}$). The lower valence band level with $J = {}^{1}/_{2}$, termed as split-off band.

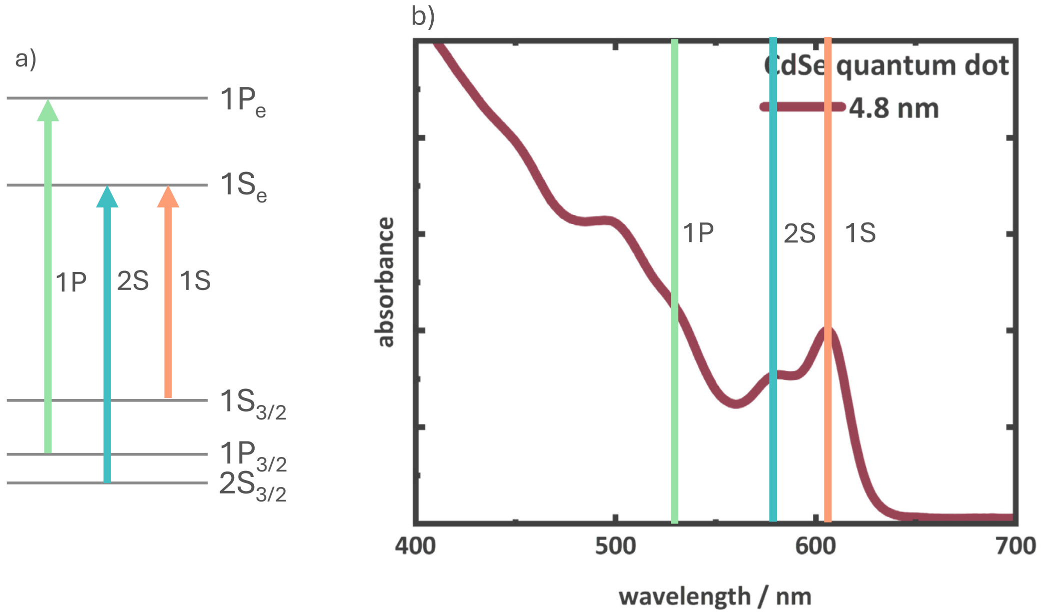

Figure 8: *(a) Electronic level structure, and (b) an absorption spectrum of CdSe QDs with the three lowest energy transitions (1S, 2S, and 1P) marked by the three lines.*

To determine the electronic configuration of the valence band levels, the coupling of Bloch wave function angular momentum ($\mathcal{J}$) cannot be ignored due to the heavier effective mass of holes in CdSe.[65] Hence, the total angular momentum of the valence band can be written as $F = J + \mathcal{J}$ and the valence band levels can be denoted as nL_F. To determine the hole energy levels, Ekimov et al.[66] developed a quantum mechanical calculation, and based on that the lowest three hole levels can be defined as $1S_{3/2}$, $1P_{3/2}$, and $2S_{3/2}$. With this, the electronic structure of CdSe QDs can be drawn as shown in Figure 8a. Figure 8 additionally shows the lowest three electronic transitions termed as $1S_{3/2}$-$1S_e$ (1S), $2S_{3/2}$-$1S_e$ (2S), $1P_{3/2}$-$1P_e$ (1P) as assigned by Norris et al.[38] which are typically observed in the steady-state absorption spectra of CdSe QDs (Figure 8b).

On the other hand, due to the strong confinement effect in CdSe QDs, processes such as electron-hole recombination cannot be explained by the particle-in-a-sphere model and need to consider the coupling of electron and hole levels (simply as an exciton but not electron and hole as different particles). This is particularly necessary to explain the photoluminescence properties. In this case, the excited state or the excitonic states are denoted as coupled conduction band and valence band levels, e.g., the lowest energy excitonic state is $1S_{3/2}1S_e$, originating from electron-hole exchange interaction between $1S_e$ (in conduction band) and $1S_{3/2}$ (in valence band) levels.[65, 67] The total angular momentum for the $1S_{3/2}1S_e$ state can be N = 1 or 2 (obtained linear combination of $1S_{3/2}$ and $1S_e$). The N = 1 or 2 states are further split by the exchange interaction forming a high-energy N = 1, bright exciton, and a lower energy N = 2, dark exciton. These states further split into five states due to the crystal field interaction originating from crystal anisotropy, e.g., in wurtzite lattice. These states are called exciton fine structures. The upper energy states denoted by U represent the states involved in light absorption states and the lower energy states denoted by L represent the emitting states. After photoexcitation, the transition (~ 200 meV) between U states to L is facilitated by phonon emission. This is one of the major reasons for the Stoke's shift observed in CdSe QD photoluminescence. After the crystal field splitting, the nature of the low energy state remains the same, $N_m = 2$ being the low energy dark state and $N_m = 1$ being the bright state. The bright and the dark states are separated by a few to 10s of meV and the population can be thermally redistributed. This also contributes to the Stoke's shift depending on temperature. At low temperatures, the low-energy dark state contributes to photoluminescence. At sufficiently high temperatures (i.e., when $kT >>$ Stokes's shift energy, k is Boltzmann constant), the exciton population is equally distributed over the dark and the bright states. The photoluminescence spectrum of CdSe QDs is described in the next section.

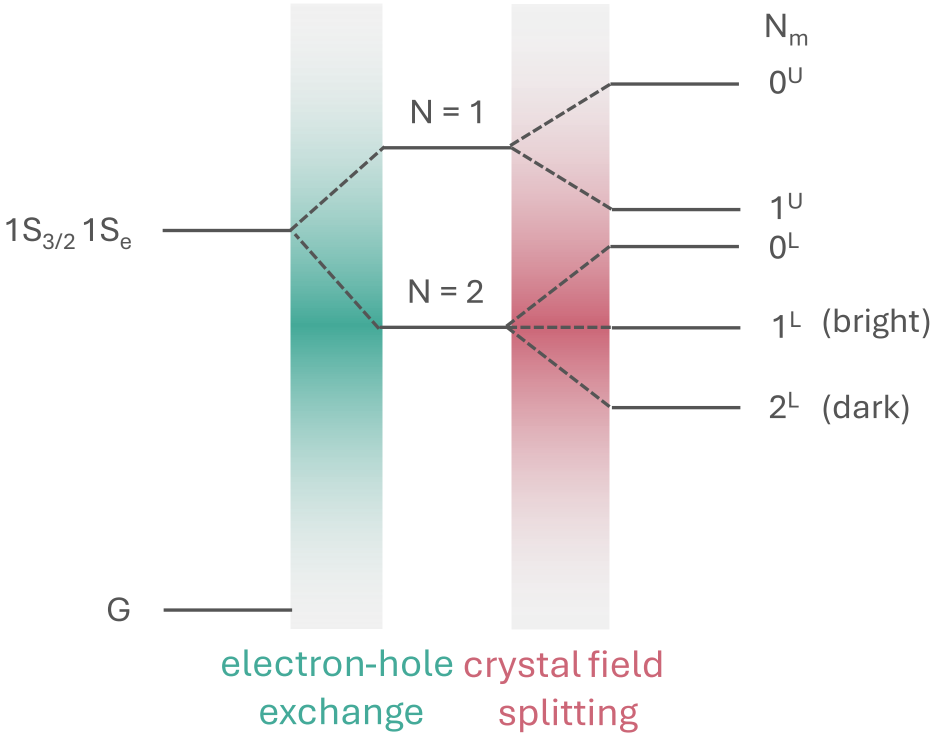

Figure 9: *Schematic of exciton fine structure splitting the first excitonic state ($1S_{3/2}1S_e$) in CdSe QDs. G represents the ground state.*

2.3 *Exciton and Multiexcitons in CdSe QDs*

Upon photoexcitation of CdSe QDs, an electrostatically bound electron-hole pair is formed, called exciton. When the photoexcitation is in high energy, the electron and hole populate higher energy levels forming hot excitons or separately can be called as hot electron or hole. These hot carriers undergo Auger cooling or phonon-assisted cooling to populate the lowest energy level as shown in the schematic (Figure 10b). This process usually occurs in the ultra-fast time scale (~100s of fs). When the cooling process is completed, radiative electron-hole recombination takes place at the lowest energy transition (Figure 10b) resulting in the band-edge photoluminescence (Figure 10a).

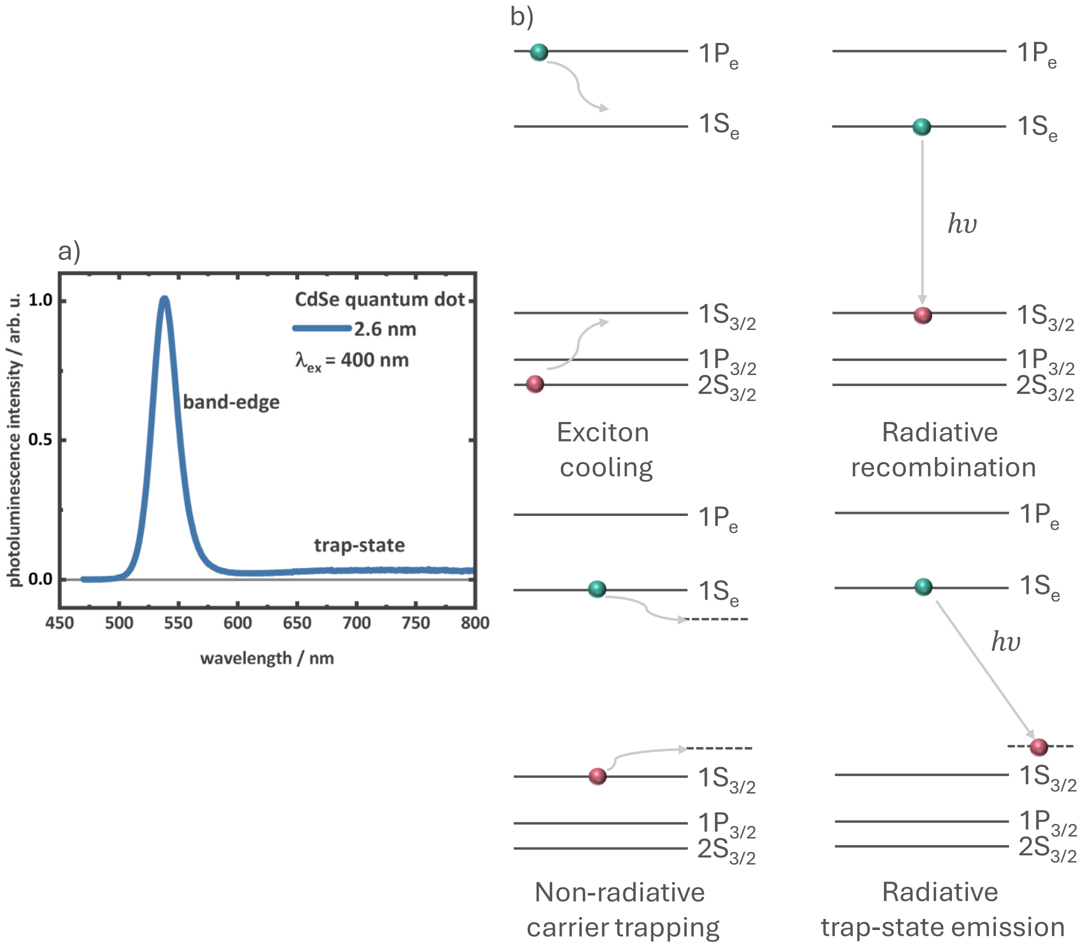

Figure 10: *(a) Photoluminescence spectra of 2.6 nm QD upon 400 nm photoexcitation. (b) Schematics of exciton cooling, radiative recombination, non-radiative surface trapping, and an example of radiative recombination involving a trap state.*

On the other hand, due to the small volume of QDs, a large proportion of atoms are located at or near the surface, leading to an increased impact of surface defects.[68]

These surface defects originate from the unsaturated surface atoms of the QDs, especially at the NC's edges or corners, which are not fully coordinated or bonded, leading to dangling bonds or vacancies.[69] The dangling bonds are responsible for the formation of a distribution of energy levels being close to the conduction band (originated from Cd-sites) and valence band (originated from the Se-sites) (Figure 10b).[59, 60] After photoexcitation, the electron-hole pair can non-radiatively get trapped to these surface sites (Figure 10b). Due to the localization of charge carriers on the trap states, electron-hole recombination can also take place involving the surface trap-state resulting in trap state emission appearing at the lower energy side to the band-edge position as shown in Figure 10a.[69, 70] However, these surface trap-states can be reduced by passivating with surface ligands. In colloidal synthesis of CdSe QDs, phosphine and phosphonic acid-based surface ligands are used to passivate the surface resulting in a reduction of trap-state emission.[59] On the other hand, surface trap states can additionally be increased with specific surface ligands.[59, 60] The surface trap-states play a crucial role in applications like photocatalysis by facilitating charge separation and enhancing photocatalytic activity.[71] These trap-states can capture electrons or holes, preventing their immediate recombination and allowing them to participate in surface chemical reactions. This extended carrier lifetime increases the likelihood of interactions with reactant molecules, driving redox processes essential for photocatalysis.[71] Utilizing the advantage of surface modification in colloidal QDs, one can perform ligand exchange to achieve the desired trap-state density via suitable surface ligands.[60] As discussed before, a variety of surface ligands, including phosphines, carboxylates, thiolates, amines, and inorganic ligands (e.g., S^{2-}, I^{-}, etc.) can be used to passivate the QD surface. All ligands exhibiting distinctive properties can be utilized for this purpose.[59] Surface ligands having anchoring groups such as thiols, amines etc. introduces additional trap states within the band gap. The energetic position (with respect to the CdSe QD energy levels) can differ in different ligands depending on the anchoring group, due to which electron traps (positioning close to the conduction band) or hole traps (positioning close to the valence band) can be generated leading to strong effect in the photoluminescence properties. For example, thiols are known to be strong hole acceptors resulting in strong band-edge photoluminescence quenching.[72] Similarly, inorganic ligands, e.g., S^{2-} are also a strong hole quencher and on the other hand useful in QD thin films with improved carrier transport.[62, 73, 74] The fundamental analysis of exciton properties upon ligand exchange can be performed utilizing steady-state absorption, photoluminescence spectroscopy, and time-resolved spectroscopic techniques. The effect of hole trapping can be monitored by band-edge photoluminescence quenching and increased trap-state emission.

Another important aspect of CdSe QDs, and semiconductor NCs in general, is their crystal vibration or phonon.[75] A phonon is a quantized mode of vibration occurring in a crystalline solid, representing the collective vibration of atoms or ions within the material. Depending on the mode vibration, phonon modes in QDs are primarily classified as optical and acoustic modes. Acoustic phonons correspond to low-energy vibrations where atoms oscillate in phase, affecting the acoustic wave propagation through the crystal, whereas optical phonons involve out-of-phase vibrations between atoms in the lattice creating a dipole that can couple with electromagnetic waves.[76] The acoustic phonon mode in colloidal QDs is particularly interesting as it exhibits a strong influence of quantum confinement effects and the mechanical coupling of the surface ligand with the inorganic core.[77] In the recent years a mechanical influence (originating from the mass of the surface ligand) of surface ligands on the acoustic phonon frequency has been discuseed.[77] The effect of surface ligands on the longitudinal acoustic (LA) mode in CdSe QD can be seen as a mass-loading effect, where heavier surface ligand induce inertial resistance and reduce the LA phonon frequency. The LA phonon mode on the other hand modulates the photoluminescence linewidth via exciton-phonon coupling.[78] Moreover, it has also been shown in previous work, that the LA mode plays a dominant role in non-radiative carrier trapping[79] as well as charge carrier transport[76] in QD thin films. This indicates that the investigation of the LA mode is not only important for size or surface ligand characterization but also for evaluating exciton dynamics in radiative and non-radiative processes.

One unique property of CdSe QDs and semiconductor NCs in general is the formation of multiple exciton pairs known as multiexcitons. This process is facilitated by the high absorption cross section and high degeneracy of energy levels. Multiexcitons are bound states involving two or more pairs of excitons. Different events can lead to the formation of multiexcitons, e.g., consecutive absorption of multiple photons, and multiexciton generation (MEG)[27] where a single photon (having atleast twice the higher energy than the band gap) absorption leads to the formation of multiple excitons. With the number of exciton pairs, multiexcitons are termed as biexciton (BX, two exciton pairs), triexciton (TX, three exciton pairs) etc. The energy level diagram of multiexciton states in CdSe QDs is shown in Figure 11.

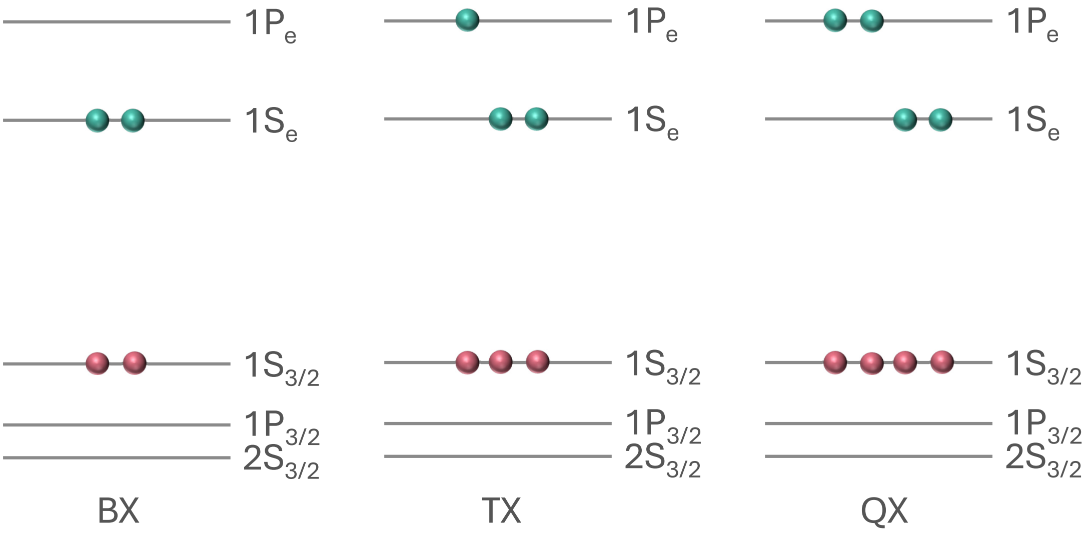

Figure 11: *A schematic of electronic level diagram of BX, TX, and QX in CdSe QDs.*

The strong spatial confinement of charge carriers in NCs leads to stronger Coulombic interactions between electrons and holes, which results in enhanced non-radiative Auger processes like impact ionization, Auger cooling, Auger recombination, and Auger ionization.[35] Impact ionization occurs via relaxation of a charge carriers from a high energy level by exciting an electron from a valence band level. Auger cooling[80, 81] is the process in which an electron-hole scattering results in simultaneous relaxation of one carrier and excitation of the other. On the other hand, Auger ionization and Auger recombination processes occur because of the scattering of similar carriers i.e., electron-electron or hole-hole. In Auger ionization, the electron-hole exchange energy is transferred to a third carrier, promoting it to a surface defect state.[82] The Auger recombination process plays the most dominating role in semiconductor NCs, involving the decay of multiexciton states via promoting a third carrier to a higher energy level by the electron-hole exchange energy.[36]

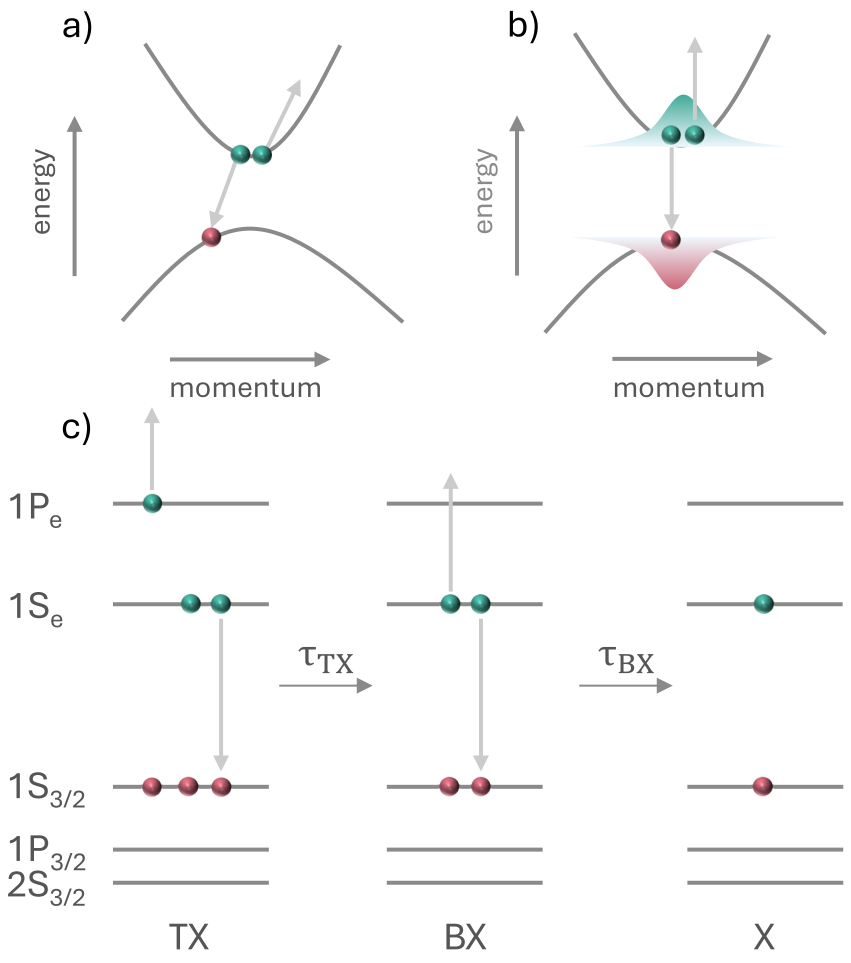
a)
b)
energy
energy
momentum
momentum
c)
1P$_e$
1S$_e$
1S$_{3/2}$
1P$_{3/2}$
2S$_{3/2}$
τ_{TX}
τ_{BX}
TX
BX
X

Figure 12: *The three-carrier Auger recombination process in a (a) bulk material, and in a (b) semiconductor NC. (c) Multiexciton recombination process in CdSe QDs, via Auger recombination process.*

In a bulk semiconductor, when n number of charge carriers are generated by photoexcitation, the annihilation process can be described by the rate law.

$$\frac{dn}{dt} = -A\,n - Bn^2 - Cn^3 \tag{6}$$

Where, A is the rate constant for trapping of charge carriers to defect sites following a first-order kinetics, B is the rate constant of radiative recombination following a second-order kinetics and C is the Auger constant. Hence, the rate law only for the Auger recombination can be written as,

$$\frac{dn}{dt} = -Cn^3 \tag{7}$$

In the case of a NC ensemble, n can be defined as the average number of excitons, $< N >$, per NC volume, V, $n = < N > V^{-1}$. With this, Eq. (7) can be modified as

$$\frac{d < N >}{dt} = -D < N >^3$$

The parameter $D = CV^{-2}$ and the lifetime of $< N >$ can be derived as

$$\tau_{<N>} = (B \times < N >^2)^{-1} \tag{9}$$

The average number of excitons $< N >$ depends on the photon density (J) of excitation and the absorption cross section (α):

$$< N > = J \times \alpha \tag{10}$$

However, in contrast to a bulk semiconductor (as shown in Eq. (7)), the Auger recombination process in NCs occurs via a cascade mechanism, i.e. stepwise relaxation of quantized multiexciton states (e.g., $N = 2, 3, 4$ named as BX, TX, QX respectively).[36] Briefly, when a N^{th} order multiexciton is generated, the annihilation process will be

$$N \rightarrow N - 1 \rightarrow N - 2 \ldots . 2 \rightarrow 1 \rightarrow \tag{11}$$

until it ends up with a single exciton, following a first-order kinetic law in each relaxation step. The rate laws for each consecutive step can be written as,

$$\frac{d[N]}{dt} = -\frac{[N]}{\tau_N} \tag{12}$$

$$\frac{d[N-1]}{dt} = \frac{[N]}{\tau_N} - \frac{[N-1]}{\tau_{N-1}}$$

$$\frac{d[N-2]}{dt} = \frac{[N-1]}{\tau_{N-1}} - \frac{[N-2]}{\tau_{N-2}} \, ..so\ on$$

where, τ_N is the lifetime of N^{th} order multiexciton state. $[N]$, $[N-1]$, are the concentration of the respective multiexciton states. The initial concentration of each N^{th} order of exciton is characterized by the probability P_N of population upon excitation. When the NC ensemble is excited in the high fluence regime with high degeneracy of energy levels, independent events of excitation will occur.[83] Hence, the initial population probability P_N can be described by Poisson distribution[36] as follows:

$$P_{N,0} = \frac{<N>^N \times e^{-<N>}}{N!} \tag{13}$$

In the rate equations $[N]$ can be exchanged with the population probability and Eq. (12) can be rewritten as

$$\frac{dP_N}{dt} = -\frac{P_N}{\tau_N}$$

$$\frac{dP_{N-1}}{dt} = \frac{P_N}{\tau_N} - \frac{P_{N-1}}{\tau_{N-1}} \tag{14}$$

$$\frac{dP_{N-2}}{dt} = \frac{P_{N-1}}{\tau_{N-1}} - \frac{P_{N-2}}{\tau_{N-2}} \, ..so\ on$$

Therefore, the lifetime of a multiexciton state can be determined by solving Eq. (14) provided $P_{N,0}$ as the initial occupancy is known. The relation between P_N and $<N>$ is

$$<N> = \sum_N N \times P_N \tag{15}$$

Hence, the expression of the overall decay process of $<N>$, via the cascade kinetic model (Eq. (11)), can be written by combining Eq. (14) and Eq. (15) as

$$\frac{d<N>}{dt} = -\sum_{N}^{1} \frac{P_N}{\tau_N} \tag{16}$$

When N excitons are generated upon photoexcitation, and it is approximated that the relative distribution of NC occupancy is very small, i.e., $< N > \approx N$, the ensemble average lifetime can be derived from Eq. 10 as,

$$\tau_{<N>} = < N > \times \tau_N \tag{17}$$

Now by comparing Eq. (9) and Eq. (17), one can derive two crucial expressions,

$$\tau_N \propto N^3 \tag{18}$$

$$\tau_N \propto V \tag{19}$$

Eq. (18) shows cubic dependency on N, indicating that a three-particle model is followed through the cascade and Eq. (19) exhibits a linear dependency on the NC volume. Eq. (19) provides an important aspect in engineering materials for a desired multiexciton lifetime by controlling its size or shape.

In the recent years, a substantial number of theoretical and experimental studies have been conducted to examine the spectral and dynamical characteristics of multiexcitons in semiconductor NCs.[36, 65, 84-86] The spectroscopic techniques employed for the analysis of multiexciton formation and recombination dynamics primarily encompass TA[84, 87] spectroscopy and time-resolved photoluminescence[88-90] (tr-PL) spectroscopy. Both the methods are important in providing insights into multiexciton dynamics. The TA signal, with the complex combination of effects from state-filling and Stark shifts, offers a more comprehensive representation of the electronic population of multiexcitons, providing insights into their spectral shape and amplitude.[65, 91, 92] In recent years, most of the studies have extensively focused their investigations on BX, the lowest multiexciton, and only a few up to TX. The major focus has been to determine the size dependency on multiexciton lifetime. The cubic dependency of BX lifetime with CdSe QDs radius (i.e., linear with volume) as predicted by Eq. (19) has been previously reported.[36, 93] Similar dependencies were observed in PbSe,[36] HgTe,[94] InAs[95] QDs and perovskite NCs[96, 97]. Multiexciton lifetime is not only dependent on the size of the particle but also the surface structure.[98] When a QD has a high number of surface defects resulting in carrier trapping, it decouples the electron-hole wavefunctions leading to the suppression of Auger recombination.

2.4 Transient Absorption Spectroscopy

TA spectroscopy is a time-resolved technique commonly used to study the exciton dynamics of QDs. It involves exciting QD particles with a short pump pulse of light to promote electrons to higher energy levels, followed by a probe pulse at various time delays to measure changes in absorbance in the QDs. The technique captures how excitonic states evolve over time, providing insights into processes such as energy transfer, charge separation, and electron-hole recombination. The TA setup used in this work is illustrated in Figure 13. The experimental details are described in Appendix A.

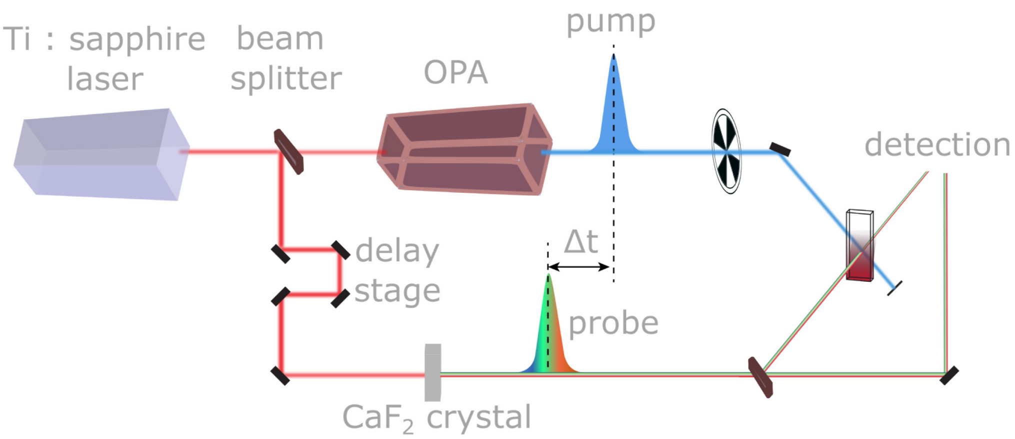

Figure 13: *Schematic of the femtosecond TA set-up used in this thesis work.*

The method involves two primary sources, a pump and a probe originating from a femtosecond laser (for fs-TA). The short pump pulse excites the samples by promoting the majority of the samples in the ground state to the excited state. Immediately after that event, a probe pulse (usually spanning a broad range of wavelengths) is used to measure the absorption of the sample at different times after excitation. Experimentally, the arrival of the probe pulse (with respect to the pump pulse) is controlled by an optical or an electronic delay state, so that the probe pulse can measure the absorption of the pump excited sample at different times after excitation. The use of a white light probe is crucial because it allows measurement across a wide spectral range, capturing multiple transitions that occur in the excited state. The key feature of TA spectroscopy is the pump-on and pump-off measurement approach. In a pump-on (P_{on}) measurement, the pump pulse excites the sample, while in a pump-off (P_{off}) measurement, the pump pulse is absent, and only the probe pulse interacts with the sample in its ground state. The difference between these two conditions is essential because it allows the isolation of the transient absorption signal, which results solely from changes in the sample due to excitation. This way a differential absorption ($\Delta A\ (\lambda, t)$) spectrum is obtained as shown in Eq. (20).

$$\Delta A\ (\lambda, t) = log\left(\frac{P_{ref}(\lambda, t)}{P_{on}(\lambda, t)}\right)\left(\frac{P_{ref}(\lambda, t)}{P_{off}(\lambda, t)}\right) \tag{20}$$

This spectrum as a function of wavelength (λ) and delay time (t) reflects how absorption changes as a function of time after excitation, giving insights into the excited-state dynamics. The P_{ref} is a reference probe pulse recorded without going through the sample.

In a transient absorption spectrum, the observed signals are ground-state bleach (GSB), stimulated emission (SE), and photoinduced absorption (PIA). GSB arises when the ground-state population is depleted after excitation, causing a reduction in absorption at the wavelengths corresponding to ground-state transitions. SE occurs when the excited state radiatively relaxes back to the ground state, emitting light at characteristic wavelengths. The PIA is observed when the excited state itself absorbs further energy, corresponding to transitions from the excited state to higher energy levels. In combination with these signals a 2D data set as a function of λ, and t is collected which contains spectral development of excited species over the delay time (Figure 14a). A typical TA spectrum of CdSe QDs is shown in Figure 14c.

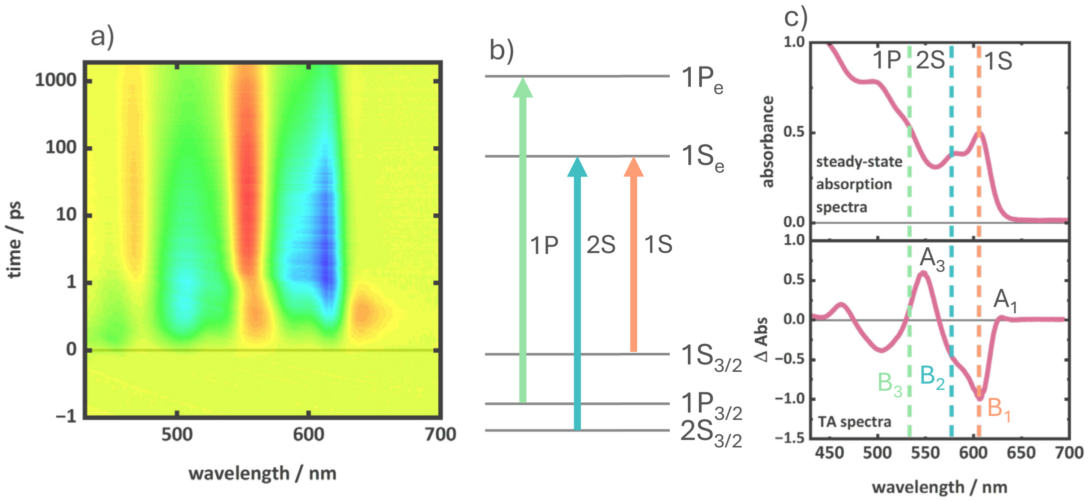

Figure 14: *(a) 2D plot of TA data representing the evolution of ΔA as function of λ, and* t. *(b) electronic level diagram of CdSe QD showing the lowest three electronic transitions. (c) steady-state absorption and TA spectra (at 1900 ps) of CdSe QD representing the spectral features of the lowest three electronic transitions.*

In Figure 14c, the typical spectral features of CdSe QDs are illustrated. The negative bleach signals of the lowest three electronic transitions in the steady-state absorption spectrum, 1S, 2S, and 1P are labeled as B_1, B_2, and B_3. Additionally, two distinct positive PIA features red shifted from the B_1, and B_3 are observed and labeled as A_1 and A_3. These TA signals of CdSe QDs are caused mainly by two effects: the state-filling effect and the Coulomb effect or Stark effect. The state-filling effect is a phenomenon, where the filling of quantized electronic levels leads to the bleach of the corresponding transition populating this level in the transient spectra because of Pauli exclusion principle.[84, 99] For example, when the $1S_e$ level in the conduction band of CdSe QDs with 2-fold degeneracy is filled by the pump excitation, the corresponding optical transitions involving the $1S_e$ level cannot take place, resulting in bleaching of this signal. Due to this effect, one can determine the carrier population by analyzing the relative change of bleach amplitudes with respect to pump intensity. On the other hand, the effect of Coulomb interaction on the TA signal arises from the carrier-induced Stark effect.[91] The local fields of the pump-generated carriers cause energetic shifts in optical transitions as well as changes in oscillator strengths. Unlike the state-filling effect, the carrier-induced Stark effect modulates the spectral position optical transitions and effects also transition unoccupied energy levels. With the help of these distinctive features, one can locate the population of conduction band levels and consequently their temporal changes, for instance during, electron-hole recombination, electron transfer, and energy transfer etc.

To investigate multiexciton properties, experiments with increasing pump intensity are performed. Increasing pump intensity allows simultaneous absorption of multiple photons leading to the formation of multiexcitons. The analysis of multiexciton dynamics in TA data is commonly conducted through single wavelength multiexponential fitting of the B_1 kinetics, which corresponds to the band-edge decay.[65, 84] With the formation of multiexciton states, the bleach signal increases, resulting from increasing state-filling effect. Additionally, the kinetics traces show with increasing pump intensity, hence multiexciton formation, additional fast decaying components which are assigned to multiexciton annihilation due to the fast Auger recombination processes. To extract the multiexciton lifetime, the data is modeled from the Auger recombination model (as previously described) Eq. (14) needs to be solved. However, when high-order multiexcitons populate simultaneously both the $1S_e$ and $1P_e$ (can also be higher levels with higher order multiexcitons) levels, the spectral signatures change over the whole spectral range. For instance, the A_1 feature exhibits a negative signal in the multiexciton regime and a positive signal in the exciton regime. If the intensity-dependent TA spectra are evaluated by single wavelength fit, such spectral signatures will not be properly investigated. Due to this a global fit regarding the entire range of wavelengths probed and for varying intensities is necessary to extract complete temporal and spectral evolution.[83, 100] In the global fitting, the intensity-dependent TA data is treated as a sum of the spectra ($S_N(\lambda)$) corresponding to each multiexciton species, N. The spectral shape of S_N is considered as independent of pump intensity and delay time but only its weight varies with an amplitude co-efficient $A_N(t,J)$, which is dependent on pump intensity (J). $A_N(t,J)$ is related to P_N, with which the initial concentration of multiexciton species is determined by using Poisson probability as shown in Eq. (13). With this, the intensity-dependent TA spectra are simulated as,

$$\Delta A(\lambda, t, J) = \sum_N A_N(t, J)\, S_N(\lambda) \tag{21}$$

To extract the multiexciton lifetimes, the Auger recombination model (as described in Eq. (14)) is used. Further, to determine the multiexciton spectra and lifetimes, a fitting routine capable of handling a large free parameter range is required. To this end, a method based on Markov Chain Monte Carlo (MCMC) sampling has been established by Ashner et al.[101] to fit intensity-dependent TA data. In this fitting routine, the multiexciton lifetimes, spectra, and an intensity parameter (corresponding to absorption cross section) are simultaneously fitted to deconvolute the three-dimensional ($\Delta A(\lambda, t, J)$) TA dataset.

MCMC sampling is an efficient method to fit such a large data set to obtain multiple fit parameters with high precision. It is a technique used to sample complex probability distributions, especially when direct sampling is difficult. To establish the fitting routine in the TA data, a framework of Bayesian inference is used. Bayesian inference is a statistical method that updates the probability estimate of having a parameter. It is based on Bayes' Theorem, which combines the prior distribution of a parameter with the likelihood of observed data to produce a revised probability (posterior distribution). This means that the conditional probability of having a certain set of parameters, θ, is described in terms of the observed data, x, which is the posterior probability. This can be calculated using Bayes' theorem as,

$$P(\theta|x) \sim P(x|\theta)\, P(\theta) \tag{22}$$

Here, the first term ($P(x|\theta)$) is the likelihood function, and the second term is the probability of a set of parameters being correct (posterior probability). To derive the posterior probability, MCMC begins by initializing a set of walkers across the parameter space. Walker refers to an individual sample or point in the parameter space that represents a possible solution or combination of model parameters. These walkers traverse the parameter space, moving based on probabilistic rules that aim to explore regions of high likelihood. Each walker proposes new positions (sets of parameters), and whether these moves are accepted or rejected depends on the likelihood of the proposed set of parameters relative to the current set. The ensemble of walkers forms a Markov chain, gradually building a comprehensive representation of the posterior probability distribution of the parameters. Each walker corresponds to a unique combination of model parameters that, in turn, produces a distinct TA dataset. To explore the posterior distribution of these parameters, the walkers undergo random variations, with each new position evaluated based on the logarithmic likelihood of the corresponding model. The acceptance of random moves is dependent on the probability of occurrence, which is determined by the log-likelihood. The algorithm continues until a sufficiently large Markov chain is generated, representing the posterior distribution of the parameters. Once the chain converges, the samples from the walkers are used to create histograms, yielding a comprehensive picture of the posterior distribution. Within the broader algorithm, MCMC functions as the optimization tool, proposing parameter sets and maintaining a record of every iteration, ultimately refining the estimation of model parameters. This algorithm exhibits a useful property, known as affine invariance, which states that the performance of the algorithm is independent of the relative scales or offsets of the different dimensions in parameter space. The key advantage of this algorithm is that it will run efficiently without any manual tuning of parameter steps in each dimension, in contrast to a simple random walk. Due to these properties, MCMC sampling is highly promising to be applied to complex datasets such as intensity-dependent TA data and will be used in this thesis for simultaneous evaluation of multiple fit parameters including, lifetime, spectra, intensity parameters.

3. Post-synthetic Modification of Colloidal CdSe QDs: Investigation of Photoluminescence and Phonon Properties

This chapter is primarily focused on the development of a synthetic strategy for the generation of colloidal CdSe QDs and the implementation of surface modifications, in conjunction with an investigation of the fundamental exciton and phonon properties. In this chapter, the basic materials for the investigation of multiexciton properties in CdSe QDs with varying QD size and surface ligands are developed. To this end, TOPO capped colloidal CdSe QDs of different sizes have been synthesized using the hot-injection method. Furthermore, ligand exchange methods have been employed for the purpose of modifying the surface with MPA, MUA, and S^{2-}*. The impact of surface trap-state modification caused by the surface ligands on the exciton properties has been evaluated through photoluminescence spectroscopy. Additionally, the acoustic phonon mode, which influences carrier trapping, photoluminescence line width etc., is monitored by Raman spectroscopy. To evaluate the effect of surface ligands, the LA phonon frequencies are analyzed as a function of the molar mass of the surface ligands.*

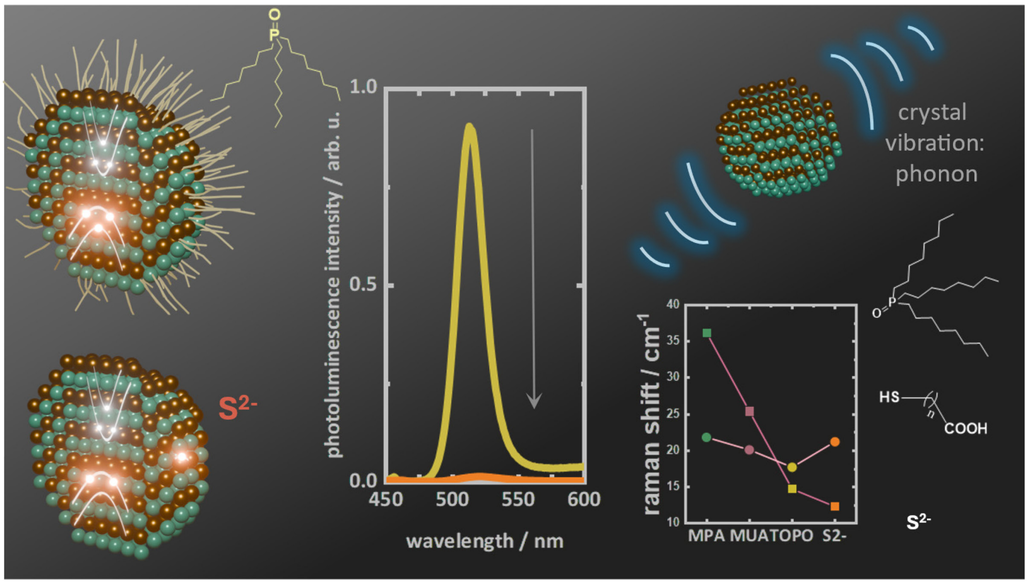
O
P
S2-
1.0
0.5
0.0
450
500
550
600
photoluminescence intensity / arb. u.
wavelength / nm
crystal vibration: phonon
raman shift / cm-1
40
35
30
25
20
15
10
MPA MUA TOPO S2-
O=P
HS
n
COOH
S2-

TOPO capped colloidal CdSe QDs of four different sizes of 2.4 nm, 4.0 nm, 4.8 nm, and 8.2 nm were synthesized via the hot injection method.[102] The experimental protocol is described in the Appendix A. Steady-state absorption spectra of the four QDs are shown in Figure 15a. The spectra exhibit the typical $1S_{3/2}$-$1S_e$ (1S), $2S_{3/2}$-$1S_e$ (2S), $1P_{3/2}$-$1P_e$ (1P) electronic transition features observed in CdSe QDs (Figure 15a).[38] The energy level diagram explaining these transitions is shown in Figure 8a. The 1S peak positions corresponding to the lowest energy band-edge transition are shown in Table 1. The QD sizes were estimated from the 1S transition in the steady-state absorption spectra using an empirical formula described by Yu et al.[103] which is additionally validated by determining QD size from TEM images (Figure 15b, c, d, and e & Figure A 2). The size distribution obtained from TEM image analysis (using imageJ 1.53A [104]) is shown in Figure A 2. With increasing size, the 1S position in the absorption spectra is redshifted because of the quantum confinement effect.[4] Similar to the 1S peak position in absorption spectra, the band edge photoluminescence peak is redshifted with increasing QD size. The band edge photoluminescence occurs due to the radiative electron-hole recombination at the band gap.[69, 72] The band edge peak positions of the QDs are listed in Table 1.

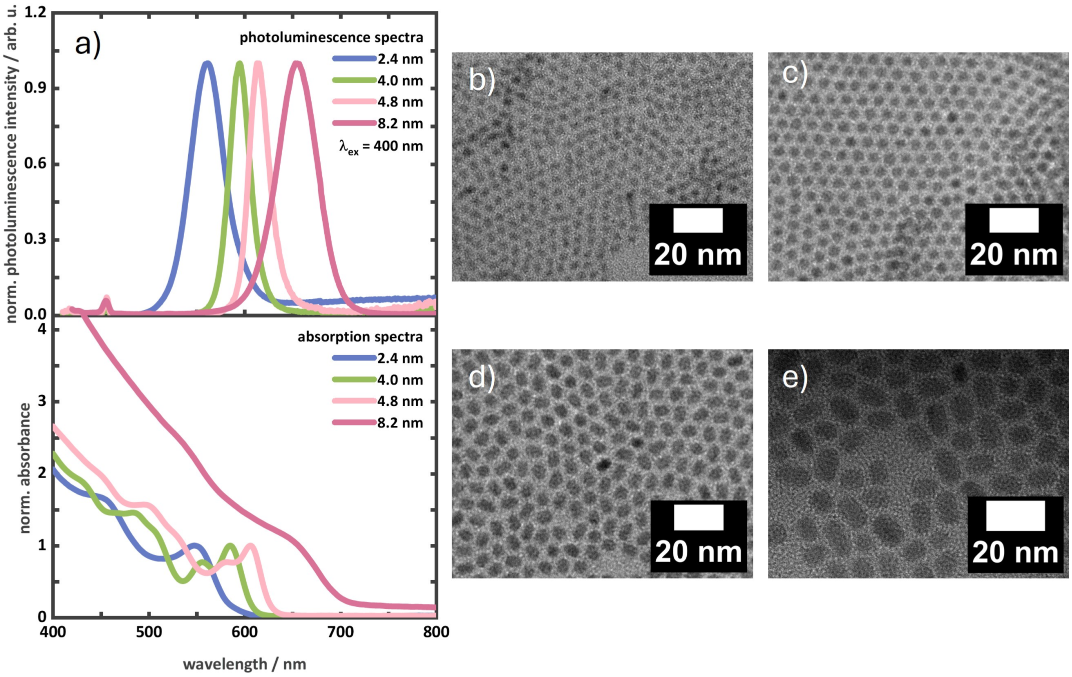

Figure 15: *(a) Steady-state absorption and normalized photoluminescence spectra (λ_{ex} = 400 nm) of TOPO capped 2.4 nm, 4.0 nm, 4.8 nm, and 8.2 nm QDs.*

Table 1: *Size determined from absorption spectra, TEM images, 1S peak position in absorption spectra, and band-edge photoluminescence peak positions of 2.4 nm, 4.0 nm, 4.8 nm, and 8.2 nm TOPO capped QDs.*

QD size/ diameter (abs. spectra)	QD size/ diameter (TEM)	**1S peak**		**band-edge photoluminescence**	
nm	**nm**	**nm**	**eV**	**nm**	**eV**
2.4	3.0±0.5	528	2.35	561	2.21
4.0	4.2±0.4	585	2.12	595	2.08
4.8	4.9±0.7	606	2.05	613	2.02
8.2	7.7±2.8	652	1.9	653	1.89

Additionally, for 2.4 nm QD, a broad emission band at wavelengths longer than 600 nm is observed originating from trap state emission (Figure 15a). Surface trap-state emission appears more pronounced in smaller QDs due to the higher surface-to-volume ratio as compared to larger QDs.[20] This effect can be quantified by determining the peak areas from a multi-gaussian fit of the photoluminescence spectra. The photoluminescence spectra were fitted with two Gaussians describing the band-edge and trap-state emission bands as shown in Figure 16a exemplarily for 2.4 nm QD. The relative contributions of band-edge and trap state emission to the total spectra in each QDs were determined from the peak areas of the fitted Gaussians (Figure 16b). It shows that the trap-state emission contribution gradually decreases with increasing QD size with good agreement with a decreasing surface-to-volume ratio, as is expected. When the QD size is small, the density of surface trap states increases due to the relatively higher number of surface atoms and dangling bonds, which results in strong trap-state emission.[63]

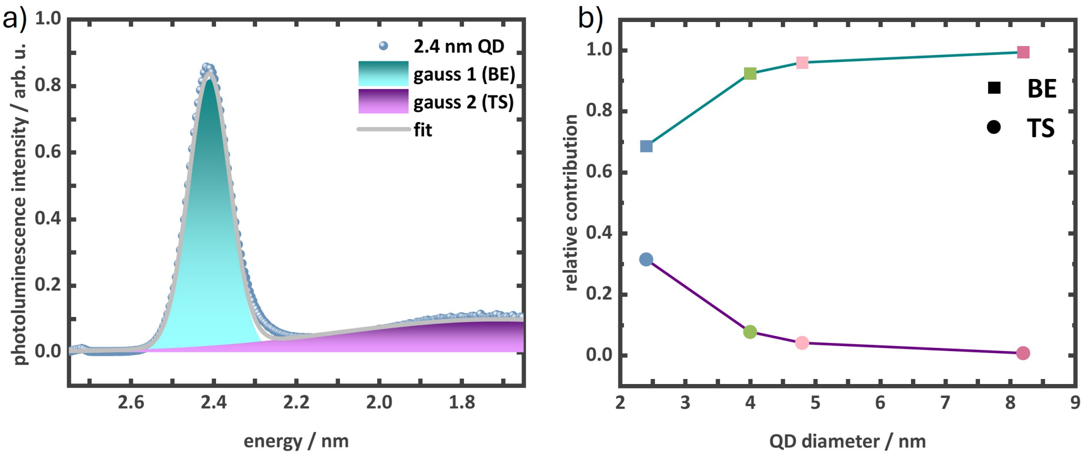

Figure 16: *(a) Gaussian fitting of the photoluminescence spectra of 2.4 nm QD. The band-edge peak (BE) is denoted by gauss 1 and the trap-state (TS) peak is denoted by gauss 2. (b) The relative contribution of band-edge (BE) and trap-state (TS) emission to the overall spectra of 2.4 nm, 4.0 nm, 4.8 nm, and 8.2 nm TOPO capped QDs.*

However, the surface trap-state density can be modulated by passivating surface traps by exchanging ligands on the QD surface.[60] To investigate further, surface modification of the TOPO capped QDs with 2.4 nm, 4.8 nm, and 8.2 nm sizes was performed with a series of surface ligands including MPA, MUA, and S^{2-}. For this a one phase ligand exchange method was adopted, where the QD solids were stirred with a concentrated ligand solution. This however didn't appear as an efficient method of ligand exchange with drastic changes in the absorption spectra (after ligand exchange), poor solubility, and irreproducibility. The major disadvantage of the one phase ligand exchange method is that it doesn't provide a solvent phase where the parent TOPO ligand after removal can be solubilized, due to which an efficient ligand exchange is challenging. To overcome this problem, ligand exchange of MPA, MUA, and S^{2-} ligands was performed via a biphasic ligand exchange method.[74, 105] The experimental details are described in Appendix A. A successful ligand exchange was validated by the FT-IR spectra (Figure A 1). In Appendix B, a detailed description of the FT-IR spectra is provided with all the vibration bands assigned according to previously reported literatures.[106-108]

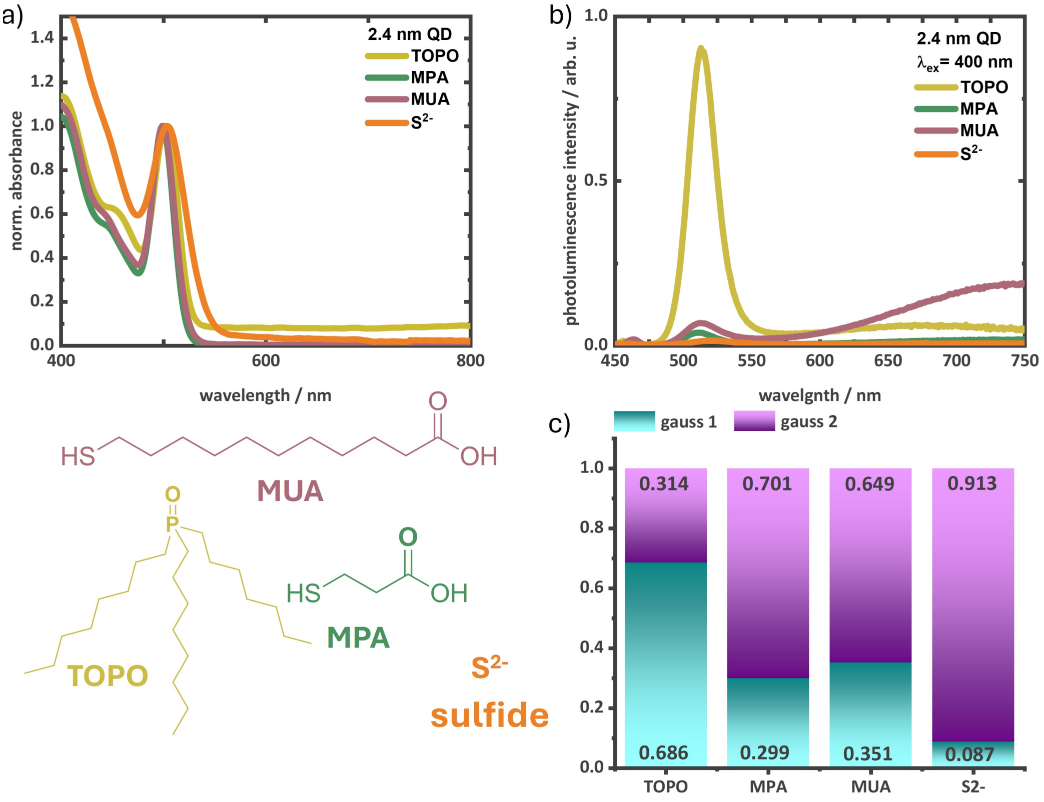

Figure 17: *(a) Steady-state absorption spectra and (b) photoluminescence spectra (λ_{ex} = 400 nm) of 2.4 nm QD with TOPO, MPA, MUA, and S^{2-} ligands. The photoluminescence spectra are normalized to the respective absorbance at λ_{ex} (400 nm). (c) The relative contribution of band-edge (gauss 1) and trap-state (gauss 2) emissions obtained from the Gaussian fitting (as shown in Figure 16a) in the photoluminescence spectra of TOPO, MPA, MUA, and S^{2-} capped 2.4 nm QD.*

Figure 17a shows the changes in the absorption spectra of the 2.4 nm TOPO, MPA, MUA, and S^{2-} capped QDs. The 1S peaks are nearly identical (in terms of spectral position and width) indicating no significant change in QD size or size distribution during ligand exchange. However, a slight change in size distribution could be expected in the S^{2-} capped QDs with a relatively broad 1S peak. The corresponding photoluminescence spectra exhibit drastic change upon ligand exchange (Figure 17b). The band-edge photoluminescence peaks are strongly quenched, and trap-state emissions are heavily increased after ligand exchange with MPA, MUA, and S^{2-} (Figure 17b). For a quantitative comparison, the Gaussian fitting (as shown in Figure 16a) was applied. The relative contribution of band-edge (gauss 1) and trap-state (gauss 2) emissions in all four ligands are shown in Figure 17c. TOPO capped QD shows the highest band-edge photoluminescence contribution with 0.686, which reduces by roughly two times in MPA and MUA and shows the lowest in S^{2-} with 0.087. On other hand, the trap-state emission contribution increases from 0.314

in TOPO to 0.913 in S^{2-} capped QD. The strong band-edge photoluminescence quenching upon MPA, MUA, and S^{2-} ligand exchange is attributed to increased non-radiative electron-hole recombination pathways due to surface hole trapping.[71] These ligands lead to the formation of new states near the valence band, in which holes, in particular, can be trapped very fast (~ 1 ps) after photoexcitation.[71] The efficiency of hole trapping among MPA, MUA and S^{2-} can be different majorly due to their different energetic positions with respect to the CdSe energy levels and number of surface ligands.[60] However, a similar effect was observed for 4.8 nm and 8.2 nm QDs (Figure 18). The MPA, MUA, and S^{2-} ligands strongly quench the band-edge photoluminescence and enhance trap-state emission with S^{2-} showing the maximum influence. This effect seems to be stronger when the QD size is smaller. For instance, with S^{2-} ligand exchange, the band-edge photoluminescence contribution in 2.4 nm QD was reduced by 7.8 times, and in 8.2 nm QD, it was reduced by 1.02 times only (i.e., nearly identical). This can mainly be because of two reasons, firstly due to the quantum confinement effect the valence band level positions differ resulting in different energy gaps between the valence band and surface trap states originating from surface ligands effecting the efficiency of trapping.[60, 109] Secondly, with the larger QD, confinement energy gets lower resulting in the smaller driving force for an efficient carrier trapping.

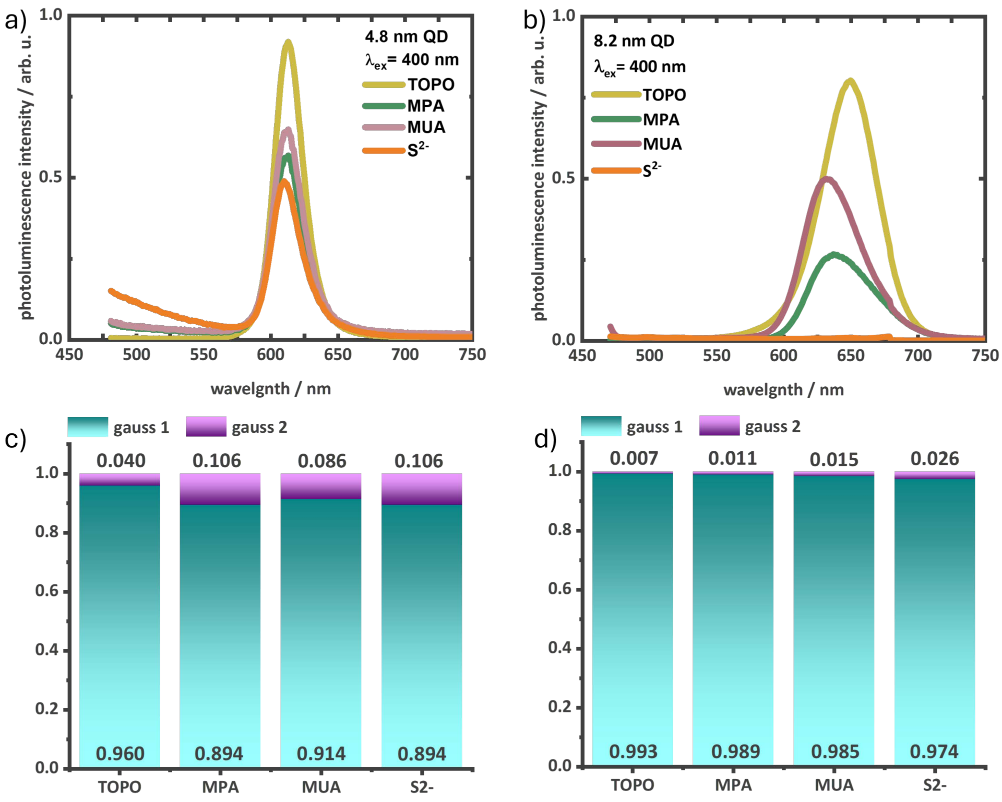

Figure 18: *Photoluminescence spectra (λ_{ex} = 400 nm) of (a) 4.8 nm QD, and (b) 8.2 nm QD with TOPO, MPA, MUA, and S^{2-} ligands. The photoluminescence spectra are normalized to the respective absorbance at λ_{ex} (400 nm). The relative contribution of band-edge (gauss 1) and trap-state (gauss 2) emissions obtained from multi-gaussian fitting (as shown in Figure 16a) in the photoluminescence spectra of TOPO, MPA, MUA, and S^{2-} capped (c)4.8 nm, and (d) 8.2 nm QD.*

The size and surface functionalization not only influence the photoluminescence properties but also the crystal vibration of QDs. Crystal vibration in QDs occurs as quantized collective vibration of atoms in the crystal lattice, which is also called as phonon. Phonon modes in QDs are primarily classified as optical and acoustic modes. The acoustic phonons correspond to low-energy vibrations where atoms oscillate in phase, affecting the acoustic wave propagation through the crystal, whereas the optical phonons involve out-of-phase vibrations between atoms in the lattice creating a dipole that can couple with electromagnetic waves.[76] Acoustic phonon modes in colloidal QDs are particularly interesting to see the mechanical influence of surface ligands.[77] Simply, the impact of surface functionalization can alternatively be probed by observing the acoustic phonon modes. To do this, Raman spectroscopy was performed on colloidal QDs deposited on CaF_2 substrates (experimental details in Appendix A) with a 808 nm laser (not resonant with QD electronic transitions). A volume holographic notch filter with 5 cm^{-1} cut was used to probe the low wavenumber acoustic modes.

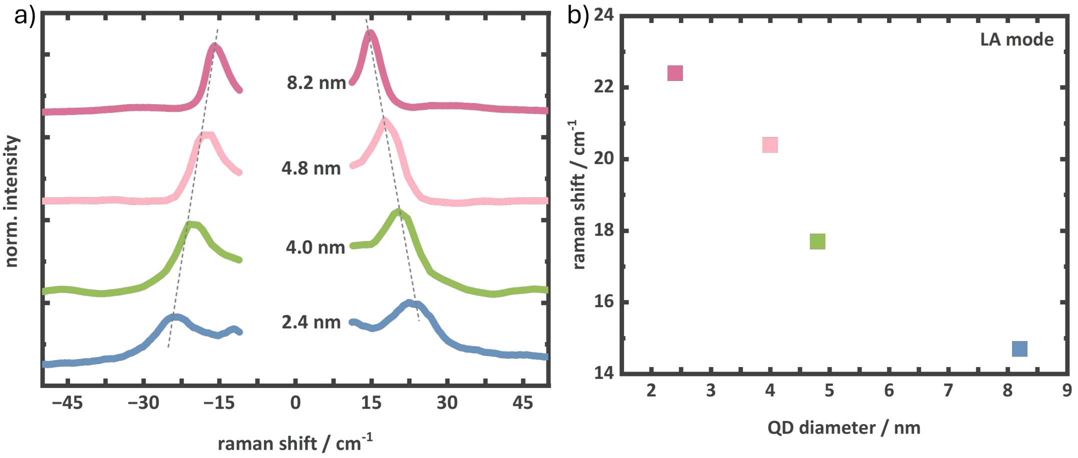

Figure 19: *(a) Raman spectra showing the LA modes of 2.4 nm, 4.0 nm, 4.8 nm, and 8.2 nm TOPO capped QDs deposited on CaF_2 substrates. (b) Representation of LA phonon frequency with QD size. The Raman spectra were cut between -10 cm^{-1} to 10 cm^{-1} to ignore the Rayleigh Scattering.*

Table 2: *LA phonon frequencies of 2.4 nm, 4.0 nm, 4.8 nm, and 8.2 nm TOPO capped QDs.*

QD size/ diameter **nm**	LA Phonon frequency **cm^{-1}**
2.4	22.4
4.0	20.4
4.8	17.7
8.2	14.9

Figure 19a shows the LA phonon modes of 2.4 nm, 4.0 nm, 4.8 nm, and 8.2 nm TOPO capped QDs deposited on CaF_2 substrates. The LA phonon frequencies of 2.4 nm, 4.0 nm, 4.8 nm, and 8.2 nm QDs appear at 22.4 cm^{-1}, 20.4 cm^{-1}, 17.7 cm^{-1}, and 14.9 cm^{-1} respectively (Table 2), which is in good agreement with previous literature.[110] With increasing QD size, the LA phonon mode frequency decreases because larger QDs have more atoms, i.e., higher effective vibrating mass, leading to lower wavenumber for the vibrational modes. Briefly, as the QD size increases, the spatial extent of the LA vibrations expands, causing a longer phonon propagation and their frequencies to decrease. This size-dependent behavior of LA phonon modes is a direct consequence of quantum confinement effects.[76, 110] As a result of the quantum confinement effect, smaller QDs have higher frequency acoustic phonon modes.

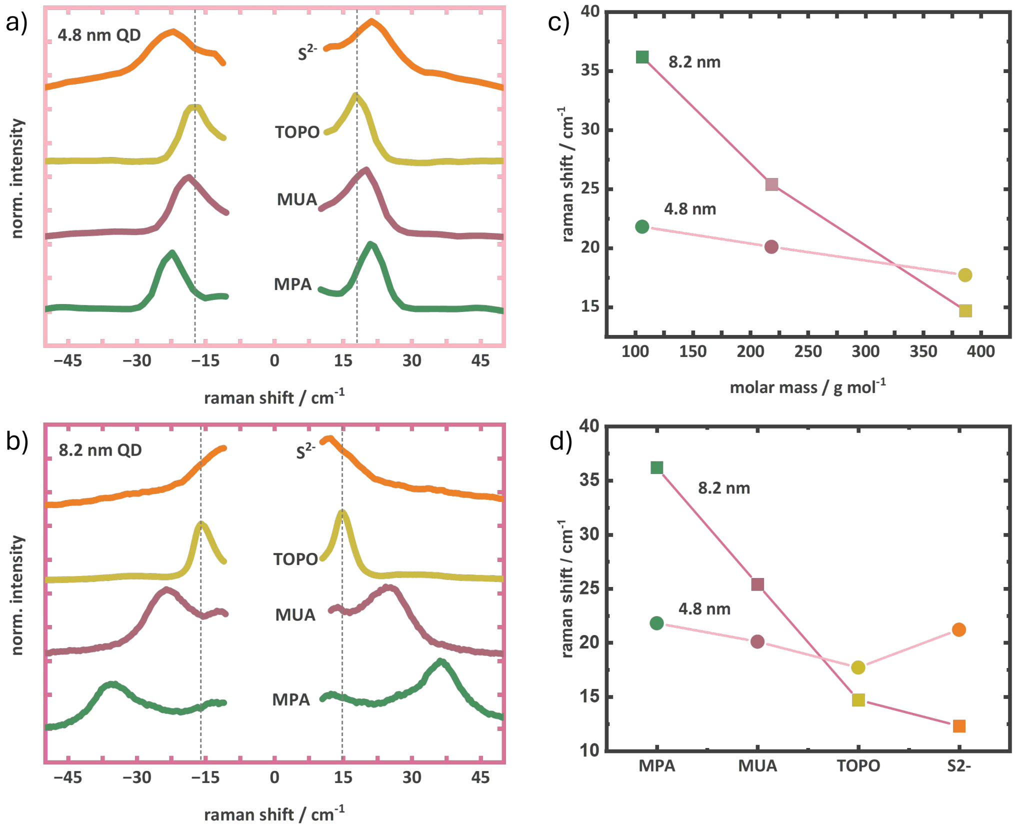

Figure 20: *LA phonon modes of TOPO, MPA, MUA, and S^{2-} capped (a) 4.8 nm, and (b) 8.2 nm QDs. (c) The variation of LA phonon mode frequencies with respect to the molar mass of TOPO, MUA and MPA ligands in 4.8 nm and 8.2 nm QDs. (d) The LA phonon mode frequencies of TOPO, MUA, MPA and S^{2-} capped 4.8 nm and 8.2 nm QDs.*

Table 3: *LA phonon frequency of TOPO, MUA, MPA, and S^{2-} capped 4.8 nm, and 8.2 nm QDs.*

QD size/ diameter **nm**	LA phonon frequency **cm^{-1}**			
	TOPO	**MUA**	**MPA**	**S^{2-}**
4.8	17.7	20.1	21.8	21.2
8.2	14.9	25.4	36.2	12.3

Further to investigate the effect of surface ligands, Raman spectroscopy was performed on TOPO, MPA, MUA, and S^{2-} capped 4.8 nm, and 8.2 nm QDs deposited on CaF_2. Figure 20a & b show the LA modes of TOPO, MPA, MUA, and S^{2-} capped 4.8 nm, and 8.2 nm QDs. The LA frequencies in different ligands seem to be significantly changing (Figure 20d). For instance, the LA modes in TOPO, MUA, MPA, and S^{2-} capped 4.8 nm QDs are respectively 17.7 cm^{-1}, 20.1 cm^{-1}, 21.8 cm^{-1}, and 21.2 cm^{-1} (Figure 20d). There is a correlation between the molar mass of the surface ligands (TOPO, MUA, and MPA) and the LA phonon frequencies as shown (Figure 20c). The LA phonon frequencies in both the 4.8 nm and 8.2 nm QDs are decreasing with increasing molar mass of the surface ligands, TOPO, MUA, and MPA (Table 3). Similar observations have previously been reported in the literature.[77] These observations indicate that mass-loading on the QD surface is the key mechanism by which surface ligands influence the vibration frequency of QDs. During LA (and acoustic vibration in general) vibration, as the QD coherently expands and contracts, the surface-bound ligands experience acceleration either outward or inward. In that case, heavier ligands exhibit greater inertial resistance to this surface displacement, resulting in a lower resonant frequency as illustrated in Figure 20c. However, S^{2-}, with the lowest molar mass among all the used surface ligands, does not show the highest LA frequency for both the QDs (Table 3 & Figure 20d). Additionally, the LA peaks for S^{2-} capped QDs seem to be relatively broader. These observations need to be carefully analyzed as S^{2-} is a single atom entity, and it can facilitate highly closed packed QD film when drop casted (as the QD solutions were drop casted for Raman spectroscopy, Appendix A). This implies that, in the S^{2-} capped QDs, the QD surface is majorly covered by neighboring QDs with very small spacing. In that case, the mechanical strain developed on a QD surface during LA vibration might also propagate to the neighboring QDs which will provide greater inertia. Consequently, the LA vibration will lose coherence at the surface resulting in faster damping which is in good agreement with the broad LA peak in S^{2-} capped QDs. Such effect of broad phonon peak and short damping has previously been observed with S^{2-} , Se^{2-} capped CdTe and CdSe QDs.[111] However, the high LA frequency in 4.8 nm S^{2-} capped QD remains unclear.

To summarize, the photoluminescence and phonon properties of four different sizes of CdSe QDs have been investigated in dependence on different surface ligands. Upon ligand exchange, MPA, MUA, and S^{2-}capped QDs exhibit strong band-edge photoluminescence quenching and enhancement of trap-state emission. Among these three ligands, S^{2-} shows the maximum effect on photoluminescence properties. The modulation of photoluminescence properties upon MPA, MUA, and S^{2-} ligand exchange is primarily due to their introduction of additional energy levels within the band gap which can trap, particularly, holes after photoexcitation. The ligand exchange process was additionally monitored by probing the LA phonon modes of CdSe QDs. A size-dependent quantum confinement effect on LA frequency was observed for four different sizes of QDs. LA phonon frequency exhibits a mass loading effect due to the mechanical strain caused by the surface ligands due to which LA frequency is lower in heavier surface ligands. Additionally, in good agreement with previous literature, the LA modes exhibit broader peak in S^{2-} capped QDs in comparison to the TOPO capped ones, owing to faster damping to LA vibration. The S^{2-} ligand exerts a pronounced influence on the photoluminescence properties of CdSe QDs, which can be attributed to its efficient hole trapping. This motivates a special focus on further investigation to explore the exciton dynamics. In the next chapter, the exciton and multiexciton properties of different sizes of TOPO capped QDs are investigated, which is further extended to the corresponding S^{2-} capped QDs to evaluate the effect of strong hole trapping on exciton and multiexciton properties using intensity-dependent TA spectroscopy.

4. Determination of High-order Multiexciton Properties by Transient Absorption Spectroscopy

In this chapter, the exciton and multiexciton properties of QDs with different sizes and surface ligands have been discussed. The properties of TOPO and S^{2-} *capped QD series of varying sizes are investigated and compared with the aim to evaluate the impact of strong hole trapping on exciton and multiexciton lifetime. The spectral and dynamical features of multiexcitons extending up to QX are investigated via intensity-dependent TA spectroscopy. To evaluate the spectral and temporal changes in the collected data set, a global fitting routine based on the MCMC sampling method is applied, which allows the determination of the spectral characteristics of the contributing exciton and multiexciton species. This additionally permits the determination of their respective population dynamics and their lifetimes. Furthermore, a multi-gaussian fitting routine is employed for the quantitative analysis of multiexciton species spectra and the determination of the multiexciton binding energy.*

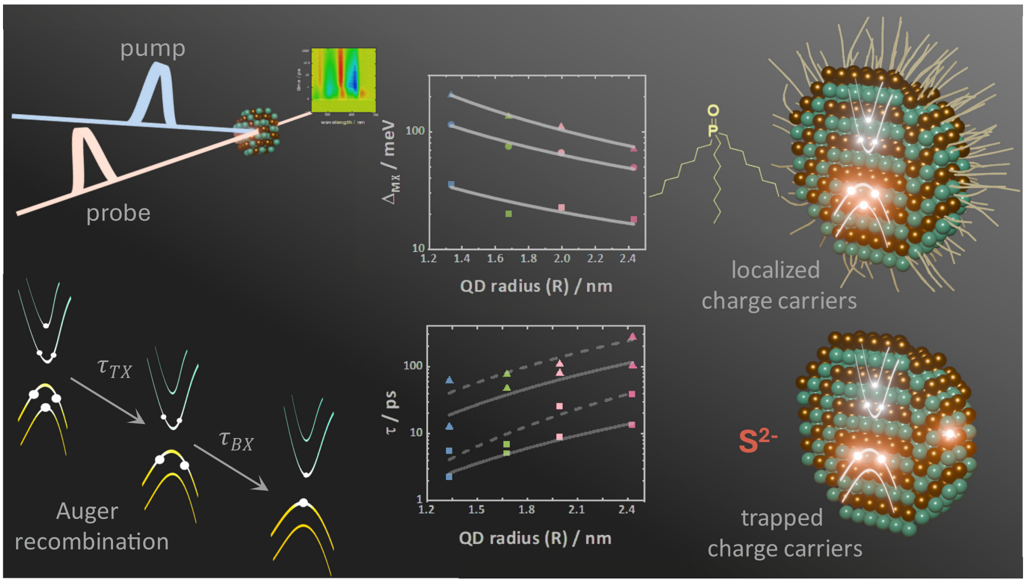
pump
probe
Δ_{MX} / meV
100
10
1.2
1.4
1.6
1.8
2.0
2.2
2.4
QD radius (R) / nm
O
P
localized
charge carriers
τ_{TX}
τ_{BX}
Auger
recombination
τ / ps
100
10
1
1.2
1.5
1.8
2.1
2.4
QD radius (R) / nm
S^{2-}
trapped
charge carriers

To investigate the exciton and multiexciton properties, TOPO and S^{2-} capped CdSe QDs with four different sizes of 2.6 nm, 3.4 nm, 4 nm, and 4.8 nm were prepared by the methods described in the previous chapter. The experimental details are described in Appendix A. Figure 21a shows the steady-state absorption spectra of the TOPO and S^{2-} capped CdSe QDs. The estimated QD size and the respective $1S_{3/2}$-$1S_e$ (1S), $2S_{3/2}$-$1S_e$ (2S), $1P_{3/2}$-$1P_e$ (1P) electronic transitions are shown in Table 4. The photoluminescence spectra of the TOPO and S^{2-} capped CdSe QDs shown in Figure A 3 describe the effect of hole trapping with strong band-edge photoluminescence quenching and enhanced trap-state emission.[62, 74, 112]

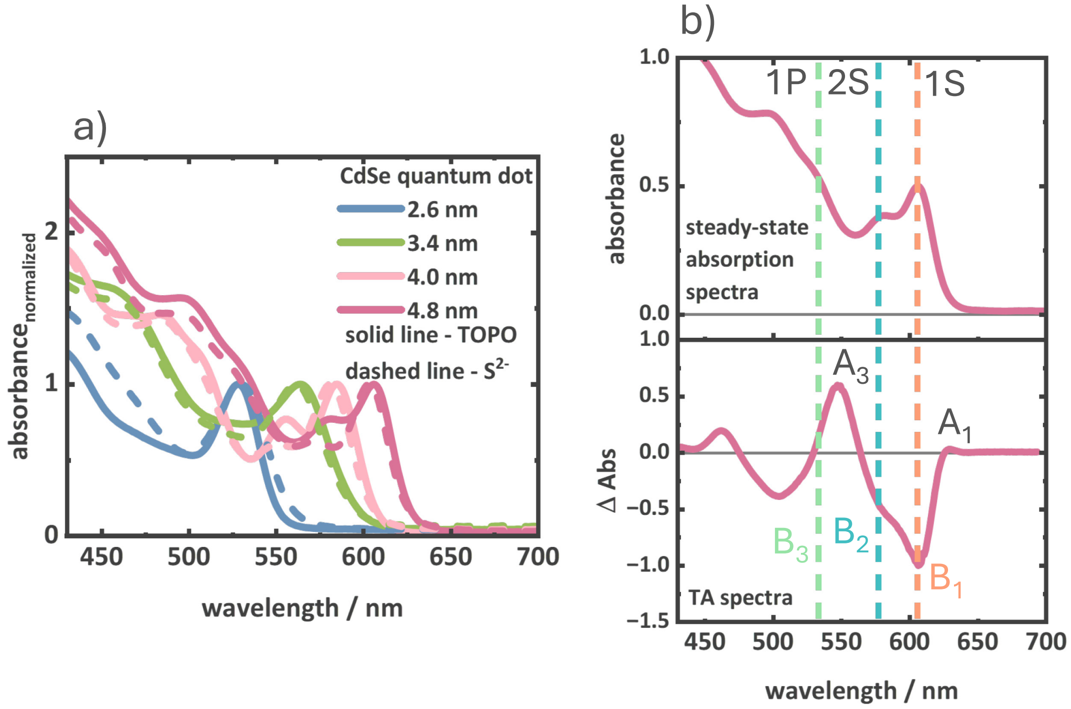

Figure 21: *(a) Steady-state absorption spectra of TOPO capped (solid lines) and S^{2-} capped (dashed lines) CdSe QDs of four different sizes. (b) steady-state absorption spectra (top panel) of the TOPO capped 4.8 nm QD with the marked 1S, 2S and 1P transitions, and the corresponding transitions are marked in the TA spectra (bottom panel) as B_1, B_2, and B_3.*

Table 4: *Table describing the three lowest optical transitions in the four TOPO capped QDs.*

QD size/ diameter	1S		2S		1P	
nm	nm	eV	nm	eV	nm	eV
2.6	528	2.35	496	2.50	426	2.91
3.4	564	2.20	537	2.31	458	2.71
4.0	585	2.12	555	2.23	504	2.46
4.8	606	2.05	581	2.13	529	2.34

Intensity-dependent transient absorption spectroscopy was performed with a pump pulse (~100 fs) of 400 nm central wavelength with varying intensities between 1.0×10^{-4} $\mu W \mu m^{-2}$ to 1.0×10^{-2} $\mu W \mu m^{-2}$ (details in Appendix C). Comparison of the TA spectra (at 1.0×10^{-4} $\mu W \mu m^{-2}$ at 1900 ps) with steady-state absorption spectra (Figure 21b) of the TOPO capped 4.8 nm QD demonstrates the characteristic bleach signals B_1, B_2, and B_3 originating at 1S, 2S, and 1P transitions. These transitions occur in the other three QDs in different spectral positions as described in Table 4. The intensity-dependent TA spectra at 2 ps for the series of TOPO capped QDs are depicted in Figure 22. The bleach amplitudes of B_1, B_2, and B_3 for all the QDs gradually increase with increasing intensity (Figure 22). For the 4 nm and 4.8 nm QDs, the B_3 shows a stronger contribution than B_1 and B_2 at 2 ps at high intensities while at low intensities B_1, and B_2 are dominant. At low intensities, the transient spectra show strong PIA features redshifted from the B_1 and B_3 signals at 2 ps, which gradually disappear with increasing intensity in the TOPO capped QDs. The PIA features are labeled as A_1, A_3 as depicted in Figure 21b. However, irrespective of the intensity, A_1 and A_3 reappear around 100 ps in the TOPO capped QDs. At the latest recorded delay time of 1900 ps, all the intensity-dependent spectra of the respective QDs look identical when normalized to the B_1 (Figure A 4). Similar features are observed for the S^{2-} capped QDs, with intensity-dependent increase of B_1, B_2, and B_3 bleaches at 2 ps (Figure 22b) and an identical spectral shape at 1900 ps (Figure A 4). Unlike the TOPO capped QDs, S^{2-} capped QDs do not exhibit the A_1 feature irrespective of intensity and delay time. Additionally, the A_3 feature is also relatively weak in comparison to the TOPO capped QDs.

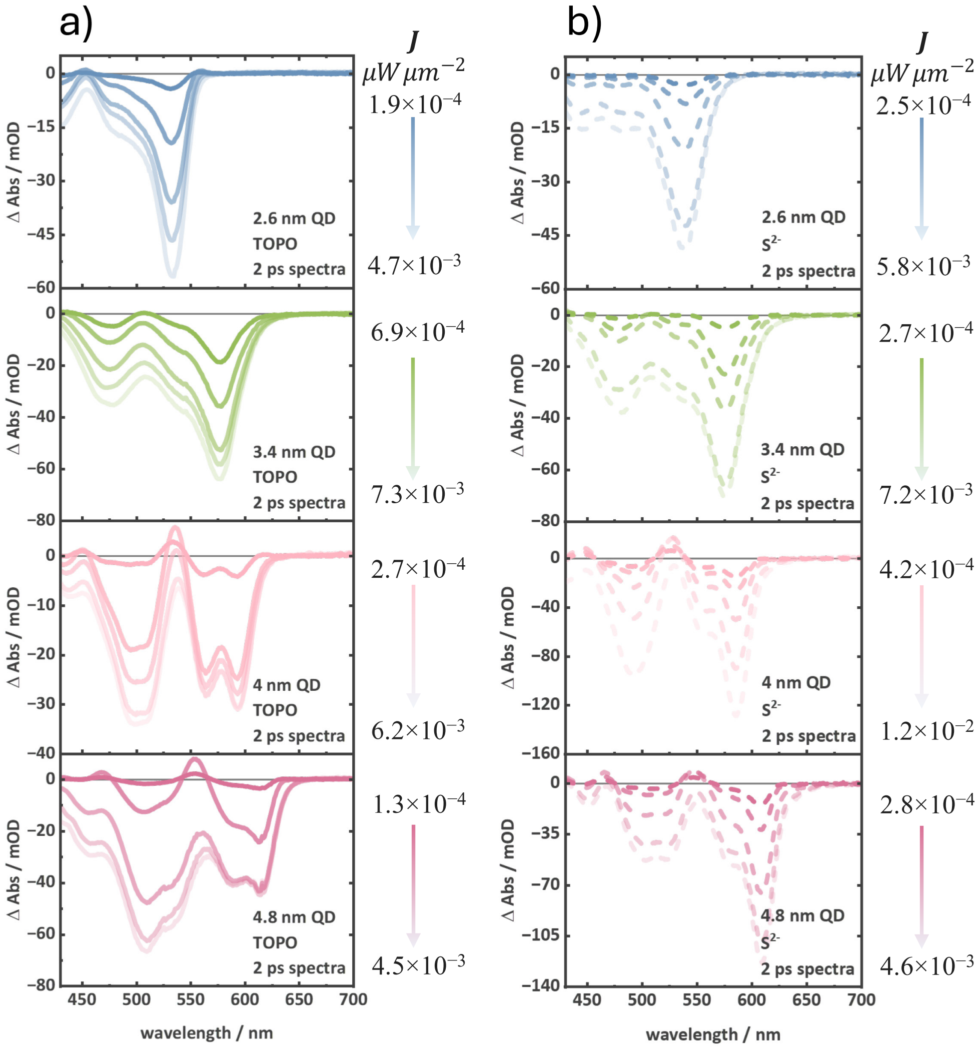

Figure 22: *Intensity-dependent TA spectra at 2 ps of (a) TOPO capped (b) S^{2-} capped CdSe QDs of four different sizes. Increasing intensity is indicated by the lines right to the panels.*

Increasing intensity not only increases the amplitude but also alters the temporal development by introducing some fast-decaying components. Figure 23a & b show the kinetics of B_1 and B_3 of the TOPO capped QDs. The B_1 feature reaches a maximum amplitude at around 1.5 ps followed by a bleach recovery. When the intensity is increased, the B_1 kinetics show additional fast components between 2 ps to 500 ps. The kinetics after 500 ps shows an identical decay independent of the intensity. On other hand, the B_3 maximum is observed at around 0.5 ps followed by bleach recovery. Similar to the B_1 kinetic traces, the B_3 kinetics also exhibit fast decaying component with increasing intensity. The kinetics of the A_1 features are shown in (Figure A 4). When the intensity is increased, the A_1 exhibits a negative signal in the early time region which develops into a positive signal showing similar decay kinetics independent of intensity. However, unlike the TOPO capped QDs, in

S^{2-} capped QDs the B_1 kinetics exhibit relatively slow decaying components in the early time (~ 2ps). On the other hand, the B_1 decay is relatively faster in the later delay time (from ~500 ps) in S^{2-} capped QDs (Figure 23c).

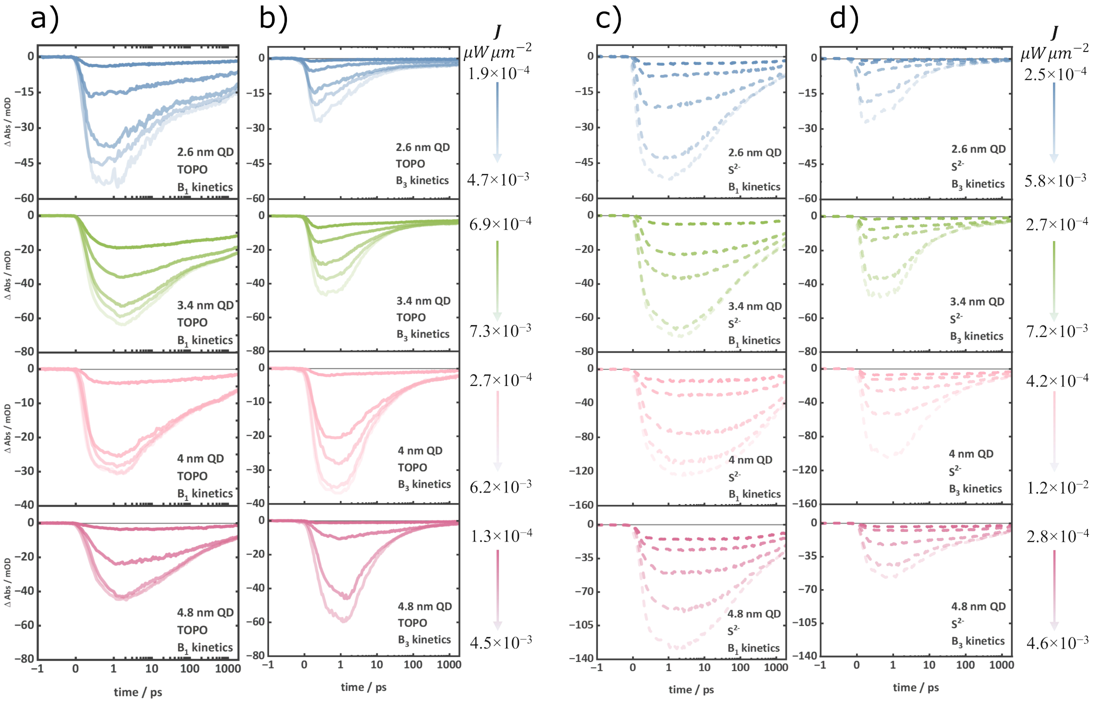

Figure 23: *Kinetics of* B_1 *and* B_3 *bleach of (a) & (b) TOPO capped, and (c) & (d)* S^{2-} *capped CdSe QDs of four different sizes. Increasing intensity is indicated by the lines right to the panels.* B_1 *position of TOPO capped 2.6 nm, 3.4 nm, 4 nm, and 4.8 nm QDs are at 530 nm, 576 nm, 590 nm, and 614 nm respectively.* B_1 *position of* S^{2-} *capped 2.6 nm, 3.4 nm, 4 nm, and 4.8 nm QDs are at 540 nm, 575 nm, 585 nm, and 610 nm respectively.*

The observed features can be assigned according to reports in the literature.[65, 84, 113] A detailed description of the origin of TA signals in CdSe QDs is given in Section 2.4. The primary contribution to the TA bleach signal in NCs such as CdSe QDs is the state filling, i.e., the population of conduction band levels with electrons.[87] For CdSe QDs, holes do not have a comparable contribution due to the higher degeneracy of the valence band states, the higher effective mass of the hole which reduces the occupation probability, and the presence of states in the valence band that are not coupled to the optical transition.[87] However, in recent studies, hole contribution to bleach signals has been reported.[114, 115] The increasing bleach contributions with increasing intensity indicate the increasing electron population in the conduction band levels.

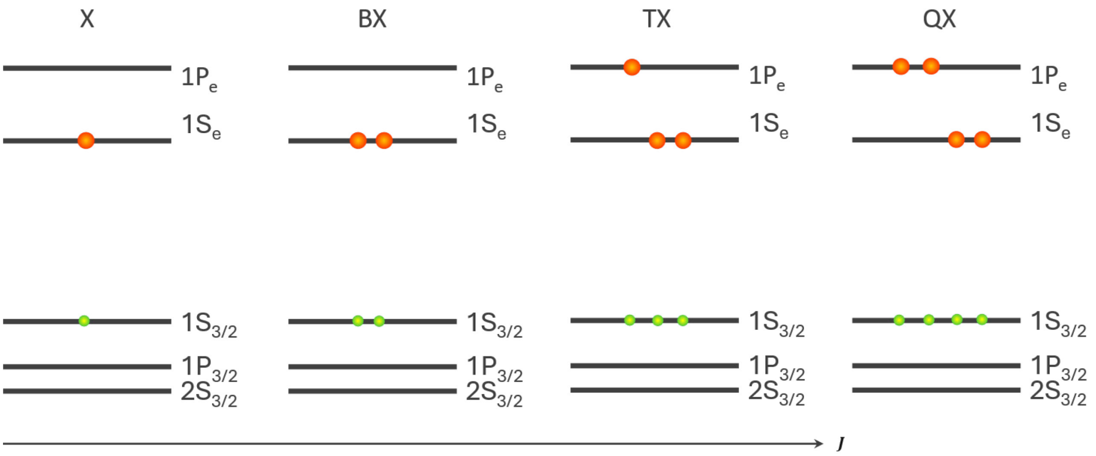

Figure 24: *The energy level diagram (not scaled) of CdSe QDs, representing the conduction band and valence band population with increasing intensity (J) which lead to the formation of, e.g., exciton (X), BX, TX, and QX.*

$1S_e$ and $1P_e$ levels in the conduction band have different spin degeneracies. $1S_e$ exhibits 2-fold degeneracy and $1P_e$ exhibit 6-fold degeneracy.[38] This means that when the $1S_e$ level is fully occupied with two electrons, the $1P_e$ level gradually starts to fill up. The strong contribution of B_3 in 4 nm and 4.8 nm QDs indicates that there are higher multiexcitons than a BX which gradually fills up the $1P_e$ level (Figure 22). The electronic structure of exciton, BX, TX, and QX are shown in Figure 24. The B_3 feature is also observable at the low intensity regime when there is majorly exciton and BX population, i.e., only the $1S_e$ level is populated (Figure 22). Such bleach signals do not originate from the state-filling effect but from the Stark effect.[65] The local fields of the carriers in exciton and BX states (as shown in Figure 24), modulate the oscillator strengths of the electronic transition, leading to the bleaching of optical transitions, e.g., the B_3 feature, without having any state-filling effect.[65, 91] The PIA (A_1) redshifted from the B_1 is ascribed to the biexciton effect.[65, 83] At low intensities when the $1S_e$ level is singly occupied, the probe pulse generates another exciton (as $1S_e$ has 2-fold degeneracy) and the attractive interaction between the excitons lower the B_1 transition energy resulting in a red-shifted PIA. The shift between A_1 and B_1 is the biexciton binding energy. The same effect occurs with the interaction at the $1P_e$ level leading to a PIA (A_3) redshifted from the B_3. Once the $1S_e$ level is fully occupied with 2 electrons (i.e. a BX is present) at high intensity, further probe absorption cannot happen resulting in a decrease of A_1. The same effect will be observed with the A_3, once the $1P_e$ level is fully occupied with 6 electrons. When the intensity increases, $1P_e$ level gradually fills (as shown in Figure 24) resulting in decreasing A_3 amplitude (Figure 22). At high intensity, A_3 is also superimposed with B_2 and B_3 with strong negative contributions. The development of spectral features with intensity strongly suggests the population of multiple carriers in the conduction band levels i.e., the formation of multiexcitons. The absence of A_1 at high intensity is an indication of filling up of the $1S_e$ level. Additionally, increasing B_3 with intensity indicates the population of $1P_e$ levels (Figure 22). On the other hand, the absence of the A_1 feature at both 2 ps and 1900 ps (Figure 22b) for the S^{2-} capped QDs might indicate a low biexciton binding energy which might lead to a strong overlap of the A_1 and B_1 features leading to absence of the A_1 feature.

The temporal changes observed in the kinetics (Figure 23) with increasing intensity have previously been reported.[65, 84, 113]The 400 nm pump excitation, which is above the $1P_e$ level, forms a hot exciton that gradually cools down to the $1S_e$ level via the $1P_e$ level in hundreds of femtoseconds which are observed in the initial rise of the B_1 and B_3 kinetics as shown in Figure 23.[84, 116, 117] Once the hot excitons start to cool down, the $1P_e$ levels fill up earlier than the $1S_e$, resulting in an early bleach maximum at 0.5 ps of B_3 followed by the B_1 at 1.5 ps. In low intensities (excitonic regime), the decay in the sub-ps regime can be attributed to the cooling of hot electrons from $1P_e$ to $1S_e$. At high intensities, the $1P_e$ level is populated with multiexcitons (as shown in Figure 24), and hence the decay kinetics additionally contain components of multiexciton recombination. However, at the same time scale, hot carriers can get trapped in surface trap states.[117, 118] After these initial ultrafast processes, the band relaxation (i.e., hot carriers cooled down to the lowest energy level) is completed up to ~1.5 ps indicated by the B_1 bleach maximum (Figure 23). On the time scale beyond 2 ps, decay of the signal occurs due to the recombination of the band edge excitonic states. The additional fast-decaying components in B_1 kinetics with increasing intensities, can be attributed to multiexciton recombination processes. When there are multiexcitons generated under high pump intensities, they undergo Auger recombination on a time scale up to a few hundreds of ps (as described in Section 2.3) until only exciton remains.[65] In the end, exciton recombines via both radiative and non-radiative processes on timescales up to tens of nanoseconds.[119, 120] Hence, the identical decay kinetics of B_1 as shown in Figure 23 after ~ 500 ps contain contribution majorly from exciton decay.

Such spectral and dynamical variation with pump intensity is well established for the formation and recombination of multiexciton via the Auger recombination process.[65, 83] The comparison of the TA spectra (Figure 22) and kinetics (Figure 23) between TOPO and S^{2-} capped QDs indicate that the exciton and multiexciton spectral shapes and lifetimes have strong influence of hole trapping which needs to be precisely evaluated. In CdSe QDs, the multiexciton recombination via Auger recombination is described as a cascade of sequential decay of multiexciton states (detailed description in Section 2.3). When N order of multiexcitons is formed, the kinetic model can be described as,

$$N \rightarrow N-1 \rightarrow N-2 \rightarrow N-3 \ldots\ldots. \rightarrow 2 \rightarrow 1 \tag{23}$$

i.e., when a TX is formed it will decay via BX to exciton (which will undergo radiative recombination). To extract multiexciton lifetime and spectra, the kinetic model as shown in Eq. (23) needs to be solved according to the differential equations described in Eq. (14). The analysis of multiexciton dynamics in TA data is commonly conducted through single wavelength multiexponential fitting of the B_1 kinetics.[65, 84] However, the intensity-dependent TA data (Figure 22) suggests that the spectral signatures of multiexcitons are not only observed in B_1, but also in B_3, A_1, and A_3, e.g., the A_1 feature is positive in exciton regime (low intensity, Figure 22), and negative in multiexciton regime (high intensity, Figure 22). Due to this, a global fitting over the entire range of wavelengths and intensities is necessary to extract complete temporal and spectral evolution. The multiexciton lifetime and spectral shape of CdSe QDs from intensity-dependent TA data have recently been demonstrated by applying a global fitting routine.[83, 100] To perform the global fitting of all the intensity-dependent TA data, the MCMC based target analysis established by Ashner et al was employed.[101] A Python-based package, KiMoPack, was used for the initial processing such as chirp correction of the intensity-dependent TA data.[121] In the global fitting, TA data is treated as a sum of the spectra ($S_N(\lambda)$) corresponding to each multiexciton species, N. The spectral shape of S_N is independent of pump intensity and delay time but only its concentration (or weight) varies with an amplitude co-efficient $A_N(t, J)$, which is dependent on pump intensity (J). The initial concentration ($A_N(0, J)$) of the contributing exciton and multiexciton states are determined with Poisson probability distribution as,

$$P_N = \frac{<N>^N \times e^{-<N>}}{N!} \tag{24}$$

i.e., P_N determines the weight ($A_N(t,J)$) of the contributing species spectra ($S_N(\lambda)$). Here $< N >$ is the average number of excitons generated by pump excitation, which is determined as,

$$< N > = \sigma \times J \tag{25}$$

Where σ is a fitting parameter which incorporates the intrinsic absorption cross-section (α) at pump wavelength (400 nm) and the pump spot size. J is the pump intensity in 'μWμm^{-2}'. Therefore, σ is obtained in 'μW^{-1}μm^{2}', which can further derive α in 'cm^{2}'as,

$$\alpha = \sigma \times \frac{chopper\, frequency \times 10^{8}}{2.01 \times 10^{12}} \tag{26}$$

With the known initial concentration of pump-excited exciton and multiexciton species (as shown in Eq. (24)), the intensity-dependent TA data is simulated as,

$$\Delta A(\lambda, t, J) = \sum_{N} A_N(t,J)\, S_N(\lambda) \tag{27}$$

The 2.6 nm and 3.4 nm QDs were fitted with the TX kinetic model shown in Eq(28) and 4.0 nm and 4.8 nm QDs are fitted with the QX kinetic model shown in Eq(29).

$$TX \xrightarrow{\tau_{TX}} BX \xrightarrow{\tau_{BX}} X \xrightarrow{\tau_{X}} \tag{28}$$

$$QX \xrightarrow{\tau_{QX}} TX \xrightarrow{\tau_{TX}} BX \xrightarrow{\tau_{BX}} X \xrightarrow{\tau_{X}} \tag{29}$$

MCMC fitting is advantageous for the simultaneous determination of species spectra of exciton and multiexciton states (i.e., all the S_N corresponding to Eq. (28) and Eq. (29)), multiexciton lifetime, and α. In the subsequent discussion, the spectra, and lifetime of multiexciton states derived from MCMC fitting of the TA data will be focused. The MCMC analysis begins at 2 ps, where all the ultrafast cooling and trapping processes are expected to be completed. Additionally, the contributions of higher order multiexcitons with much shorter lifetimes, below 2 ps cannot be determined. The longest probe delay time point in our data is 1900 ps, which does not include the complete exciton recombination regime. Consequently, the exciton lifetime may be subject to a relatively high degree of error in the fitting and will not be discussed. The MCMC fit results of the four TOPO capped QDs are shown in Figure 26a and Figure A 5 to Figure A 12 . The goodness-of-fit and accuracy of the kinetic model are reflected in the kinetics along with the fits and the contour plots of the fitted parameters (Figure A 5 to Figure A 12). The independent parameters or non-correlated parameters in the contour plot indicate a correct choice of the kinetic model for the fitting.[101]

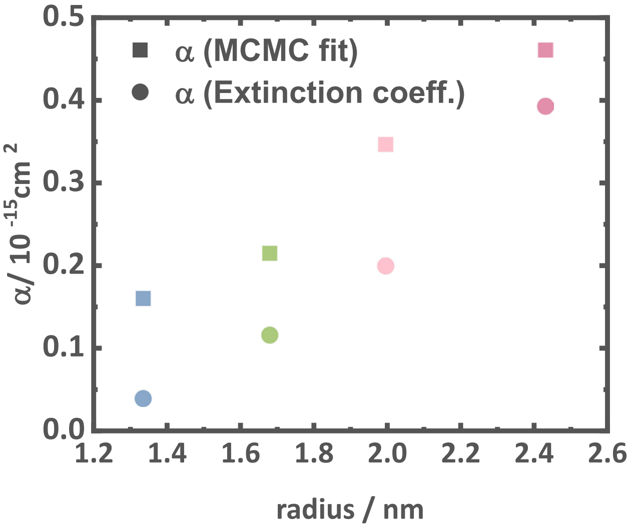

Figure 25: *Absorption-cross section (α) (at 400 nm) determined from MCMC fit and absorption-cross section (α) (at 400 nm) determined from the extinction co-efficient (at 400 nm) of the four TOPO capped QDs.*

The correct choice of the kinetic models can additionally be validated by α (derived from the fitted parameter σ, as shown in Eq. (23)) by comparing with the literature reported values (where α is determined from the extinction coefficient[28]). Figure 25 shows the α (obtained from MCMC fit) of the four QDs along with the α determined from the extinction coefficient as demonstrated by Leatherdale et al.[28]. α (at 400 nm) determined from MCMC fitting is in the same order magnitude as the one determined from extinction co-efficient. α of the QDs increase with size, in agreement with previous literature.[28] As 2.6 nm and 3.4 nm QDs have smaller α as compared to the 4.0 nm and 4.8 nm QDs, $< N >$ is also smaller when J is the same (according to Eq. (25)). This is the primary reason why the probability of forming high-order multiexciton in smaller QDs is relatively lower than in large QDs. Due to this, 2.6 nm and 3.4 nm QDs are fitted with the TX kinetic model (Eq. (28)) and 4.0 nm and 4.8

nm QDs are fitted with the QX kinetic model (Eq. (29)). Additionally, due to the shorter lifetimes (< 2 ps) in smaller QDs, multiexcitons above TX couldn't be fitted.

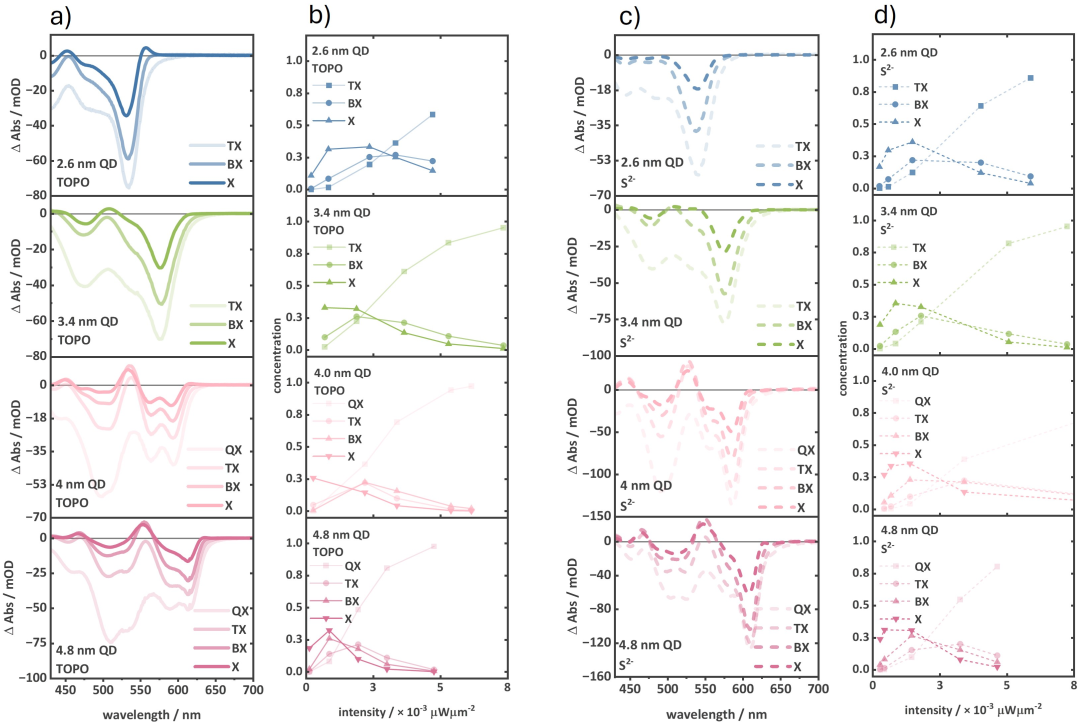

Figure 26: *(a) Multiexciton species spectra, and (b) initial concentration of multiexciton species over the pump intensities in TOPO capped QDs of four different sizes. (c) Multiexciton species spectra, and (d) initial concentration of multiexciton species over the pump intensities in* S^{2-} *capped QDs of four different sizes. X, BX, TX, and QX represent exciton, biexciton, triexciton, and tetraexciton respectively.*

Figure 26 illustrates the multiexciton species spectra of the series of TOPO and S^{2-} capped QDs. The initial concentrations (i.e., upon pump excitation) of the multiexciton states in different intensities are shown in Figure 26b & d. At low intensities, exciton concentration is higher, which gradually decreases with increasing intensity. While the high-order multiexciton concentrations are lower in low intensities, which gradually increases with intensity (Figure 26b & d). This means that, initially the TA spectra have dominant contribution of exciton at low intensity and TX (for 2.6 nm and 3.4 nm QDs) or QX (for 4.0 nm and 4.8 nm QDs) at high intensities. Therefore, the spectral features of TA spectra resemble more with the exciton spectra in low intensities and TX (for 2.6 nm and 3.4 nm QDs) or QX (for 4.0 nm and 4.8 nm QDs) at high intensities (Figure 22). For instance, the A_1 feature observed at low intensities in the TOPO capped QDs (Figure 22) is consistent with the exciton spectra. The BX, TX and QX spectra do not exhibit the A_1 feature, which is also similarly not observed in the TA spectra at high intensities (Figure 22).

The spectral shapes of multiexcitons can be explained from the proposed energy level structure as shown in (Figure 24). The increasing amplitudes of B_1, B_2, and B_3 features from exciton to QX (Figure 26a & c) are due to the increasing population in the conduction band levels ($1S_e$ or $1P_e$) corresponding to the respective transitions. The A_1 feature is observed only in the exciton spectra of the TOPO capped QDs. This is because only in exciton, the $1S_e$ level is singly occupied, allowing the biexciton effect to occur. As the $1S_e$ is fully occupied from BX to higher order multiexcitons, the biexciton effect cannot take place resulting in the absence of A_1. However, high-order multiexcitons above BX show a negative signal in the same region as the positive absorption in exciton (e.g., at 560 nm of 2.6 nm QD). A similar effect has been observed before in the TA spectra of CdSe QDs, which is attributed to SE.[122] The A_1 feature of BX formation is in S^{2-} QDs (Figure 26c). This indicates that the biexciton binding energy in S^{2-} capped QDs might be lower compared to TOPO capped QDs which can result in strong overlapping of A_1 and B_1. The A_3 feature is on the other hand a consequence of the Stark effect at the B_3 transition occurring at the $1P_e$ level. As the $1P_e$ level starts to fill from TX to QX, the A_3 amplitude gradually decreases. As the B_3 amplitude is significantly high in TX and QX, the A_3 feature shows a negative amplitude due to the spectral superposition with B_3.

Table 5: *Multiexciton lifetimes of TOPO and S^{2-} capped QDs of four different sizes determined by MCMC fitting. Parameters shown in the Table are fitted mean values and 99% confidence intervals obtained from MCMC sampling.*

	τ_{QX} $/ps$	τ_{TX} $/ps$	τ_{BX} $/ps$	τ_{QX} $/ps$	τ_{TX} $/ps$	τ_{BX} $/ps$
	TOPO			**S^{2-}**		
2.6 nm	-	$2.24_{2.23}^{2.25}$	$12.72_{12.68}^{12.73}$	-	$5.49_{5.48}^{5.50}$	$61.86_{61.78}^{61.98}$
3.4 nm	-	$5.07_{5.06}^{5.08}$	$47.12_{47.10}^{47.15}$	-	$6.86_{6.86}^{6.87}$	$76.33_{76.31}^{76.35}$
4.0 nm	$1.84_{1.83}^{1.85}$	$8.97_{8.96}^{8.98}$	$79.52_{79.48}^{79.67}$	$3.89_{3.88}^{3.90}$	$25.53_{25.49}^{25.57}$	$107.92_{107.79}^{108.04}$
4.8 nm	$2.03_{2.03}^{2.04}$	$13.58_{13.57}^{13.59}$	$104.13_{104.07}^{104.24}$	$5.40_{5.39}^{5.42}$	$38.81_{38.75}^{38.91}$	$275.83_{275.00}^{276.59}$

The multiexciton lifetimes estimated from the MCMC fitting of the TOPO and S^{2-} capped QDs are shown in Table 5. Multiexciton lifetimes exhibit an increasing trend with QD size. A cubic (3.0±0.6 for BX and 2.9±0.2 for TX) dependency (multiexciton lifetime, $\tau_{MX} \propto R^n$, where R is QD radius) with QD radius is observed for the TOPO capped QDs (Figure 27a) as expected from Eq. (19). Due to the small volume in QDs, the fast Auger recombination process plays a dominant role because of the strong overlap of charge carrier wavefunction.[65] That's why Auger lifetime is shorter in small QDs.[36] On the other hand, increasing the order of multiexciton exhibits a shorter lifetime in each QD (Table 5). Similarly, with the increasing order of multiexcitons, the charge carrier density in a particle increases which induces stronger wavefunction overlap resulting in a shorter Auger lifetime. Hence, we observe the shortest lifetime for QX while BXs exhibit the longest multiexciton lifetime. The dependence of multiexciton lifetime with the number exciton (N) reflects the kinetic mechanism involved in Auger recombination process as described in Section 2.3. In previous literature, several mechanisms have been discussed.[36] Cubic dependency stands for a three-carrier model, where e.g., an electron and a hole annihilate via exciting a third charge carrier (electron or hole). Theoretically, strongly confined charge carriers in materials like QDs exhibit cubic dependency. The quadratic model is observed in relatively larger particles where Auger recombination occurs via exciton-exciton interaction. For high-order multiexcitons, these two models become complicated because, the mani-fold degeneracy of higher energy levels creates different possibilities of carrier wave function mixing.[36] For instance, when there is a TX, the electron population is distributed over $1S_e$ and $1P_e$ levels of the conduction band, and the hole population distribution is over $1S_{3/2}$ and $1P_{3/2}$ before the ultrafast cooling and over $1S_{3/2}$ after the ultrafast cooling. In such a situation, when the charge carriers are distributed over levels with mani-fold degeneracy, multiple possibilities of transitions in Auger recombination can occur influencing the dependency of N in Auger lifetime. Taking this into account multiexciton lifetimes are scaled as a statistical model as described by Klimov et al.[36] In this case, none of the above-mentioned models showed a good fit. A power law (multiexciton lifetime, $\tau_{MX} \propto N^n$) fit was performed with the multiexciton lifetime of 4 nm and 4.8 nm QDs (the other QDs have only two multiexciton lifetimes and hence are not included in this evaluation) to check the dependence of exciton order (N), and it is estimated as 5.4±0.03 and 5.5±0.5 respectively (Figure 27b). This indicates a stronger dependency than the traditional exciton models as discussed above.

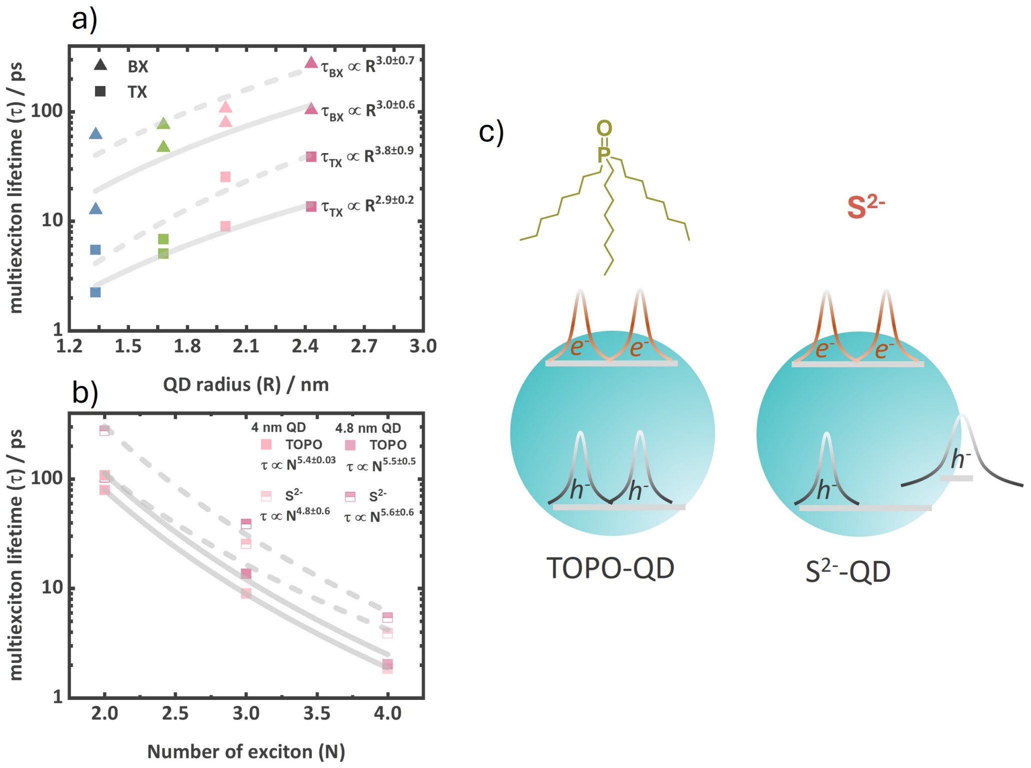

Figure 27: *(a) Radius dependency (multiexciton lifetime, $\tau_{MX} \propto R^n$) of TX and BX lifetimes of TOPO and S^{2-} capped QDs. (b) Number of exciton dependencies (multiexciton lifetime, $\tau_{MX} \propto N^n$) of TOPO and S^{2-} capped 4 nm and 4.8 nm QDs. (c) A schematic representing a TX, in a TOPO capped QD with the carrier density concentrated in the CdSe core and in a S^{2-} capped QD with a trapped hole on the surface site.*

The multiexciton lifetimes of S^{2-} capped QDs show a significant increase in comparison to the respective TOPO capped QDs (Table 5). However, the lifetimes in S^{2-} capped QDs exhibit a similar radius dependence (multiexciton lifetime, $\tau_{MX} \propto R^n$) with n = 3.0±0.7 for BX and 3.8±0.9 for TX (Figure 27a). The increase in multiexciton lifetime can be attributed to a decrease in carrier wavefunction overlap induced by carrier localization in surface trap states which suppresses the Auger process.[123, 124] A similar effect of reduction of carrier wavefunction on increased multiexciton lifetime has previously been reported. Kong et al.[41] showed an increased BX lifetime of CdSe QDs due to electron delocalization upon CdS shell growth. Similarly, Yan et al.[123] demonstrated the effect of hole trapping via phenothiazine on the increased BX lifetime of CdSe QDs. Phenothiazine exhibits a characteristic spectral feature (broad PIA in longer wavelength) of trapped holes under photoexcitation, which helps to correlate the effect of the trapped hole on multiexciton lifetime. As S^{2-} doesn't exhibit a distinguishable spectral feature, quantification of hole trapping from the TA spectra is challenging. The degree of hole trapping, on the other hand, can be determined by the extent of band edge photoluminescence quenching or enhanced trap-state emission in S^{2-} capped QDs (Figure A 3). However, there is no correlation between the change in photoluminescence and multiexciton lifetime. The dependence on exciton order (N) (multiexciton lifetime, $\tau_{MX} \propto N^n$) on multiexciton lifetime in S^{2-} is similar to the TOPO capped QDs. The 4 nm and 4.8 nm S^{2-} capped QDs exhibit exciton order (N) dependence of 4.8±0.6 and 5.6±0.6 respectively (Figure 27b) and in the TOPO capped QDs, exciton order (N) dependencies are 5.4±0.03 and 5.7±0.4 (Figure 27b). The comparable (within the fitting error) exciton order (N) dependency indicates the same order of the kinetic rate law of the Auger process. However, the comparison of exciton order (N) dependency should not necessarily be so straightforward. The consideration of different possible channels for recombination as described above with the statistical models cannot be ignored, especially for high-order multiexcitons. This is to be pointed out that these models do not consider the electronic distribution of surface trap states. To verify the participation of surface trap states in Auger recombination, the statistical models need to be modified to take the additional recombination channels into account. This might be challenging because of the undefined electronic structure of surface trap states. However, to establish the surface trap-assisted Auger recombination, as indicated by the increased multiexciton lifetime in S^{2-} capped QDs, the determination of multiexciton binding energy is important. As multiexciton binding energy has strongly been influenced by the extent of carrier wavefunction overlap influencing the Coulomb interaction, the effect of surface hole trapping must be reflected.

To determine multiexciton binding energy a quantitative analysis of the multiexciton species spectra is important with precise determination of spectral position and amplitude. Spectral positions of electronic transitions can be utilized to determine the multiexciton binding energy. The biexciton binding energy (Δ_{BX}) can be determined by the shift between the B_1 and A_1 in the exciton spectra.[83, 91, 125] Similarly, tri- (Δ_{TX}), tetra- (Δ_{QX}), and penta- (Δ_{PX}) exciton binding energies can be estimated from the shifts between B_3 and A_3 in the BX, TX, and QX spectra respectively.[83, 126] A quantitative analysis of multiexciton spectra is not only beneficial to determine multiexciton binding energy but also to exploit the state-filling effect for a relative comparison of the amplitudes to determine the conduction band level population by multiple electrons. It needs to be recalled that TA spectra are composed of the overlapping signal contributions of GSB, PIA, and SE. The GSB and SE contribute to the negative and the PIA contributes to the positive of the overall signal.[65, 127] Deconvoluting TA Spectra using a multi-gaussian fitting routine enables extraction of the pure GSB, PIA, and SE contributions.[83, 127, 128] In this fitting method, each of the GSB, PIA, and SE peaks, corresponding to the respective electronic transitions (i.e., B_1, B_2, and B_3) are fitted by multiple Gaussian functions to model the species spectra:

$$\begin{aligned} S_X(E) = &-\left[A_{B1}\left(e^{-\left(\frac{E-c_{B1}}{w_{B1}}\right)^2}\right) + A_{B2}\left(e^{-\left(\frac{E-c_{B2}}{w_{B2}}\right)^2}\right) \right. \\ &\left. + A_{B3}\left(e^{-\left(\frac{E-c_{B3}}{w_{B3}}\right)^2}\right)\right]_{GSB} \\ &+ \left[\frac{1}{2}A_{B1}\left(e^{-\left(\frac{E-c_{B1}-\Delta_{BX}}{w_{B1}}\right)^2}\right) \right. \\ &\left. + \frac{1}{2}A_{B2}\left(e^{-\left(\frac{E-c_{B2}-\Delta_{BX}}{w_{B2}}\right)^2}\right) + A^*_{B3}\left(e^{-\left(\frac{E-c^*_{B3}}{w_{B3}}\right)^2}\right)\right]_{PIA} \end{aligned} \tag{30}$$

$$\begin{aligned} S_{BX}(E) = &-\left[A_{B1}\left(e^{-\left(\frac{E-c_{B1}}{w_{B1}}\right)^2}\right) + A_{B2}\left(e^{-\left(\frac{E-c_{B2}}{w_{B2}}\right)^2}\right) \right. \\ &\left. + A_{B3}\left(e^{-\left(\frac{E-c_{B3}}{w_{B3}}\right)^2}\right)\right]_{GSB} \\ &+ \left[A_{B3}\left(e^{-\left(\frac{E-c_{B3}-\Delta_{TX}}{w_{B3}}\right)^2}\right)\right]_{PIA} \end{aligned} \tag{31}$$

$$\begin{aligned} S_{TX}(E) = &-\left[A_{B1}\left(e^{-\left(\frac{E-c_{B1}}{w_{B1}}\right)^2}\right) + A_{B2}\left(e^{-\left(\frac{E-c_{B2}}{w_{B2}}\right)^2}\right) \right. \\ &\left. + A_{B3}\left(e^{-\left(\frac{E-c_{B3}}{w_{B3}}\right)^2}\right)\right]_{GSB} \\ &+ \left[A_{B3}\left(e^{-\left(\frac{E-c_{B3}-\Delta_{QX}}{w_{B3}}\right)^2}\right)\right]_{PIA} \\ &- \left[A_{SE}\left(e^{-\left(\frac{E-c_{SE}}{w_{SE}}\right)^2}\right)\right]_{SE} \end{aligned} \tag{32}$$

$$\begin{aligned} S_{QX}(E) = &-\left[A_{B1}\left(e^{-\left(\frac{E-c_{B1}}{w_{B1}}\right)^2}\right) + A_{B2}\left(e^{-\left(\frac{E-c_{B2}}{w_{B2}}\right)^2}\right) \right. \\ &\left. + A_{B3}\left(e^{-\left(\frac{E-c_{B3}}{w_{B3}}\right)^2}\right)\right]_{GSB} \\ &+ \left[A_{B3}\left(e^{-\left(\frac{E-c_{B3}-\Delta_{PX}}{w_{B3}}\right)^2}\right)\right]_{PIA} \\ &- \left[A_{SE}\left(e^{-\left(\frac{E-c_{SE}}{w_{SE}}\right)^2}\right)\right]_{SE} \end{aligned} \tag{33}$$

S_X, S_{BX}, S_{TX}, and S_{QX} are the species spectra of exciton (X), BX, TX, and QX respectively. A represents the amplitudes, c represent the centers, and w represent the widths of the peaks associated to B_1, B_2, and B_3 transitions. The subscript GSB accounts for the B_1, B_2, and B_3 peaks and the subscript PIA accounts for A_1, A_2, and A_3 peaks in the spectra. The widths of the peaks associated with the same transitions are considered the same (e.g., the width of B_1 and A_1 is w_{B1}). The A_3 in the exciton spectra is not fitted with the same shift (i.e., Δ_{BX}). This is because the $1P_e$ level with higher polarizability than the $1S_e$ level does not necessarily result in the same magnitude of carrier-induced Stark effect.[126, 129] Multiexciton binding energy in CdSe QD is described as bound, i.e., with negative binding energy. Strandell et al.[130] reports negative multiexciton binding energy upto QX of CdSe QDs of different sizes. Similarly, the pentaexciton binding energy (Δ_{PX}) was also assumed to be from a bound pentaexciton state with negative binding energy. The SE feature in CdSe QD TA spectra is not as distinctive as the GSB and PIA. However, it is in resonance with A_1 and B_1.[122, 125] The presence of SE can be checked by determining a non-linear spectrum by adding the steady-state spectra to the TA spectra as $Abs_{NL} = \Delta\, Abs + Abs_{steady-state}$.[125] Figure A 19 shows the non-linear spectra of the multiexciton species. The negative absorption in the non-linear spectra means the amplified signal, i.e. the contribution of SE. In the previous works, SE is fitted by a single Gaussian identical to the 1S gaussian assuming that SE source is the MX state.[127] Here, it is fitted with a completely independent Gaussian peak red-shifted from the B_1 to avoid overemphasis of its origin. The SE components in the exciton and BX spectra were ignored to avoid overparameterization of fitting as there is no substantial negative contribution in the non-linear spectra. This is to be clarified that it is not claimed that exciton and BX spectra do not contain SE signals. The multiexciton species spectra with the fit of Eq. (30) – Eq. (33) are shown in Figure A 13 to Figure A 18.

The multiexciton binding energies obtained from the fit of Eq. (30) – Eq. (33) are shown in Table 6. The multiexciton binding energies of the TOPO capped QDs increase with decreasing size and increasing exciton order and exhibit weaker dependency in comparison to the lifetimes (as obtained from multiexciton binding energy, $\Delta_{MX}= R^n$ and multiexciton lifetime, $\tau_{MX} = R^n$) as shown in Figure 28. This observation matches the previous literature reports.[131] Reducing the QD size enhances wavefunction overlapping leading to increased multiexciton binding energy as well as the Auger rate as discussed above. Similarly, with increasing exciton order, carrier density increases resulting in the increased multiexciton binding energy Table 6.

Table 6: *Bi- (Δ_{BX}), tri- (Δ_{TX}), tetra- (Δ_{QX}), and penta- (Δ_{PX}) exciton binding energies obtained from the fit of Eq. (30) – Eq. (33) in the multiexciton species spectra of TOPO and S^{2-} capped CdSe QDs.*

	Δ_{BX} /meV	Δ_{TX} /meV	Δ_{QX} /meV	Δ_{PX} /meV	Δ_{BX} /meV	Δ_{TX} /meV	Δ_{QX} /meV	Δ_{PX} /meV
	TOPO				**S^{2-}**			
2.6 nm	35.9	114.4	203.6	-	-	-	-	-
3.4 nm	24.2	75.0	111.0	-	-	-	-	-
4.0 nm	22.7	66.2	109.6	155.6	15.2	54.8	89.9	119.9
4.8 nm	18.1	49.6	70.8	102.1	12.9	37.1	58.0	64.6

The fit of multiexciton species spectra with Eq. (30) – Eq. (33) was similarly achieved for 4.0 nm and 4.8 nm S^{2-} QDs are shown in Figure A 13 and Figure A 18. However, 2.6 nm and 3.4 nm S^{2-} capped QDs with the complete absence of A_1 and A_3, the Gaussian fitting was not possible. The multiexciton binding energy of the S^{2-} capped QDs are shown in Table 6. The Δ_{MX} of 4.0 and 4.8 nm S^{2-} capped QDs are smaller in comparison to the TOPO ones. The reduction of multiexciton binding energy can be explained by the reduced carrier wavefunction overlapping due to surface hole trapping. In the S^{2-} capped QDs, due to the strong surface hole trapping, electron-hole attractive interaction in the CdSe core reduces.[88] This results in a relative increase of electron-electron repulsion shifting the multiexciton states more towards an unbound state resulting in lowering multiexciton binding energy.[88, 132] As described previously, the positions of the PIA peaks with respect to their GSB peaks can determine multiexciton binding energy. This means that when the binding is significantly low, both the PIA and the respective GSB will have a strong overlap in the spectral position resulting in changing the GSB amplitude and width while the PIA feature being absent.[128] Figure 28a and c show multiexciton binding energy obtained the B_1 and A_1 of the exciton spectra of TOPO and S^{2-} capped 4.8 nm QD. It can clearly be seen that the stronger overlapping of B_1 and A_1 components leads to the vanishing of the overall A_1 feature to the red of the B_1 in the S^{2-} capped QD. This indicates that the PIA features (in particular the A_1) in S^{2-} capped 2.6 nm and 3.4 nm QD spectra are in stronger overlap with the respective GSB due to very low multiexciton binding energy. The fitting routine using the Eq. (30) – Eq. (33) are not sufficient to resolve such differences.

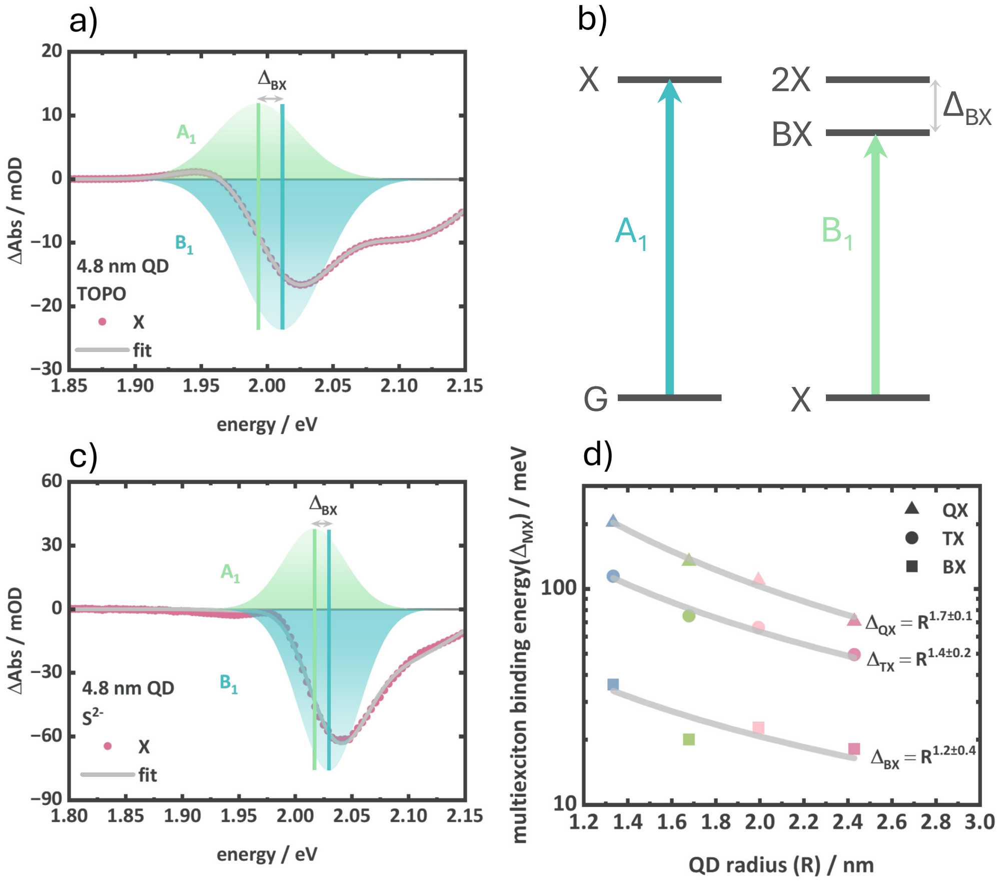

Figure 28: *The A_1 and B_1 peak obtained from the multi-gaussian fitting of Eq. (30) of 4.8 nm (a) TOPO capped and (c) S^{2-} capped QD. The figures demonstrate the extent of A_1 and B_1 overlapping, which determines the BX binding energy (Δ_{BX}). (b) A schematic of excitonic state diagram, representing the optical transitions corresponding to A_1 and B_1 in exciton (X). (d) Radius dependency ($\Delta_{MX} \propto R^n$) of multiexciton binding energy (Δ_{MX}) of BX, TX and QX obtained from the multi-gaussian fit of Eq. (30) – Eq. (33).*

To summarize, the multiexciton lifetime and spectral shape of up to QX from four different sizes of colloidal CdSe QDs with two surface ligands have been evaluated by utilizing global fitting of intensity-dependent TA spectra. The multiexciton lifetimes exhibit the 'universal volume scaling' independent of the surface ligand TOPO or S^{2-}. Upon S^{2-} ligand exchange of the series of QDs, multiexciton lifetimes have significantly increased. This is attributed to the reduction of carrier wavefunction overlapping due to strong hole trapping by S^{2-} surface traps resulting in suppression of the Auger process. A quantitative spectral evaluation was performed with the exciton and multiexciton species spectra, which simplifies understanding of the complex interplay between state-filling and Stark effect in TA signal of CdSe QDs. With this, multiexciton binding energies was determined up to pentaexciton. The multiexciton binding energies exhibit weak volume scaling in good agreement with previous literature. The reduction of multiexciton binding energy in S^{2-} capped QDs indicates a relative decrease in electron-hole Coulomb attraction while an increase in electron-electron Coulomb repulsion. This behaviour can be expected due to the hole localization in surface trap states of S^{2-} QDs.

5. Observing High-order Multiexciton Dynamics under Weak and Strong Electronic Coupling in QD Thin Films

This chapter presents a discussion of the intensity-dependent TA spectra of TOPO and S^{2-} *capped QD thin films, with the objective of elucidating the dependence of multiexciton properties on inter-QD interactions. The Chapter 4 elucidates the impact of hole trapping on prolonged multiexciton lifetime and decreased multiexciton binding energy. This is ascribed to a reduction in the extent of carrier wavefunction overlapping. In QD thin films, the strong inter-QD coupling results in a more pronounced effect of exciton delocalization, which could also severally impact multiexciton properties. Therefore, this chapter presents a comparative study of QD thin films having weak and strong inter-QD coupling with TOPO and* S^{2-} *ligands respectively. For this, thin films of TOPO capped and* S^{2-} *capped QDs are fabricated via drop casting. Prior to conducting intensity-dependent TA, steady-state photoluminescence spectroscopy is performed to verify the occurrence of unique thin film phenomena. Moreover, the intensity-dependent TA spectra of the QD thin films have been subjected to analysis using MCMC to investigate the multiexciton spectral shape and lifetime.*

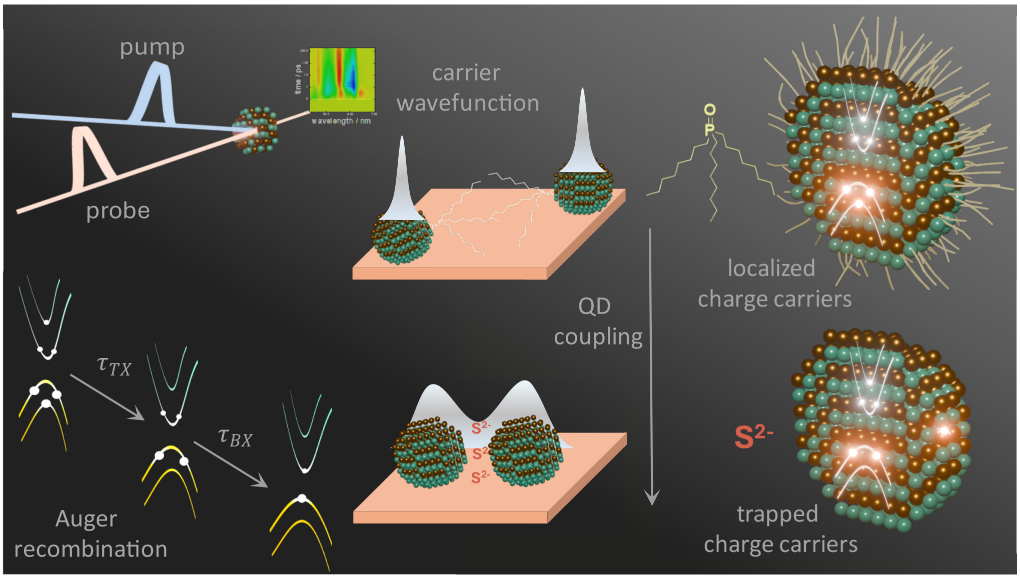
pump
time / ps
wavelength / nm
carrier
wavefunction
probe
O
P
localized
charge carriers
QD
coupling
τ_{TX}
τ_{BX}
S2-
S2-
S2-
S2-
Auger
recombination
trapped
charge carriers

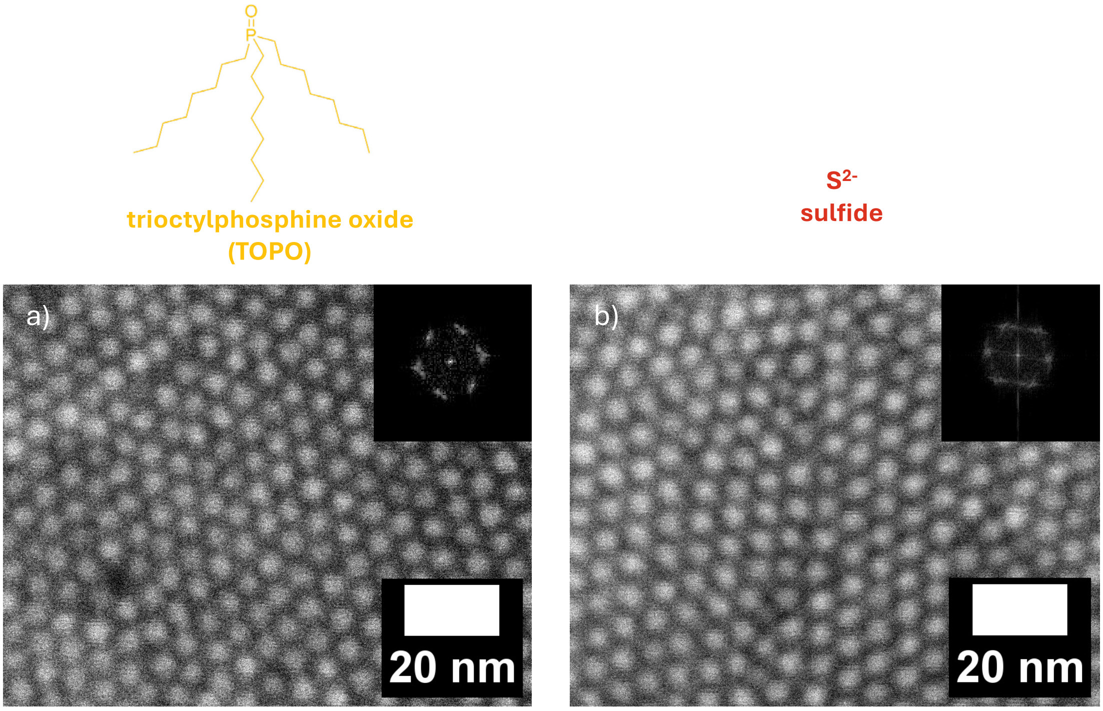

Figure 29: *SEM images of 4.0 nm QDs with surface ligands (a) TOPO, and (b) S^{2-}. The SEM images were collected by drop casting the QD solutions on silicon wafers. The insets in the SEM images represent the fast-fourier-transformed (FFT) images used to determine the distances between QDs.*

The TOPO capped CdSe QDs of four different sizes of 2.6 nm, 3.4 nm, 4.0 nm, and 4.8 nm as discussed in Chapter 4 were synthesized via the hot injection method (Appendix A). The respective S^{2-} capped QDs were obtained from biphasic ligand exchange as discussed in Chapter 4 (experimental details in Appendix A). QD thin films were prepared by drop casting the colloidal solutions (TOPO capped QDs in toluene, and S^{2-} capped QDs in NMF) of the QDs on glass substrates. Figure 29 shows the SEM images of 4.0 nm QD thin film with TOPO and S^{2-} ligands. In the SEM images, 4.0 nm QDs exhibit an ordered hexagonal close packing with an average spacing of 6.6 nm with TOPO (Figure 29a) and 5.4 nm with S^{2-} (Figure 29b). The spacings in the superlattice formed between QDs were determined by fast-fourier-transformation (FFT) of the SEM images. The spacing between QDs obtained is the average distance between the centers of two QDs. The bulky nature of TOPO ligands keeps the QDs well separated in thin films, while for S^{2-}, QDs are closely packed with smaller distances to each other. The 2.6 nm, 3.4 nm, and 4.0 nm TOPO capped QDs also exhibit a similar hexagonal close packing with an average spacing of ~ 6 nm. However, the corresponding S^{2-} QDs (of 2.6 nm, and 3.4 nm) are not well resolved due to the insufficient contrast to distinguish the spacing between QDs.

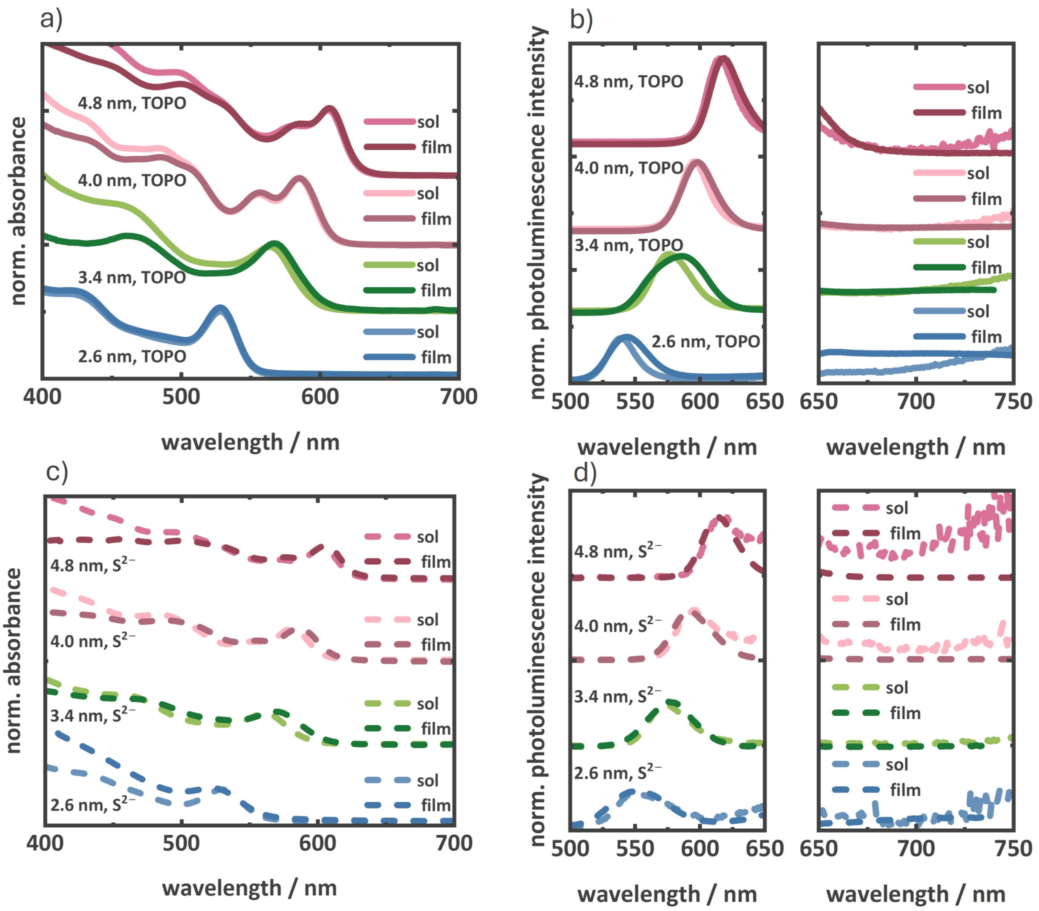

Figure 30: *(a) Steady-state absorption, and (b) photoluminescence spectra of TOPO capped 2.6 nm, 3.4 nm, 4.0 nm, and 4.8 nm QDs both in solution (sol), and thin films (film). (c) steady-state absorption, and (d) photoluminescence spectra of* S^{2-} *capped 2.6 nm, 3.4 nm, 4.0 nm, and 4.8 nm QDs both in solution (sol), and thin films (film). The left panels in (b) and (d) depict the normalized band-edge photoluminescence and in the right panels, the zoomed view of the trap-state emissions is shown. A background correction to remove the scattering contribution in the thin film absorption spectra was performed as described in Figure A 20.*[133]

Steady-state absorption and photoluminescence spectra of the four QDs in both solution and film are shown in Figure 30. The absorption spectra of QD thin films show strong wavelength-dependent scattering which was corrected by fitting a polynomial background correction[133] function as illustrated in Figure A 20. The comparison of the absorption spectra of TOPO and S^{2-} capped 2.6 nm, 3.4 nm, 4.0 nm, and 4.8 nm QDs shows nearly identical (peak position and width) 1S peaks in solution and in the layers (Figure 30a & c). However, a slight red shift (ranging from 12 meV to 20 meV) has been observed in the thin film photoluminescence spectra. This shift is majorly due to the electronic coupling and energy transfer (originating from the size distribution) between closely packed QDs in thin film.[134, 135] Due to the bulky nature of TOPO, steric hindrance prevent the extreme proximity of QDs in thin film, due to this the inter-QD interactions are relatively weak. On other hand, the photoluminescence spectra of TOPO capped 2.6 nm QDs exhibits a stronger trap-state emission in the film (Figure 30b). This is attributed to the distortion of coordinately bound TOPO ligands, which opens up non-passivated surface sites resulting in surface trap-states.[136] The electronic coupling between QDs in thin film can be tuned by the spacing[8, 137] between QDs, where the S^{2-} capped QD thin films can be a great example as understood from the SEM analysis (Figure 29b).

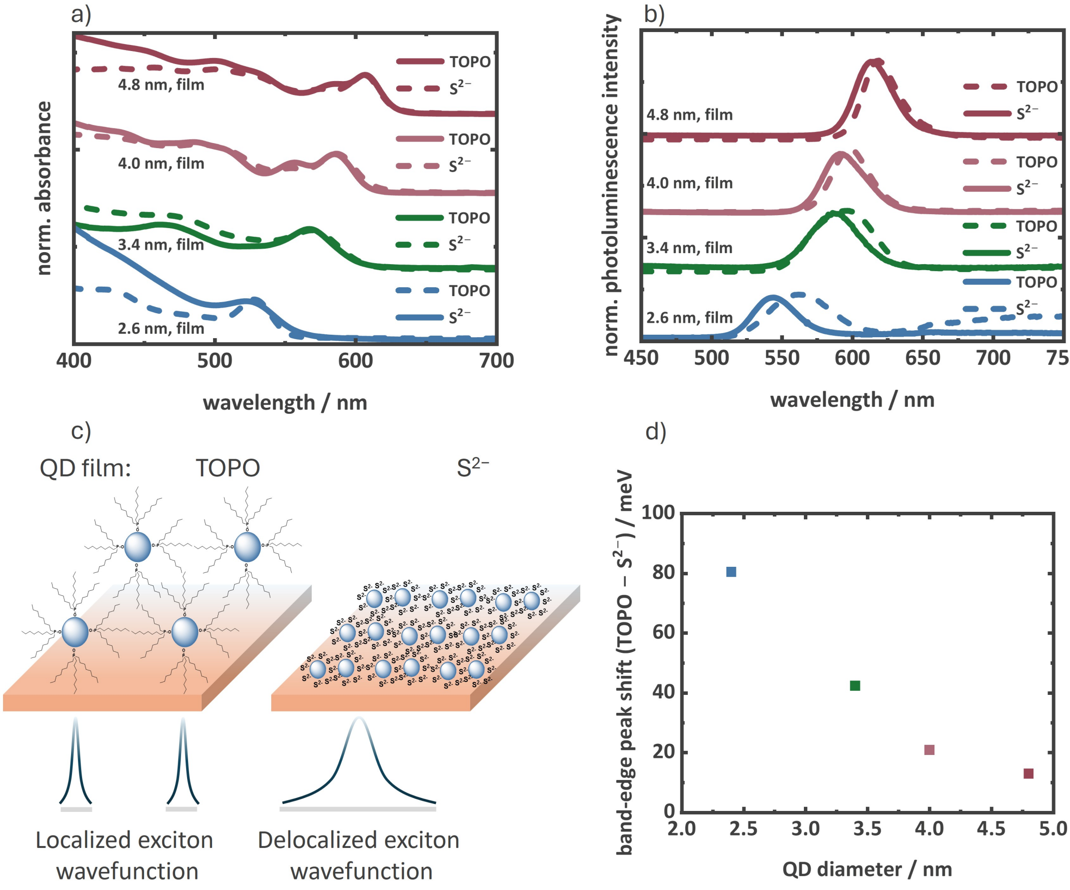

Figure 31: *(a) Steady-state absorption spectra, and (b) photoluminescence spectra of thin films of TOPO and* S^{2-} *capped 2.6 nm, 3.4 nm, 4.0 nm, and 4.8 nm QDs. A background correction to remove the scattering contribution in the thin film absorption spectra was performed as described in Figure A 20.*[133] *(c) A schematic of localized excitons in well separated TOPO capped QD thin film, and delocalized excitons in closed-packed* S^{2-}*capped QD thin film. (d) Plot representing the red-shifts, observed in* S^{2-}*capped QD thin film with respect to the respective TOPO capped QDs, as a function of QD size.*

To investigate this, steady-state absorption and photoluminescence spectra of the S^{2-} capped QD thin films (drop casted on glass substrates) were collected (Figure 31). The band-edge photoluminescence peaks in S^{2-} capped QD thin films are significantly redshifted compared to the photoluminescence peaks of the corresponding TOPO capped QDs (Figure 31b). This effect was relatively weak in TOPO capped QD thin films (compared to the TOPO capped QD solution, Figure 30b). The observed red-shifts in S^{2-} capped QD thin films are induced by strong electronic coupling due to closely spaced QDs.[138] In TOPO capped QD thin films, QDs are sufficiently separated with a minimal QD interaction due to the bulky chemical structure of TOPO, while S^{2-} being a single atomic entity brings the QDs very close. This results in the delocalization of exciton wavefunction (as illustrated in Figure 31c) leading to the decrease of overall band-gap, due to which band-edge photoluminescence is observed at higher wavelengths compared to the TOPO capped QDs. Additionally, the extent of the red shift was observed to be changing with QD sizes (Figure 31d). The S^{2-} capped 2.6 nm, 3.4 nm, 4.0 nm, and 4.8 nm QD thin films exhibit red shifts (with respect to the corresponding TOPO QD films) of 80.5 meV, 42.5 meV, 20.9 meV and 13.0 meV, respectively. Figure 31d shows that the shift is increasing with lowering QD size. This is because the effect of exciton delocalization is stronger in small QDs due to the high confinement energy.[139] These observations indicate that after photoexcitation in QD thin films, the exciton dynamics is strongly influenced by the QD size and the spacing between them. To investigate further also on the impact on the multiexciton properties, intensity-dependent TA spectroscopy was performed on the QD thin films to extract exciton and multiexciton lifetimes and spectral shape. As 2.6 nm and 3.4 nm QD thin films possess the extreme influence of electronic coupling (as seen in Figure 31), these two QDs were chosen to collect intensity-dependent TA data. The intensity-dependent TA spectra of TOPO and S^{2-} capped 2.6 nm and 3.4 nm QD solution were discussed in Chapter 4, which will be reused in this chapter for a comparative analysis. To collect intensity-dependent TA spectra of the thin films, QD solutions were drop casted on glass substrates, and an inert film holder with constant N_2 flow was used to prevent photo-oxidation. To collect the intensity-dependent TA spectra, a similar range of pump intensities (1.2×10^{-4} to 4.3×10^{-3} $\mu W \mu m^{-2}$) was used as for the corresponding solution measurements. The experimental details are described in Appendix A.

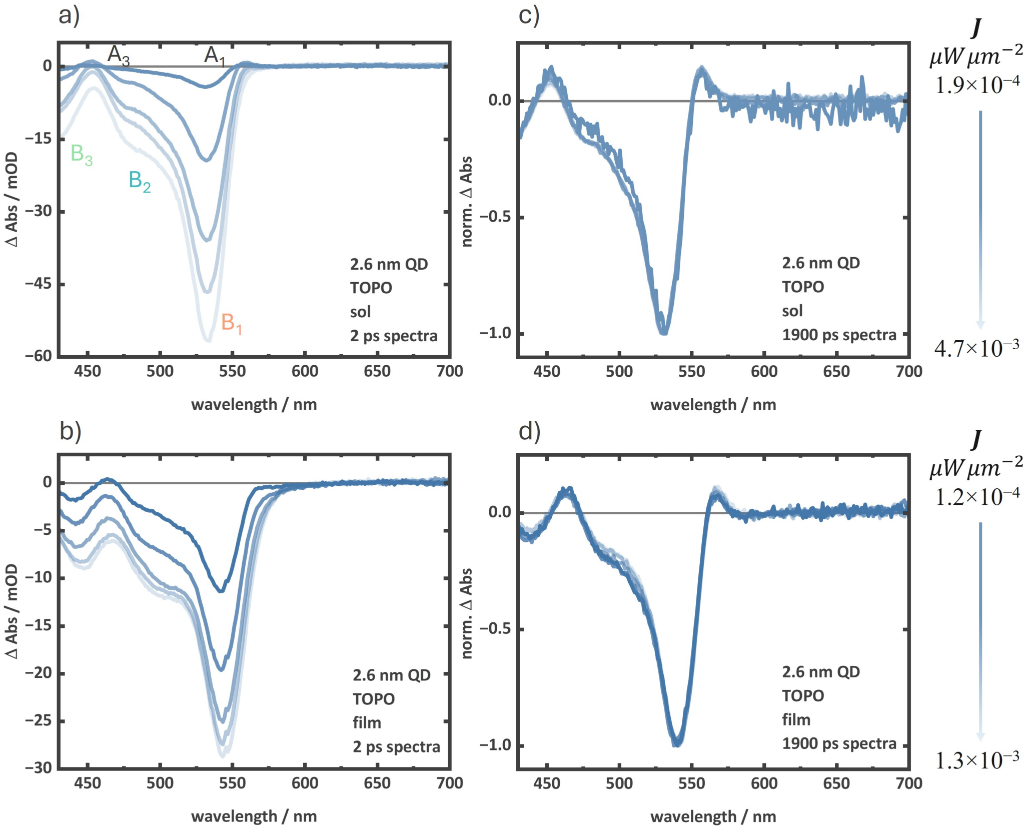

Figure 32: *Intensity-dependent TA spectra at 2 ps of TOPO capped 2.6 nm QD in (a) solution, and (b) film. Normalized (at B_1 bleach) intensity-dependent TA spectra at 1900 ps of TOPO capped 2.6 nm QD in (c) solution, and (d) film. The change of intensity is depicted by the arrow on the left with the highest and the lowest intensity used.*

The intensity-dependent TA spectra of TOPO capped 2.6 nm QD thin film exhibit similar spectral features as in solution as shown in Figure 32a & b. The typically observed B_1, B_2, B_3, A_1, and A_3 features in the TA spectra of CdSe QDs are marked in Figure 32a, which were already discussed in detail in Chapter 4 & 2.3. In short, the B_1, B_2, and B_3 are the bleach features corresponding to the three lowest 1S, 2S, and 1P electronic transitions. The A_1, and A_3 are PIA features that occur redshifted from 1S and 1P transitions respectively. Similar to the TA spectra in solution, B_1, B_2, and B_3 bleach features in the thin film of 2.6 nm TOPO capped QD increase amplitude with increasing intensity originating from increasing state-filling effect with higher population in conduction band levels. Similarly, the A_1, and A_3 features decrease with increasing intensity, because of decreasing carrier-induced Stark effect. At 1900 ps, the intensity-dependent TA spectra are identical when normalized at B_1 for both solution and thin film of TOPO capped 2.6 nm QD. This is due to the dominant exciton species concentration (left after completion of Auger recombination) at 1900 ps as discussed in Chapter 4. The identical intensity-dependent spectral features in solution and thin films of TOPO capped 2.6 nm QD concludes that the multiexciton recombination processes in TOPO capped thin films can be explained by the TX kinetic model as shown in Eq. (28). Similarly, the intensity-dependent TA spectra of a thin film of TOPO capped 3.4 nm QD thin film exhibit similar features as in solution, indicating a consistent Auger recombination process for multiexciton recombination (Appendix D, Figure A 21).

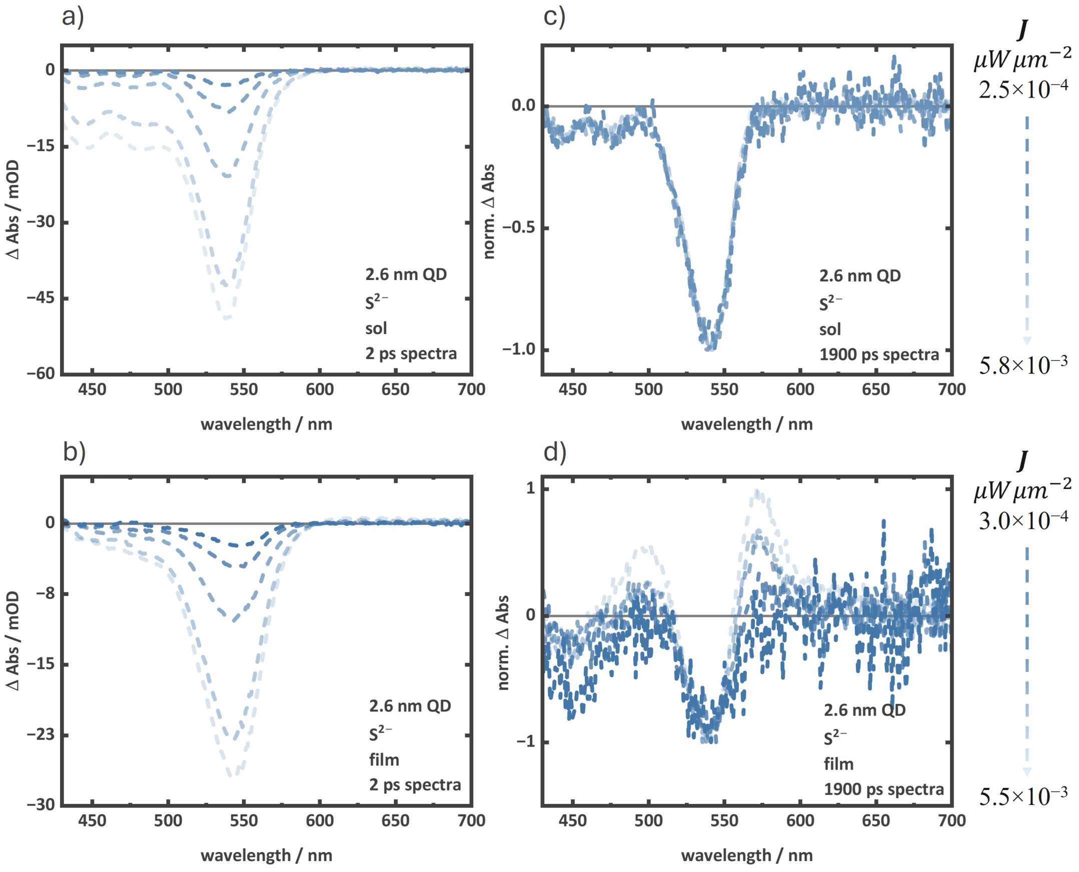

Figure 33: *Intensity-dependent TA spectra at 2 ps of S^{2-} capped 2.6 nm QD in (a) solution, and (b) film. Normalized (at B_1 bleach) intensity-dependent TA spectra at 1900 ps of TOPO capped 2.6 nm QD in (c) solution, and (d) film. The change of intensity is depicted by the arrow on the left with the highest and the lowest intensity used.*

Figure 33 shows the intensity-dependent TA spectra of S^{2-} capped 2.6 nm QD thin film and solution. The thin film spectra of S^{2-} capped 2.6 nm QD exhibit significant differences from the solution. The B_1 feature at 2 ps, however shows a similar behaviour with increasing amplitudes with intensities (Figure 33a & b). The B_2 and B_3 bleaches are not pronounced in the thin film spectra. Similar to the solution spectra, A_1, and A_3 features in thin film also are not observed at 2 ps (Figure 33a & b).

On other hand, at 1900 ps the intensity-dependent TA spectra of S^{2-} capped 2.6 nm QD thin film show intensity-dependent spectral change with pronounced A_1, and A_3 features (Figure 33c & d). The A_1 and A_3 features are highly prominent at 1900 ps, which gradually increase with increasing intensity (Figure 33d). Similar spectral features are also observed in the intensity-dependent TA spectra of S^{2-} capped 3.4 nm QD thin film (Figure A 22). The A_1 and A_3 features in S^{2-} capped QD solution was however not observed due to small multiexciton binding energy (as described in Chapter 4). On the other hand, at 1900 ps, due to the dominating exciton population, the spectral shape of intensity-dependent TA spectra look identical as previously observed for 2.6 nm, 3.4 nm, 4.0 nm, and 4.8 nm TOPO and S^{2-} capped QD solutions (Figure 22, Chapter 4). This feature is also observed in the 2.6 nm (Figure 32d), and 3.4 nm (Figure A 21b) TOPO capped QD thin film.

Further, to evaluate the temporal evolution of the spectral features, the kinetic traces in QD thin film are plotted to compare with the solution data (2.6 nm QDs in Figure 34, 3.4 nm QDs in Figure A 21d & Figure A 22d). Figure 34 shows the B_1 kinetics of TOPO and S^{2-} capped 2.6 nm QD both in solution and film. The B_1 kinetics in TOPO capped QD thin film show similar intensity-dependent behaviour as the solution kinetics (Figure 34a & b). As with the solution kinetics, B_1 in thin film shows a maximum amplitude at ~ 1.5 ps, which further gradually decays. The initial decay time (starting from ~ 1.5 ps) shows additional fast decaying components with increasing intensity, attributed to fast Auger recombination of multiexciton states.[65] However, in the thin films, the B_1 kinetics show relatively slow decaying features. After ~ 100 ps, the B_1 kinetics exhibit a similar decay trend over all intensities due to the dominant exciton contribution which is also in good agreement with the solution data .[65, 84] Hence, the similar spectral and kinetic features of the solution and film of TOPO capped 2.6 nm QDs confirm the TX kinetic decay model for multiexciton recombination as shown in Eq. (28). The TX kinetic decay model can additionally be hypothesized because of the measurement in the same range of pump intensities.

On the other hand, similar to the unique spectral features in S^{2-} capped QD thin film, the B_1 kinetic traces in 2.6 nm QD thin film also exhibit unique differences compared to the solution (Figure 34c & d). The maximum amplitude in the B_1 kinetics means the completion of carrier relaxation at the $1S_e$ level, which has been observed at ~ 1.5 ps for the TOPO and S^{2-} capped QD solution (shown in Chapter 4) as well as the 2.6 nm TOPO capped QD film (Figure 34b). As opposed to that, in S^{2-} capped QD thin film, B_1 maxima is at ~ 0.5 ps, indicating a faster relaxation of hot carriers to the $1S_e$ level. On other hand, unlike in solution (Figure 34e), the B_1 kinetics in the thin film do not exhibit intensity-dependent features, rather they are close to identical in all the intensities when normalized (Figure 34f). As the fast-decaying components corresponding to multiexciton Auger recombination observed in the early time region (e.g., in the B_1 kinetics of 2.6 nm TOPO capped QD thin film, Figure 34e) in intensity-dependent B_1 kinetics are not pronounced, the TX kinetic model (Eq. (28)) fit to extract exciton and multiexciton lifetime might be challenging. Moreover, the faster relaxation to the $1S_e$ level (indicated by completed B_1 bleach formation at ~ 0.5 ps), and identical B_1 kinetic in all intensities for S^{2-} capped QD thin film, indicates a fast exciton delocalization from the hot state dominating over band relaxation. This means that the carriers from the hot multiexciton states might tend to delocalize to the neighbouring QDs in the ultrafast time regime (before 0.5 ps), which will cause a faster state filling in the $1S_e$ levels (of the neighbouring QDs) as indicated by the B_1 bleach maxima at ~ 0.5 ps. In this case, there will not be any available multiexciton states in the QD ensemble, rather delocalized excitons over the QD thin film. Due to this, the typical Auger recombination process cannot occur as indicated by the absence of the typical fast decaying components (due to Auger recombination) and identical B_1 kinetics in all intensities for the S^{2-} capped QD thin film.

As shown in Figure 33d, the intensity-dependent features in S^{2-} capped 2.6 nm QD thin film are particularly observed in A_1 and A_3 features at 1900 ps with strong and broad peaks increasing with intensity. Hence, a comparative analysis of these features is necessary. The A_1 kinetics of S^{2-} capped 2.6 nm QD thin film is shown in Figure 35c along with the A_1 kinetics of TOPO capped 2.6 nm QD in both solution and film (Figure 35a & b). As previously discussed, the A_1 feature is ascribed as the biexciton effect originating at exciton species with a PIA involving the $1S_e$ level which is observed over the whole range of time starting from ~1.5 ps at low intensities and after ~ 100 ps at high intensities (Figure A 4c).[91] However, the A_1 feature before ~1.5 ps additionally needs a careful analysis to understand the ultrafast exciton delocalization process (as hypothesized above). In the TOPO capped QD solution, there is an initial (close to time zero) rise of the A_1 feature with a positive signal immediately after time zero, which gradually decays upto ~1.5 ps (Figure 35a). When the intensity is high the A_1 feature at ~ 1.5 ps exhibits negative signal (Figure 35a) which further turns into a positive signal (the biexciton effect). The time of the A_1 features turning into a positive signal (i.e., the start of biexciton effect) after ~ 1.5 ps are different in different intensities. When the intensity is increased the formation of this positive A_1 feature is delayed. The similar effect is observed also for the TOPO capped QD thin film (Figure 35b). However, in the S^{2-} capped 2.6 nm QD thin film (Figure 35c), the A_1 kinetics are slightly different compared to the respective TOPO capped QD film. In the S^{2-} capped 2.6 nm QD thin film (Figure 35c), the negative A_1 feature is formed at ~1.5 ps, however the start of the biexciton effect (i.e., the A_1 feature showing a positive signal) is same (at ~100 ps) in all intensities (Figure 35c).

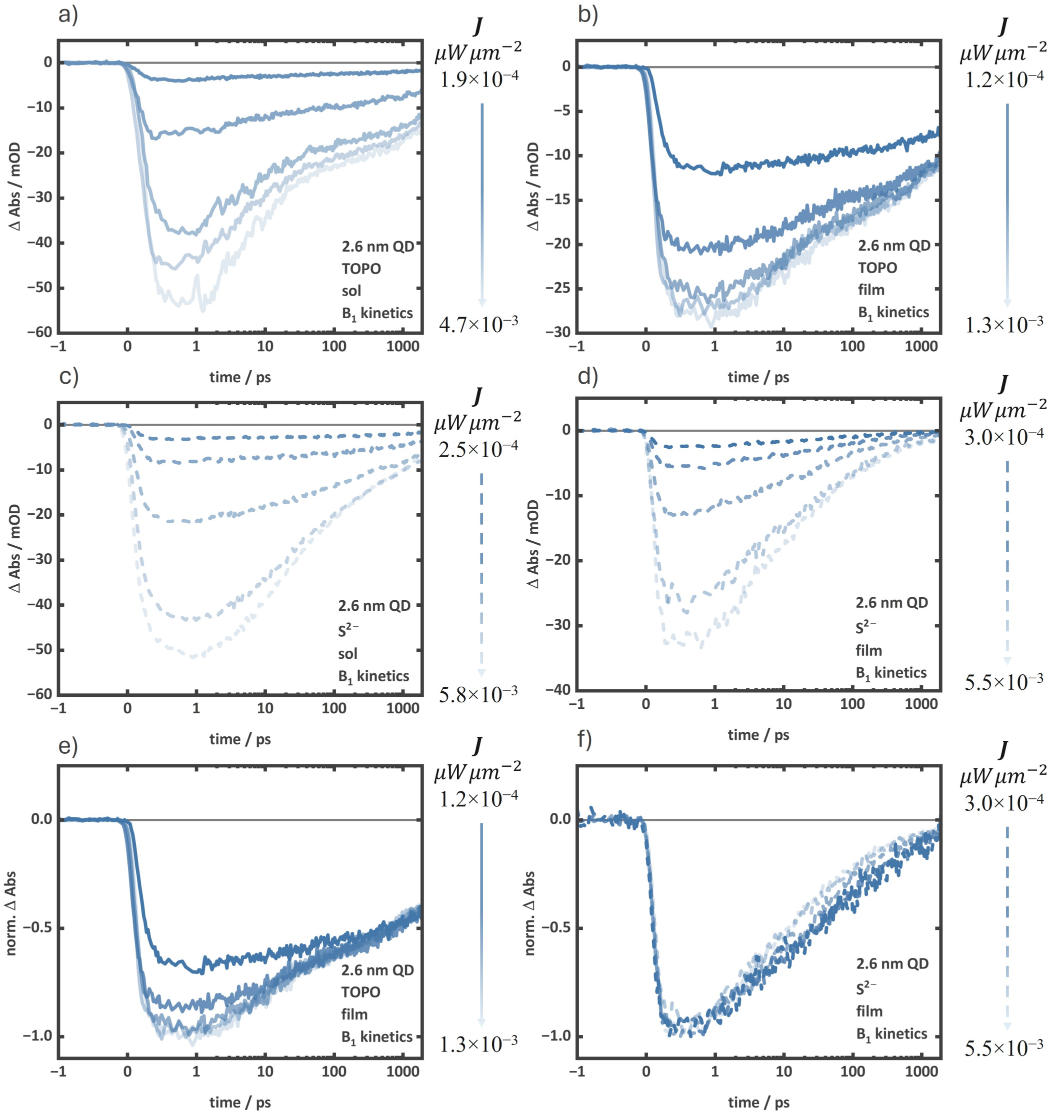

Figure 34: *Intensity-dependent B_1 kinetics of TOPO capped 2.6 nm QD in (a) solution, and (b) film. Intensity-dependent B_1 kinetics of S^{2-} capped 2.6 nm QD in (c) solution, and (d) film. Normalized Intensity dependent B_1 kinetics of (e) TOPO capped, and (f) S^{2-} capped 2.6 nm QD film. The change of intensity is depicted by the arrow on the left with the highest and the lowest intensity used.*

The initial (close to time zero) rise of A_1 with a positive signal is due to the formation of hot states, as the pump excitation is at 400 nm, well above the $1P_e$ levels.[65, 117] When the carriers are in the higher energy levels immediately after pump interaction, Stark-effect is highly dominant over the state-filling effect. The hot carriers (populating high electronic levels) with strong local field, modulate the oscillator strength of the optical transitions resulting in strong PIA, e.g., the A_1 feature. After that, the hot carriers gradually cool down to the $1S_e$ level via Auger cooling or phonon cooling upto ~ 1.5 ps (indicated by completed B_1 bleach formation at ~ 1.5 ps TOPO capped 2.6 nm QD, Figure 34a & b).[117] This effect is reflected in the A_1 kinetics where it shows maximum negative amplitude at ~ 1.5 ps indicating a completion of carrier relaxation. At ~ 1.5 ps, the change of A_1 amplitudes with intensities is due to the carrier population of multiexciton states (i.e., because of the biexciton effect being dominant in low intensities and being absent in high intensities). At low intensities (exciton regime), when the hot carrier relaxation process is completed, the $1S_e$ level is singly occupied, and the biexciton effect takes place forming a positive A_1 feature, while at high intensities the biexciton effect gradually vanishes. Moreover, the delayed recovery time of the A_1 feature to a positive signal with increasing intensity is because of different recombination times of multiexciton states. After the hot carrier relaxation is completed at ~ 1.5 ps, exciton or multiexciton recombination takes place depending on the intensity. At high intensity, TX and BX species are present in TOPO capped 2.6 nm QD solution (as discussed in Chapter 4) with lifetimes of 2.2 ps and 12.7 ps respectively (Table 5). After the TX and BX recombination events, the A_1 feature turns positive as a biexciton effect indicating the presence of exciton. As increasing intensity increases BX and TX concentration, the recovery of A_1 feature to exhibit the biexciton effect (with a positive signal) is delayed compensating the BX and TX lifetime. The same effect is also observed for TOPO capped 2.6 nm QD thin film. However, the hot carrier relaxation is relatively faster in the A_1 kinetics of the TOPO capped 2.6 nm QD thin film compared to the solution (Figure 35a & b).

On other hand, the A_1 feature in S^{2-} capped 2.6 nm QD thin film shows contrasting behaviour (Figure 35c). This is to be reminded that in S^{2-} capped 2.6 nm QD solution, the A_1 was not observed due to small BX binding energy originating from surface hole localization (Chapter 4, Figure 28), hence in thin film also the same should be consistent. In contrast, the A_1 kinetics turn positive at ~ 100 ps and similarly the spectra at 1900 ps show strong A_1 bands. In S^{2-} capped 2.6 nm QD thin film (Figure

35c), the recovery of A_1 to a positive feature (i.e., the biexciton effect) is at ~ 100 ps in all the intensities. Once the positive A_1 feature is formed, the decay trend afterwards is similar in all intensities. On other hand, the hot carrier relaxation in S^{2-} capped 2.6 nm QD thin film as observed in the A_1 kinetics is at ~ 1.2 ps (Figure 35c), while in B_1 kinetics (Figure 34d), it is at ~ 0.5 ps. This indicates that the hot carrier cooling is not occurring solely at the $1S_e$ level but also via other channels. Because of the strong electronic coupling in S^{2-} capped QD thin film, a fast exciton delocalization from the hot state dominating over band relaxation might take place.

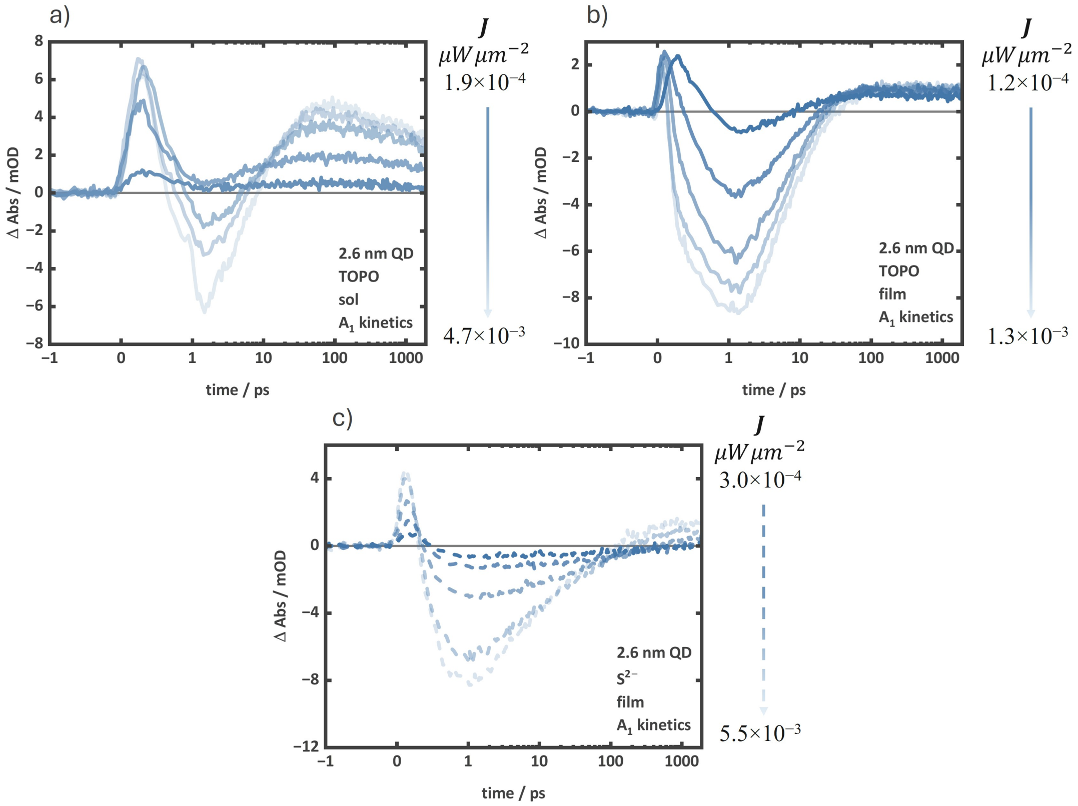

Figure 35: *Intensity-dependent A_1 kinetics of TOPO capped 2.6 nm QD in (a) solution, and (b) film. (c) Intensity-dependent A_1 kinetics of S^{2-} capped 2.6 nm QD film. The change of intensity is depicted by the arrow on left with the highest and the lowest intensity used.*

The comparative analysis of the intensity-dependent TA spectra and the kinetics, as described above, of the TOPO and S^{2-} capped QD thin films and solutions suggests that the hot multiexciton states might undergo ultrafast delocalization to the neighbouring QDs without going through the typical Auger recombination. However, for a comparative study of the intensity-dependent TA data of the QD thin films and solution (as discussed in Chapter 4), the global fitting routine based on MCMC was employed. A detailed description of the method has previously been discussed in Chapter 4. The intensity dependent TA spectra of 2.6 nm and 3.4 nm TOPO and S^{2-}

capped QD thin film were fitted the TX kinetic model (Eq. (28)). To keep a comparable analysis with the solution data (as discussed in Chapter 4), the TA data for thin film was chosen in the range of 2 ps – 1900 ps, and 430 nm – 700 nm for MCMC fitting. The MCMC fit results are shown in the Appendix D (Figure A 23 to Figure A 26, and Table A 9 to Table A 12). The multiexciton spectra obtained from MCMC fit are shown in Figure 36.

$$\mathrm{TX} \xrightarrow{\tau_{TX}} \mathrm{BX} \xrightarrow{\tau_{BX}} \mathrm{MX} \xrightarrow{\tau_{MX}}$$

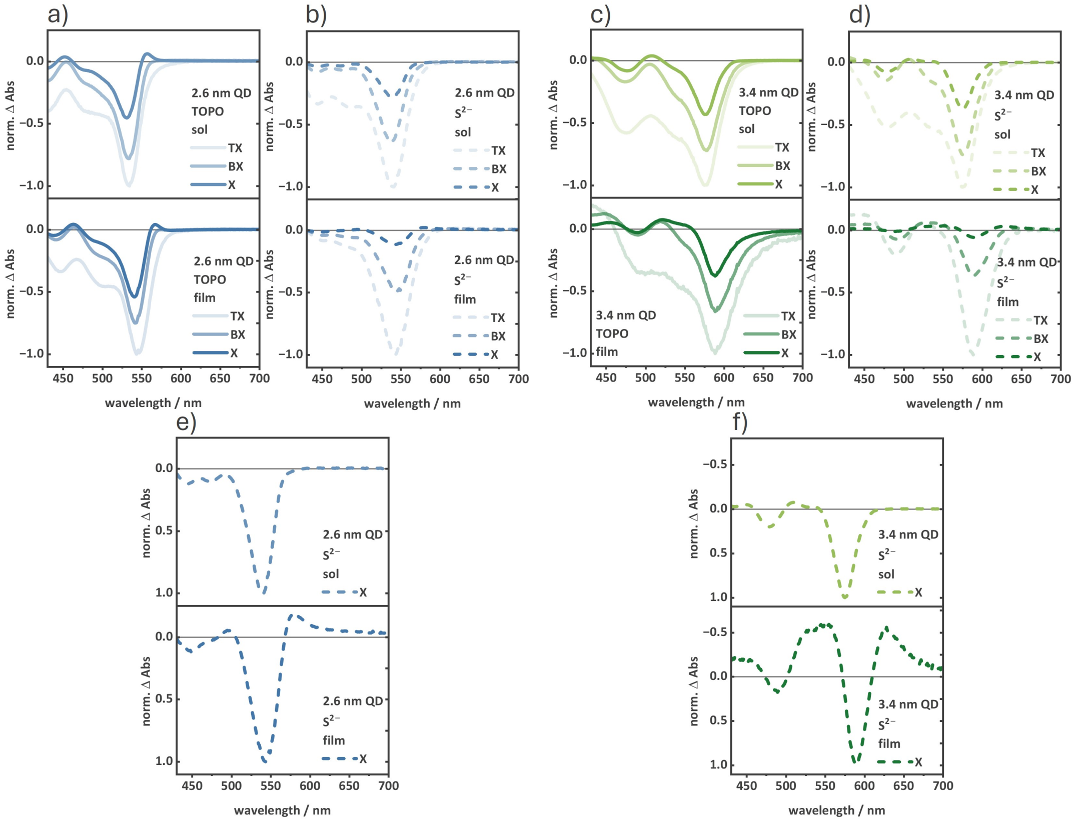

Figure 36: Multiexciton species spectra obtained from MCMC fitting of (a) TOPO, and (b) S^{2-} capped 2.6 nm QD solution and thin film. Multiexciton species spectra obtained from MCMC fitting of (c) TOPO, and (d) S^{2-} capped 3.4 nm QD solution and thin film. The species spectra were normalized at the B_1 of TX spectra. Exciton (X) species spectra of (e) S^{2-} capped 2.6 nm QD solution and thin film, and (f) S^{2-} capped 3.4 nm QD solution and thin film.

As indicated by the similar raw data in solution and thin film of TOPO capped both 2.6 nm, and 3.4 nm QDs, the spectra obtained from the MCMC fit (Figure 36a & c) also exhibit similar features. This concludes that the spectral features of multiexciton states do not change in a weak inter-QD coupling condition. However, in S^{2-} capped QD thin films, the exciton and multiexciton spectra do not show the same multiexciton features as the corresponding solution spectra. An increasing B_1 feature from exciton to TX is however consistent (with the multiexciton spectra in solution), although the ratios (e.g., amplitude of BX:exciton) have changed. Figure 36b & d shows that the exciton spectra has a drastic change in S^{2-} capped QD thin film compared to the solution spectra, with pronounced A_1 and A_3 features (which was expected from the raw data comparison (Figure 33). The exciton spectra of the S^{2-} capped QDs are separately plotted in Figure 36e & f. The A_1 features in the exciton spectra of S^{2-} capped QD thin films are broad and extended to longer wavelengths. The broad PIA region in the long wavelength is typically described as a contribution of surface trapped hole.[74, 140] From the previous discussion of the raw data, it is understood that the A_1 feature observed in S^{2-} capped QD cannot be the biexciton effect. This indicates that the contribution in exciton spectra could be a superposition of exciton, delocalized exciton, and surface trapped hole.

The multiexciton lifetimes estimated from MCMC fitting of the TOPO and S^{2-} capped 2.4 nm and 3.4 nm QD solution and thin film are shown in Table 7. The multiexciton lifetimes exhibit an increasing trend with QD size similar to the QD solutions (Table 5). On the other hand, with increasing exciton order, multiexciton lifetime decreases. The multiexciton lifetimes in TOPO capped QDs have increased in thin films compared to the solutions. As the intensity-dependent spectral and kinetic features are similar in both solution and thin film, the increased multiexciton lifetime in thin film indicates the effect of either weak electronic coupling, or additional trap states due to ligand shell deformation in TOPO capped QD film. Additionally, in QD films, due to the inherent size distribution, resonance energy transfer process also take place.[135] Due to the simultaneous occurrence of such complex events, it is challenging to figure out the core reason of increased lifetime in TOPO capped QD film. However, in Figure 30 it is shown that the TOPO capped 2.6 nm and 3.4 nm QDs exhibit higher trap-state emission in thin film than in solution due to the ligand shell deformation resulting in increased surface trap-states.[136] As previously observed (in Chapter 4), increased surface-traps localize holes resulting in reduced carrier wave function overlapping leading to suppressed Auger recombination process. Hence, the increased multiexciton lifetimes in TOPO capped QD film (compared to the solution) can be attributed to the trap-assisted Auger process. On other hand, in the S^{2-} capped QD films, multiexciton lifetimes decrease in comparison to the solution. However, this data needs careful analysis. As discussed before, the comparison of raw data of solution and films of S^{2-} capped QD suggests that multiexciton states tend to delocalize from the hot states directly without following the Auger recombination model. Although from the MCMC fitting, three species spectra (of TX, BX, and exciton) were obtained; assigning these spectra to multiexciton states might be misleading due to the absence of the typical multiexciton features. similarly, the lifetimes obtained from MCMC fitting for S^{2-} capped QD films might not deliver a clearer picture of multiexciton recombination in strong coupling conditions.

Table 7: *Multiexciton lifetime and absorption cross-section (α) of TOPO and S^{2-} capped 2.6 nm and 3.4 nm QD solution and thin film determined by MCMC fit. Parameters shown in the Table are the mean values and 99% confidence intervals obtained from MCMC sampling.*

	τ_{TX} /ps	τ_{BX} /ps	$\alpha \times 10^{-15}$ /cm^2	τ_{TX} /ps	τ_{BX} /ps	$\alpha \times 10^{-15}$ /cm^2
	TOPO			**S^{2-}**		
	Solution					
2.6 nm	$2.24_{2.23}^{2.25}$	$12.72_{12.68}^{12.73}$	$1.6013_{1.6010}^{1.6028}$	$5.49_{5.48}^{5.50}$	$61.86_{61.78}^{61.98}$	$2.042_{2.041}^{2.043}$
3.4 nm	$5.07_{5.06}^{5.08}$	$47.12_{47.10}^{47.15}$	$2.149_{2.148}^{2.149}$	$6.865_{6.862}^{6.867}$	$76.33_{76.31}^{76.35}$	$2.176_{2.176}^{2.177}$
	film					
2.6 nm	$4.73_{4.71}^{4.73}$	$37.05_{36.92}^{37.14}$	$1.716_{1.715}^{1.717}$	$2.50_{2.47}^{2.51}$	$47.02_{46.88}^{47.18}$	$3.089_{3.087}^{3.093}$
3.4 nm	$6.83_{6.80}^{6.86}$	$78.88_{78.75}^{79.08}$	$3.094_{3.091}^{3.097}$	$2.93_{2.90}^{2.94}$	$57.35_{57.08}^{57.63}$	$3.341_{3.335}^{3.347}$

To summarize, weak and strong electronic coupling of QDs in thin films were achieved via deposition of TOPO and S^{2-} capped colloidal CdSe QDs of different sizes. The effect of electronic coupling in QD thin film was monitored by photoluminescence spectroscopy. Due to highly closed packed structure and smaller spacing, S^{2-} capped

QDs exhibit strong electronic coupling indicated by a prominent red-shift of the band-edge photoluminescence peak, while this effect is relatively weaker in TOPO capped QD film. Additionally, the trap-state emission gets pronounced in thin film of TOPO capped QDs due to the distortion of the ligand shell, resulting in increased surface trap states.

The multiexciton properties remain unchanged (compared to the one in solution) in weakly coupled QD systems i.e., in the TOPO capped QD films. However, the multiexciton lifetimes were increased in TOPO capped QD films compared to the solution, which is attributed to the trap-assisted Auger process, activated upon distortion of the ligand shells. The S^{2-} capped QD films do not exhibit a clear multiexciton recombination feature, rather indicates ultrafast delocalization of hot multiexcitons, without going through the typical Auger recombination model.

6. Deposition of CdSe NCs in Highly Porous SiO_2 Matrices – In-situ Growth vs. Infiltration Methods

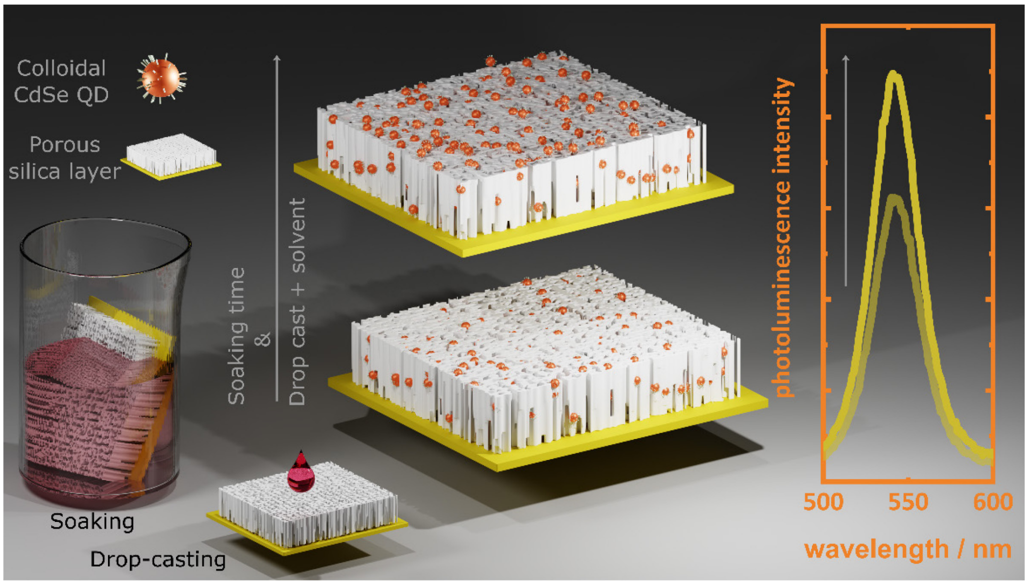
Colloidal
CdSe QD
Porous
silica layer
Soaking
Drop-casting
Soaking time
&
Drop cast + solvent
photoluminescence intensity
500
550
600
wavelength / nm

This chapter is based on the published research article '*Materials* 2024, 17, 4379'. In this chapter, methods of fabricating CdSe QD thin films using porous silica matrix as a template. Porous silica layers were fabricated by atomic layer deposition followed by selective wet chemical etching to achieve certain pore sizes. The SILAR method was utilized for in-situ growth of CdSe NCs, which leads to a broad size distribution of the NCs resulting in broad absorption features and poor photoluminescence quantum yield. To overcome this problem, the colloidal CdSe QDs were infiltrated to the porous matrix using a soaking and a drop casting strategy. This chapter focuses on a comparative analysis of these strategies to evaluate the quality of the layers by investigating the structures and optical properties.

Authors contribution: The porous silica layers were produced in the group of A. Szeghalmi. The QD deposition techniques (SILAR, and infiltration), and CdSe QD synthesis was developed and performed in the group of M. Wächtler. The spectroscopic measurements (absorption spectra, photoluminescence spectra, and tr-PL) were performed in the group of M. Wächtler. I and M. Dilshad conducted the experiments of QD deposition, and spectroscopic measurements under the supervision of M. Wächtler. M. Diegel performed the X-ray diffraction. J. Dellith performed the energy-dispersive X-ray spectrometry and SEM. J. Plentz performed secondary ion mass spectrometry. Andreas Unsdisz collected the TEM images. The formal analysis of all the collected data was performed by me under the supervision of M. Wächtler. The original draft of the published article was prepared by me which was edited and evaluated by all the authors.

In the following, the published article entitled 'Deposition of CdSe NCs in Highly Porous SiO_2 Matrices – In-situ Growth vs. Infiltration Methods' is presented. © 2024 by the authors. Licensee MDPI, Basel, Switzerland. This article is an open access article distributed under the terms and conditions of the Creative Commons Attribution (CC BY) license (https://creativecommons.org/licenses/by/4.0/).

materials

MDPI

Article

Deposition of CdSe Nanocrystals in Highly Porous SiO_2 Matrices—In Situ Growth vs. Infiltration Methods

Raktim Baruah [1,2], Munira Dilshad [2], Marco Diegel [2], Jan Dellith [2], Jonathan Plentz [2], Andreas Undisz [3,4], Adriana Szeghalmi [5,6] and Maria Wächtler [1,2,*]

[1] Department of Chemistry and State Research Center OPTIMAS, RPTU Kaiserslautern-Landau, 67663 Kaiserslautern, Germany
[2] Leibniz Institute of Photonic Technology, 07745 Jena, Germany
[3] Institute of Materials Science and Engineering, Chemnitz University of Technology, 09125 Chemnitz, Germany
[4] Otto Schott Institute of Material Research, Metallic Materials, Friedrich Schiller University, 07743 Jena, Germany
[5] Institute of Applied Physics, Friedrich Schiller University Jena, 07745 Jena, Germany
[6] Fraunhofer Institute for Applied Optics and Precision Engineering, 07745 Jena, Germany
* Correspondence: maria.waechtler@chem.rptu.de

Abstract: Embedding quantum dots into porous matrices is a very beneficial approach for generating hybrid nanostructures with unique properties. In this contribution we explore strategies to dope nanoporous SiO_2 thin films made by atomic layer deposition and selective wet chemical etching with precise control over pore size with CdSe quantum dots. Two distinct strategies were employed for quantum dot deposition: in situ growth of CdSe nanocrystals within the porous matrix via successive ionic layer adsorption reaction, and infiltration of pre-synthesized quantum dots. To address the impact of pore size, layers with 10 nm and 30 nm maximum pore diameter were used as the matrix. Our results show that though small pores are potentially accessible for the in situ approach, this strategy lacks controllability over the nanocrystal quality and size distribution. To dope layers with high-quality quantum dots with well-defined size distribution and optical properties, infiltration of preformed quantum dots is much more promising. It was observed that due to higher pore volume, 30 nm porous silica shows higher loading after treatment than the 10 nm porous silica matrix. This can be related to a better accessibility of the pores with higher pore size. The amount of infiltrated quantum dots can be influenced via drop-casting of additional solvents on a pre-drop-casted porous matrix as well as via varying the soaking time of a porous matrix in a quantum dot solution. Luminescent quantum dots deposited via this strategy keep their luminescent properties, and the resulting thin films with immobilized quantum dots are suited for integration into optoelectronic devices.

Keywords: CdSe quantum dot; thin film; porous silica

check for updates

Citation: Baruah, R.; Dilshad, M.; Diegel, M.; Dellith, J.; Plentz, J.; Undisz, A.; Szeghalmi, A.; Wächtler, M. Deposition of CdSe Nanocrystals in Highly Porous SiO_2 Matrices—In Situ Growth vs. Infiltration Methods. *Materials* **2024**, *17*, 4379. https://doi.org/10.3390/ma17174379

Academic Editor: Weiqing Zhang

Received: 12 August 2024
Revised: 30 August 2024
Accepted: 2 September 2024
Published: 5 September 2024

Copyright: © 2024 by the authors. Licensee MDPI, Basel, Switzerland. This article is an open access article distributed under the terms and conditions of the Creative Commons Attribution (CC BY) license (https://creativecommons.org/licenses/by/4.0/).

1. Introduction

Semiconductor nanocrystals (NCs) have emerged as the pivotal material in nanotechnology for the applications in optoelectronics as well as sensing and biomedical imaging, owing to their unique size-dependent optoelectronic properties [1]. Among them, quantum dots (QDs) stand out for their excellent and wide-ranging optical and electronic properties, which can be adjusted by varying their size. As the size of the QD is reduced, discrete quantized energy levels are observed in contrast to the continuous energy band structure observed in bulk materials [2,3]. This phenomenon is a consequence of the strong spatial confinement of electron and hole motion when the QD size is below the Bohr radius [2,3]. One of the most extensively studied systems comprises cadmium selenide (CdSe) QDs. CdSe QDs exhibit narrow photoluminescence spectra and can be designed to show high photoluminescence quantum yields (PLQYs); they are therefore highly suitable for device applications such as in light-emitting diodes (LEDs) [4–6] or in sensing [7,8] applications. The tunability of electronic properties via size allows for the optimization of the valence band and conduction band energy levels allowing emission color, or ensures sufficient driving force for the energy and electron transfer processes forming the basis for sensing [7–9] concepts or the application of QDs as light absorbers to drive photocatalytic reactions [10–12]. The synthesis of high-quality (with respect to crystallinity and control over size distribution) CdSe QDs is achieved via the well-established hot injection method [13,14]. QDs resulting from this synthetic approach are usually capped with long-chain aliphatic surface ligands, e.g., tri-octylphosphine oxide, octadecylphosphonic acid, oleic acid, hexadecylamine, etc. [15]. The surface ligands provide colloidal stability, stabilize the surface of the QDs, and saturate dangling bonds, which are the source of surface trap states or introduce additional trapping states, depending on the anchoring functional group of the surface ligand [16–18]. Surface functionalization can also alter the dispersibility of the QDs in different solvents, rendering them suitable for applications in various solvent environments, e.g., in aqueous environments for sensing in biological systems [7] or photocatalytic applications [12,19] in aqueous environments.

The colloidal solutions of the QDs have the advantage to allow for solution processing, e.g., to generate thin films with controlled homogeneity and packing density, enabling fine tuning of optoelectronic properties and allowing for much more flexibility and large-scale processing compared to methods such as chemical vapor deposition, epitaxial growth, etc. [20,21]. For many applications, dispersed NCs have to be transferred into thin film architectures, e.g., for application in LEDs [22,23], materials for photovoltaic devices [24–26], photoelectrode materials for photocatalytic applications [27] and sensors [28], or optoelectronic devices [29] for detection of radiation. Beyond thin film production by deposition of particles on substrates, immobilization and thin film production by integration of QDs into porous matrices, e.g., mesoporous silica, is a very interesting approach. The porous matrices support ordered assembly controlled by the structure of the porous matrix [30] or can be used to control size [31] via pore sizes of the matrix serving as a template. The porous matrix surrounding can shield the QDs from environmental factors such as oxygen and moisture and improve light extraction [32], reducing thermal effects and leading to improving long-term stability and efficiency, as observed, e.g., for LED devices [31,33,34]. Furthermore, porous matrices can support the targeted function by reduction of non-radiative recombination, contributing to improved quantum efficiency and brightness of the LEDs [35], or support charge carrier separation by co-immobilizing donors and acceptors, reducing charge carrier transfer distances and enhancing photocatalytic performances [36]. Furthermore, it can facilitate efficient diffusion of reactants and products, leading to improved reaction rates and yields in photocatalytic processes in the confined surrounding of the pores [37].

Two general strategies exist to deposit QDs inside a porous matrix. For a direct generation of NCs within the porous material, the successive ionic layer adsorption and reaction (SILAR) approach can be used [30,38,39]. For example, Besson et al. [30] and Wang et al. [39] demonstrate the growth of CdS QDs and CdSe QDs, respectively, in porous silica matrices via in situ growth of QDs inside the pores. Short immersion times and repeated cycles allow for control over loading and particle sizes, though with limited precision and broad size distributions [30]. To overcome the missing precision in controlling size and size distribution of NCs generated via the SILAR method within the porous matrices, infiltration of pre-synthesized particles employing methods with high control over size distributions can be employed. This approach has been used to deposit colloidal QDs inside mesoporous silica particles in the so-called “wet mixing method” [33,34,40], but also has been adapted to porous silica layers by soaking in a solution of dispersed QDs [41].

In this contribution, we investigate strategies for the incorporation of nanocrystalline CdSe into porous silica layers with pore diameters in the 10 s of nm range produced via atomic layer deposition (ALD) [42]. Fabrication methods based on ALD are shown to be advantageous with respect to control over thickness of the porous layer and rigidity of the porous structure compared to sol-gel methods [43–45]. Two general strategies are employed to deposit nanocrystalline CdSe into the porous material: in situ growth of CdSe NCs using the SILAR approach and infiltration of pre-synthesized QDs. Analysis of the structure and optical properties of the thin films with dependence on experimental parameters, e.g., pore size and deposition times, is performed to evaluate the quality of the produced layers.

2. Materials and Methods

For the NC synthesis, the following chemicals were used: Tri-octylphosphine oxide (TOPO, 99%), Trioctylphosphine (TOP, 97%), Cadmium oxide (CdO, 99.99%), Cadmium acetate hydrate (Cd $(OAc)_2 \cdot xH_2O$, 99.99%), Selenium (Se, 99.99%), Sodium selenide (Na_2Se, 95%), Toluene (99.8% anhydrous) and Methanol (99.8% anhydrous), purchased from Sigma Aldrich, and Octadecylphosphonic acid (ODPA, 97%), purchased from Carl Roth (Karlsruhe, Germany).

CdSe QDs were synthesized following established protocols [46,47]. A total of 60 mg of cadmium oxide (CdO), 0.28 g of octadecylphosphine oxide (ODPA), and 3.0 g of tri-octylphosphine oxide (TOPO) were mixed in a 25 mL three-neck flask. The mixture was heated to 80 °C under a N_2 atmosphere until melting under stirring. A vacuum was applied to remove traces of water, and after bubble formation stopped, the mixture was heated to 150 °C and evacuated for 1 h. Then, under N_2 flow, the reaction mixture was heated up, and at around 300 °C the solution became optically clear and colorless. At 320 °C, 1.5 g of trioctylphosphine (TOP) was injected into the solution. When the temperature reached 380 °C, a solution of TOP–Se (0.058 g Se dissolved in 0.360 g TOP) was injected, and the temperature was kept at 370 °C for 5 min. Then, the reaction mixture was cooled down by removing the heating mantle, and when the temperature reached 60 °C, 10 mL toluene was injected. After the synthesis, QDs were precipitated by adding 10 mL MeOH to the reaction mixture, with centrifugation at 5300 rpm. The precipitate was redispersed in toluene, and was repeatedly precipitated and redispersed for cleaning three more times. Finally, the QDs were redispersed in 10 mL of toluene and stored inside a glove box (N_2 atmosphere).

Nanoporous SiO_2 layers were prepared using the methods reported by Ghazaryan et al. [42] Briefly, a heterostructure of SiO_2–Al_2O_3 was deposited by atomic layer deposition (ALD) using a sequence of 2 cycles of SiO_2 and 3 or 4 cycles of Al_2O_3. The sequence was repeated 230 and 330 times, respectively. The growth rate of the SiO_2 and Al_2O_3 was about 0.1 nm/cycle. The film thickness of the [2:3]x230 sample was 123 nm, with 230 nm for the [2:4]x330 sample, as estimated by spectroscopic ellipsometry measurements. After deposition, the Al_2O_3 was selectively etched in H_3PO_4 (85%) solution, and a porous SiO_2 matrix was formed. The maximum pore size as estimated in a previous work by SEM was 10 nm and 30 nm, being smaller when less Al_2O_3 was removed from the SiO_2 matrix [42]. Porous silica layers were prepared both on fused silica to enable optical characterization and on silicon substrates to perform electron microscopy (Plano Gmbh, Wetzlar, Germany) for imaging.

QDs were grown in situ in the pores of the silica matrix by the Successive Ionic Layer Adsorption Reaction (SILAR) method at room temperature following a protocol described by Sankapal et al. [48] The porous silica layer (either on fused silica or silicon substrate) was immersed first into a Cd $(OAc)_2$ solution (40 mL Cd $(OAc)_2$ in methanol, 5 µM) for 5 min. After taking it out, the layer was rinsed with methanol and dried under vacuum. Then, the layer was immersed into a Na_2Se solution (40 mL Na_2Se in methanol, 6 µM) for 5 min, followed by rinsing with methanol and drying under vacuum. This completed one cycle of immersion. The immersion procedure was repeated several times, and layers were produced by applying 5, 10, 15, and 20 immersion cycles.

To infiltrate pre-synthesized QDs into porous silica, two strategies were applied—drop-casting of a QD solution on porous silica layers and immersion and soaking of porous silica layers in a QD solution. For drop-casting, 100 µL of QD solution (3 µM, toluene) was dropped on porous silica layers. Once the solvent was completely evaporated, the layers were rinsed with toluene to remove QDs just adsorbed at the surface and dried under vacuum. For some of the layers, after the initial drop-casting step using a solution of QDs, an additional amount of solvent was dropped on the substrates to wash QDs just sitting on the surface into the pores. Alternatively, the porous silica layers were immersed in 3 mL of QD solution (0.4 µM, toluene) to soak QDs into the pores. Soaking times of 0.5 h, 2 h, and 24 h, followed by rinsing with toluene and drying under vacuum, were applied. For comparison and to prove infiltration into the porous structure, a normal glass substrate, cleaned by washing with acetone, methanol, Hellmanex, and water, was drop-casted with 100 µL of QD solution (3 µM, toluene), and one other normal glass substrate was immersed in a QD solution (0.4 µM, toluene) for 24 h followed by washing with toluene.

UV–vis absorption spectroscopy in the wavelength range from 200 nm to 1000 nm was performed using a Jasco V-780 spectrophotometer (Jasco, Hachioji, Tokyo, Japan) . Colloidal dispersions were measured in a 1 cm quartz cuvette, and for thin film measurements a special film holder was used. Absorption spectra measured in thin films contained strong wavelength-dependent scattering contributions, which were corrected via fitting a polynomial background [49] as described in Figure S1.

The photoluminescence spectra of the QD solution were recorded in a 1 cm cuvette using a FLS 980 Edinburgh Instruments (Livingston, UK) Fluorimeter upon excitation at 400 nm. The photoluminescence spectra of the porous silica layers on fused silica were recorded using a Horiba Fluorolog-3 (Glasgow, Scotland). The excitation wavelength was set to 400 nm.

To determine the photoluminescence lifetimes, Time Correlated Single Photon Counting (TCSPC) was performed with a Horiba DeltaFlex spectrometer (Glasgow, Scotland) with a pulsed NanoLED (peak wavelength of 389 nm, pulse duration of 1.3 ns) from Horiba. For this, QD solutions were prepared in a 1 cm quartz cuvette. QD thin films and porous layers were measured using a suitable thin film holder.

Transmission Electron Microscopy (TEM) images were recorded using a JEM-ARM200F NEOARM (Jeol) (Jeol, Akishima, Tokyo, Japan) operating at 80 kV. For this, Colloidal QDs were deposited on a carbon-coated Cu grid (purchased from PLANO GmbH, Wetzlar, Germany). To evaluate the average size and size distribution of the particles, the images were processed using an ImageJ 1.53a program [50].

Scanning Electron Microscopy (SEM) images of QDs deposited on silicon wafers and porous silica on silicon wafers were recorded using a JEOL JSM-6700F scanning electron microscope (Jeol, Akishima, Tokyo, Japan) . Additionally, cross-sectional images of the porous silica layers were collected after breaking the substrate and depositing a carbon layer.

For elemental analysis, Energy Dispersive X-ray Spectrometry (EDX) on porous silica layers on silicon wafers using a Bruker silicon drift detector SDD-5030 (Brucker Corporation, Billerica, MA, USA) (30 mm^2 detector area) with 10 keV electron energy was performed. Grazing incidence X-ray diffraction (GIXRD) on porous silica layers on fused silica was performed using a PANalytical X'Pert Pro MPD (Malvern Panalytical, Malvern, Worcestershire, UK) ((Cu-Kα radiation, 1.541 Å) with an omega angle of 2°, a 2theta range from 10° to 90°, a 0.026° step size, and measuring times from 1 h to 15 h).

Secondary Ion Mass Spectrometry (SIMS) was performed using a Hiden Analytical SIMS Workstation equipped with 5 keV Cesium and Oxygen ion sources for ionization and sputtering for the material within a spot of 50 µm and a high-transmission quadrupole secondary ion mass spectrometer (Hiden Analytical Ltd., Westbrook, Warrington, UK) . A layer of less than 10 nm Pt was deposited on top for electrically conductive surfaces to prevent electrical charging during measurement.

3. Results and Discussion

Porous silica layers were prepared using atomic layer deposition (ALD) of a heterostructure of SiO_2:Al_2O_3, followed by selective etching of Al_2O_3 [42]. In order to systematically investigate the extent of QD deposition by applying different methods, porous layers with two different pore sizes were prepared. Top view and cross section SEM images of the porous layers are shown in Figure S3. Maximum pore sizes of 10 nm and 30 nm were determined from SEM images. The thicknesses of the layers are in the range from 123 nm and 230 nm.

The first preparation route applied was to grow CdSe NCs directly inside the porous matrix. For this, a SILAR protocol was adopted [48]. Methanolic solutions of Cd $(OAc)_2$ as the Cd^{2+} source and Na_2Se as the Se^{2-} source were used. A 5 min immersion of the porous layer into the Cd (OAc_2) solution led to a monolayer adsorption of Cd^{2+} ions attached to the porous surface via Van der Waals and electrostatic forces. Loosely bound Cd^{2+} ions were removed by rinsing the porous layers before immersion into a Na_2Se solution, which initiated the reaction of Cd^{2+} and Se^{2-} to form CdSe. Further successive cycles of immersions of the porous layers into Cd $(OAc)_2$ and Na_2Se solutions led to successive growth of CdSe NCs. To observe the growth in the successive immersion steps, samples were prepared with 5, 10, 15, and 20 immersions for both the layers with 10 nm and 30 nm pore size.

Steady-state UV–vis absorption spectroscopy was performed on the porous silica layers, which shows absorption features below 700 nm (Figure 1). With the number of immersion steps, the absorption feature increases in intensity, and the onset of absorption shifts to higher wavelengths. This indicates, on the one hand, an increased loading of the SiO_2 matrix with CdSe, and on the other hand, an increase of the crystal size of the CdSe deposited (Figure 1). Similar behavior was observed upon in situ growth of CdS NCs on TiO_2 via the SILAR method [48]. Typically, CdSe QDs exhibit distinctive electronic transitions from the valence band to the conduction band due to the presence of quantized energy levels at the band edges [51]. In contrast, the absorption spectra show only very broad features, without any distinct peak. This can be related to a broad size distribution caused by uncontrolled growth of CdSe crystals and aggregation of smaller NCs, with an increasing number of immersion cycles forming larger particles. The absorption features of the layers with 30 nm pore size exhibit a notable increase in absorbance with the number of immersion cycles. In contrast, the absorption of the layers with 10 nm pore size show a pronounced rise from the initial immersions to 10 cycles, followed by a saturation. This suggests that the limited pore volume of 10 nm pore-sized layers is fully occupied by the NCs or that narrow parts of the porous structure are clogged, preventing further deposition of CdSe, while the 30 nm pore-sized layers continue to fill. No photoluminescence was detected from the layers. This potentially is due to low crystal quality, i.e., low crystallinity and a high density of the NCs grown via this method.

To evaluate the crystal quality, the samples were characterized by GIXRD. Figure 2 shows the GIXRD patterns from porous silica layers with in situ grown CdSe QDs. As the CdSe crystallites grown inside 10 nm and 30 nm pores are very small in size, the corresponding XRD peaks are broadened but seem to grow in and slightly sharpen with increasing immersion cycles [52]. The broad and less intense XRD peaks of CdSe NCs make it very challenging to distinguish between the hexagonal phases. However, conducting the in situ growth at room temperature increases the likelihood of cubic crystal phase formation. From a thermodynamic perspective, the cubic phase is more stable at lower temperatures, while the hexagonal phase is more stable at higher temperatures [52]. It seems, at least from the dataset of the sample with the 30 nm pore size, that with the number of immersions, XRD peaks evolve, with the potentially growing size of the embedded crystallites representing a cubic pattern with its characteristic 2theta peaks at 24.84° (111) and 42.83° (220) (ICSD: 620421). Nevertheless, this conclusion needs to be regarded with care. On the other hand, due to smaller pore volume, CdSe QDs grown in 10 nm pores seem to be smaller than in 30 nm pores, indicated by even broader XRD peaks than the layers of the 30 nm pore size.

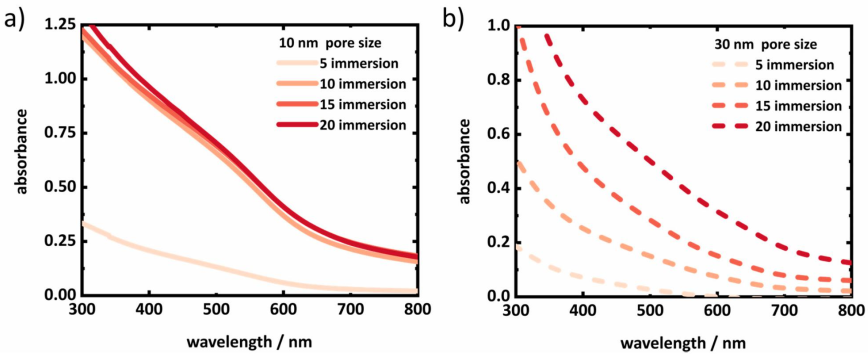

Figure 1. Absorption spectra of porous silica layers on fused silica substrates of (**a**) 10 nm and (**b**) 30 nm pore size with different numbers of SILAR immersion cycles. The absorption spectra of the thin films contain strong wavelength-dependent scattering contributions. A correction for this scattering contribution, as suggested in the supporting information Figure S1, could not be performed reliably for these samples, because it was not possible to assign the region of no absorption, due to the broad absorption feature, in the investigated spectral range.

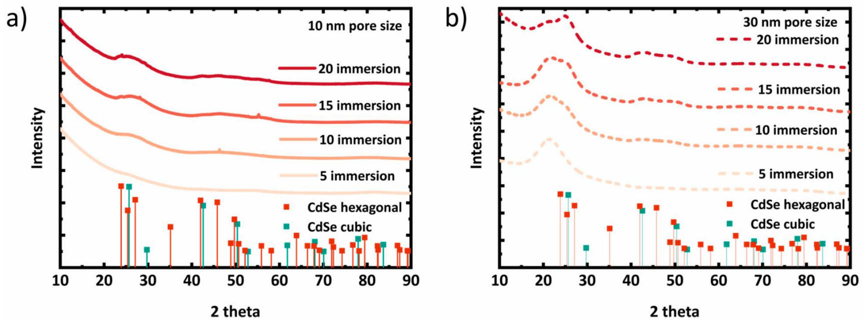

Figure 2. XRD pattern of porous silica layers (on fused silica substrate): (**a**) 10 nm and (**b**) 30 nm pore size with different numbers of SILAR immersion steps. The XRD patterns shown in the figure are without any background correction.

Further, to observe the CdSe QDs in the porous matrices, Energy Dispersive X-ray Spectrometry (EDX) was performed. Figure 3 depicts the EDX spectra of 10 nm and 30 nm porous layers. While collecting the EDX spectra, an area of 200 μm^2 was exposed to the electron beam. In comparison to spot analysis, this large area of exposure gives a good comparability among different samples, lowering the danger of local overestimation. For both the 10 nm and 30 nm pore-sized layers, there is a relative increase in the intensities of the Cd and Se peaks with the number of immersion cycles (Figure 3). The increasing Cd and Se peak intensities reflect the increasing amount of Cd and Se deposited in the layers with every SILAR immersion cycle.

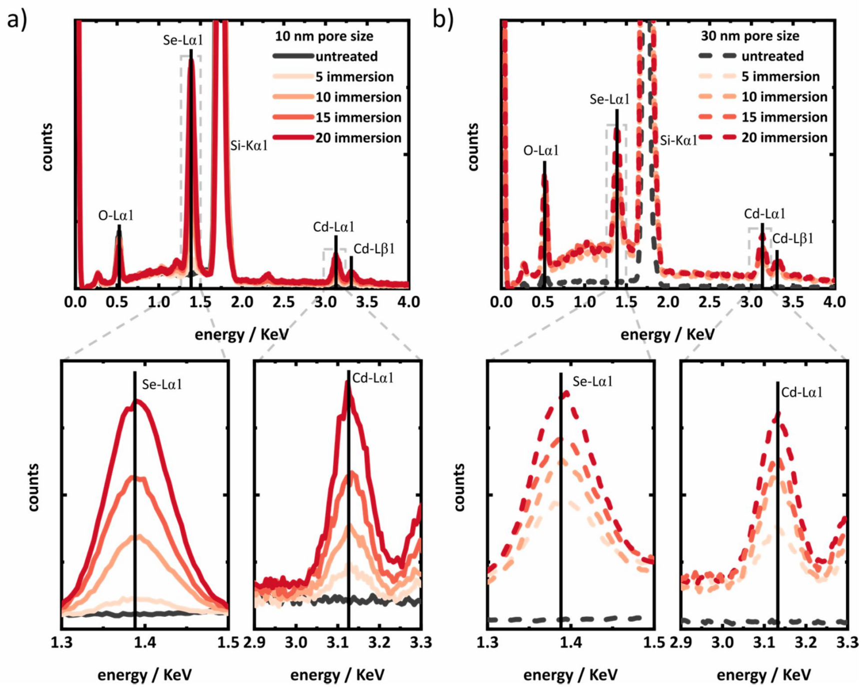

Figure 3. EDX spectra of porous silica layers (Si wafers) of (**a**) 10 nm and (**b**) 30 nm pore size with different SILAR immersions. Respective bottom panels show the zoomed regions of Se and Cd peaks.

SEM images of porous layers in silicon wafers were collected to observe the local structure of CdSe NCs in the porous structure. Figure 4 and Figure S4 depict the SEM images of 30 nm and 10 nm pore-sized layers, respectively. Because the resolution of SEM is not sufficient to image single NCs, which might be even more complex in the case of a broad size distribution, a clear presence of CdSe NCs cannot be confirmed from the top view image. Nevertheless, it appears from the top view images that the pores gradually fill with an increasing number of immersion cycles.

To summarize, the in situ SILAR growth leads to the deposition of CdSe NCs on the porous matrix. Steady-state absorption and photoluminescence spectroscopy, as well as XRD and EDX analysis complemented by SEM imaging, indicates that the NCs are probably deposited within the porous network. However, the deposition at the surface cannot be ruled out and prevented. The NCs exhibit indications of a cubic phase with low crystallinity and a broad size distribution. Additionally, they demonstrate an absence of photoluminescence, which is likely related to the high number of trap states, which in turn decreases the PLQY. For any optoelectronic applications, it is essential to embed particles with better controllable properties, such as distinct electronic transitions, controllable size, and high crystalline NCs that support high PLQYs. The synthesis of highly crystalline CdSe NCs with a narrow size distribution via the SILAR method is a challenging process, necessitating the exploration of alternative strategies. These strategies must be capable of embedding NCs with high crystallinity and controllable properties, including a narrow size distribution. This leads us to seek an alternative porous silica and CdSe QD ensemble that exhibits superior performance, including a high PLQY, good crystallinity, and a narrow size distribution.

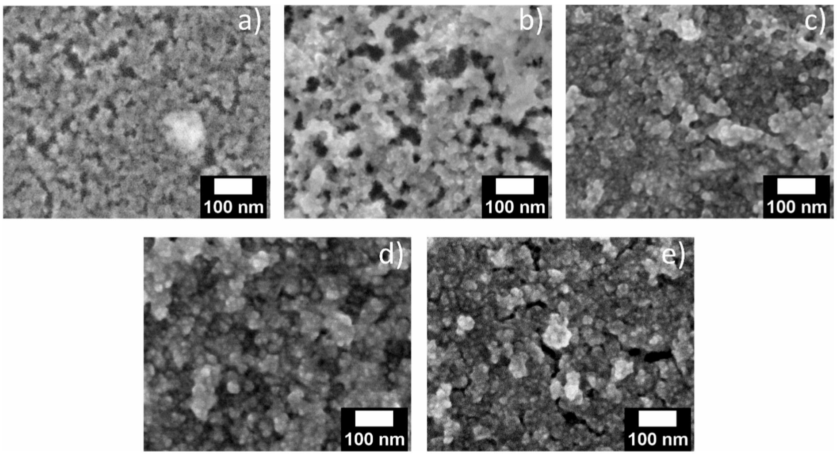

Figure 4. SEM images of (**a**) untreated porous silica layers of 30 nm pore size in silicon wafer and with (**b**) 5, (**c**) 10, (**d**) 15, and (**e**) 20 SILAR immersions.

To achieve this goal, we employed an alternative method, which allowed us to benefit from the well-controlled properties of colloidal QDs synthesized via hot injection methods performed at high temperatures (usually > 300 °C), resulting in CdSe QDs with precise control over size and size distribution, high crystallinity, high PLQY, narrow photoluminescence band width, etc. [14]. However, such synthesis routes are typically not applicable for embedding CdSe QDs directly during synthesis into porous silica layers due to the lack of thermal stability of the silica matrix in that temperature range [53]. Additionally, the crystal growth in the hot injection method undergoes a fast nucleation mechanism [14], which is hindered by the porous matrix, resulting in inefficient growth inside the pores. As this rules out the feasibility of employing the hot injection method for direct growth within the porous layer, we explore the possibility of deposition and infiltration of pre-synthesized QDs into the porous silica matrix.

For our study, CdSe QDs were pre-synthesized via hot injection (see experimental) [46,47]. The QDs were majorly covered with TOPO as the surface ligand, along with TOP and ODPA (used with Se and Cd precursors in the QD synthesis), which made them dispersible in non-polar solvents like toluene, chloroform, hexane, etc. The absorption spectra of the pure QD dispersion (toluene) shows the characteristic electronic transition from the valence band to conduction band levels (Figure 5a). The feature at 537 nm corresponds to the lowest excitonic band edge $1S_{(e)}$-$1S_{3/2(h)}$ transition [51]. A band gap of the QDs of 2.2 ± 0.04 eV was derived from Tauc's plot, which is in agreement with the band edge photoluminescence peak position (547 nm, 2.26 eV) [54]. The absolute PLQY is 3.9%. The diameter of the QD was estimated from the spectral position of the lowest excitonic transition in the absorption spectra by the empirical formula derived by Yu et al. [55] to approximately 2.9 nm, in good agreement with the average diameter determined by statistical analysis of TEM images (3.2 ± 0.5 nm, Figure 5b and Figure S5a,b). Furthermore, a thin film was prepared by drop-casting the QDs on a silicon wafer to visualize the QDs in layers via SEM (Figure 5c).

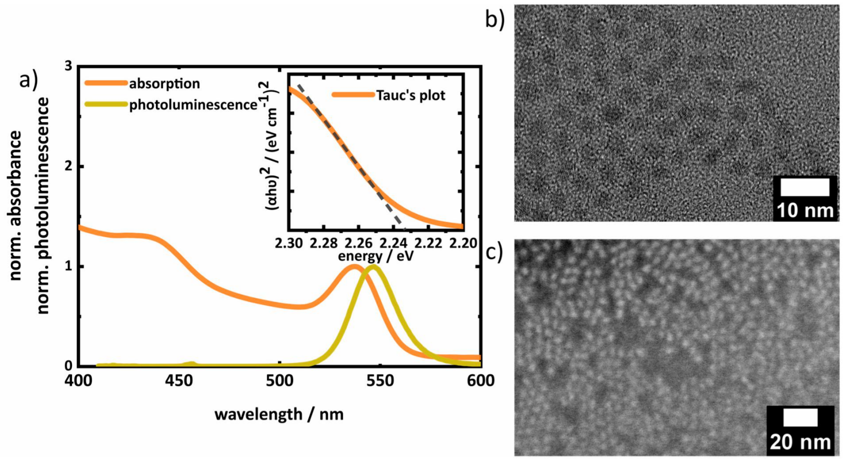

Figure 5. (**a**) Normalized absorption and photoluminescence spectra (λ_{ex} 400 nm) of the CdSe QDs with 2.9 nm diameter in toluene and Tauc's plot for band gap calculation (inset). (**b**) TEM and (**c**) SEM image (on silicon wafer) of 2.9 nm CdSe QDs used in this study.

Pre-synthesized CdSe QDs were infiltrated into porous silica of pore size 10 nm and 30 nm via (a) drop-casting of a QD solution (3 µM) in toluene on the porous silica layers and (b) soaking porous silica layers in a QD solution (0.4 µM) in toluene. We started with a simple drop-casting followed by washing the layers with toluene to remove QDs sitting just on top of the surface. To induce higher infiltration of QDs, an additional amount of solvent (toluene) was dropped on the layers after the first step of drop-casting followed by washing the layer in toluene. In the soaking method, porous layers were immersed in a QD solution. The loading of QDs was influenced by soaking time. Because of the surface ligand TOPO, QDs are hydrophobic. Therefore, in each washing step after infiltration, the QDs sitting on the hydrophilic porous layer surface should be effectively removed.

The deposition of pre-synthesized QDs on porous silica layers was confirmed by steady-state UV–vis absorption spectroscopy and photoluminescence spectroscopy. Figures 6 and S6 show the spectra of porous silica layers after QD infiltration. The absorption spectra were corrected for background signal from the substrate and scattering contributions from the porous layer (see Supplementary Information Figure S1). The characteristic feature of the lowest band edge transition ($1S_{(e)}$-$1S_{3/2(h)}$) is clearly visible in the absorption spectra of the treated layers, which confirms the presence of QDs. After QD infiltration via both drop-casting and soaking, for the porous layers with 30 nm pore size a higher absorbance is observed than for the layer with 10 nm pore size. This is an indication of a higher loading of QDs in bigger pores (i.e., 30 nm) than in 10 nm pores, which indicates an easier accessibility of the larger pores for the QDs. For the drop-casting routine, treatment with additional solvent resulted in a relative increase compared to the drop-casted layers without additional solvent treatment (Figure 6a). For the soaking strategy, the amount of QDs infiltrated into the pores increases with time of soaking. The gradual increase of the absorption of QDs in porous layers for soaking times 0.5 h to 2 h (Figure S6a) and 2 h to 24 h (Figure 6c) indicate the increase of the amount of infiltrated QDs. The band edge photoluminescence peak of the QDs at 541 nm in the photoluminescence spectra of the porous layers further confirms the presence of QDs in the treated porous layers (Figures 6b,d and S6b). Due to the inhomogeneous distribution of QDs and strong scattering contributions, quantitative comparison of both absorbance and photoluminescence intensity among samples is not possible. It can still be assumed that due to higher loading of QDs, porous silica layers of 30 nm pore size show higher photoluminescence intensity than the layer of 10 nm pore size for all infiltration methods (Figures 6 and S6). Similar to the absorption spectra, additional drop-casting of toluene increases the photoluminescence intensity due to higher infiltration of QDs. On the other hand, the photoluminescence intensity also increases with soaking time (Figures 6d and S6b).

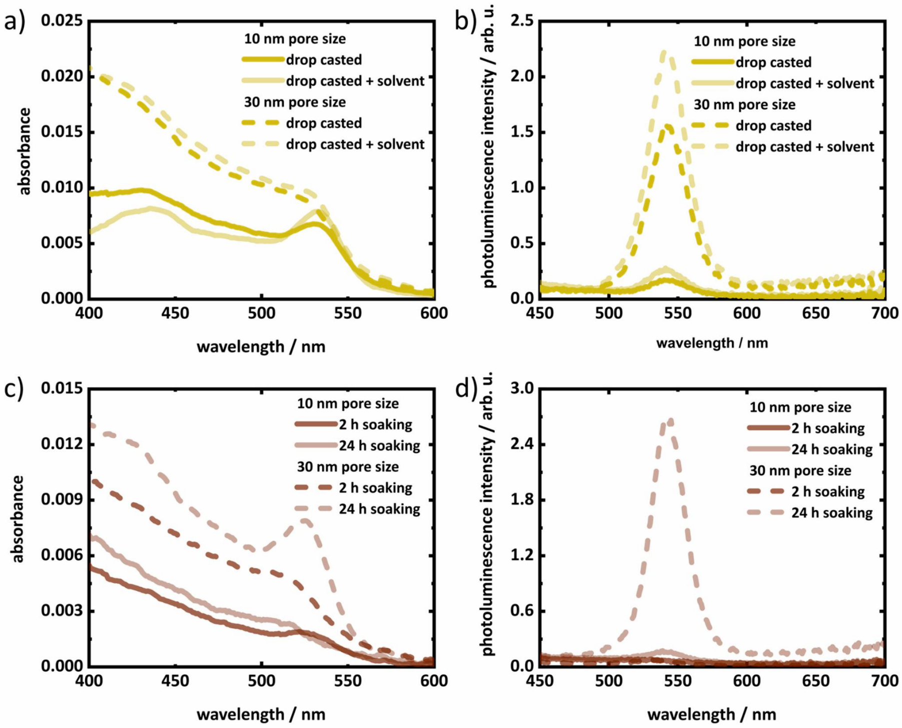

Figure 6. Absorption spectra (**a**) and photoluminescence spectra (**b**) of 10 nm (solid lines) and 30 nm (dashed line) porous layers treated by drop-casting and drop-casted followed by solvent treatment. Absorbance spectra (**c**) and photoluminescence spectra (**d**) of 10 nm (solid lines) and 30 nm (dashed line) porous layers with 2 h and 24 h soaking. The wavelength scattering correction as described in Figure S1 was employed in the absorption spectra (**a**,**c**).

Figures 7 and S7 show the decay traces of pure QDs (in both solution and film) and the treated porous layers. These traces were modeled using a multiexponential function with three components, and the fitted data are presented in Table S1. The average photoluminescence lifetime was determined by amplitude-weighted averaging of the time constants. The pure QD solution has an average lifetime of 38.7 ns, which is reduced to 19.2 ns when deposited on a glass substrate. This reduction is attributed to inter-QD interactions, such as non-radiative energy transfer within layer due to the inhomogeneous QD size distribution [56–58]. The photoluminescence decay of QD-infiltrated porous layers is also faster, as shown in Table S1. Porous layers with higher QD loading, as indicated by absorption and photoluminescence spectroscopy, exhibit faster photoluminescence decay. The average photoluminescence lifetime of the 30 nm drop-casted layers is 20.1 ns. However, with the addition of additional solvents, the lifetime decreases to 15.5 ns. Similarly, with increased soaking time, the photoluminescence lifetime of the 30 nm porous layer decreases from 17.8 ns to 11.7 ns. This trend is also observed for the 10 nm porous layers. It is expected that a higher loading of QDs will result in a denser packing inside the pores, leading to a stronger interaction between QDs. Therefore, the faster decay of photoluminescence in porous layers with higher QD loading is attributed to stronger interaction, leading to enhanced non-deactivation. However, there is no significant difference in the photoluminescence lifetime as dependent on pore sizes.

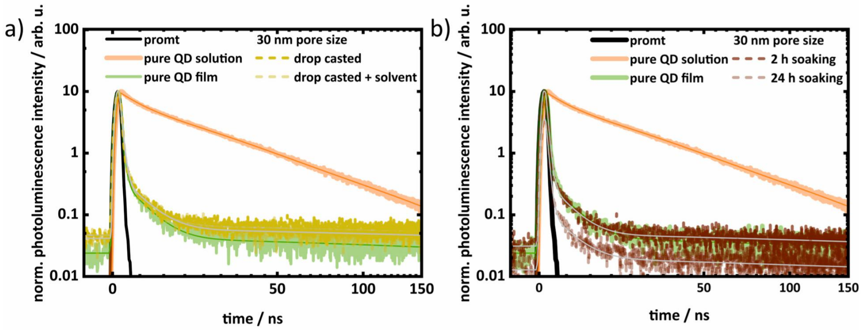

Figure 7. Decay kinetic traces of 30 nm porous layers with QD infiltration via (**a**) drop-casting and (**b**) soaking along with the pure QD both in solution and thin film.

From steady-state absorption and photoluminescence spectroscopy, we can only derive information on the presence of QDs on the substrates in general; it is not possible to distinguish between QDs infiltrated in the pores or just sitting at the surface. An indication of infiltration is that after treating a glass substrate following the soaking method, no QDs are deposited on the substrate (for absorption spectra, see supporting information; Figure S8a). Similar behavior was observed following the drop-casting method, where absorbance at the first excitonic peak was reduced by a factor of six after washing, as depicted in Figure S8b. This indicates that QDs deposited on the surface are removed after the washing step of QD infiltration in porous layers, i.e., the spectra recorded are from the QDs inside pores.

For further proof for the successful deposition of QDs inside the pores of the porous matrix, scanning electron microscopy (SEM) images were collected for porous layers on silicon substrates treated via the methods described above. Due to the insufficient contrast, it is difficult to localize QDs in the porous matrix in a top-view image. Nevertheless, the opening of the pores at the surface of the structure (Figure 8a) seems to be smaller after infiltration (Figure 8b–e), which could be caused by QD infiltration and filling of the pores. Figure 8b,c compares the drop-casted layer with a drop-casted layer with additional solvent treatment, which indicates an increased pore filling after additional solvent treatment, in agreement with the results from absorption and photoluminescence spectroscopy. On the other hand, porous structures gradually fill with soaking time due to higher infiltration (Figure 8d,e). Similar behavior was observed for 10 nm pore-sized layers (Figure S9). Unfortunately, due to limited spatial resolution of the method, cross-sectional images and EDX elemental mapping could not be collected to directly determine the presence of QDs inside the porous layers.

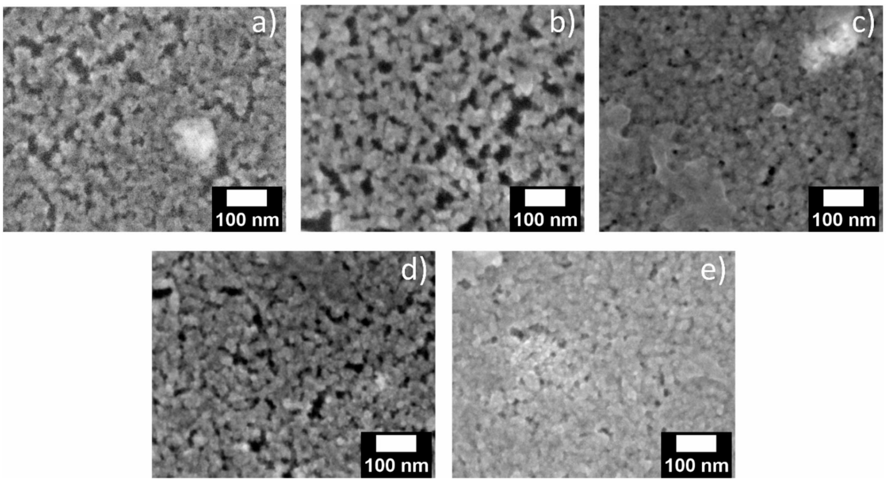

Figure 8. SEM images of (**a**) untreated, (**b**) QD drop-casted, (**c**) QD drop-casted + solvent, (**d**) soaked for 0.5 h and (**e**) soaked for 24 h porous silica layers of 30 nm pore size in silicon wafer.

To collect further proof of the presence of CdSe QDs inside the pores of the porous silica layers, Secondary Ion Mass Spectrometry (SIMS) was performed with a depth profile. A layer of less than 10 nm Platinum (Pt) was deposited on top of the porous layer for electrical non-charging and as an indicator for when the porous layer structure was reached in the sputtering process. The layer system of thin Pt film (for electrical non-charging) on porous layers on the Si wafer were sputtered by an ion beam of the SIMS setup. The secondary ions generated from the material were recorded over the depth. Figure 9 shows the SIMS depth profile of a QD infiltrated porous silica layer of 30 nm pore size. Generated secondary ions from the porous layers were detected with respect to time (plotted in the *X*-axis), which is correlated to the depth of the layer. The region of interest in the SIMS depth profiles is between the two dashed lines, which corresponds to the porous layer. As expected, the untreated porous layer does not contain Cd, which is why no signal is observed (Figure 9a). Figure 9b,c depicts the presence of Cd in the porous layers. Even after washing the porous layers after infiltration, there seems to be small amounts of QDs on the surface, which are seen in the early period (before the dashed line at 1 min) as a less intense Cd signal. Moving towards the depth of the porous layer, the Cd concentration detected increases, which indicates that a higher amount of Cd is present inside the porous layers. The Cd signal levels off with increasing depth, and no signal is detected once the sputtering reaches the Si wafer (dashed line at 6 min). Similar behavior was observed for the layers with 10 nm pore size (see Supplementary Material Figure S10). Hence, the presence of CdSe QDs in the pores is ensured by the SIMS data shown above. The measurement reveals a gradient of deposition of CdSe across the layer and demonstrates that deeper pores may not be reached in the deposition process.

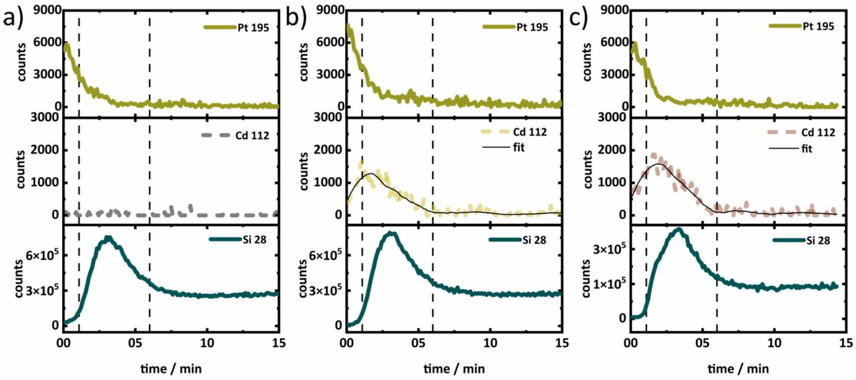

Figure 9. SIMS results of (**a**) drop-casted and untreated, (**b**) drop-casted and solvent treated, and (**c**) soaked for 24 h porous silica layers of 30 nm pore size. The panels from top to bottom correspond to Pt, Cd, and Si concentration. The dashed line at 1 min indicates the position of the top of the porous structure (Pt signal disappears). The second dashed line (6 min) corresponds to the end of porous silica layer, which is determined from the end point of the intense signal of the Si species. After that, the signal of Si is from the non-porous Si wafers.

To summarize, we showed the successful infiltration of pre-synthesized CdSe QDs into porous silica thin films with 10 nm and 30 nm pore sizes. It was observed that due to a higher pore volume, 30 nm porous silica shows higher loading after treatment than the 10 nm porous silica matrix. This can be related to a better accessibility of the pores with a higher pore size. The amount of infiltrated QDs can be influenced via drop-casting of additional solvent on a pre-drop-casted porous matrix as well as via varying the soaking time of a porous matrix in a QD solution. Via this method, a porous thin film matrix can be doped with luminescent QDs, which keep their luminescent properties upon deposition. This cannot be achieved via the SILAR process, which lacks controllability over nanocrystal quality and size distribution.

Supplementary Materials: The following supporting information can be downloaded at: https://www.mdpi.com/article/10.3390/ma17174379/s1, Figure S1: Raw absorption spectra of QD infiltrated porous silica layers, fitted scattering curve, and corrected absorption spectra; Figure S2: Uncorrected absorption spectra of untreated porous silica layers of 10 nm and 30 nm pore sizes; Figure S3: 30 nm porous layer with (a) Top-view, (b) cross-section SEM images and 10 nm porous layers with (c) Top-view, and (d) cross-section SEM images; Figure S4: SEM images of (a) untreated porous silica layers of 10 nm pore size in silicon wafer and with (b) 5, (c) 10, (d) 15, and (e) 20 SILAR immersions; Figure S5: (a) TEM image and (b) size distribution determined from TEM image analysis of CdSe QDs. The average size is determined to be 3.2 ± 0.5 nm with an FWHM of 0.5 nm; Figure S6: Absorption spectra (a) and photoluminescence spectra (b) of 10 nm (solid lines) and 30 nm (dashed line) porous layers after 0.5 h and 2 h soaking in a QD solution; Figure S7: Decay kinetic traces of 10 nm porous layers with QD infiltration via (a) drop-casting and (b) soaking along with the pure QD both in solution and thin film; Figure S8: Absorption spectra of glass substrate (a) soaked in a solution of pre-synthesized CdSe QD. 'Soaking: before washing' was recorded after removing the substrate from the QD solution, and 'soaking: after washing' was recorded after washing the substrate removed from QD solution. Absorption spectra of glass substrate (b) drop-casted with pre-synthesized CdSe QD. 'Drop casting: before washing' was recorded after drop-casting of QDs, and 'drop casting: after washing' was recorded after washing the substrate drop-casted with QDs; Figure S9: SEM images of (a) untreated, (b) QD drop-casted, (c) QD drop-casted + solvent, (d) soaked for 0.5 h, and (e) soaked for 24 h porous silica layers of 10 nm pore size in silicon wafer; Figure S10: SIMS depth profile of the Pt, Cd, and Si concentration of (a) untreated, (b) drop-casted + solvent, and (c) soaked for 24 h

QD in porous silica layers of 10 nm pore size; Figure S11: XRD pattern of pre-synthesized CdSe QD drop-casted on silicon wafer; Table S1: Fitting parameters obtained from triexponential fitting. τ and A are the time component and relative amplitude. τ_{av} is the average lifetime. Time components are presented in nanoseconds, 'ns'.

Author Contributions: Conceptualization, M.W. and A.S.; methodology, M.W., A.S. and R.B.; validation, R.B. and M.W.; formal analysis, R.B.; investigation, R.B., M.D. (Munira Dilshad), M.D. (Marco Diegel), J.D., J.P. and A.U.; resources, M.W.; data curation, R.B. and M.W.; writing—original draft preparation, R.B.; writing—review and editing, R.B., M.D. (Marco Diegel), J.D., J.P., A.U., A.S. and M.W.; visualization, R.B.; supervision, M.W.; project administration, M.W.; funding acquisition, M.W. All authors have read and agreed to the published version of the manuscript.

Funding: This work was financially supported by the German Research Foundation (DFG) under Project No. 398816777—CRC 1375 (NOA, C04 and B03). The EDX and XRD facilities are partially supported by the European Fund for Regional Development (EFRE) under the Project No. FKZ 2023 HSB 0025. Financial support by the German Research Foundation (DFG) within the infrastructure grant 390918228—INST 275/391-1 (A.U.) is acknowledged.

Institutional Review Board Statement: Not applicable.

Informed Consent Statement: Not applicable.

Data Availability Statement: The original contributions presented in the study are included in the article/Supplementary Material; further inquiries can be directed to the corresponding author.

Acknowledgments: We are grateful to Uwe Brückner (Leibniz IPHT) for the SIMS measurements.

Conflicts of Interest: The authors declare no conflicts of interest.

References

1. Koole, R.; Groeneveld, E.; Vanmaekelbergh, D.; Meijerink, A.; de Mello Donegá, C. Size Effects on Semiconductor Nanoparticles. In *Nanoparticles: Workhorses of Nanoscience*; de Mello Donegá, C., Ed.; Springer: Berlin/Heidelberg, Germany, 2014; pp. 13–51.
2. Bawendi, M.G.; Steigerwald, M.L.; Brus, L.E. The Quantum-Mechanics of Larger Semiconductor Clusters (Quantum Dots). *Annu. Rev. Phys. Chem.* **1990**, *41*, 477–496. [CrossRef]
3. Ekimov, A.I.; Efros, A.L.; Onushchenko, A.A. Quantum Size Effect in Semiconductor Microcrystals. *Solid State Commun.* **1985**, *56*, 921–924. [CrossRef]
4. Shu, Y.; Lin, X.; Qin, H.; Hu, Z.; Jin, Y.; Peng, X. Quantum Dots for Display Applications. *Angew. Chem.* **2020**, *59*, 22312–22323. [CrossRef] [PubMed]
5. Singh, V.; Priyanka; More, P.V.; Hemmer, E.; Mishra, Y.K.; Khanna, P.K. Magic-sized CdSe nanoclusters: A review on synthesis, properties and white light potential. *Mater. Adv.* **2021**, *2*, 1204–1228. [CrossRef]
6. Shirasaki, Y.; Supran, G.J.; Bawendi, M.G.; Bulovic, V. Emergence of colloidal quantum-dot light-emitting technologies. *Nat. Photonics* **2013**, *7*, 13–23. [CrossRef]
7. Zhou, J.; Liu, Y.; Tang, J.; Tang, W.H. Surface ligands engineering of semiconductor quantum dots for chemosensory and biological applications. *Mater. Today* **2017**, *20*, 360–376. [CrossRef]
8. Silvi, S.; Credi, A. Luminescent sensors based on quantum dot–molecule conjugates. *Chem. Soc. Rev.* **2015**, *44*, 4275–4289. [CrossRef]
9. Shamirian, A.; Ghai, A.; Snee, P.T. QD-Based FRET Probes at a Glance. *Sensors* **2015**, *15*, 13028–13051. [CrossRef]
10. Xiang, X.L.; Wang, L.X.; Zhang, J.J.; Cheng, B.; Yu, J.G.; Macyk, W. Cadmium Chalcogenide (CdS, CdSe, CdTe) Quantum Dots for Solar-to-Fuel Conversion. *Adv. Photonics Res.* **2022**, *3*, 2200065. [CrossRef]
11. Li, X.B.; Tung, C.H.; Wu, L.Z. Semiconducting quantum dots for artificial photosynthesis. *Nat. Rev. Chem.* **2018**, *2*, 160–173. [CrossRef]
12. Holmes, M.A.; Townsend, T.K.; Osterloh, F.E. Quantum confinement controlled photocatalytic water splitting by suspended CdSe nanocrystals. *Chem. Commun.* **2012**, *48*, 371–373. [CrossRef]
13. Murray, C.B.; Norris, D.J.; Bawendi, M.G. Synthesis and characterization of nearly monodisperse CdE (E = sulfur, selenium, tellurium) semiconductor nanocrystallites. *J. Am. Chem. Soc.* **1993**, *115*, 8706–8715. [CrossRef]
14. Chang, J.; Waclawik, E.R. Colloidal semiconductor nanocrystals: Controlled synthesis and surface chemistry in organic media. *RSC Adv.* **2014**, *4*, 23505–23527. [CrossRef]
15. Yin, Y.; Alivisatos, A.P. Colloidal nanocrystal synthesis and the organic-inorganic interface. *Nature* **2005**, *437*, 664–670. [CrossRef] [PubMed]
16. Peterson, M.D.; Cass, L.C.; Harris, R.D.; Edme, K.; Sung, K.; Weiss, E.A. The Role of Ligands in Determining the Exciton Relaxation Dynamics in Semiconductor Quantum Dots. *Annu. Rev. Phys. Chem.* **2014**, *65*, 317–339. [CrossRef]

17. Lim, S.J.; Ma, L.; Schleife, A.; Smith, A.M. Quantum dot surface engineering: Toward inert fluorophores with compact size and bright, stable emission. *Coord. Chem. Rev.* **2016**, *320*, 216–237. [CrossRef]
18. Hartley, C.L.; Kessler, M.L.; Dempsey, J.L. Molecular-Level Insight into Semiconductor Nanocrystal Surfaces. *J. Am. Chem. Soc.* **2021**, *143*, 1251–1266. [CrossRef]
19. Chen, Y.J.; Yu, S.; Fan, X.B.; Wu, L.Z.; Zhou, Y. Mechanistic insights into the influence of surface ligands on quantum dots for photocatalysis. *J. Mater. Chem. A* **2023**, *11*, 8497–8514. [CrossRef]
20. Micheel, M.; Baruah, R.; Kumar, K.; Wächtler, M. Assembly, Properties, and Application of Ordered Group II-VI and IV-VI Colloidal Semiconductor Nanoparticle Films. *Adv. Mater. Interfaces* **2022**, *9*, 2270157. [CrossRef]
21. Boles, M.A.; Engel, M.; Talapin, D.V. Self-Assembly of Colloidal Nanocrystals: From Intricate Structures to Functional Materials. *Chem. Rev.* **2016**, *116*, 11220–11289. [CrossRef]
22. Rogach, A.L.; Gaponik, N.; Lupton, J.M.; Bertoni, C.; Gallardo, D.E.; Dunn, S.; Li Pira, N.; Paderi, M.; Repetto, P.; Romanov, S.G.; et al. Light-Emitting Diodes with Semiconductor Nanocrystals. *Angew. Chem.* **2008**, *47*, 6538–6549. [CrossRef] [PubMed]
23. Wood, V.; Bulovic, V. Colloidal quantum dot light-emitting devices. *Nano. Rev.* **2010**, *1*, 5202. [CrossRef] [PubMed]
24. Semonin, O.E.; Luther, J.M.; Beard, M.C. Quantum dots for next-generation photovoltaics. *Mater. Today* **2012**, *15*, 508–515. [CrossRef]
25. Tang, J.A.; Sargent, E.H. Infrared Colloidal Quantum Dots for Photovoltaics: Fundamentals and Recent Progress. *Adv. Mater.* **2011**, *23*, 12–29. [CrossRef]
26. Liu, Z.K.; Yuan, J.Y.; Hawks, S.A.; Shi, G.Z.; Lee, S.T.; Ma, W.L. Photovoltaic Devices Based on Colloidal PbX Quantum Dots: Progress and Prospects. *Sol. RRL* **2017**, *1*, 1600021. [CrossRef]
27. Jin, L.; Zhao, H.G.; Wang, Z.M.M.; Rosei, F. Quantum Dots-Based Photoelectrochemical Hydrogen Evolution from Water Splitting. *Adv. Energy Mater.* **2021**, *11*, 2003233. [CrossRef]
28. Qureshi, A.; Shaikh, T.; Niazi, J.H. Semiconductor quantum dots in photoelectrochemical sensors from fabrication to biosensing applications. *Analyst* **2023**, *148*, 1633–1652. [CrossRef]
29. Li, N.; Mahalingavelar, P.; Vella, J.H.; Leem, D.S.; Azoulay, J.D.; Ng, T.N. Solution-processable infrared photodetectors: Materials, device physics and applications. *Mater. Sci. Eng. R Rep.* **2021**, *146*, 100643. [CrossRef]
30. Besson, S.; Gacoin, T.; Ricolleau, C.; Jacquiod, C.; Boilot, J.P. 3D quantum dot lattice inside mesoporous silica films. *Nano. Lett.* **2002**, *2*, 409–414. [CrossRef]
31. Demchyshyn, S.; Roemer, J.M.; Groiss, H.; Heilbrunner, H.; Ulbricht, C.; Apaydin, D.; Böhm, A.; Rütt, U.; Bertram, F.; Hesser, G.; et al. Confining metal-halide perovskites in nanoporous thin films. *Sci. Adv.* **2017**, *3*, e1700738. [CrossRef]
32. Li, J.S.; Tang, Y.; Li, Z.T.; Ding, X.R.; Yu, B.H.; Lin, L.W. Largely Enhancing Luminous Efficacy, Color-Conversion Efficiency, and Stability for Quantum-Dot White LEDs Using the Two-Dimensional Hexagonal Pore Structure of SBA-15 Mesoporous Particles. *ACS Appl. Mater. Interfaces* **2019**, *11*, 18808–18816. [CrossRef]
33. Wang, H.C.; Lin, S.Y.; Tang, A.C.; Singh, B.P.; Tong, H.C.; Chen, C.Y.; Lee, Y.C.; Tsai, T.L.; Liu, R.S. Mesoporous Silica Particles Integrated with All-Inorganic CsPbBr3 Perovskite Quantum-Dot Nanocomposites (MP-PQDs) with High Stability and Wide Color Gamut Used for Backlight Display. *Angew. Chem.* **2016**, *55*, 7924–7929. [CrossRef] [PubMed]
34. Li, J.S.; Tang, Y.; Li, Z.T.; Li, J.X.; Ding, X.R.; Yu, B.H.; Yu, S.D.; Ou, J.Z.; Kuo, H.C. Toward 200 Lumens per Watt of Quantum-Dot White-Light-Emitting Diodes by Reducing Reabsorption Loss. *ACS Nano.* **2021**, *15*, 550–562. [CrossRef] [PubMed]
35. Fan, M.; Huang, J.P.; Turyanska, L.; Bian, Z.F.; Wang, L.C.; Xu, C.Y.; Liu, N.; Li, H.B.; Zhang, X.Y.; Zhang, C.X.; et al. Efficient All-Perovskite White Light-Emitting Diodes Made of In Situ Grown Perovskite-Mesoporous Silica Nanocomposites. *Adv. Funct. Mater.* **2023**, *33*, 2215032. [CrossRef]
36. Ren, H.; Li, Y.M.; Li, W.J.; Zhai, Q.C.; Cheng, L. Lead-halide perovskite quantum dots embedded in mesoporous silica as heterogeneous photocatalysts combined with organocatalysts for asymmetric catalysis. *Green Chem.* **2024**, *26*, 6068–6077. [CrossRef]
37. Wang, T.Q.; Tian, B.B.; Han, B.; Ma, D.R.; Sun, M.Z.; Hanif, A.; Xia, D.H.; Shang, J. Recent Advances on Porous Materials for Synergetic Adsorption and Photocatalysis. *Energy Environ. Mater.* **2022**, *5*, 711–730. [CrossRef]
38. Meng, L.; Zhao, F.Y.; Zhang, J.B.; Luo, R.X.; Chen, A.F.; Sun, L.N.; Bai, S.L.; Tang, G.S.; Lin, Y. Preparation of monodispersed PbS quantum dots on nanoporous semiconductor thin film by two-phase method. *J. Alloys Compd.* **2014**, *595*, 51–54. [CrossRef]
39. Wang, P.; Zhu, Y.H.; Yang, X.L.; Li, C.Z.; Du, H.L. Synthesis of CdSe nanoparticles into the pores of mesoporous silica microspheres. *Acta Mater.* **2008**, *56*, 1144–1150. [CrossRef]
40. Gao, X.H.; Nie, S.M. Doping mesoporous materials with multicolor quantum dots. *J. Phys. Chem. B* **2003**, *107*, 11575–11578. [CrossRef]
41. Calvo, M.E.; Hidalgo, N.; Schierholz, R.; Kovács, A.; Fernández, A.; Bellino, M.G.; Soler-Illia, G.J.A.A.; Míguez, H. Full solution processed mesostructured optical resonators integrating colloidal semiconductor quantum dots. *Nanoscale* **2015**, *7*, 16583–16589. [CrossRef]
42. Ghazaryan, L.; Kley, E.B.; Tünnermann, A.; Szeghalmi, A. Nanoporous SiO_2 thin films made by atomic layer deposition and atomic etching. *Nanotechnology* **2016**, *27*, 255603. [CrossRef] [PubMed]
43. Pérez-Anguiano, O.; Wenger, B.; Pugin, R.; Hofmann, H.; Scolan, E. Controlling Mesopore Size and Processability of Transparent Enzyme-Loaded Silica Films for Biosensing Applications. *ACS Appl. Mater. Interfaces* **2015**, *7*, 2960–2971. [CrossRef]

44. Raman, N.K.; Anderson, M.T.; Brinker, C.J. Template-based approaches to the preparation of amorphous, nanoporous silicas. *Chem. Mater.* **1996**, *8*, 1682–1701. [CrossRef]
45. Liu, Y.; Ren, W.; Zhang, L.Y.; Yao, X. New method for making porous SiO_2 thin films. *Thin Solid Films* **1999**, *353*, 124–128. [CrossRef]
46. Amirav, L.; Alivisatos, A.P. Photocatalytic Hydrogen Production with Tunable Nanorod Heterostructures. *J. Phys. Chem. Lett.* **2010**, *1*, 1051–1054. [CrossRef]
47. Carbone, L.; Nobile, C.; De Giorgi, M.; Sala, F.D.; Morello, G.; Pompa, P.; Hytch, M.; Snoeck, E.; Fiore, A.; Franchini, I.R.; et al. Synthesis and micrometer-scale assembly of colloidal CdSe/CdS nanorods prepared by a seeded growth approach. *Nano. Lett.* **2007**, *7*, 2942–2950. [CrossRef]
48. Sankapal, B.R.; Salunkhe, D.B.; Majumder, S.; Dubal, D.P. Solution-processed CdS quantum dots on TiO_2: Light-induced electrochemical properties. *RSC Adv.* **2016**, *6*, 83175–83184. [CrossRef]
49. Geissler, D.; Wurth, C.; Wolter, C.; Weller, H.; Resch-Genger, U. Excitation wavelength dependence of the photoluminescence quantum yield and decay behavior of CdSe/CdS quantum dot/quantum rods with different aspect ratios. *Phys. Chem. Chem. Phys.* **2017**, *19*, 12509–12516. [CrossRef]
50. Schneider, C.A.; Rasband, W.S.; Eliceiri, K.W. NIH Image to ImageJ: 25 years of image analysis. *Nat. Methods* **2012**, *9*, 671–675. [CrossRef]
51. Norris, D.J.; Bawendi, M.G. Measurement and assignment of the size-dependent optical spectrum in CdSe quantum dots. *Phys. Rev. B* **1996**, *53*, 16338–16346. [CrossRef]
52. Deng, Z.T.; Cao, L.; Tang, F.Q.; Zou, B.S. A new route to zinc-blende CdSe nanocrystals: Mechanism and synthesis. *J. Phys. Chem. B* **2005**, *109*, 16671–16675. [CrossRef] [PubMed]
53. Hu, X.G.; Zrazhevskiy, P.; Gao, X.H. Encapsulation of Single Quantum Dots with Mesoporous Silica. *Ann. Biomed. Eng.* **2009**, *37*, 1960–1966. [CrossRef] [PubMed]
54. Abdelhady, A.L.; Afzaal, M.; Malik, M.A.; O'Brien, P. Flow reactor synthesis of CdSe, CdS, CdSe/CdS and CdSeS nanoparticles from single molecular precursor(s). *J. Mater. Chem.* **2011**, *21*, 18768–18775. [CrossRef]
55. Yu, W.W.; Qu, L.; Guo, W.; Peng, X. Experimental Determination of the Extinction Coefficient of CdTe, CdSe, and CdS Nanocrystals. *Chem. Mater.* **2003**, *15*, 2854–2860. [CrossRef]
56. Crooker, S.A.; Hollingsworth, J.A.; Tretiak, S.; Klimov, V.I. Spectrally resolved dynamics of energy transfer in quantum-dot assemblies: Towards engineered energy flows in artificial materials. *Phys. Rev. Lett.* **2002**, *89*, 186802. [CrossRef]
57. Kagan, C.R.; Murray, C.B.; Bawendi, M.G. Long-range resonance transfer of electronic excitations in close-packed CdSe quantum-dot solids. *Phys. Rev. B* **1996**, *54*, 8633–8643. [CrossRef]
58. Akselrod, G.M.; Prins, F.; Poulikakos, L.V.; Lee, E.M.Y.; Weidman, M.C.; Mork, A.J.; Willard, A.P.; Bulovic, V.; Tisdale, W.A. Subdiffusive Exciton Transport in Quantum Dot Solids. *Nano. Lett.* **2014**, *14*, 3556–3562. [CrossRef]

Disclaimer/Publisher's Note: The statements, opinions and data contained in all publications are solely those of the individual author(s) and contributor(s) and not of MDPI and/or the editor(s). MDPI and/or the editor(s) disclaim responsibility for any injury to people or property resulting from any ideas, methods, instructions or products referred to in the content.

Supporting Information

Correction for scattering background of porous layer absorption spectra

To remove the scattering contribution in the collected absorption spectra, a theoretical wavelength dependent scattering function is applied as follows:

$$S = A \times \lambda^{n}$$

This function fitted in the absorption spectra, in the region where there is no absorption of QDs. Here, the wavelength λ is in nm, and the exponent n has values from −4 (Rayleigh scattering for spherical and small particles) to −1 (for larger and non-spherical particles). A represents the background contribution to the absorption spectra [1].

After fitting the scattering function, it was extrapolated to the whole wavelength range, which was then subtracted from the original absorption spectra to obtain the corrected absorption spectra.

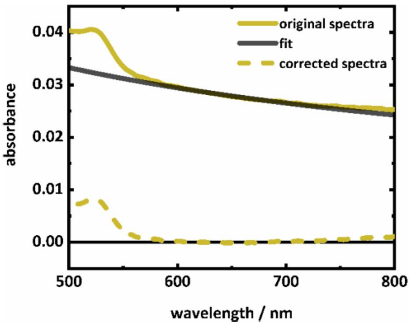

Figure S1. Raw absorption spectra of QD infiltrated porous silica layers, fitted scattering curve, and corrected absorption spectra.

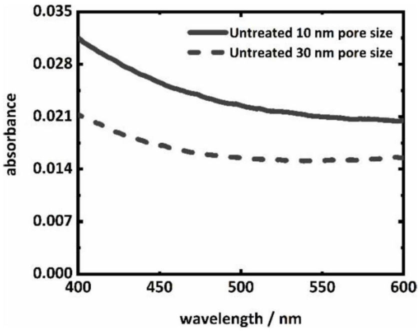

Figure S2. Uncorrected absorption spectra of untreated porous silica layers of 10 nm and 30 nm pore sizes.

Porous silica layers

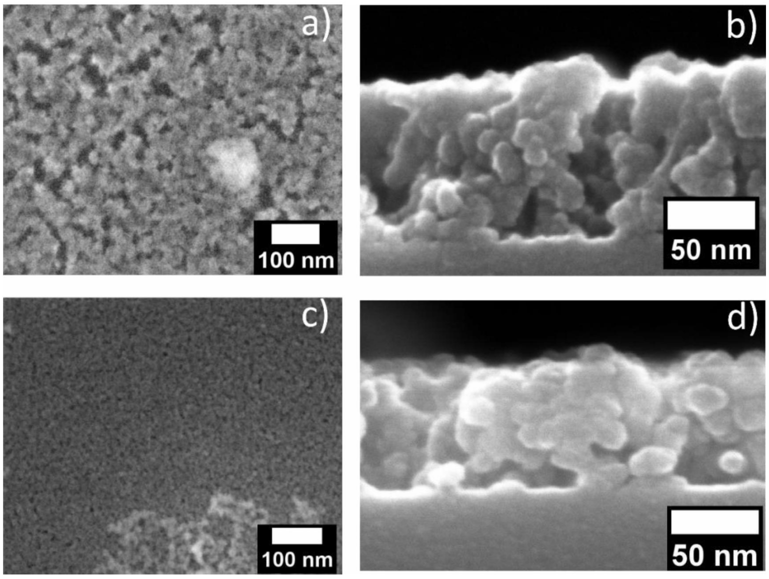
a)
100 nm
b)
50 nm
c)
100 nm
d)
50 nm

Figure S3. 30 nm porous layer with (**a**) Top-view, (**b**)cross-section SEM images and 10 nm porous layers with (**c**) Top-view, and (**d**) cross-section SEM images.

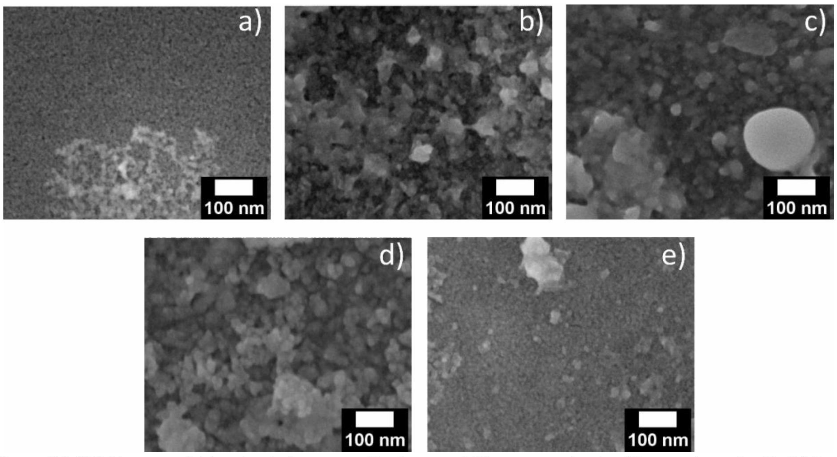
a)
100 nm
b)
100 nm
c)
100 nm
d)
100 nm
e)
100 nm

Figure S4. SEM images of (**a**) untreated porous silica layers of 10 nm pore size in silicon wafer and with (**b**) 5, (**c**) 10, (**d**) 15, and (**e**) 20 SILAR immersions.

Size distribution colloidal quantum dots

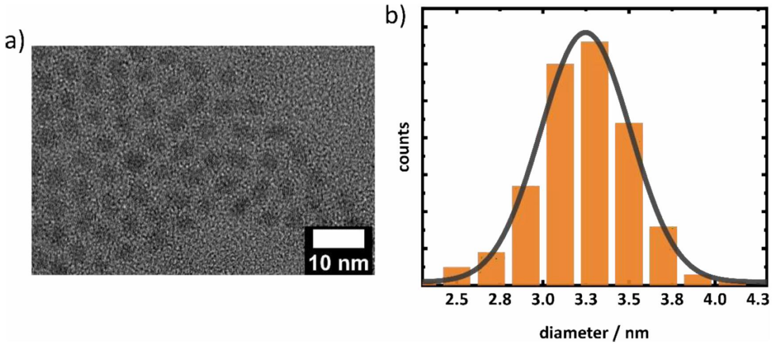

Figure S5. (**a**) TEM image and (**b**) size distribution determined from TEM image analysis of CdSe QDs. The average size is determined to be 3.2±0.5 nm with an FWHM of 0.5 nm.

Absorption spectra and photoluminescence spectra of samples treated by soaking

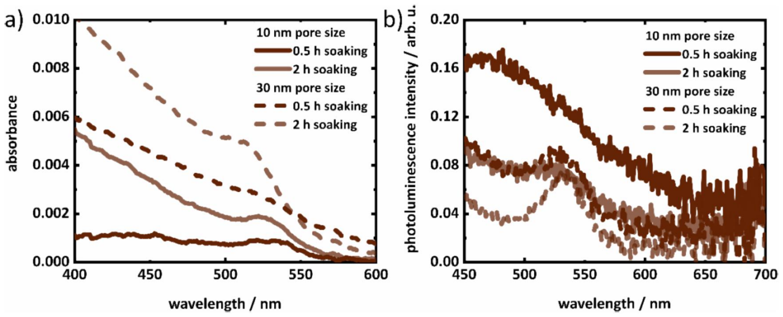

Figure S6. Absorption spectra (**a**) and photoluminescence spectra (**b**) of 10 nm (solid lines) and 30 nm (dashed line) porous layers after 0.5 h and 2 h soaking in a QD solution.

TCSPC data analysis

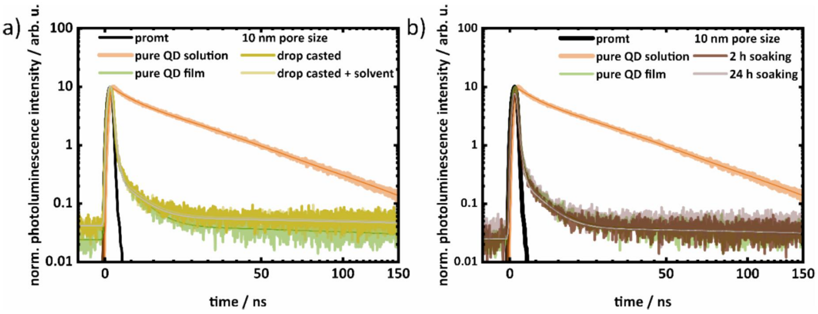

Figure S7. Decay kinetic traces of 10 nm porous layers with QD infiltration via (**a**) drop-casting and (**b**) soaking along with the pure QD both in solution and thin film.

The decay curves were fitted by applying a tri-exponential function:

$$y = y_0 + A_1 e^{-x/\tau_1} + A_2 e^{-x/\tau_2} + A_3 e^{-x/\tau_3}$$

with τ_1, τ_2 and τ_3 being the time components, and A_1, A_2 and A_3 being the pre-exponential factors representing the respective relative amplitudes. The amplitude average lifetime, τ_{av}, was determined according to the equation below.

$$\tau_{av} = \frac{\sum_{i=1}^{n} A_i \tau_i}{\sum_{i=1}^{n} A_i}$$

Fitted parameters obtained from the tri-exponential fitting and the respective average lifetime of all the samples are tabulated below.

Table S1. Fitting parameters obtained from triexponential fitting. τ and A are the time component and relative amplitude. τ_{av} is the average lifetime. Time components are presented in nanoseconds, 'ns'.

Sample		τ_1	τ_2	τ_3	A_1	A_2	A_3	τ_{av}
Pure QD solution		4.2±0.08	20.4±0.52	70.7±0.7	10.3±0.1	50.1±0.2	39.6±0.1	**38.7**±0.5
Pure QD film		0.4±0.004	4.6±0.2	138.6±16.1	77.3±0.3	9.4±0.2	13.3±0.6	**19.2**±2.9
10 nm pore size	drop-casted	0.4±0.005	4.7±0.2	138.1±17.4	76.5±0.3	8.9±0.2	14.6±0.7	**20.9**±3.4
	drop-casted + solvent	0.5±0.004	4.8±0.2	121.6±31.7	80.9±0.3	8.03±0.2	11.03±0.6	**14.1**±4.2
30 nm	drop-casted	0.4±0.005	4.3±0.2	131.7±18.0	75.3±0.3	10±0.2	14.2±0.8	**20.1**±3.5

pore size	drop -casted + solvent	0.4±0.005	4.8±0.2	123.4±28.1	77.4±0.3	10.8±0.2	11.9±0.8	**15.5**±4.3
10 nm pore size	2 h soaking	0.4±0.005	4.7±0.2	196.5±32.9	72.4±0.4	9.5±0.2	18±0.1	**36.2**±7.9
	24 h soaking	0.4±0.005	4.3±0.2	146.9±31.8	77.2±0.3	9.7±0.2	13.1±0.6	**20**±5.2
30 nm pore size	2 h soaking	0.4±0.005	4.3±0.2	132.7±26.6	78.6±0.3	8.5±0.2	12.9±0.7	**17.8**±4.3
	24 h soaking	0.4±0.005	4.3±0.2	146.9±31.8	77.2±0.3	9.7±0.2	13.1±0.6	**11.7**±4.7

QD deposition on glass substrate

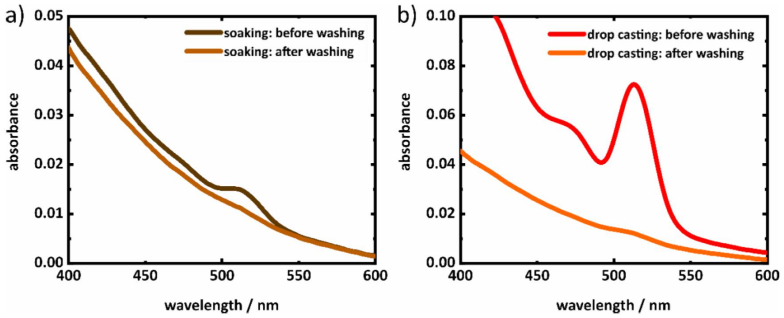

Figure S8. Absorption spectra of glass substrate (**a**) soaked in a solution of pre-synthesized CdSe QD. 'Soaking: before washing' was recorded after removing the substrate from the QD solution, and 'soaking: after washing' was recorded after washing the substrate removed from QD solution. Absorption spectra of glass substrate (**b**) drop-casted with pre-synthesized CdSe QD. 'Drop casting: before washing' was recorded after drop-casting of QDs, and 'drop casting: after washing' was recorded after washing the substrate drop-casted with QDs.

SEM images of treated layers

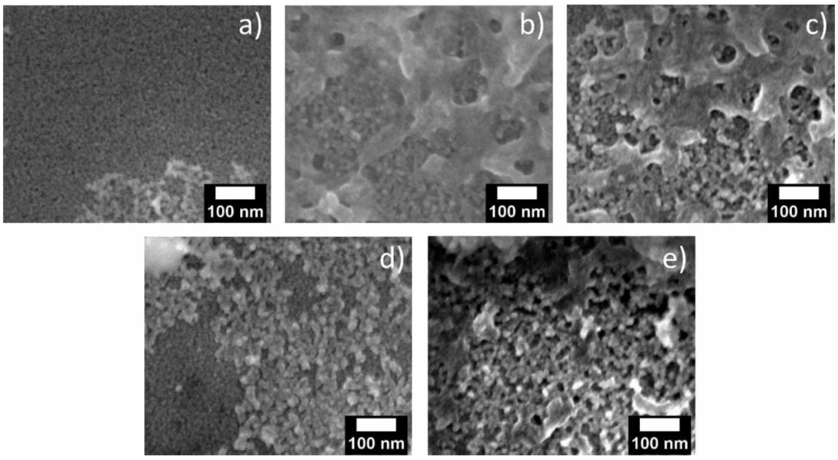

Figure S9. SEM images of (**a**) untreated, (**b**) QD drop-casted, (**c**) QD drop-casted + solvent, (**d**) soaked for 0.5 h, and (**e**) soaked for 24 h porous silica layers of 10 nm pore size in silicon wafer.

SIMS measurements

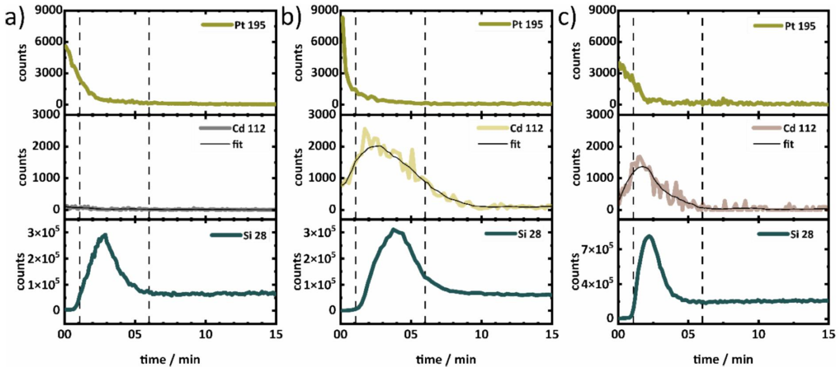

Figure S10. SIMS depth profile of the Pt, Cd, and Si concentration of (**a**) untreated, (**b**) drop-casted + solvent, and (**c**) soaked for 24 h QD in porous silica layers of 10 nm pore size.

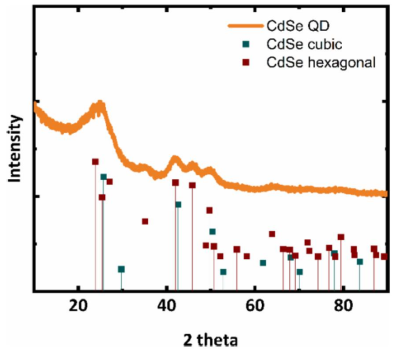

Figure S11. XRD pattern of pre-synthesized CdSe QD drop-casted on silicon wafer.

References

1. Geissler, D.; Wurth, C.; Wolter, C.; Weller, H.; Resch-Genger, U. Excitation wavelength dependence of the photoluminescence quantum yield and decay behavior of CdSe/CdS quantum dot/quantum rods with different aspect ratios. *Phys. Chem. Chem. Phys.* **2017**, *19*, 12509-12516.

7. Summary & Outlook

CdSe QDs, owing to their size tunable optoelectronic properties, narrow photoluminescence linewidth, high photoluminescence quantum yields etc., have been a prime interest of intensive research for numerous applications, including light-emitting diodes, solar concentrators, photocatalysis, photovoltaics, and nanocrystal lasers. The dynamics of excitons and multiexcitons govern the photophysics behind QD based applications. For example, effective separation of electron and hole enhances photocatalytic efficiency, while multiexcitons with long lifetimes enhance the optical gain, thereby increasing laser performance. In recent years, it has been demonstrated that the properties of excitons and multiexcitons can be modified by altering the size and the surface properties of QDs. Therefore, to develop suitable materials for optoelectronic applications, it is essential to gain a comprehensive understanding of the mechanisms underlying the size and surface modification induced changes in exciton and multiexciton properties.

With this motivation, the influence of QD size, surface modification, and inter-QD coupling on the exciton and multiexciton properties of QDs in solutions and thin films were investigated in this thesis entitled 'Exciton and Multiple Exciton Dynamics in Colloidal Semiconductor Nanocrystals'. For this purpose, colloidal TOPO capped CdSe QDs with different sizes were synthesized via hot injection method, which is described in Chapter 3. By exploiting a biphasic ligand exchange protocol, MPA, MUA, and S^{2-} capped QDs were prepared. The impact of the surface ligands on electronic properties was evaluated by absorption and photoluminescence spectroscopy. A strong photoluminescence quenching and enhancement of trap-state emission was observed with the ligands, MPA, MUA, and S^{2-} originating from the hole trapping at the surface sites introduced by the ligands. Further, acoustic phonon modes of the CdSe QDs with these surface ligands were monitored by applying Raman spectroscopy, as the acoustic phonon vibration influences the carrier trapping processes as well as photoluminescence linewidth. It was observed that the phonon frequency is lower with the heavier surface ligands. This mass loading effect is due to the mechanical strain caused by the surface ligands which provides an inertial resistance lowering the phonon frequencies.

In Chapter 4, the exciton and multiexciton dynamics were investigated for the two surface functionalizations that showed the most pronounced differences from the previous investigations: the TOPO capped and the S^{2-} capped QDs. For this excitation intensity-dependent TA spectroscopy was performed on the colloidal TOPO capped and the S^{2-} capped QDs. By applying a MCMC target analysis for a global fitting of the received intensity-dependent TA dataset, spectral and dynamical features of excitons and multiexcitons were extracted, allowing a detailed analysis of the multiexciton dynamics. Through this method, multiexcitons up to QX were detected and the decay process was described by a cascade Auger recombination model. Multiexciton lifetimes in both TOPO and the S^{2-} capped QDs show a cubic relation with the QD radius in good agreement with theoretical predictions. The S^{2-} capped QDs show prolonged multiexciton lifetimes compared to the TOPO capped QDs. This effect can be attributed to a suppression of Auger recombination due to the reduction in carrier wavefunction overlap originating from strong surface hole trapping in the S^{2-} capped QDs. Moreover, by employing a Gaussian fitting method in the exciton and multiexciton spectra, the multiexciton binding energies are determined. The S^{2-} capped QDs show smaller binding energies compared to the respective TOPO capped QDs, which is also related to the strong surface hole trapping in S^{2-} capped QDs resulting in reduced electron-hole wavefunction overlap.

In Chapter 5, the exciton and multiexciton properties of TOPO and S^{2-} capped QD thin films were investigated by intensity dependent TA spectroscopy. Thin films were fabricated by drop casting of colloidal QDs. Photoluminescence spectroscopy was performed to investigate the effect of closely packed QDs in thin films and the presence of electronic interaction between neighboring QDs. Due to strong electronic coupling in S^{2-} capped QDs, the band-edge photoluminescence peak positions are red shifted with respect to the QDs solution. No such strong redshift is observed for TOPO-capped QD thin films due to the long aliphatic chains of TOPO increasing the distance of the QDs within the layers preventing electronic coupling. The intensity-dependent TA spectra of the QD thin films were also evaluated through the global fitting based on MCMC sampling to determine the multiexciton spectra and lifetimes. The TOPO capped QD thin films show the identical multiexciton recombination models as in the solutions, and thus exhibit nearly identical multiexciton spectral shape and lifetime. However, in the S^{2-} capped QD thin films, the typical spectral signatures of multiexciton recombination were not observed in contrast to the corresponding solutions. Rather, the unique spectral shapes and kinetic traces in the S^{2-} capped QD thin films suggest that the multiexcitons undergo exciton delocalization in the ultrafast time regime dominating over the Auger recombination process.

In Chapter 6, synthetic strategies to fabricate QD thin films embedded in a porous silica matrix are demonstrated as novel thin film materials containing immobilized QDs for optoelectronic applications. For this, two methods were utilized– in-situ growth of CdSe NCs in porous silica matrix and infiltration of pre-synthesized CdSe QDs into the porous matrix. The SILAR method was used for in-situ growth of CdSe NCs within the porous silica matrix. However, the uncontrolled growth in SILAR method results in a broad size distribution of NCs resulting in broad absorption features and absence of photoluminescence due to high density of defect states. Therefore, to overcome this problem, QDs synthesized via hot-injection method were deposited inside the porous matrix by infiltration of the pores of the silica matrix. The infiltration was achieved either via drop casting a QD solution on the porous layers or by soaking the porous layers in a QD solution. The QDs infiltrated via these two methods keep their luminescent properties, resulting in thin films with high quality and well defined immobilized QDs suited for integration into optoelectronic devices.

Throughout the studies in this thesis, detailed mechanistic insight into how QD size and surface functionalization affect exciton and multiexciton properties has been explored. The exciton and multiexciton lifetime tunability through the QD size, following the universal volume scaling, allows one to design a potential material with a desired multiexciton lifetime. Similarly, the prolonged multiexciton lifetimes due to the surface traps introduced by the surface ligands makes colloidal QD a highly promising material for applications such as photocatalysis. Moreover, long multiexciton lifetimes increase optical gain lifetime which is highly demanding for NC laser applications. On the other hand, the investigations performed on QD thin films unfold the tunability of carrier mobilization via the size of surface ligand. By the use of a bulky surface ligand such as TOPO, a QD thin film can retain the exciton and multiexciton properties as in the colloidal QD solution. To achieve high carrier mobility, short inorganic ligands such as S^{2-} is useful in QD thin films. The S^{2-} capped QD thin films are shown to possess strong inter-QD coupling which allows ultrafast delocalization of exciton and multiexcitons dominating over Auger recombination process. The colloidal QDs, with the interplay of size tunable synthesis, surface modification, and solution processing, provide a multidimensional tunability of exciton and multiexciton properties.

When considering the prospects of the work performed in this thesis, an obvious continuation is to extend the spectroscopic investigation to more exploit the trap-assisted Auger process to unfold the mechanism of prolonged multiexciton lifetime upon surface trapping. The Auger recombination model considered in this thesis is a three-particle carrier scattering process, and follows a third order kinetic model, which however was found to be fifth order in this work. In the recent studies, a phonon-assisted Auger process has also been demonstrated resulting in long multiexciton lifetime. Typically, in QDs the carrier scattering process is dominant due to the extended carrier wavefunction in the momentum space. However, the initial study in this thesis shows a strong influence of surface ligands on the phonon properties. Hence, the effect of phonon on the Auger process cannot completely be ruled out. To investigate further in this direction, temperature and intensity dependent TA spectroscopy will be helpful to simultaneously monitor the phonon vibration and the Auger process. Such an experiment will also be highly informative for systems such as the S^{2-} capped QD thin films to track the carrier mobility in strongly coupled QDs.

8. Zusammenfassung und Ausblick

CdSe-QDs sind aufgrund ihrer in der Größe einstellbaren optoelektronischen Eigenschaften, ihrer schmalen Photolumineszenz-Linienbreite, ihrer hohen Photolumineszenz-Quantenausbeute usw. für zahlreiche Anwendungen, darunter Leuchtdioden, Solarkonzentratoren, Photokatalyse, Photovoltaik und Nanokristall-Laser, von vorrangigem Interesse und werden intensiv erforscht. Die Dynamik von Exzitonen und Multiexzitonen bestimmt die Photophysik von QD-basierten Anwendungen. So erhöht beispielsweise eine effektive Trennung von Elektronen und Löchern die photokatalytische Effizienz, während Multiexzitonen mit langer Lebensdauer die optische Verstärkung und damit die Laserleistung erhöhen. In den letzten Jahren wurde gezeigt, dass die Eigenschaften von Exzitonen und Multiexzitonen durch Veränderung der Größe und der Oberflächeneigenschaften von QDs modifiziert werden können. Um geeignete Materialien für optoelektronische Anwendungen zu entwickeln, ist es daher wichtig, ein umfassendes Verständnis der Mechanismen zu erlangen, die den durch Größen- und Oberflächenmodifikation hervorgerufenen Veränderungen der Exzitonen- und Multiexzitonen-Eigenschaften zugrunde liegen.

Aus dieser Motivation heraus wurde in dieser Arbeit mit dem Titel 'Exciton and Multiple Exciton Dynamics in Colloidal Semiconductor Nanocrystals' der Einfluss von QD-Größe, Oberflächenmodifikation und Inter-QD-Kopplung auf die Exzitonen- und Multiexzitonen-Eigenschaften von QDs in Lösungen und dünnen Filmen untersucht. Zu diesem Zweck wurden kolloidale TOPO-funktionalisierte CdSe-QDs mit unterschiedlichen Größen mittels hot-injection verfahren synthetisiert, was in Kapitel 3 beschrieben wird. Durch Ausnutzung eines biphasischen Ligandenaustauschprotokolls wurden MPA, MUA und S^{2-} funktionalisierte QDs hergestellt. Der Einfluss der Oberflächenliganden auf die elektronischen Eigenschaften wurde durch Absorptions- und Photolumineszenzspektroskopie untersucht. Mit den Liganden MPA, MUA und S^{2-} wurde eine starke Löschung der Photolumineszenz und eine Verstärkung der Trap-State-Emission beobachtet, die auf das Einfangen von Löchern an den durch die Liganden eingeführten surface defect sites zurückzuführen ist. Des Weiteren wurden die akustischen Phononenmoden der

CdSe-QDs mit diesen Oberflächenliganden durch Raman-Spektroskopie überwacht, da die akustische Phononenschwingung die carrier trapping prozesse sowie die Photolumineszenz-Linienbreite beeinflusst. Es wurde beobachtet, dass die Phononenfrequenz mit den schwereren Oberflächenliganden niedriger ist. Dieser Effekt ist auf die mechanische Belastung durch die Oberflächenliganden zurückzuführen, die einen Trägheitswiderstand erzeugt, der die Phononenfrequenzen senkt.

In Kapitel 4 wurde die Exzitonen- und Multiexzitonendynamik für die beiden Oberflächenfunktionalisierungen untersucht, die die deutlichsten Unterschiede in den vorangegangenen Untersuchungen aufwiesen: die TOPO- und die S^{2-} funktionalisierten QDs. Zu diesem Zweck wurde anregungsintensitätsabhängige TA-Spektroskopie an den kolloidalen TOPO-verkappten und den S^{2-} verkappten QDs durchgeführt. Durch Anwendung einer MCMC-Zielanalyse für eine globale Anpassung des erhaltenen intensitätsabhängigen TA-Datensatzes wurden spektrale und dynamische Merkmale von Exzitonen und Multiexzitonen extrahiert, was eine detaillierte Analyse der Multiexzitonendynamik ermöglichte. Mit dieser Methode wurden Multiexzitonen bis zu QX nachgewiesen und der Zerfallsprozess wurde durch ein Kaskaden-Auger-Rekombinationsmodell beschrieben. Die Multiexzitonen-Lebensdauer sowohl in TOPO als auch in den QDs mit S^{2-} Oberflächenliganden zeigt eine kubische Beziehung zum QD-Radius in guter Übereinstimmung mit theoretischen Vorhersagen. Die mit S^{2-} funktionalisierten QDs weisen im Vergleich zu den QDs mit TOPO-Oberflächenliganden verlängerte Multiexzitonen-Lebensdauern auf. Dieser Effekt kann auf eine Unterdrückung der Auger-Rekombination zurückgeführt werden, die auf die Verringerung der Überlappung der Ladungsträger-Wellenfunktion zurückzuführen ist, die sich aus der starken Lokalisierung von Löchern an der Oberfläche der S^{2-} verkappten QDs in Fehlstellenzuständen ergibt. Durch die Anwendung einer Gaußschen Anpassungsmethode in den Exzitonen- und Multiexzitonenspektren wurden außerdem die Multiexzitonen-Bindungsenergien bestimmt. Die mit S^{2-} verkappten QDs weisen im Vergleich zu den entsprechenden QDs mit TOPO-Liganden geringere Bindungsenergien auf, was auch mit dem starken Einfangen von Löchern an der Oberfläche in QDs mit S^{2-}-Liganden zusammenhängt, was zu einer geringeren Überlappung der Elektron-Loch-Wellenfunktion führt.

In Kapitel 5 wurden die Exzitonen- und Multiexzitonen-Eigenschaften von TOPO und S^{2-} verkappten QD-Dünnschichten durch intensitätsabhängige TA-Spektroskopie untersucht. Die Dünnschichten wurden durch drop casting von kolloidalen QDs hergestellt. Photolumineszenzspektroskopie wurde durchgeführt, um den Effekt von dicht gepackten QDs in dünnen Filmen und das Vorhandensein von elektronischen Wechselwirkungen zwischen benachbarten QDs zu untersuchen. Aufgrund der starken elektronischen Kopplung in S^{2-} funktionalisierten QDs unterliegen die Positionen der Bandkanten-Photolumineszenz-Peaks gegenüber der QD-Lösung einer Rotverschiebung. Bei TOPO-bedeckten QD-Dünnschichten wird keine so starke Rotverschiebung beobachtet, da die langen aliphatischen Ketten von TOPO den Abstand der QDs innerhalb der Schichten vergrößern und so eine elektronische Kopplung verhindern. Die intensitätsabhängigen TA-Spektren der QD-Dünnschichten wurden auch durch die globale Anpassung auf der Grundlage von MCMC-Sampling ausgewertet, um die Multiexzitonspektren und -lebensdauern zu bestimmen. Die TOPO-funktionalisierten QD-Dünnschichten zeigen die gleichen Multiexzitonen-Rekombinationsmodelle wie in den Lösungen und weisen daher nahezu identische Multiexzitonenspektren und -lebensdauern auf. In den S^{2-} funktionalisierten QD-Dünnschichten wurden jedoch im Gegensatz zu den entsprechenden Lösungen nicht die typischen spektralen Signaturen der Multiexzitonen-Rekombination beobachtet. Die einzigartigen spektralen Formen und kinetischen Spuren in den S^{2-} verkappten QD-Dünnschichten deuten vielmehr darauf hin, dass die Multiexzitonen im ultraschnellen Zeitbereich eine Exzitonen-Delokalisierung erfahren, welche über den Auger-Rekombinationsprozess dominiert.

In Kapitel 6 werden synthetische Strategien zur Herstellung von QD-Dünnschichten, die in eine poröse Siliziumdioxidmatrix eingebettet sind, als neuartige Dünnschichtmaterialien mit immobilisierten QDs für optoelektronische Anwendungen vorgestellt. Dazu wurden zwei Methoden angewandt: zum einen in-situ-Wachstum von CdSe-NCs in einer porösen Siliziumdioxid-Matrix und zum Anderen Infiltration von vorsynthetisierten CdSe-QDs in die poröse Matrix. Die SILAR-Methode wurde für das in-situ-Wachstum der CdSe-NCs in der porösen Siliziumdioxidmatrix verwendet. Das unkontrollierte Wachstum bei der SILAR-Methode führt jedoch zu einer breiten Größenverteilung der NCs, was zu breiten Absorptionsmerkmalen und dem Fehlen von Photolumineszenz aufgrund der hohen Dichte von Defektzuständen führt. Um dieses Problem zu überwinden, wurden die mit der hot-injection verfahren synthetisierten QDs in der porösen Matrix durch Infiltration der Poren der Silicamatrix abgeschieden. Die Infiltration wurde entweder durch drop casting einer QD-Lösung auf die porösen Schichten oder durch Immersion der porösen Schichten in einer QD-Lösung erreicht. Die mit diesen beiden Methoden infiltrierten QDs behalten ihre Lumineszenzeigenschaften, was zu dünnen Filmen mit qualitativ hochwertigen und gut definierten immobilisierten QDs führt, die sich für die Integration in optoelektronische Geräte eignen.

In den Studien dieser Arbeit wurde ein detailierter mechanistischer Einblick in die Auswirkungen der QD-Größe und der Oberflächenfunktionalisierung auf die Exziton- und Multiexziton-Eigenschaften gewonnen. Die Abstimmbarkeit der Exzitonen- und Multiexzitonenlebensdauer durch die QD-Größe, die dem Größenquantisierungseffekt folgt, ermöglicht es, ein potenzielles Material mit einer gewünschten Multiexzitonenlebensdauer zu entwickeln. Ebenso macht die verlängerte Multiexzitonenlebensdauer aufgrund der durch die Oberflächenliganden eingeführten Oberflächendefektzustände kolloidale QD zu einem vielversprechenden Material für Anwendungen wie die Photokatalyse. Darüber hinaus erhöhen lange Multiexzitonenlebensdauern die optische optical gain lebensdauer, die für NC-Laseranwendungen sehr wichtig ist. Auch konnte durch Untersuchungen an QD-Dünnschichten die Abstimmbarkeit der Ladungsträgermobilisierung über die Art des Oberflächenliganden erschlossen werden. Durch die Verwendung eines sperrigen Oberflächenliganden wie TOPO kann ein QD-Dünnfilm die Exzitonen- und Multiexzitonen-Eigenschaften wie in der kolloidalen QD-Lösung beibehalten. Um eine hohe Ladungsträgerbeweglichkeit zu erreichen, sind kurze anorganische Liganden wie S^{2-} in QD-Dünnschichten nützlich. Die S^{2-} verkappten QD-Dünnfilme weisen eine starke elektronische Kopplung zwischen den QDs auf, die eine ultraschnelle Delokalisierung von Exzitonen und Multiexzitonen ermöglicht, welche über den den Auger-Rekombinationsprozess dominiert. Die kolloidalen QDs, mit dem Zusammenspiel der Vorteile der größenabstimmbaren Synthese, der Oberflächenmodifikation und der Lösungsverarbeitung, bieten eine multidimensionale Abstimmbarkeit der Exziton- und Multiexzitoneneigenschaften.

In Anbetracht der in dieser Arbeit vorgestellten Ergebnisse wäre es von Vorteil, die spektroskopische Untersuchung zu erweitern, um ein tieferes Verständnis des durch Defektzustände unterstützten Auger-Prozesses und seiner Rolle im

Mechanismus der verlängerung der Multiexzitonen-Lebensdauern zu gewinnen. Das in dieser Arbeit betrachtete Auger-Rekombinationsmodell ist three-particle carrier scattering prozess, der einem kinetischen Modell dritter Ordnung folgt. In dieser Arbeit wurde jedoch festgestellt, dass es sich um ein Modell fünfter Ordnung handelt. In neueren Studien wurde auch ein phononenunterstützter Auger-Prozess nachgewiesen, der zu einer verlängerten Multiexzitonenlebensdauer führt. In Quantenpunkten ist der Prozess der Ladungsträgerstreuung aufgrund der ausgedehnten Wellenfunktion der Ladungsträger im Impulsraum in der Regel der dominierende Mechanismus. Die erste Studie, die in dieser Arbeit vorgestellt wurde, zeigt jedoch einen signifikanten Einfluss der Oberflächenliganden auf die Phononeneigenschaften. Daher kann die Möglichkeit nicht ausgeschlossen werden, dass Phononen einen Einfluss auf den Auger-Prozess haben. Um dies weiter zu untersuchen, wird die temperatur- und intensitätsabhängige TA-Spektroskopie nützlich sein, um die Phononenschwingung und den Auger-Prozess gleichzeitig zu überwachen. Ein solches Experiment wird auch für Systeme wie die S^{2-} verkappten QD-Dünnschichten sehr informativ sein, um die Ladungsträgerbeweglichkeit in stark gekoppelten QDs zu verfolgen.

Bibliography

(1) Kovalenko, M. V.; Manna, L.; Cabot, A.; Hens, Z.; Talapin, D. V.; Kagan, C. R.; Klimov, V. I.; Rogach, A. L.; Reiss, P.; Milliron, D. J.; Guyot-Sionnnest, P.; Konstantatos, G.; Parak, W. J.; Hyeon, T.; Korgel, B. A.; Murray, C. B.; Heiss, W. Prospects of Nanoscience with Nanocrystals. *ACS Nano* 2015, *9* (2), 1012-1057.

(2) Odom, T. W. Colours at the nanoscale: Printable stained glass. *Nat. Nanotechnol* 2012, *7* (9), 550-551.

(3) Bawendi, M. G.; Steigerwald, M. L.; Brus, L. E. The Quantum-Mechanics of Larger Semiconductor Clusters (Quantum Dots). *Annu. Rev. Phys. Chem.* 1990, *41*, 477-496.

(4) Ekimov, A. I.; Efros, A. L.; Onushchenko, A. A. Quantum Size Effect in Semiconductor Microcrystals. *Solid State Commun.* 1985, *56* (11), 921-924.

(5) Efros, A. L.; Efros, A. L. Interband Absorption of Light in a Semiconductor Sphere. *Soviet physics. Semiconductors.* 1982, *16* (7), 772-775.

(6) Itoh, T.; Kirihara, T. Excitons in CuCl Microcrystals Embedded in NaCl. *J. Lumin.* 1984, *31-2* (Dec), 120-122.

(7) Brus, L. Electronic Wave-Functions in Semiconductor Clusters - Experiment and Theory. *J. Phys. Chem.* 1986, *90* (12), 2555-2560.

(8) Murray, C. B.; Norris, D. J.; Bawendi, M. G. Synthesis and characterization of nearly monodisperse CdE (E = sulfur, selenium, tellurium) semiconductor nanocrystallites. *J. Am. Chem. Soc.* 1993, *115* (19), 8706-8715.

(9) Shu, Y.; Lin, X.; Qin, H.; Hu, Z.; Jin, Y.; Peng, X. Quantum Dots for Display Applications. *Angew. Chem.* 2020, *59* (50), 22312-22323.

(10) Singh, V.; Priyanka; More, P. V.; Hemmer, E.; Mishra, Y. K.; Khanna, P. K. Magic-sized CdSe nanoclusters: a review on synthesis, properties and white light potential. *Mater. Adv.* 2021, *2* (4), 1204-1228.

(11) Shirasaki, Y.; Supran, G. J.; Bawendi, M. G.; Bulovic, V. Emergence of colloidal quantum-dot light-emitting technologies. *Nat. Photonics* 2013, *7* (1), 13-23.

(12) Zhou, J.; Liu, Y.; Tang, J.; Tang, W. H. Surface ligands engineering of semiconductor quantum dots for chemosensory and biological applications. *Mater. Today* 2017, *20* (7), 360-376.

(13) Silvi, S.; Credi, A. Luminescent sensors based on quantum dot–molecule conjugates. *Chem. Soc. Rev.* 2015, *44* (13), 4275-4289.

(14) Xiang, X. L.; Wang, L. X.; Zhang, J. J.; Cheng, B.; Yu, J. G.; Macyk, W. Cadmium Chalcogenide (CdS, CdSe, CdTe) Quantum Dots for Solar-to-Fuel Conversion. *Adv. Photonics Res.* 2022, *3* (11).

(15) Li, X. B.; Tung, C. H.; Wu, L. Z. Semiconducting quantum dots for artificial photosynthesis. *Nat. Rev. Chem.* 2018, *2* (8), 160-173.

(16) Holmes, M. A.; Townsend, T. K.; Osterloh, F. E. Quantum confinement controlled photocatalytic water splitting by suspended CdSe nanocrystals. *Chem. Commun.* 2012, *48* (3), 371-373.

(17) Chang, J.; Waclawik, E. R. Colloidal semiconductor nanocrystals: controlled synthesis and surface chemistry in organic media. *RSC Adv.* 2014, *4* (45), 23505-23527.

(18) Yin, Y.; Alivisatos, A. P. Colloidal nanocrystal synthesis and the organic-inorganic interface. *Nature* 2005, *437* (7059), 664-670.

(19) Peterson, M. D.; Cass, L. C.; Harris, R. D.; Edme, K.; Sung, K.; Weiss, E. A. The Role of Ligands in Determining the Exciton Relaxation Dynamics in Semiconductor Quantum Dots. *Annu. Rev. Phys. Chem.* 2014, *65*, 317-339.

(20) Lim, S. J.; Ma, L.; Schleife, A.; Smith, A. M. Quantum dot surface engineering: Toward inert fluorophores with compact size and bright, stable emission. *Coord. Chem. Rev.* 2016, *320*, 216-237.

(21) Hartley, C. L.; Kessler, M. L.; Dempsey, J. L. Molecular-Level Insight into Semiconductor Nanocrystal Surfaces. *J. Am. Chem. Soc.* 2021, *143* (3), 1251-1266.

(22) Chen, Y. J.; Yu, S.; Fan, X. B.; Wu, L. Z.; Zhou, Y. Mechanistic insights into the influence of surface ligands on quantum dots for photocatalysis. *J. Mater. Chem. A* 2023, *11* (16), 8497-8514.

(23) Jin, L.; Zhao, H. G.; Wang, Z. M. M.; Rosei, F. Quantum Dots-Based Photoelectrochemical Hydrogen Evolution from Water Splitting. *Adv. Energy Mater.* 2021, *11* (12), 2003233.

(24) Wu, K. F.; Lian, T. Q. Quantum confined colloidal nanorod heterostructures for solar-to-fuel conversion. *Chem. Soc. Rev.* 2016, *45* (14), 3781-3810.

(25) Kirmam, A. R.; Luther, J. M.; Abolhasani, M.; Amassian, A. Colloidal Quantum Dot Photovoltaics: Current Progress and Path to Gigawatt Scale Enabled by Smart Manufacturing. *ACS Energy Lett* 2020, *5* (9), 3069-3100.

(26) Klimov, V. I. Mechanisms for photogeneration and recombination of multiexcitons in semiconductor nanocrystals: Implications for lasing and solar energy conversion. *J. Phys. Chem. B* 2006, *110* (34), 16827-16845.

(27) Beard, M. C. Multiple Exciton Generation in Semiconductor Quantum Dots. *J. Phys. Chem. Lett.* 2011, *2* (11), 1282-1288.

(28) Leatherdale, C. A.; Woo, W. K.; Mikulec, F. V.; Bawendi, M. G. On the absorption cross section of CdSe nanocrystal quantum dots. *J. Phys. Chem. B* 2002, *106* (31), 7619-7622.

(29) Lenngren, N.; Garting, T.; Zheng, K. B.; Abdellah, M.; Lascoux, N.; Ma, F.; Yartsev, A.; Zídek, K.; Pullerits, T. Multiexciton Absorption Cross Sections of CdSe Quantum Dots Determined by Ultrafast Spectroscopy. *J. Phys. Chem. Lett.* 2013, *4* (19), 3330-3336.

(30) Ahn, N.; Livache, C.; Pinchetti, V.; Klimov, V. I. Colloidal Semiconductor Nanocrystal Lasers and Laser Diodes. *Chem. Rev.* 2023, *123* (13), 8251-8296.

(31) Zhu, H. M.; Yang, Y.; Lian, T. Q. Multiexciton Annihilation and Dissociation in Quantum Confined Semiconductor Nanocrystals. *Acc. Chem. Res* 2013, *46* (6), 1270-1279.

(32) Ben-Shahar, Y.; Philbin, J. P.; Scotognella, F.; Ganzer, L.; Cerullo, G.; Rabani, E.; Banin, U. Charge Carrier Dynamics in Photocatalytic Hybrid Semiconductor-Metal Nanorods: Crossover from Auger Recombination to Charge Transfer. *Nano Lett.* 2018, *18* (8), 5211-5216.

(33) Liu, Y. W.; Cullen, D. A.; Lian, T. Q. Slow Auger Recombination of Trapped Excitons Enables Efficient Multiple Electron Transfer in CdS-Pt Nanorod Heterostructures. *J. Am. Chem. Soc.* 2021, *143* (48), 20264-20273.

(34) García-Santamaría, F.; Chen, Y. F.; Vela, J.; Schaller, R. D.; Hollingsworth, J. A.; Klimov, V. I. Suppressed Auger Recombination in "Giant" Nanocrystals Boosts Optical Gain Performance. *Nano Lett.* 2009, *9* (10), 3482-3488.

(35) Melnychuk, C.; Guyot-Sionnest, P. Multicarrier Dynamics in Quantum Dots. *Chem. Rev.* 2021, *121* (4), 2325-2372.

(36) Klimov, V. I.; McGuire, J. A.; Schaller, R. D.; Rupasov, V. I. Scaling of multiexciton lifetimes in semiconductor nanocrystals. *Phys. Rev. B* 2008, *77* (19).

(37) Klimov, V. I.; Mikhailovsky, A. A.; McBranch, D. W.; Leatherdale, C. A.; Bawendi, M. G. Quantization of multiparticle Auger rates in semiconductor quantum dots. *Science* 2000, *287* (5455), 1011-1013.

(38) Norris, D. J.; Bawendi, M. G. Measurement and assignment of the size-dependent optical spectrum in CdSe quantum dots. *Phys. Rev. B* 1996, *53* (24), 16338-16346.

(39) Pietryga, J. M.; Park, Y. S.; Lim, J. H.; Fidler, A. F.; Bae, W. K.; Brovelli, S.; Klimov, V. I. Spectroscopic and Device Aspects of Nanocrystal Quantum Dots. *Chem. Rev.* 2016, *116* (18), 10513-10622.

(40) Efros, A. L.; Rosen, M. The electronic structure of semiconductor nanocrystals. *Annu. Rev. Mater. Res.* 2000, *30*, 475-521.

(41) Kong, D. G.; Jia, Y. Y.; Ren, Y. P.; Xie, Z. X.; Wu, K. F.; Lian, T. Q. Shell-Thickness-Dependent Biexciton Lifetime in Type I and Quasi-Type II CdSe@CdS Core/Shell Quantum Dots. *J. Phys. Chem. C* 2018, *122* (25), 14091-14098.

(42) Micheel, M.; Baruah, R.; Kumar, K.; Wächtler, M. Assembly, Properties, and Application of Ordered Group II-VI and IV-VI Colloidal Semiconductor Nanoparticle Films. *Adv. Mater. Interfaces* 2022, *9* (28).

(43) Boles, M. A.; Engel, M.; Talapin, D. V. Self-Assembly of Colloidal Nanocrystals: From Intricate Structures to Functional Materials. *Chem. Rev.* 2016, *116* (18), 11220-11289.

(44) Chang, J.; Waclawik, E. R. Colloidal semiconductor nanocrystals: controlled synthesis and surface chemistry in organic media. *RSC Adv.* 2014, *4* (45), 23505-23527.

(45) Donegá, C. D. Synthesis and properties of colloidal heteronanocrystals. *Chem. Soc. Rev.* 2011, *40* (3), 1512-1546.

(46) Parvizian, M.; Bechter, J.; Huber, J.; Chettata, N.; De Roo, J. An Experimental Introduction to Colloidal Nanocrystals through InP and InP/ZnS Quantum Dots. *J. Chem. Educ.* 2023, *100* (4), 1613-1620.

(47) Cho, K. S.; Talapin, D. V.; Gaschler, W.; Murray, C. B. Designing PbSe nanowires and nanorings through oriented attachment of nanoparticles. *J. Am. Chem. Soc.* 2005, *127* (19), 7140-7147.

(48) Reiss, P.; Carriere, M.; Lincheneau, C.; Vaure, L.; Tamang, S. Synthesis of Semiconductor Nanocrystals, Focusing on Nontoxic and Earth-Abundant Materials. *Chem Rev* 2016, *116* (18), 10731-10819.

(49) LaMer, V. K.; Dinegar, R. H. Theory, production and mechanism of formation of monodispersed hydrosols. *J. Am. Chem. Soc.* 1950, *72* (11), 4847-4854.

(50) Sugimoto, T. Underlying mechanisms in size control of uniform nanoparticles. *J. Colloid Interface Sci* 2007, *309* (1), 106-118.

(51) Peng, X.; Wickham, J.; Alivisatos, A. P. Kinetics of II-VI and III-V Colloidal Semiconductor Nanocrystal Growth: "Focusing" of Size Distributions. *J. Am. Chem. Soc.* 1998, *120* (21), 5343-5344.

(52) Yang, Y. A.; Wu, H. M.; Williams, K. R.; Cao, Y. C. Synthesis of CdSe and CdTe nanocrystals without precursor injection. *Angew. Chem.* 2005, *44* (41), 6712-6715.

(53) Sankapal, B. R.; Salunkhe, D. B.; Majumder, S.; Dubal, D. P. Solution-processed CdS quantum dots on TiO2: light-induced electrochemical properties. *RSC Adv.* 2016, *6* (86), 83175-83184.

(54) Besson, S.; Gacoin, T.; Ricolleau, C.; Jacquiod, C.; Boilot, J. P. 3D quantum dot lattice inside mesoporous silica films. *Nano Lett.* 2002, *2* (4), 409-414.

(55) Wang, P.; Zhu, Y. H.; Yang, X. L.; Li, C. Z.; Du, H. L. Synthesis of CdSe nanoparticles into the pores of mesoporous silica microspheres. *Acta Mater.* 2008, *56* (5), 1144-1150.

(56) Wang, H. C.; Lin, S. Y.; Tang, A. C.; Singh, B. P.; Tong, H. C.; Chen, C. Y.; Lee, Y. C.; Tsai, T. L.; Liu, R. S. Mesoporous Silica Particles Integrated with All-Inorganic CsPbBr3 Perovskite Quantum-Dot Nanocomposites (MP-PQDs) with High Stability and Wide Color Gamut Used for Backlight Display. *Angew. Chem.* 2016, *55* (28), 7924-7929.

(57) Owen, J. The coordination chemistry of nanocrystal surfaces. *Science* 2015, *347* (6222), 615-616.

(58) Pearson, R. G. Hard and soft acids and bases. *J. Am. Chem. Soc.* 1963, *85* (22), 3533-3539.

(59) Green, M. The nature of quantum dot capping ligands. *J. Mater. Chem.* 2010, *20* (28), 5797-5809.

(60) Giansante, C. Surface Chemistry Control of Colloidal Quantum Dot Band Gap. *J. Phys. Chem. C* 2018, *122* (31), 18110-18116.

(61) Liu, M.; Tang, G.; Liu, Y.; Jiang, F. L. Ligand Exchange of Quantum Dots: A Thermodynamic Perspective. *J. Phys. Chem. Lett.* 2024, *15* (7), 1975-1984.

(62) Nag, A.; Kovalenko, M. V.; Lee, J. S.; Liu, W. Y.; Spokoyny, B.; Talapin, D. V. Metal-free Inorganic Ligands for Colloidal Nanocrystals: S, HS, Se, HSe, Te, HTe, TeS, OH, and NH as Surface Ligands. *J. Am. Chem. Soc.* 2011, *133* (27), 10612-10620.

(63) Smith, A. M.; Nie, S. M. Semiconductor Nanocrystals: Structure, Properties, and Band Gap Engineering. *Acc. Chem. Res* 2010, *43* (2), 190-200.

(64) Efros, A. L.; Brus, L. E. Nanocrystal Quantum Dots: From Discovery to Modern Development. *ACS Nano* 2021, *15* (4), 6192-6210.

(65) Klimov, V. I. Spectral and dynamical properties of multiexcitons in semiconductor nanocrystals. *Annu Rev Phys Chem* 2007, *58*, 635-673.

(66) Ekimov, A. I.; Hache, F.; Schanne-Klein, M. C.; Ricard, D.; Flytzanis, C.; Kudryavtsev, I. A.; Yazeva, T. V.; Rodina, A. V.; Efros, A. L. Absorption and intensity-dependent photoluminescence measurements on CdSe quantum dots: assignment of the first electronic transitions. *J. Opt. Soc. Am. B* 1993, *10* (1), 100-107.

(67) Xia, J. B. Electronic-Structures of Zero-Dimensional Quantum Wells. *Phys. Rev. B* 1989, *40* (12), 8500-8507.

(68) Samuel, B.; Mathew, S.; Anand, V. R.; Correya, A. A.; Nampoori, V. P. N.; Mujeeb, A. Surface defect assisted broad spectra emission from CdSe quantum dots for white LED application. *Mater. Res. Express* 2018, *5* (2), 025009.

(69) Hu, L.; Wu, H. Z. Influence of size and surface state emission on photoluminescence of CdSe quantum dots under UV irradiation. *J. Lumin.* 2016, *177*, 306-313.

(70) Dou, H. B.; Yuan, C. Z.; Zhu, R. X.; Li, L.; Zhang, J. H.; Weng, T. C. Impact of Surface Trap States on Electron and Energy Transfer in CdSe Quantum Dots Studied by Femtosecond Transient Absorption Spectroscopy. *Nanomaterials* 2024, *14* (1).

(71) Ye, Y.; Wang, X. L.; Ye, S.; Xu, Y. X.; Feng, Z. C.; Li, C. Charge-Transfer Dynamics Promoted by Hole Trap States in CdSe Quantum Dots-Ni

Photocatalytic System. *J. Phys. Chem. C* 2017, *121* (32), 17112-17120.

(72) Baker, D. R.; Kamat, P. V. Tuning the Emission of CdSe Quantum Dots by Controlled Trap Enhancement. *Langmuir* 2010, *26* (13), 11272-11276.

(73) Schnitzenbaumer, K. J.; Dukovic, G. Chalcogenide-Ligand Passivated CdTe Quantum Dots Can Be Treated as Core/Shell Semiconductor Nanostructures. *J. Phys. Chem. C* 2014, *118* (48), 28170-28178.

(74) Schnitzenbaumer, K. J.; Labrador, T.; Dukovic, G. Impact of Chalcogenide Ligands on Excited State Dynamics in CdSe Quantum Dots. *J. Phys. Chem. C* 2015, *119* (23), 13314-13324.

(75) Klein, M. C.; Hache, F.; Ricard, D.; Flytzanis, C. Size Dependence of Electron-Phonon Coupling in Semiconductor Nanospheres - the Case of Cdse. *Phys. Rev. B* 1990, *42* (17), 11123-11132.

(76) Poyser, C. L.; Czerniuk, T.; Akimov, A.; Diroll, B. T.; Gaulding, E. A.; Salasyuk, A. S.; Kent, A. J.; Yakovlev, D. R.; Bayer, M.; Murray, C. B. Coherent Acoustic Phonons in Colloidal Semiconductor Nanocrystal Superlattices. *ACS Nano* 2016, *10* (1), 1163-1169.

(77) Mork, A. J.; Lee, E. M. Y.; Dahod, N. S.; Willard, A. P.; Tisdale, W. A. Modulation of Low-Frequency Acoustic Vibrations in Semiconductor Nanocrystals through Choice of Surface Ligand. *J. Phys. Chem. Lett.* 2016, *7* (20), 4213-4216.

(78) Besombes, L.; Kheng, K.; Marsal, L.; Mariette, H. Acoustic phonon broadening mechanism in single quantum dot emission. *Phys. Rev. B* 2001, *63* (15).

(79) Bozyigit, D.; Yazdani, N.; Yarema, M.; Yarema, O.; Lin, W. M. M.; Volk, S.; Vuttivorakulchai, K.; Luisier, M.; Juranyi, F.; Wood, V. Soft surfaces of nanomaterials enable strong phonon interactions. *Nature* 2016, *531* (7596), 618-622.

(80) Efros, A. L.; Kharchenko, V. A.; Rosen, M. Breaking the Phonon Bottleneck in Nanometer Quantum Dots - Role of Auger-Like Processes. *Solid State Commun.* 1995, *93* (4), 281-284.

(81) Vurgaftman, I.; Singh, J. Effect of Spectral Broadening and Electron-Hole Scattering on Carrier Relaxation in Gaas Quantum Dots. *Appl. Phys. Lett.* 1994, *64* (2), 232-234.

(82) Chepic, D. I.; Efros, A. L.; Ekimov, A. I.; Vanov, M. G.; Kharchenko, V. A.; Kudriavtsev, I. A.; Yazeva, T. V. Auger Ionization of Semiconductor Quantum Drops in a Glass Matrix. *J. Lumin.* 1990, *47* (3), 113-127.

(83) Labrador, T.; Dukovic, G. Simultaneous Determination of Spectral Signatures and Decay Kinetics of Excited State Species in Semiconductor Nanocrystals Probed by Transient Absorption Spectroscopy. *J. Phys. Chem. C* 2020, *124* (15), 8439-8447.

(84) Klimov, V. I. Optical nonlinearities and ultrafast carrier dynamics in semiconductor nanocrystals. *J. Phys. Chem. B* 2000, *104* (26), 6112-6123.

(85) Philbin, J. P.; Rabani, E. Electron-Hole Correlations Govern Auger Recombination in Nanostructures. *Nano Lett.* 2018, *18* (12), 7889-7895.

(86) Vaxenburg, R.; Rodina, A.; Shabaev, A.; Lifshitz, E.; Efros, A. L. Nonradiative Auger Recombination in Semiconductor Nanocrystals. *Nano Lett.* 2015, *15* (3), 2092-2098.

(87) Klimov, V. I.; McBranch, D. W.; Leatherdale, C. A.; Bawendi, M. G. Electron and hole relaxation pathways in semiconductor quantum dots. *Phys. Rev. B* 1999, *60* (19), 13740-13749.

(88) Achermann, M.; Hollingsworth, J. A.; Klimov, V. I. Multiexcitons confined within a subexcitonic volume: Spectroscopic and dynamical signatures of neutral and charged biexcitons in ultrasmall semiconductor nanocrystals. *Phys. Rev. B* 2003, *68* (24).

(89) Utzat, H.; Shulenberger, K. E.; Achorn, O. B.; Nasilowski, M.; Sinclair, T. S.; Bawendi, M. G. Probing Linewidths and Biexciton Quantum Yields of Single Cesium Lead Halide Nanocrystals in Solution. *Nano Lett.* 2017, *17* (11), 6838-6846.

(90) Shulenberger, K. E.; Bischof, T. S.; Caram, J. R.; Utzat, H.; Coropceanu, I.; Nienhaus, L.; Bawendi, M. G. Multiexciton Lifetimes Reveal Triexciton Emission Pathway in CdSe Nanocrystals. *Nano Lett.* 2018, *18* (8), 5153-5158.

(91) Klimov, V.; Hunsche, S.; Kurz, H. Biexciton Effects in Femtosecond Nonlinear Transmission of Semiconductor Quantum Dots. *Phys. Rev. B* 1994, *50* (11), 8110-8113.

(92) Klimov, V.; Hunsche, S.; Kurz, H. Coulomb Effects in Femtosecond Nonlinear Transmission of Semiconductor Nanocrystals. *Phys. Status Solidi B* 1995, *188* (1), 259-267.

(93) Pandey, A.; Guyot-Sionnest, P. Multicarrier recombination in colloidal quantum dots. *J. Chem. Phys.* 2007, *127* (11).

(94) Melnychuk, C.; Guyot-Sionnest, P. Slow Auger Relaxation in HgTe Colloidal Quantum Dots. *J. Phys. Chem. Lett.* 2018, *9* (9), 2208-2211.

(95) Robel, I.; Gresback, R.; Kortshagen, U.; Schaller, R. D.; Klimov, V. I. Universal Size-Dependent Trend in Auger Recombination in Direct-Gap and Indirect-Gap Semiconductor Nanocrystals. *Phys. Rev. Lett.* 2009, *102* (17).

(96) Li, Y. L.; Luo, X.; Ding, T.; Lu, X.; Wu, K. F. Size- and Halide-Dependent Auger Recombination in Lead Halide Perovskite Nanocrystals. *Angew. Chem.* 2020, *59* (34), 14292-14295.

(97) Castañeda, J. A.; Nagamine, G.; Yassitepe, E.; Bonato, L. G.; Voznyy, O.; Hoogland, S.; Nogueira, A. F.; Sargent, E. H.; Cruz, C. H. B.; Padilha, L. A. Efficient Biexciton Interaction in Perovskite Quantum Dots Under Weak and Strong Confinement. *ACS Nano* 2016, *10* (9), 8603-8609.

(98) Califano, M. Suppression of Auger Recombination in Nanocrystals via Ligand-Assisted Wave Function Engineering in Reciprocal Space. *J. Phys. Chem. Lett.* 2018, *9* (8), 2098-2104.

(99) Schaller, R. D.; Klimov, V. I. Non-poissonian exciton populations in semiconductor nanocrystals via carrier multiplication. *Phys. Rev. Lett.* 2006, *96* (9).

(100) Shulenberger, K. E.; Sherman, S. J.; Jilek, M. R.; Keller, H. R.; Pellows, L. M.; Dukovic, G. Exciton and biexciton transient absorption spectra of CdSe quantum dots with varying diameters. *J. Chem. Phys.* 2024, *160* (1).

(101) Ashner, M. N.; Winslow, S. W.; Swan, J. W.; Tisdale, W. A. Markov Chain Monte Carlo Sampling for Target Analysis of Transient Absorption Spectra. *J. Phys. Chem. A* 2019, *123* (17), 3893-3902.

(102) Carbone, L.; Nobile, C.; De Giorgi, M.; Sala, F. D.; Morello, G.; Pompa, P.; Hytch, M.; Snoeck, E.; Fiore, A.; Franchini, I. R.; Nadasan, M.; Silvestre, A. F.; Chiodo, L.; Kudera, S.; Cingolani, R.; Krahne, R.; Manna, L. Synthesis and micrometer-scale assembly of colloidal CdSe/CdS nanorods prepared by a seeded growth approach. *Nano Lett.* 2007, *7* (10), 2942-2950.

(103) W. William Yu, L. Q., Wenzhuo Guo, and Xiaogang Peng. Experimental Determination of the Extinction Coefficient of CdTe, CdSe, and CdS Nanocrystals. *Chem. Mater.* 2003, *15*, 2854-2860.

(104) Schneider, C. A.; Rasband, W. S.; Eliceiri, K. W. NIH Image to ImageJ: 25 years of image analysis. *Nat Methods* 2012, *9* (7), 671-675.

(105) Kodanek, T.; Banbela, H. M.; Naskar, S.; Adel, P.; Bigall, N. C.; Dorfs, D. Phase transfer of 1-and 2-dimensional Cd-based nanocrystals. *Nanoscale* 2015, *7* (45), 19300-19309.

(106) Lin-Vien, D. C., N.B.; Fateley, W.G.; Grasselli, J.G. *The Handbook of infrared and raman characteristic frequencies of organic molecules*; Academic Press: San Diego, 1991.

(107) Navarro, D. A. G.; Watson, D. F.; Aga, D. S.; Banerjee, S. Natural Organic Matter-Mediated Phase Transfer of Quantum Dots in the Aquatic Environment. *Environ Sci Technol* 2009, *43* (3), 677-682.

(108) Mohamed, N. B. H.; Ben Brahim, N.; Mrad, R.; Haouari, M.; Ben Chaâbane, R.; Negrerie, M. Use of MPA-capped CdS quantum dots for sensitive detection and quantification of Co2+ ions in aqueous solution. *Anal. Chim. Acta* 2018, *1028*, 50-58.

(109) Brown, P. R.; Kim, D.; Lunt, R. R.; Zhao, N.; Bawendi, M. G.; Grossman, J. C.; Bulovic, V. Energy Level Modification in Lead Sulfide Quantum Dot Thin Films through Ligand Exchange. *ACS Nano* 2014, *8* (6), 5863-5872.

(110) Saviot, L.; Champagnon, B.; Duval, E.; Kudriavtsev, I. A.; Ekimov, A. I. Size dependence of acoustic and optical vibrational modes of CdSe nanocrystals in glasses. *J. Non-Cryst. Solids* 1996, *197* (2-3), 238-246.

(111) Schnitzenbaumer, K. J.; Dukovic, G. Comparison of Phonon Damping Behavior in Quantum Dots Capped with Organic and Inorganic Ligands. *Nano Lett.* 2018, *18* (6), 3667-3674.

(112) Nag, A.; Chung, D. S.; Dolzhnikov, D. S.; Dimitrijevic, N. M.; Chattopadhyay, S.; Shibata, T.; Talapin, D. V. Effect of Metal Ions on Photoluminescence, Charge Transport, Magnetic and Catalytic Properties of All-Inorganic Colloidal Nanocrystals and Nanocrystal Solids. *J. Am. Chem. Soc.* 2012, *134* (33), 13604-13615.

(113) Morgan, D. P.; Kelley, D. F. What Does the Transient Absorption Spectrum of CdSe Quantum Dots Measure? *J. Phys. Chem. C* 2020, *124* (15), 8448-8455.

(114) Liu, C. M.; Peterson, J. J.; Krauss, T. D. Uncovering Hot Hole Dynamics in CdSe Nanocrystals. *J. Phys. Chem. Lett.* 2014, *5* (17), 3032-3036.

(115) Grimaldi, G.; Geuchies, J. J.; van der Stam, W.; du Fossé, I.; Brynjarsson, B.; Kirkwood, N.; Kinge, S.; Siebbeles, L. D. A.; Houtepen, A. J. Spectroscopic Evidence for the Contribution of Holes to the Bleach of Cd-Chalcogenide Quantum Dots. *Nano Lett.* 2019, *19* (5), 3002-3010.

(116) Nozik, A. J. Spectroscopy and hot electron relaxation dynamics in semiconductor quantum wells and quantum dots. *Annu. Rev. Phys. Chem.* 2001, *52*, 193-231.

(117) Kambhampati, P. Hot Exciton Relaxation Dynamics in Semiconductor Quantum Dots: Radiationless Transitions on the Nanoscale. *J. Phys. Chem. C* 2011, *115* (45), 22089-22109.

(118) Klimov, V. I.; Mikhailovsky, A. A.; McBranch, D. W.; Leatherdale, C. A.; Bawendi, M. G. Mechanisms for intraband energy relaxation in semiconductor quantum dots: The role of electron-hole interactions. *Phys. Rev. B* 2000, *61* (20), 13349-13352.

(119) Knowles, K. E.; McArthur, E. A.; Weiss, E. A. A Multi-Timescale Map of Radiative and Nonradiative Decay Pathways for Excitons in CdSe Quantum Dots. *ACS Nano* 2011, *5* (3), 2026-2035.

(120) McArthur, E. A.; Morris-Cohen, A. J.; Knowles, K. E.; Weiss, E. A. Charge Carrier Resolved Relaxation of the First Excitonic State in CdSe Quantum Dots Probed with

Near-Infrared Transient Absorption Spectroscopy. *J. Phys. Chem. B* 2010, *114* (45), 14514-14520.

(121) Müller, C.; Pascher, T.; Eriksson, A.; Chabera, P.; Uhlig, J. KiMoPack: A python Package for Kinetic Modeling of the Chemical Mechanism. *J. Phys. Chem. A* 2022, *126* (25), 4087-4099.

(122) Sewall, S. L.; Cooney, R. R.; Dias, E. A.; Tyagi, P.; Kambhampati, P. State-resolved observation in real time of the structural dynamics of multiexcitons in semiconductor nanocrystals. *Phys. Rev. B* 2011, *84* (23).

(123) Yan, C.; Weinberg, D.; Jasrasaria, D.; Kolaczkowski, M. A.; Liu, Z. J.; Philbin, J. P.; Balan, A. D.; Liu, Y.; Schwartzberg, A. M.; Rabani, E.; Alivisatos, A. P. Uncovering the Role of Hole Traps in Promoting Hole Transfer from Multiexcitonic Quantum Dots to Molecular Acceptors. *ACS Nano* 2021, *15* (2), 2281-2291.

(124) Yang, W. X.; Yang, Y. W.; Kaledin, A. L.; He, S.; Jin, T.; McBride, J. R.; Lian, T. Q. Surface passivation extends single and biexciton lifetimes of InP quantum dots. *Chem. Sci* 2020, *11* (22), 5779-5789.

(125) Kambhampati, P. Unraveling the the Structure and Dynamics of Excitons in Semiconductor Quantum Dots. *Acc. Chem. Res* 2011, *44* (1), 1-13.

(126) Kobayashi, Y.; Tamai, N. Size-Dependent Multiexciton Spectroscopy and Moderate Temperature Dependence of Biexciton Auger Recombination in Colloidal CdTe Quantum Dots. *J. Phys. Chem. C* 2010, *114* (41), 17550-17556.

(127) Zhang, C.; Do, T. N.; Ong, X. W.; Chan, Y. T.; Tan, H. S. Understanding the features in the ultrafast transient absorption spectra of CdSe quantum dots. *Chem Phys* 2016, *481*, 157-164.

(128) Palato, S.; Seiler, H.; Baker, H.; Sonnichsen, C.; Brosseau, P.; Kambhampati, P. Investigating the electronic structure of confined multiexcitons with nonlinear spectroscopies. *J. Chem. Phys.* 2020, *152* (10).

(129) Bonati, C.; Mohamed, M. B.; Tonti, D.; Zgrablic, G.; Haacke, S.; van Mourik, F.; Chergui, M. Spectral and dynamical characterization of multiexcitons in colloidal CdSe semiconductor quantum dots. *Phys. Rev. B* 2005, *71* (20).

(130) Strandell, D. P.; Ghosh, A.; Zenatti, D.; Nagpal, P.; Kambhampati, P. Direct Observation of Higher Multiexciton Formation and Annihilation in CdSe Quantum Dots. *J. Phys. Chem. Lett.* 2023, *14* (30), 6904-6911.

(131) Sewall, S. L.; Cooney, R. R.; Anderson, K. E. H.; Dias, E. A.; Sagar, D. M.; Kambhampati, P. State-resolved studies of biexcitons and surface trapping dynamics in semiconductor quantum dots. *J. Chem. Phys.* 2008, *129* (8).

(132) Reimer, M. E.; Dalacu, D.; Poole, P. J.; Williams, R. L. Biexciton binding energy control in site-selected quantum dots. *J. Phys. Conf. Ser* 2010, *210*, 012019.

(133) Geissler, D.; Wurth, C.; Wolter, C.; Weller, H.; Resch-Genger, U. Excitation wavelength dependence of the photoluminescence quantum yield and decay behavior of CdSe/CdS quantum dot/quantum rods with different aspect ratios. *Phys. Chem. Chem. Phys.* 2017, *19* (19), 12509-12516.

(134) Crooker, S. A.; Hollingsworth, J. A.; Tretiak, S.; Klimov, V. I. Spectrally resolved dynamics of energy transfer in quantum-dot assemblies: Towards engineered energy flows in artificial materials. *Phys. Rev. Lett.* 2002, *89* (18).

(135) Kagan, C. R.; Murray, C. B.; Bawendi, M. G. Long-range resonance transfer of electronic excitations in close-packed CdSe quantum-dot solids. *Phys. Rev. B* 1996, *54* (12), 8633-8643.

(136) De Nolf, K.; Cosseddu, S. M.; Jasieniak, J. J.; Drijvers, E.; Martins, J. C.; Infante, I.; Hens, Z. Binding and Packing in Two-Component Colloidal Quantum Dot Ligand Shells: Linear versus Branched Carboxylates. *J. Am. Chem. Soc.* 2017, *139* (9), 3456-3464.

(137) Crisp, R. W.; Schrauben, J. N.; Beard, M. C.; Luther, J. M.; Johnson, J. C. Coherent Exciton Delocalization in Strongly Coupled Quantum Dot Arrays. *Nano Lett.* 2013, *13* (10), 4862-4869.

(138) Zhang, H. T.; Hu, B.; Sun, L. F.; Hovden, R.; Wise, F. W.; Muller, D. A.; Robinson, R. D. Surfactant Ligand Removal and Rational Fabrication of Inorganically Connected Quantum Dots. *Nano Lett.* 2011, *11* (12), 5356-5361.

(139) Cohen, E.; Gdor, I.; Romero, E.; Yochelis, S.; van Grondelle, R.; Paltiel, Y. Achieving Exciton Delocalization in Quantum Dot Aggregates Using Organic Linker Molecules. *J. Phys. Chem. Lett.* 2017, *8* (5), 1014-1018.

(140) Jasrasaria, D.; Philbin, J. P.; Yan, C.; Weinberg, D.; Alivisatos, A. P.; Rabani, E. Sub-Bandgap Photoinduced Transient Absorption Features in CdSe Nanostructures: The Role of Trapped Holes. *J. Phys. Chem. C* 2020, *124* (31), 17372-17378.

Appendix A

Chemicals

Trioctylphosphine oxide (TOPO, 99 %), Trioctylphosphine (TOP, 97%), Cadmium oxide (CdO, 99.99 %), Selenium (Se, 99.99 %), Sodium sulfide (Na_2S, 98%), Toluene (99.8 % anhydrous), N-methylformamide (NMF, 99%), Hexane (95% anhydrous), acetonitrile (MeCN, 99.8% anhydrous), Acetone (99.5%), 3-mercaptopropanoic acid (MPA, 99 %), 11-mercaptoundecanoic acid (MUA, 95 %), and Methanol (MeOH, 99.8 % anhydrous) were purchased from Sigma Aldrich and Octadecylphosphonic acid (ODPA, 97 %) was purchased from Carl Roth.

Experimental

Synthesis of Colloidal CdSe QDs: CdSe QDs were synthesized using a well-established hot-injection method. 60 mg of CdO, 0.28 g of ODPA and 3.0 g of TOPO were mixed in a 25 mL three-necked flask. The mixture was heated to 80 °C under an N_2 atmosphere with stirring until melting and then vacuum was applied, causing bubbles to form in the reaction mixture. When bubble formation stopped, the vacuum was broken with N_2 flow, and the mixture was heated to 150 °C and evacuated again for 1 hour. After that the vacuum was broken with N_2 flow and the temperature was raised to 380 °C. The mixture becomes optically clear and colourless at around 300 °C. At 320 °C, 1.5 g of TOP was injected into the mixture. When the temperature reached 380 °C, a solution of TOP:Se (0.058 g Se dissolved in 0.36 g TOP) was injected and the reaction mixture was immediately cooled by removing the heating mantle. To speed up the cooling of the reaction mixture, a bucket of cold water was used to immerse the flask while it was in the Schlenk line. At 60 °C, 10 mL of toluene was injected into the mixture. After synthesis, 10 mL of methanol was added to the reaction mixture to precipitate the QDs, followed by centrifugation at 5300 rpm. The precipitate was redispersed in toluene and the same step was repeated three more times for purification. Finally, the QDs were dispersed in 10 mL of toluene and stored in the glove box.

Injecting TOP:Se at 380 °C yielded 2.4 nm and 2.6 nm QDs. To synthesize 3.4 nm QDs, TOP:Se was injected at 370 °C and the reaction mixture was cooled immediately by removing the heating mantle. To synthesize the larger QDs, TOP:Se was injected at 370 °C and, instead of immediate cooling, the reaction mixture was held at 370 °C for 3 min (for 4 nm), 5 min (for 4.8 nm) and 1 h (for 8.2 nm). The purification process for all the QDs was same as described above.

MPA & MUA Ligand exchange: Sulfide ligand exchange was performed using a biphasic method. For this, 500 μL of QD solution was precipitated with 500 μL of MeOH followed by centrifugation at 5300 rpm for 10 min. The supernatant was discarded, and the precipitate was redispersed in 500 μL of hexane. Separately, a 0.2 M 500 μL methanolic solution of MPA/MUA was prepared. To this solution a methanolic solution of 0.2 M 500 μL KOH was added. The final 1 mL of MPA/MUA solution was carefully added to the QD solution in hexane. At this moment, the methanol phase is transparent, and the hexane phase shows the QD colour. This solution was stirred for 12 hrs. After the ligand exchange reaction was completed, the hexane phase looked transparent while the methanol phase with the QD colour. To this solution 2 mL of hexane was added to increase the transparent phase, which was then removed. The remaining methanol phase was centrifuged at 5300 rpm for 10 min. The supernatant was discarded, and the precipitate was redispersed in 0.1 M 1 mL aqueous solution of KOH. To this solution 2 mL of chloroform was added. The chloroform phase was removed after 5 min and the remaining QD solution was centrifuged at 5300 rpm for 10 min. After this step of centrifugation, the QD is left in the supernatant, and some white powders were precipitated. The QD solution was carefully taken out and stored in the glove box.

S^{2-} Ligand exchange: Sulfide ligand exchange was performed using a biphasic method. For this, 1 mL of QD solution was precipitated with 1 mL of MeOH followed by centrifugation at 5300 rpm for 10 min. The supernatant was discarded, and the precipitate was redispersed in 1 mL of hexane. Then 1 mL of Na_2S (1M, NMF) solution was added to the QD solution in hexane and two separate phases of NMF (transparent) and hexane (QD colour) were observed. It was then stirred for 2 hours. After 2 hours, it was clearly observed that the QDs were transferred to the NMF phase, indicating a successful ligand exchange. The clear hexane phase was removed. Next, 2 mL of hexane was added to the QD solution, which was again removed after 5 minutes of

stirring. Then 2 mL MeCN was added to precipitate the QDs in NMF, followed by centrifugation at 5300 rpm for 10 min. Finally, the QDs were dispersed in 1 mL NMF.

Thin film fabrication: QD thin films were prepared via drop-casting. The deposition was carried out on glass substrates for spectroscopic measurements, silicon wafers for SEM, and on CaF_2 substrates to record IR spectra. The substrates were cleaned for 20 min in an ultrasonic bath in methanol. Subsequently, the substrates were treated for 20 min in an ultrasonic bath in 2% aqueous Hellmanex solution. After washing twice with distilled water (each time for 20 min in the ultrasonic bath), the substrates were dried and stored in a glovebox under an inert atmosphere. 40 µL of QD solution was drop casted on the substrates inside glove box and kept until the solvents are (toluene for TOPO capped QDs, NMF for S^{2-} capped QDs) evaporated. Then the substrates were kept under vacuum for 5 min (for the QDs in toluene), and 30 min (for the QDs in NMF) for a complete removal of solvents.

UV-vis absorption spectroscopy: Steady state UV-vis absorption spectra were collected in a Jasco V-600 spectrophotometer in the wavelength range from 200 nm to 800 nm. A 1 cm quartz cuvettes were used for QD solutions. Steady state UV-vis absorption spectra of the QD films were collected in transmission mode using a thin film holder in a Jasco V-600 spectrophotometer in the wavelength range from 200 nm to 800 nm. The absorption spectra of QD films shows strong wavelength dependent scattering which was corrected by fitting a polynomial background function as described in Figure A 20.

Photoluminescence spectroscopy: Photoluminescence spectra of QD solutions, prepared in 1 cm quartz cuvettes, was performed using a FLS 980 Edinburgh Fluorimeter with 400 nm excitation wavelength. Photoluminescence spectra of QD films were collected in Horiba Fluorolog 3 with 400 nm excitation wavelength.

Transmission Electron Microscopy (TEM): Colloidal QDs were deposited on a carbon-coated Cu grid (purchased from Plano GmbH) followed by vacuum drying. Transmission electron microscopy (TEM) images were recorded in conventional (TEM) and scanning mode (STEM) using a JEM-ARM200F NEOARM (Jeol) operating at 80 kV, equipped with a spherical aberration corrector, brightfield (BF), annular bright-field (ABF), and annular dark-field (ADF) detectors. To process the

TEM images to determine QD size and size distribution, imageJ 1.53A program was used.

Scanning electron microscopy (SEM): SEM images of QD films were collected using a dual-beam HELIOS NanoLab G3 UC scanning electron microscope. To collect SEM images, 40 µL of QD solutions were deposited on silicon wafer via drop casting.

Fourier Transformed Infrared Spectroscopy (FTIR): FTIR spectra were collected in a Brucker Tensor 27 spectrometer on attenuated total reflection (ATR) mode. To do this, colloidal QD solutions were drop casted on CaF_2 substrates.

Raman Spectroscopy: Raman spectra of QDs were collected by using a 808 nm laser source from Ondax coupled with a microscope stage. A volume holographic notch filter with 5 cm−1 cut was used to cut the Reyleigh line so that low wavenumber region can be probed. A WiTec UHTS Raman spectrometer was used to collect the Raman spectra. The colloidal QDs were drop casted on CaF2 substrates to perform Raman spectroscopy.

Transient absorption spectroscopy (TA): TA spectroscopy was conducted using a 1 kHz Ti:sapphire laser (Astrella, Coherent, USA) with an output pulse of approximately 100 fs temporal width at 800 nm central wavelength. The fundamental beam was divided into two portions, one to generate a 400 nm probe pulse through an optical parametric amplifier (TOPAS, Light Conversion, Lithuania) and the other to focus the beam into a rotating CaF_2 crystal to generate a spectrally broad probe pulse (white light). The beam generating the probe pulse travels through an optical delay line that can move up to 2 ns. To exclude anisotropic signal, relative polarization of the pump and probe was set to the magic angle, 54.7°. For the measurements, the repetition rate of the pump pulse was reduced to 500 Hz using a mechanical chopper. The detection system consisted of a Czerny-Turner spectrograph and a CCD detector. To remove the pump scattering, a 405 nm long pass filter was used before the detector. The pump power was varied by a rotating neutral density filter wheel (ThorLab) and measured by a power meter. Five power points varied from 15 µW to 1500 µW were recorded for each sample. The Gaussian profile of the pump beam was recorded using a beam profiler to estimate the area. The pump power density (intensity) is determined by dividing the power by the respective area. 1 mm quartz inert cuvettes were used for the QD solutions and for thin films an inert thin film holder was used with constant N_2 flow.

The chirp correction of the TA data was done using a Python-based package, KiMoPack. The chirp-corrected data was then cut to the window of 2 ps to 1900 ps and 430 nm to 700 nm to perform Markov Chain Monte Carlo fitting.

Appendix B

Supporting information for 'Post-synthetic Modification of Colloidal CdSe QDs: Investigation of Photoluminescence and Phonon Properties'

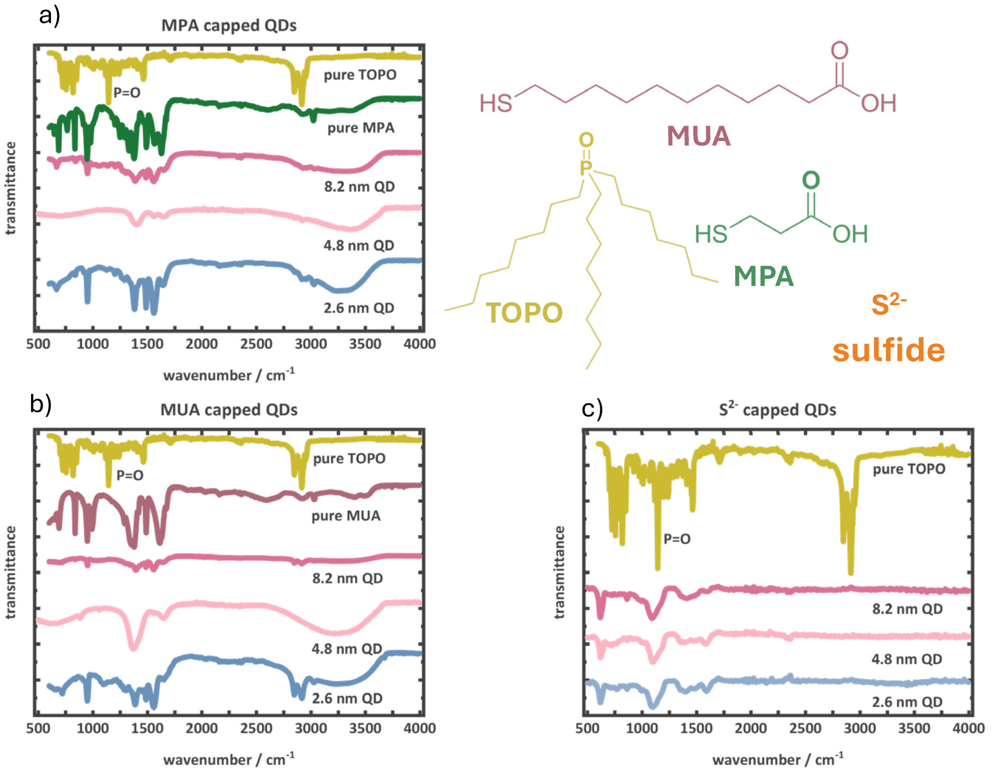

Figure A 1: *FT-IR spectra of 2.4 nm, 4.8 nm, and 8.2 nm QDs capped with (a) MPA, (b) MUA, and (c)* S^{2-}*. Along with the IR spectra of QDs, pure ligand spectra are also plotted. The P=O band vibration in pure TOPO spectra is specially marked in all the panels to indicate the efficient removal of TOPO ligands.*

The TOPO ligand has the characteristic, P=O stretching at 1092 cm^{-1}, $-CH_2$ asymmetric stretching at 2924 cm^{-1}, $-CH_3$ asymmetric stretching at 2950 cm^{-1}, and P–C stretching at 694 cm^{-1}. The P=O stretching of TOPO appears at 1143 cm^{-1} while bound to the QD surface. Figure A 1a shows the FT-IR spectra of the MPA capped QDs in comparison with pure TOPO and pure MPA. The MPA ligands shows characteristic vibration of –OH stretching ranging from 3300 – 3600 cm^{-1}, C=O asymmetric stretching at 1630 cm^{-1}, and a broad S–H stretching band at 2557 cm^{-1}. Upon MPA ligand exchange, the P=O stretching (of TOPO) has vanished in the FT-IR spectra indicating an efficient removal of TOPO ligands. The FT-IR spectra (Figure A 1a) of the QDs, exhibits the O–H stretching, C=O stretching (shifted to 1557 cm^{-1}) indicating the presence of MPA. On the other hand, the S–H stretching band (of MPA) disappears in the QD spectra indicating the presence of MPA on the QD surface as MPA passivates the QD surface as thiolate (–S^{-}). Figure A 1b shows the FT-IR spectra of the MUA capped QDs in comparison with pure TOPO and pure MUA. The MUA ligands show characteristic vibration of –OH stretching ranging from 3300 – 3600 cm^{-1}, C=O asymmetric stretching at 1771 cm^{-1}, and a broad S–H stretching band at 2551 cm^{-1}. Upon MUA ligand exchange, the P=O stretching (of TOPO) has vanished in the FT-IR spectra indicating an efficient removal of TOPO ligands. The FT-IR spectra (Figure A 1b) of the QDs, exhibits the O–H stretching, C=O stretching (shifted to 1551 cm^{-1}) indicating the presence of MUA. Similar to the MPA QDs, in MUA capped QD FT-IR spectra, the S–H band vanishes indicating the passivation of MUA on QD surface. Figure A 1c shows the FT-IR spectra of the S^{2-} capped QDs in comparison with pure TOPO. In the FT-IR spectra of the S^{2-} capped QDs, no vibration band is expected in the range of 500 cm^{-1} – 4000 cm^{-1}. However, in the window of 500 cm^{-1} – 1700 cm^{-1}, a few vibration bands are present in the QD spectra. These bands are originated from the residual NMF in the QDs (the S^{2-} capped QDs were dispersed in NMF, which has a high boiling point, hence complete removal of the solvent is challenging). All the vibration bands have been assigned according to previously reported literatures.

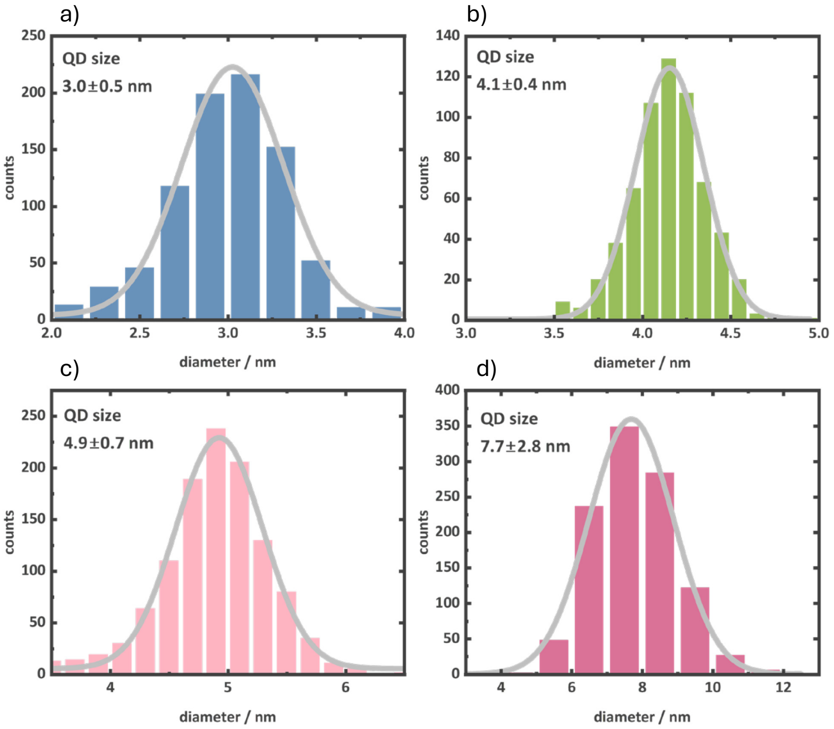

***Figure A 2:** Size distribution of the QDs obtained from TEM analysis.*

Appendix C

Supporting information for 'Determination of High-order Multiexciton Properties by Transient Absorption Spectroscopy'

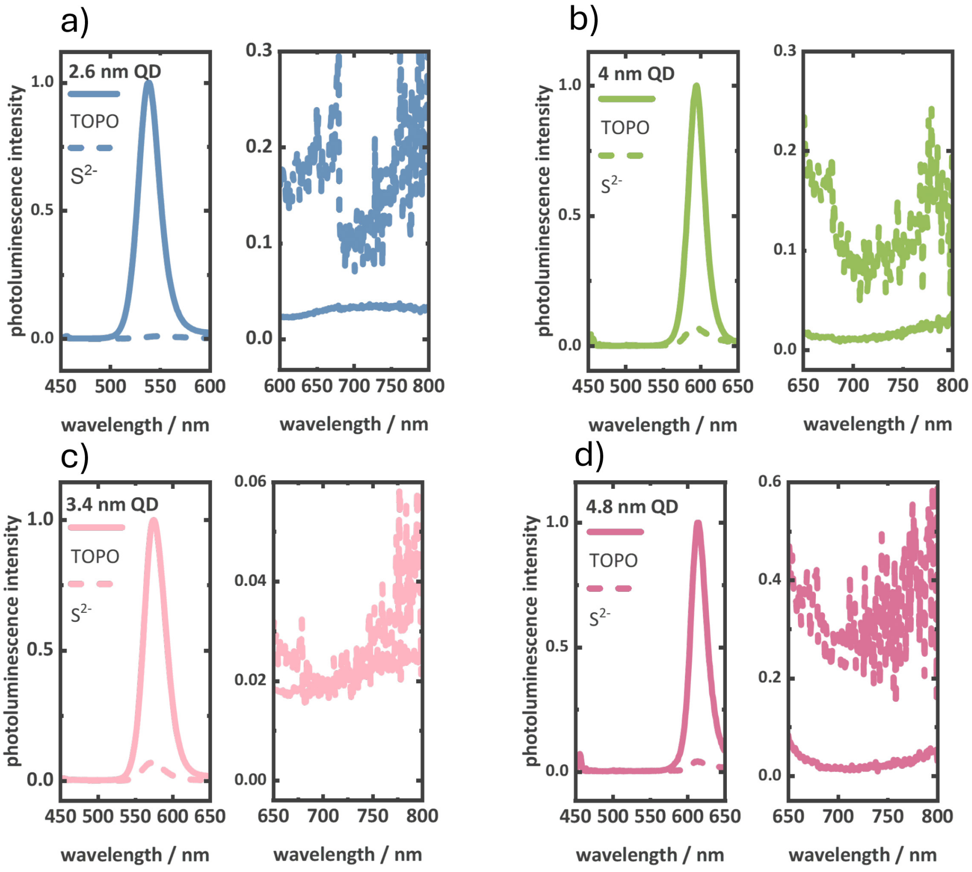

Figure A 3: *Photoluminescence spectra of (a) 2.6 nm, (b) 3.4 nm, (c) 4 nm and (d) 4.8 nm, TOPO capped and S^{2-} capped QDs. In each of the figures, the left panel represents the band-edge photoluminescence, and the right panel represents the trap-state photoluminescence. Band-edge photoluminescence spectra are corrected by the respective absorbance at excitation wavelength (λ_{ex} 400 nm). Trap-state photoluminescence spectra are plotted while normalizing at the band-edge peak maxima. The photoluminescence spectra indicate strong surface hole trapping resulting in band-edge photoluminescence quenching and enhancement of trap-state emission (detailed description Chapter 3).*

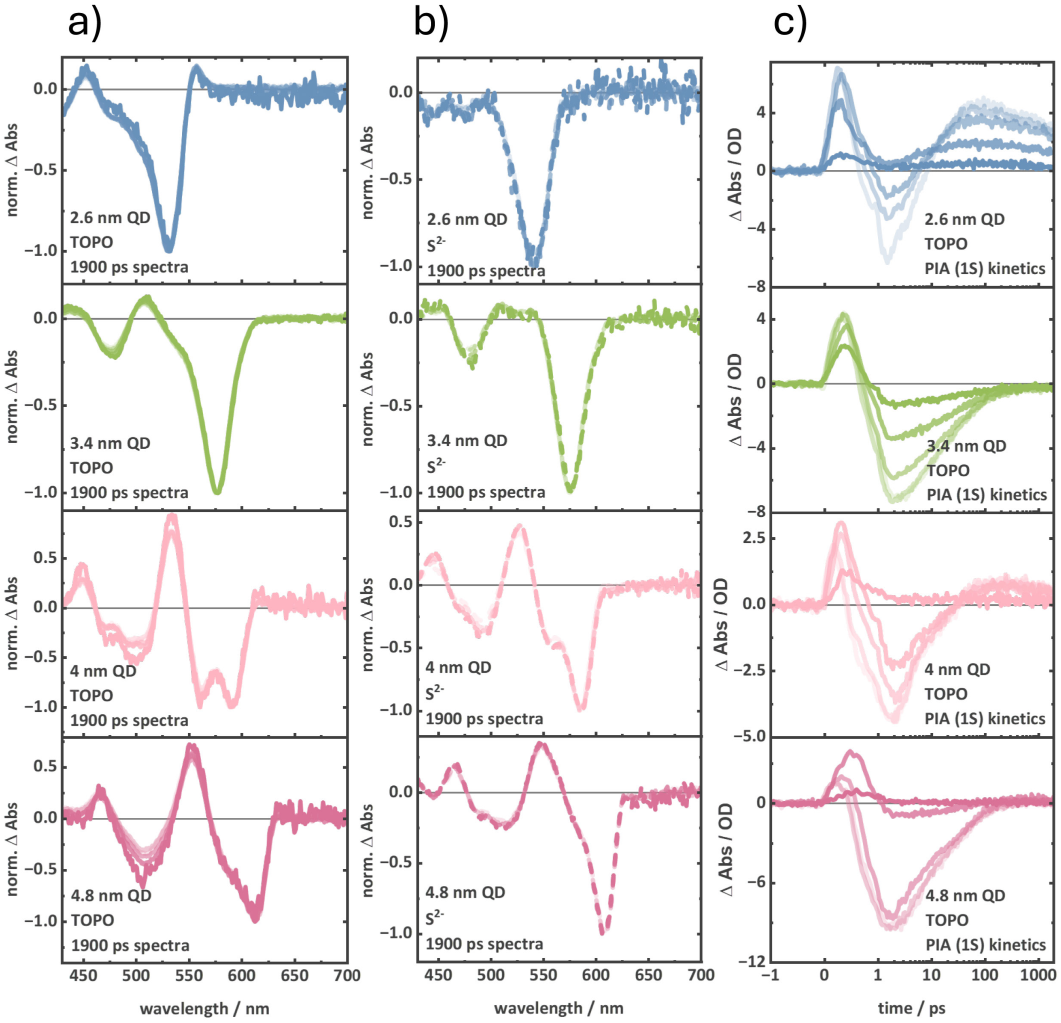

Figure A 4: *Intensity-dependent TA spectra (normalized at* B_1 *bleach) of (a) TOPO capped and, (b)* S^{2-} *capped QDs at 1900 ps. (c) Kinetics of* A_1 *feature of TOPO capped QDs. The* A_1 *features are centered at 557 nm for 2.6 nm QD, 590 nm for 3.4 nm QD, 616 nm for 4.0 nm QD and 636 nm for 4.8 nm QD.*

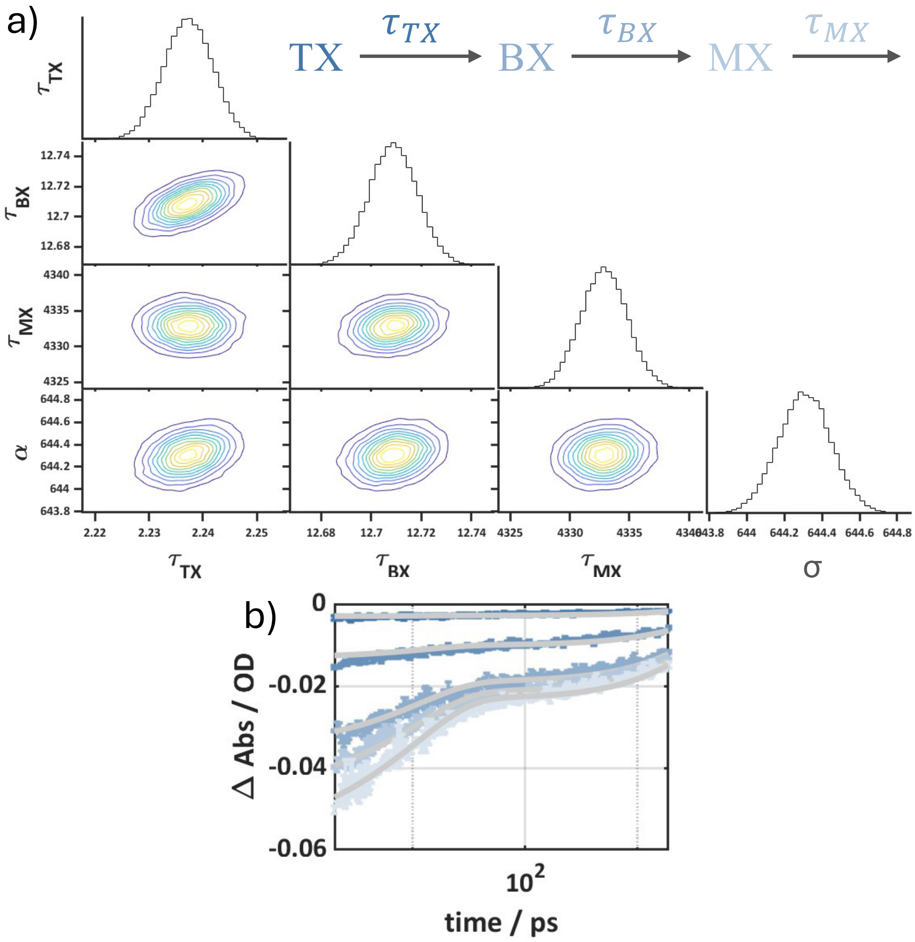

Figure A 5: *TX model was used for MCMC fitting of 2.6 nm TOPO capped QD. (a) Contour plot representing the fit parameters obtained from MCMC. (b) Intensity dependent kinetics of B_1 bleach with the fit (grey lines).*

Table A 1: *Intensities used for MCMC fitting of TOPO capped 2.6 nm QD and < N >, σ and, α obtained from MCMC fitting.*

Intensity $\mu W \mu m^{-2}$	**< *N* >**	***σ*** $\mu W^{-1} \mu m^{2}$	***α*** cm^{2}
0.0002	0.1	644.1	1.6×10^{-15}
0.0008	0.5		
0.0024	1.5		
0.0033	2.1		
0.0047	3.0		

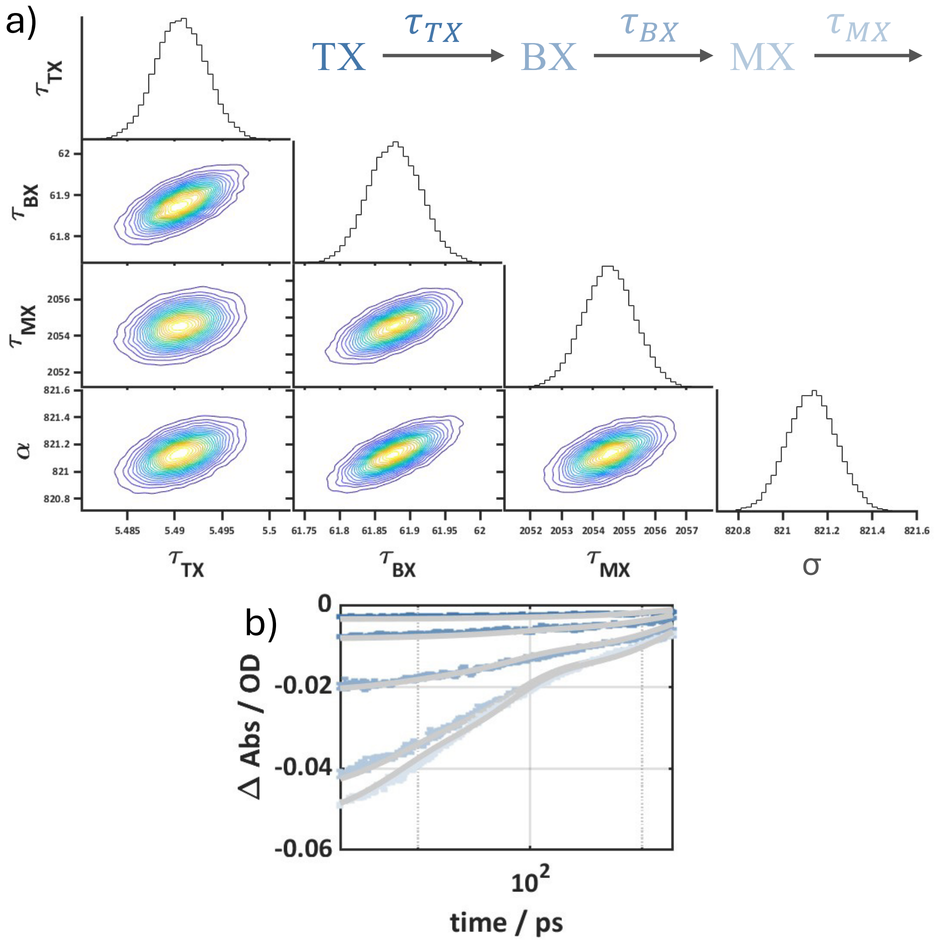

Figure A 6: *TX model was used for MCMC fitting of 2.6 nm* S^{2-}*capped QD. (a) Contour plot representing the fit parameters obtained from MCMC. (b) Intensity dependent kinetics of* B_1 *bleach with the fit (grey lines).*

Table A 2: *Intensities used for MCMC fitting of* S^{2-}*capped 2.6 nm QD and* $< N >$*, σ and, α obtained from MCMC fitting.*

Intensity **µWµm^{-2}**	$< N >$	**σ** **µW^{-1}µm^{2}**	**α** **cm^{2}**
0.0003	0.2	821.1	2.0×10^{-15}
0.0006	0.5		
0.0015	1.2		
0.0040	3.3		
0.0059	4.8		

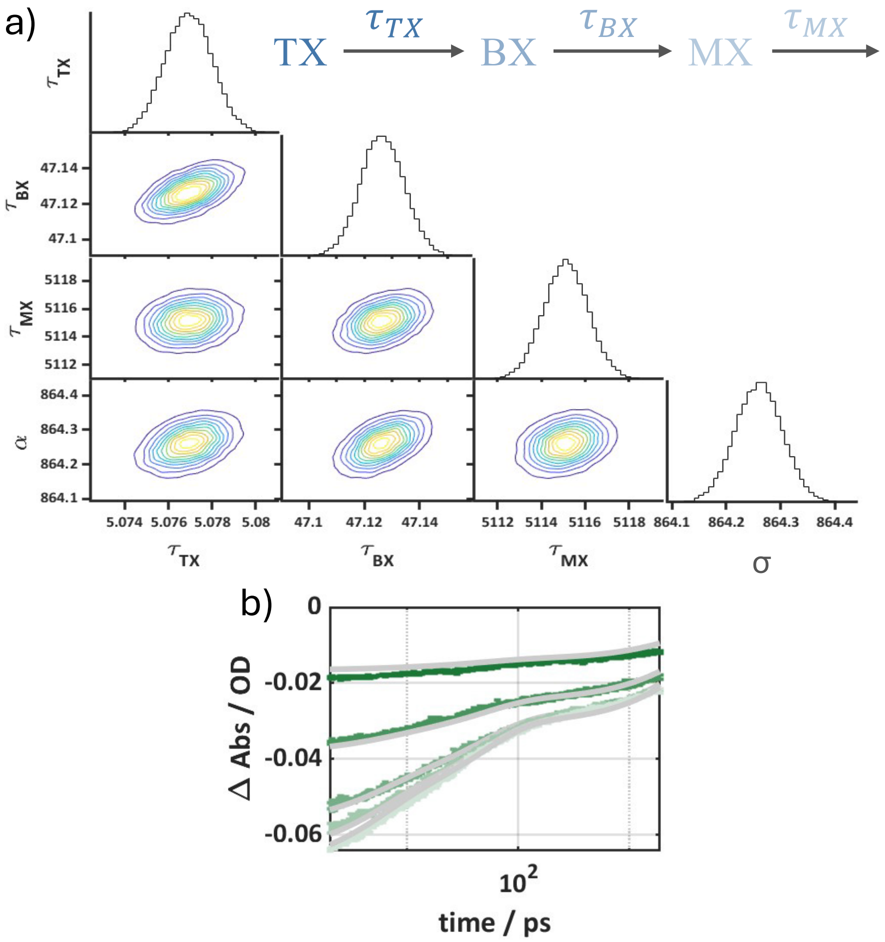

Figure A 7: *TX model was used for MCMC fitting of 3.4 nm TOPO capped QD. (a) Contour plot representing the fit parameters obtained from MCMC. (b) Intensity dependent kinetics of* B_1 *bleach with the fit (grey lines).*

Table A 3: *Intensities used for MCMC fitting of TOPO capped 3.4 nm QD and* $< N >$, *σ and, α obtained from MCMC fitting.*

Intensity $\mu W \mu m^{-2}$	$< N >$	**σ $\mu W^{-1} \mu m^{2}$**	**α cm^{2}**
0.0007	0.6	864.3	2.2×10^{-15}
0.0019	1.6		
0.0037	3.1		
0.0053	4.5		
0.0073	6.3		

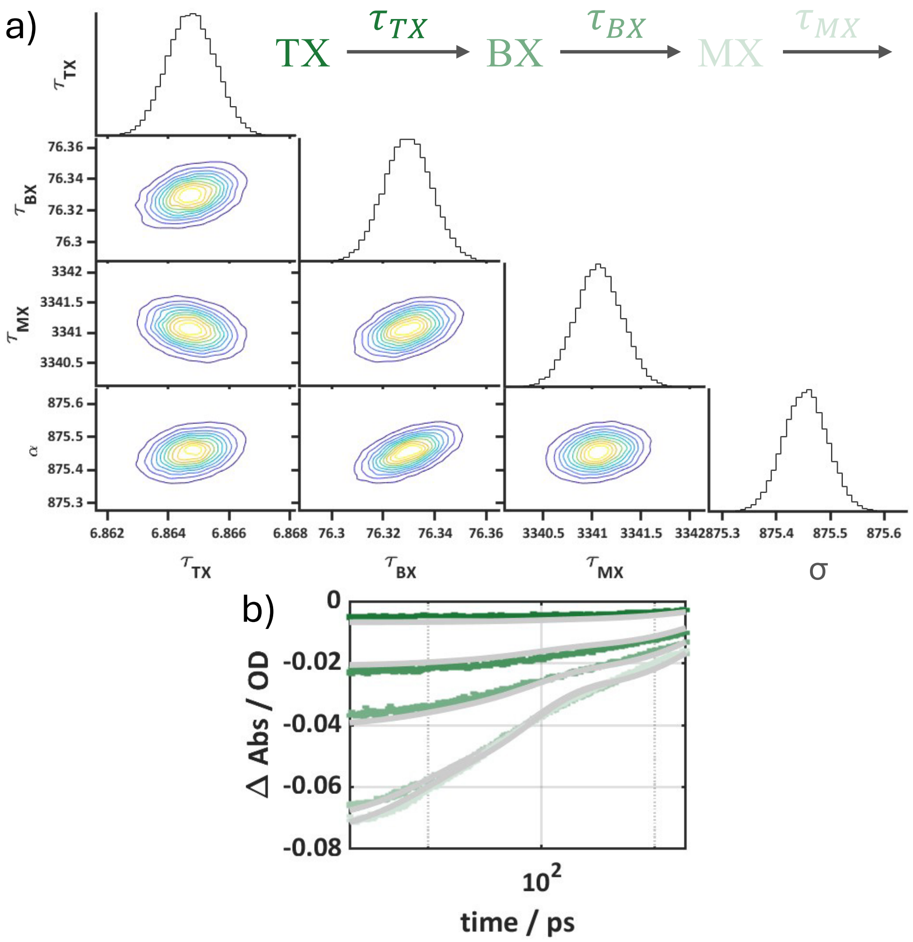

Figure A 8: *TX model was used for MCMC fitting of 3.4 nm S^{2-}capped QD. (a) Contour plot representing the fit parameters obtained from MCMC. (b) Intensity dependent kinetics of B_1 bleach with the fit (grey lines).*

Table A 4: *Intensities used for MCMC fitting of S^{2-}capped 3.4 nm QD and < N >, σ and, α obtained from MCMC fitting.*

Intensity **μWμm^{-2}**	**< *N* >**	***σ*** **μW^{-1}μm^2**	***α*** **cm^2**
0.0003	0.2	875.5	2.2×10^{-15}
0.0009	0.7		
0.0018	1.6		
0.0050	4.4		
0.0072	6.3		

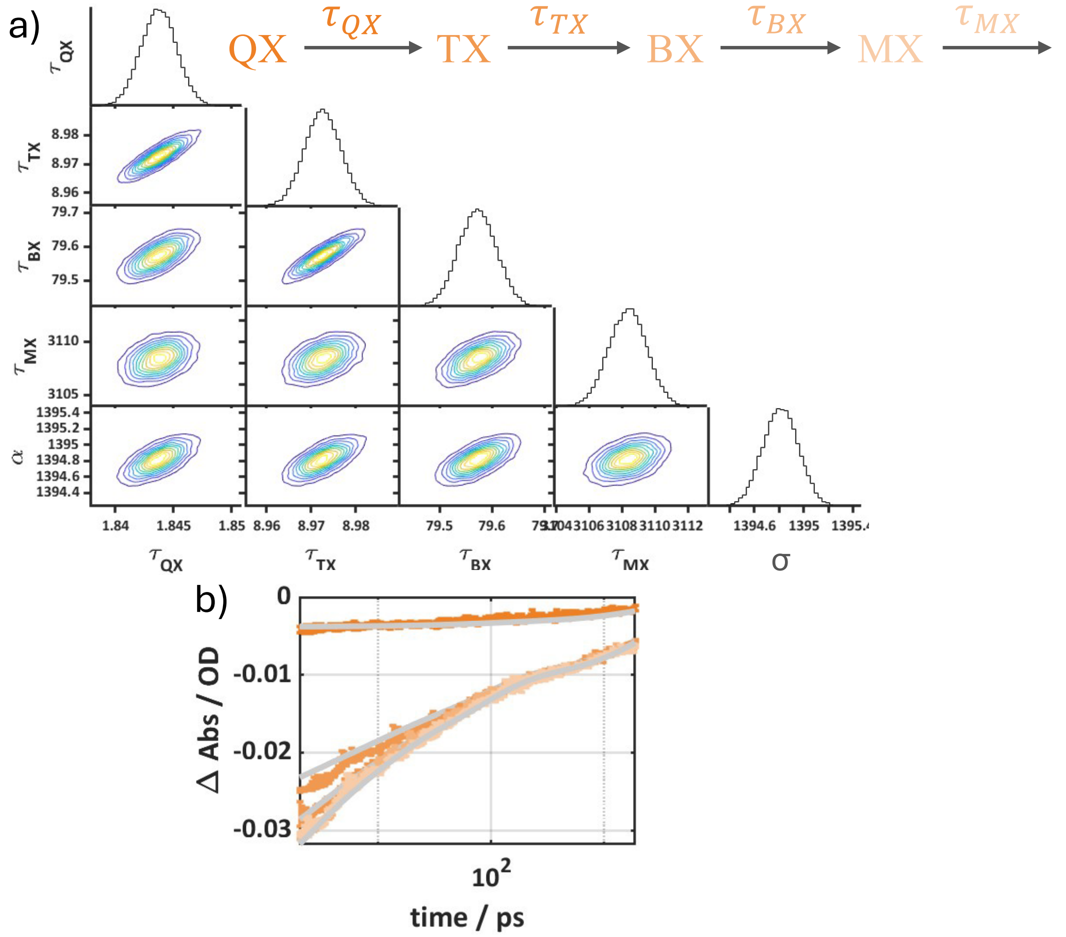

Figure A 9: *QX model was used for MCMC fitting of 4.0 nm TOPO capped QD. (a) Contour plot representing the fit parameters obtained from MCMC. (b) Intensity dependent kinetics of* B_1 *bleach with the fit (grey lines).*

Table A 5: *Intensities used for MCMC fitting of TOPO capped 4.0 nm QD and < N >, σ and, α obtained from MCMC fitting.*

Intensity **μWμm^{-2}**	**< *N* >**	***σ*** **μW^{-1}μm^2**	***α*** **cm^2**
0.0003	0.4	1394.8	3.5 × 10^{-15}
0.0022	3.0		
0.0034	4.7		
0.0054	7.5		
0.0062	8.6		

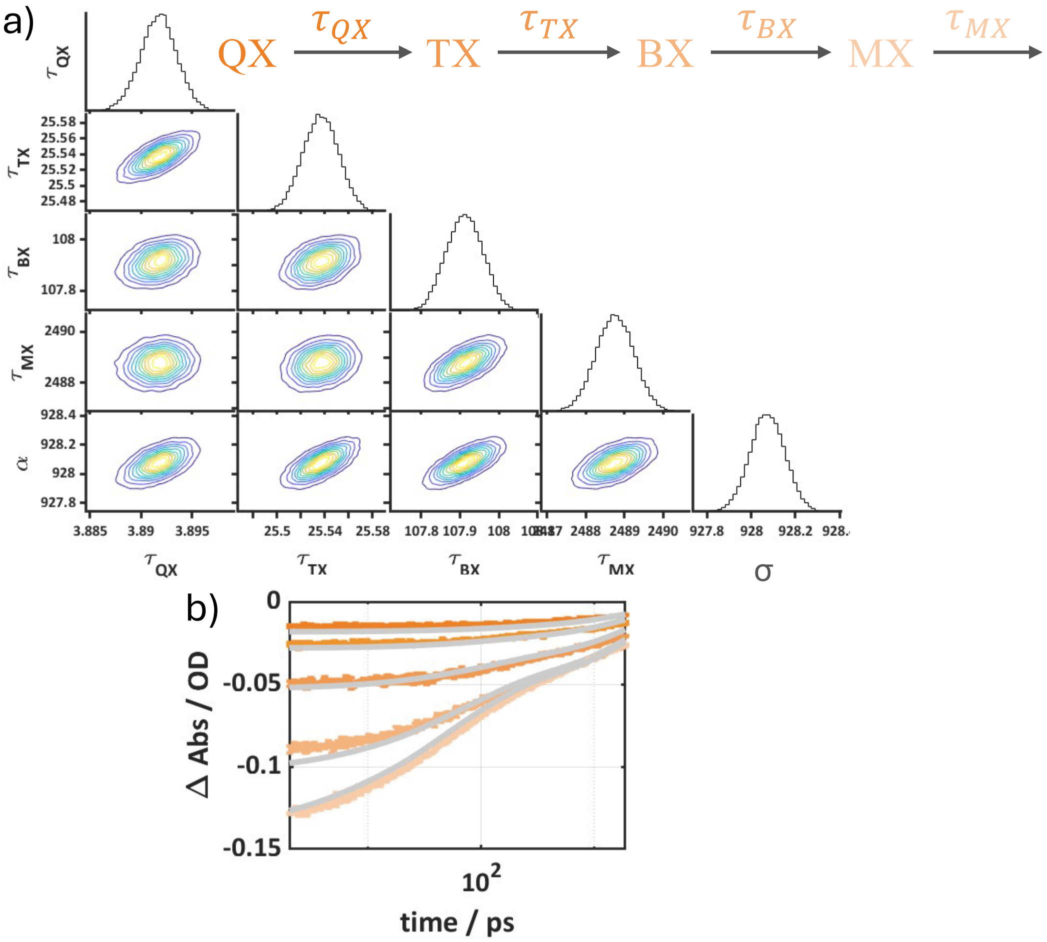

Figure A 10: *QX model was used for MCMC fitting of 4.0 nm S^{2-}capped QD. (a) Contour plot representing the fit parameters obtained from MCMC. (b) Intensity dependent kinetics of B_1 bleach with the fit (grey lines).*

Table A 6: *Intensities used for MCMC fitting of S^{2-}capped 4.0 nm QD and < N >, σ and, α obtained from MCMC fitting.*

Intensity **$\mu W \mu m^{-2}$**	**< *N* >**	***σ*** **$\mu W^{-1} \mu m^2$**	***α*** **cm^2**
0.0004	0.4	928.1	2.3×10^{-15}
0.0007	0.6		
0.0014	1.3		
0.0034	3.2		
0.0122	11.3		

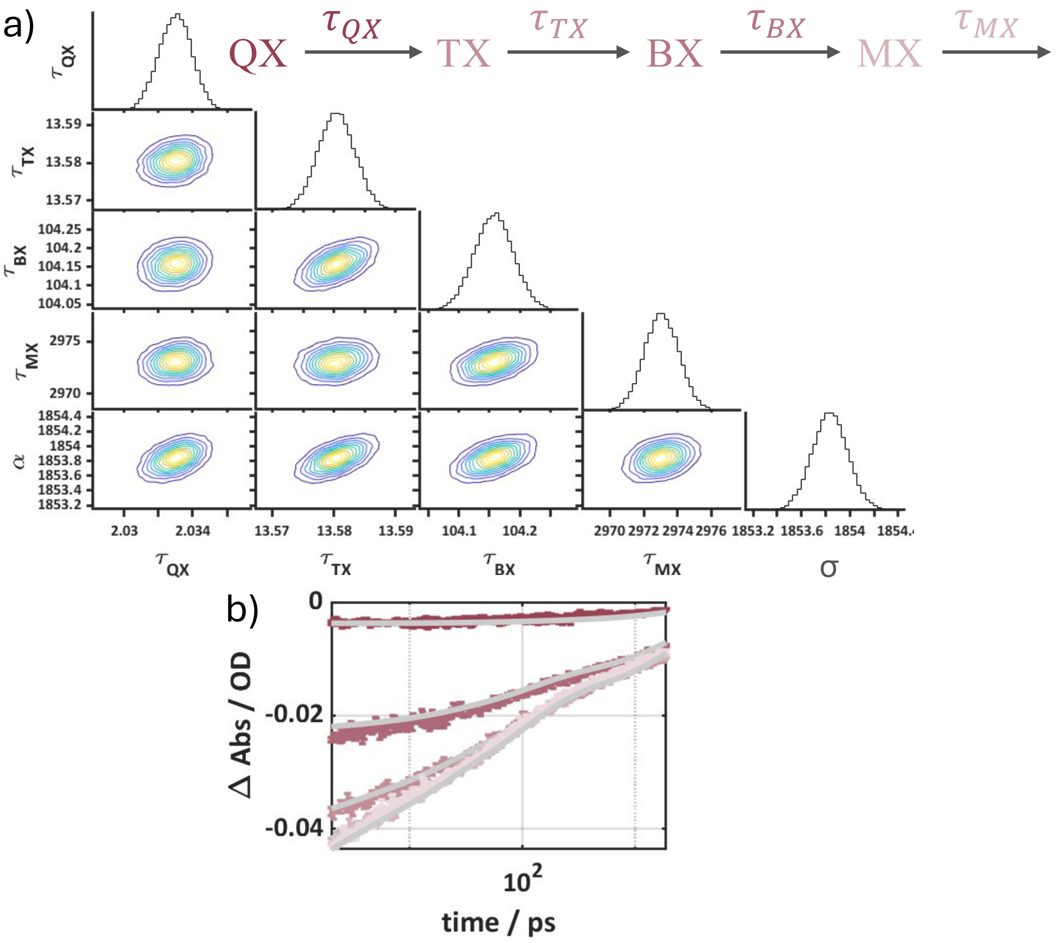

Figure A 11: *QX model was used for MCMC fitting of 4.8 nm TOPO capped QD. (a) Contour plot representing the fit parameters obtained from MCMC. (b) Intensity dependent kinetics of* B_1 *bleach with the fit (grey lines).*

Table A 7: *Intensities used for MCMC fitting of TOPO capped 4.8 nm QD and* $< N >$, *σ and, α obtained from MCMC fitting.*

Intensity **µWµm^{-2}**	$< N >$	**σ** **µW^{-1}µm^2**	**α** **cm^2**
0.0001	0.2	1853.7	4.6×10^{-15}
0.0009	1.6		
0.0019	3.6		
0.0030	5.6		
0.0048	8.8		

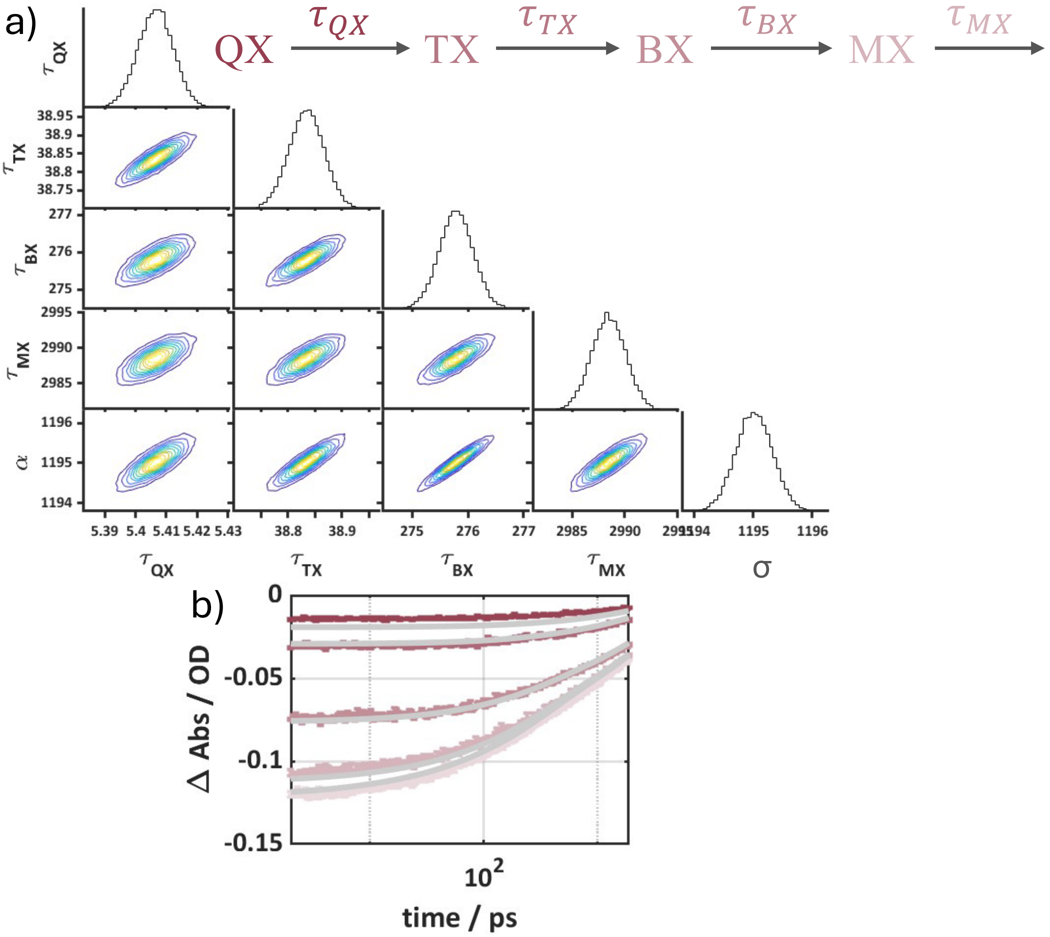

Figure A 12: *QX model was used for MCMC fitting of 4.8 nm S^{2-}capped QD. (a) Contour plot representing the fit parameters obtained from MCMC. (b) Intensity dependent kinetics of B_1 bleach with the fit (grey lines).*

Table A 8: *Intensities used for MCMC fitting of S^{2-} capped 4.8 nm QD and < N >, σ and, α obtained from MCMC fitting.*

Intensity $\mu W \mu m^{-2}$	**< N >**	**σ $\mu W^{-1} \mu m^2$**	**α cm^2**
0.0003	0.3	1195.1	2.9×10^{-15}
0.0004	0.5		
0.0014	1.7		
0.0033	3.8		
0.0046	5.5		

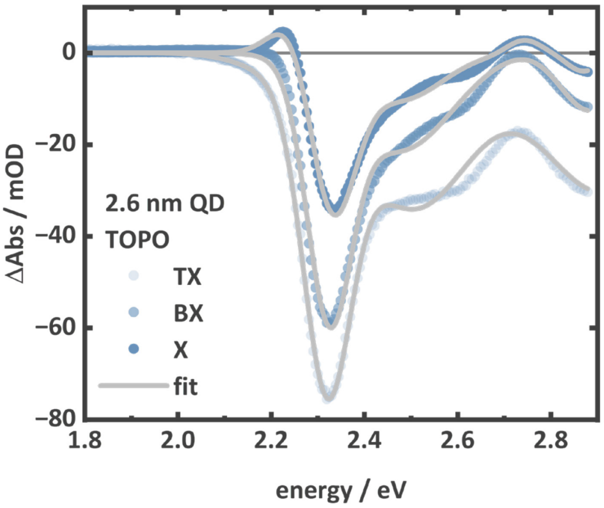

Figure A 13: *TX, BX, and exciton spectra of TOPO capped 2.6 nm QD along with the respective gaussian fits.*

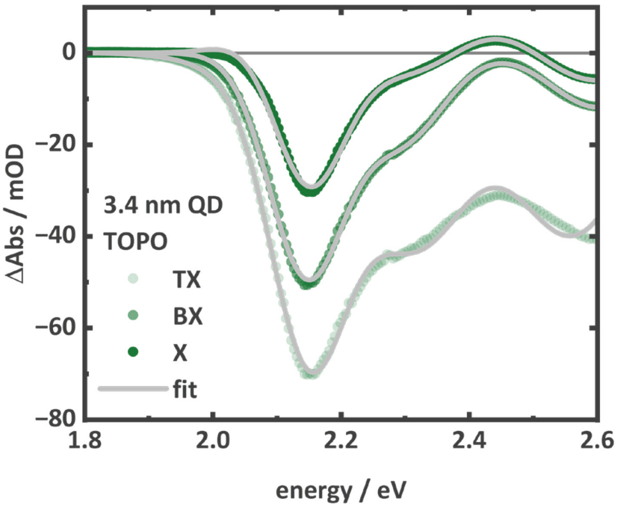

Figure A 14: *TX, BX, and exciton spectra of TOPO capped 3.4 nm QD along with the respective gaussian fits.*

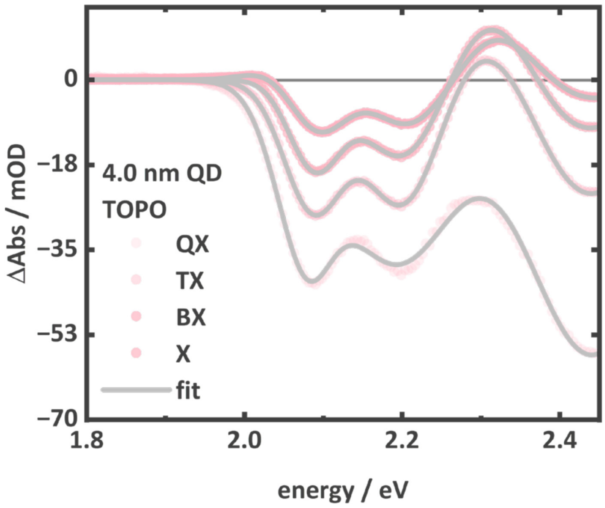

Figure A 15: *QX, TX, BX, and exciton spectra of TOPO capped 4.0 nm QD along with the respective gaussian*

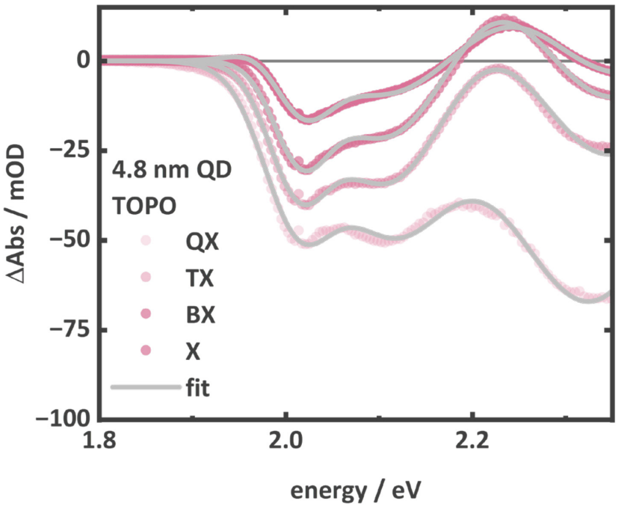

Figure A 16: *QX, TX, BX, and exciton spectra of TOPO capped 4.8 nm QD along with the respective gaussian fits.*

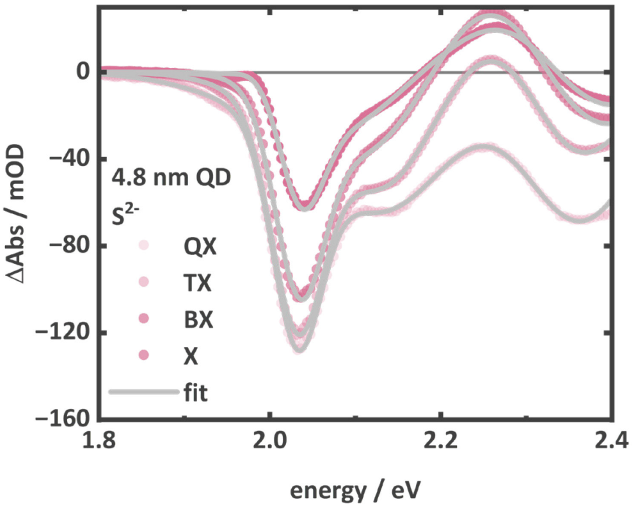

Figure A 17: *QX, TX, BX, and exciton spectra of S^{2-}capped 4.0 nm QD along with the respective gaussian fits.*

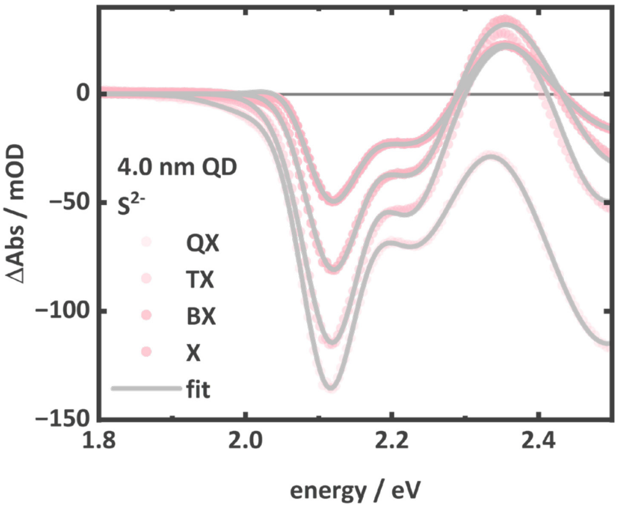

Figure A 18: *QX, TX, BX, and exciton spectra of S^{2-}capped 4.8 nm QD along with the respective gaussian fits.*

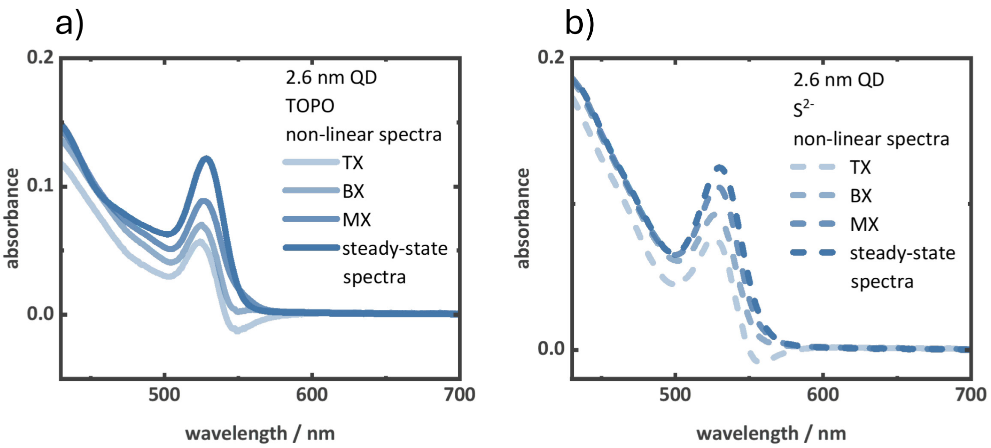

Figure A 19: *non-linear spectra derived from the multiexciton species spectra of (a) TOPO capped (b)* S^{2-} *capped 2.6 nm QD.*

Appendix D

Supporting information for 'Observing High-order Multiexciton Dynamics under Weak and Strong Electronic Coupling in QD Thin Films'

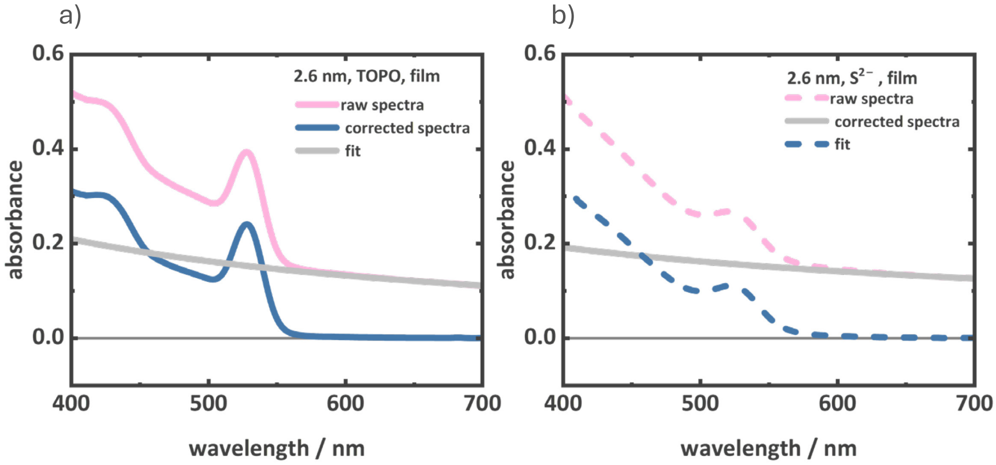

Figure A 20: *Raw absorption spectra of QDs infiltrated porous silica layers, fitted scattering curve, and corrected absorption spectra.*

To remove the scattering contribution in the collected absorption spectra of QD thin films, a theoretical wavelength dependent scattering function,

$$S = A \times \lambda^n \tag{34}$$

was fitted in the absorption spectra, in the region where there is no absorption of QDs. Here, wavelength λ is in nm and the exponent *n* with values from − 4 (Rayleigh scattering for spherical and small particles) to −1 (for larger and non-spherical particles). *A* represents the background contribution to the absorption spectra.

After fitting the scattering function, it was extrapolated to the whole wavelength range, which was then subtracted from the original absorption spectra to get the corrected absorption spectra.

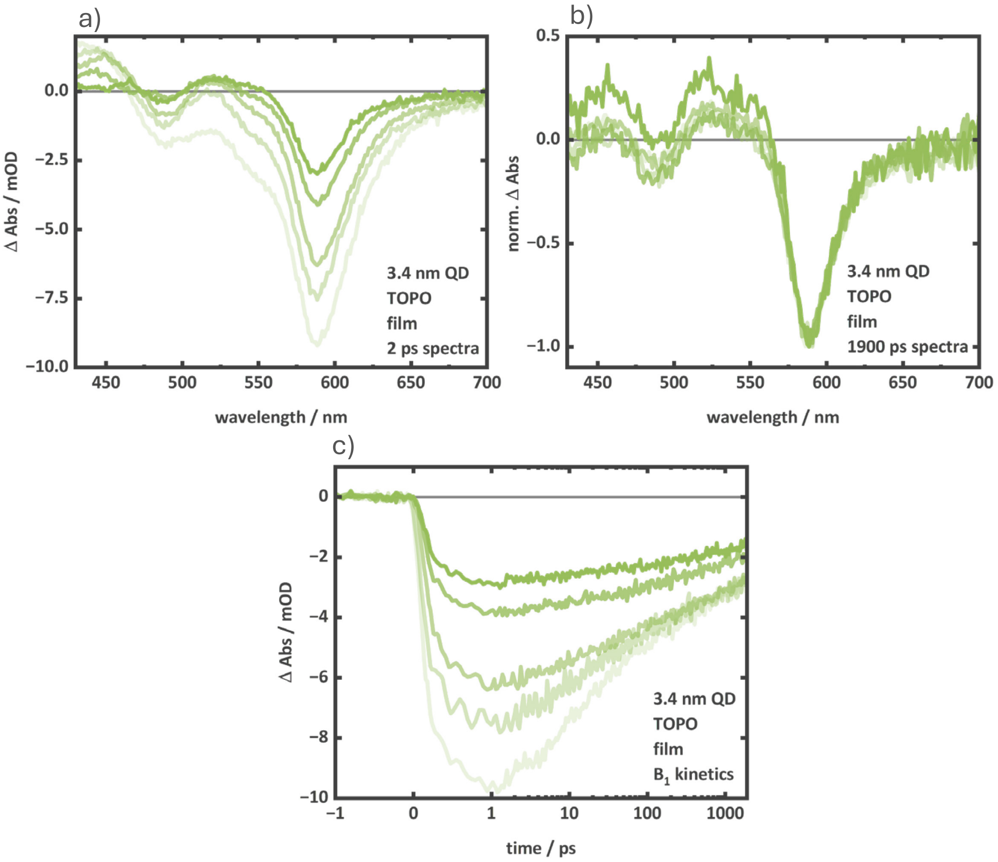

Figure A 21: *intensity-dependent TA spectra of TOPO capped 3.4 nm QD thin film at (a)2 ps, and at 1900 ps (normalized at* B_1*). (c) intensity-dependent* B_1 *kinetics of TOPO capped 3.4 nm QD thin film.*

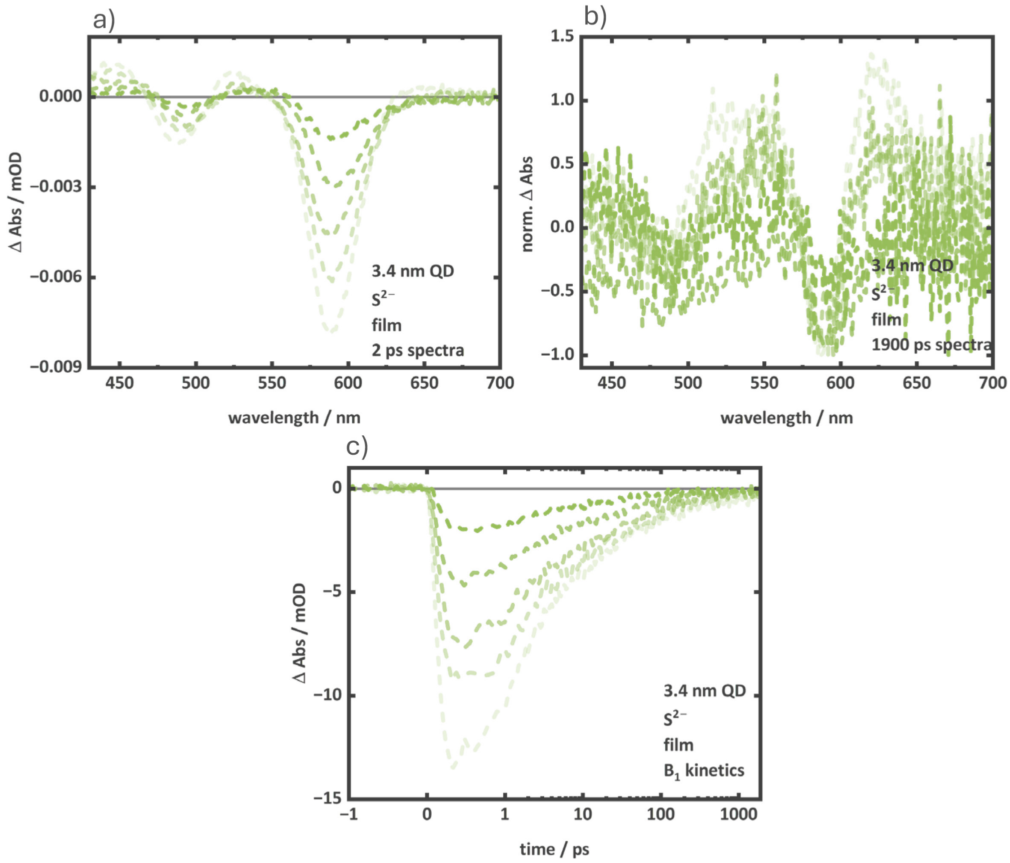

Figure A 22: *intensity-dependent TA spectra of* S^{2-} *capped 3.4 nm QD thin film at (a)2 ps, and at 1900 ps (normalized at* B_1*). (c) intensity-dependent* B_1 *kinetics of* S^{2-}*capped 3.4 nm QD thin film.*

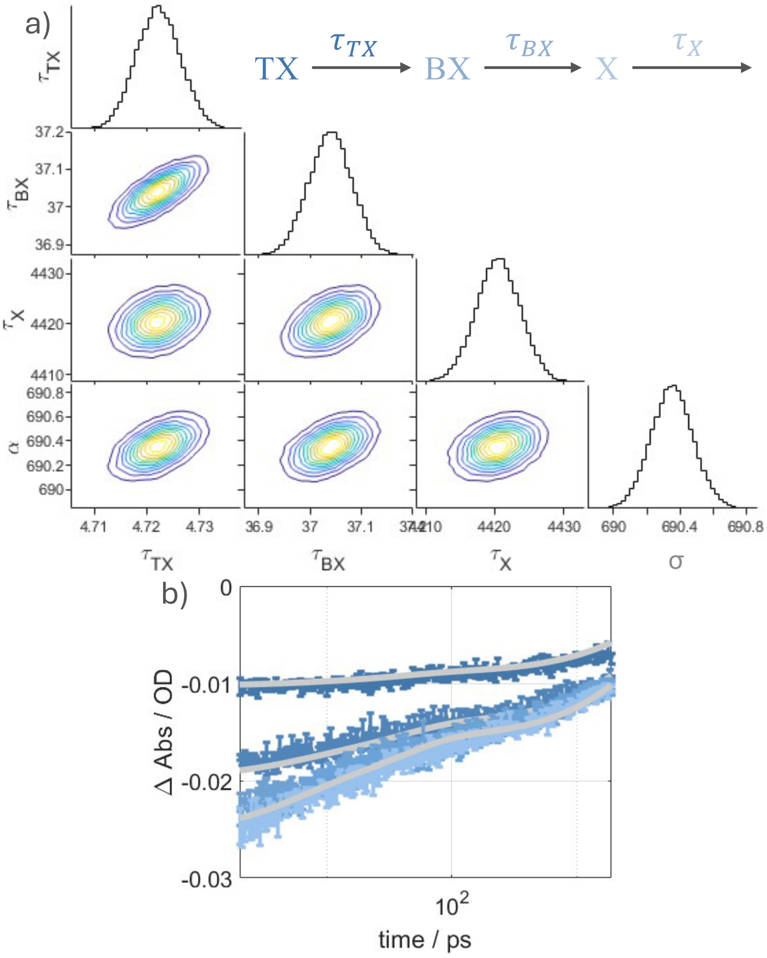

Figure A 23: *TX model was used for MCMC fitting of 2.6 nm TOPO capped QD in thin film. (a) Contour plot representing the fit parameters obtained from MCMC. (b) Intensity dependent kinetics of* B_1 *bleach with the fit (grey lines).*

Table A 9: *Intensities used for MCMC fitting of TOPO capped 2.6 nm QD thin film and* $< N >$*,* σ *and,* α *obtained from MCMC fitting.*

Intensity $\mu W \mu m^{-2}$	$< N >$	σ $\mu W^{-1} \mu m^{2}$	α cm^{2}
0.0012	0.8	690.2	1.7×10^{-15}
0.0034	2.4		
0.0070	4.8		
0.0104	7.2		
0.0136	9.4		

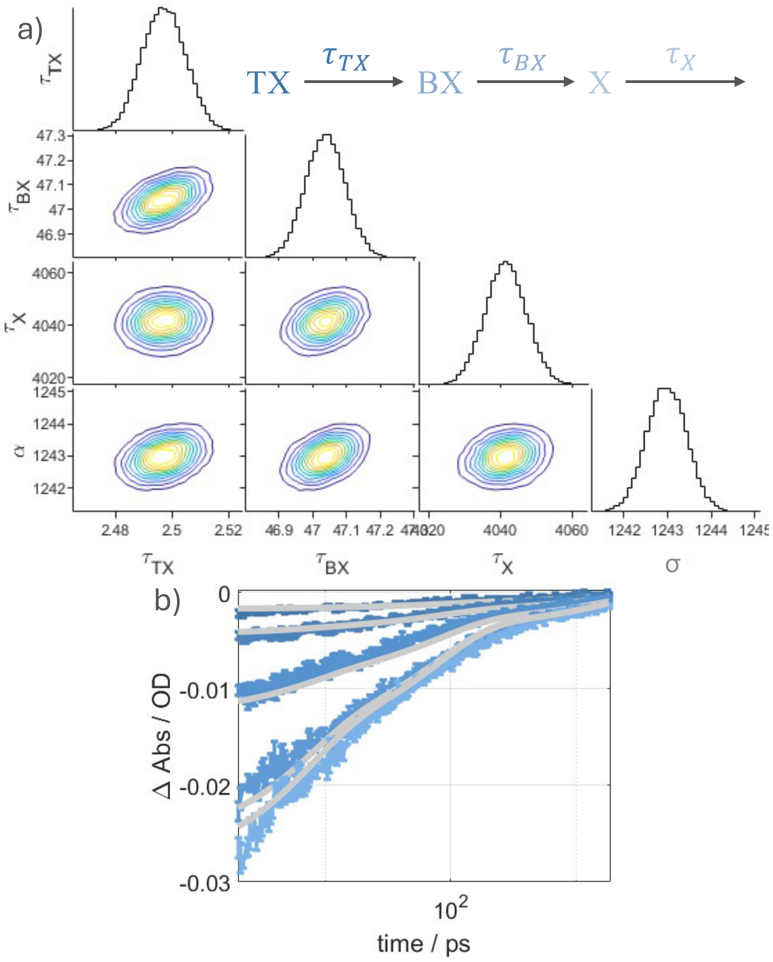

Figure A 24: *TX model was used for MCMC fitting of 2.6 nm* S^{2-} *capped QD in thin film. (a) Contour plot representing the fit parameters obtained from MCMC. (b) Intensity dependent kinetics of* B_1 *bleach with the fit (grey lines).*

Table A 10: *Intensities used for MCMC fitting of* S^{2-} *capped 2.6 nm QD thin film and* $< N >$*, σ and, α obtained from MCMC fitting.*

Intensity **μWμm⁻²**	$< N >$	**σ** **μW⁻¹μm²**	**α** **cm²**
0.0003	0.3	1244.4	3.1×10^{-15}
0.0006	0.5		
0.0014	1.2		
0.0037	3.0		
0.0055	4.5		

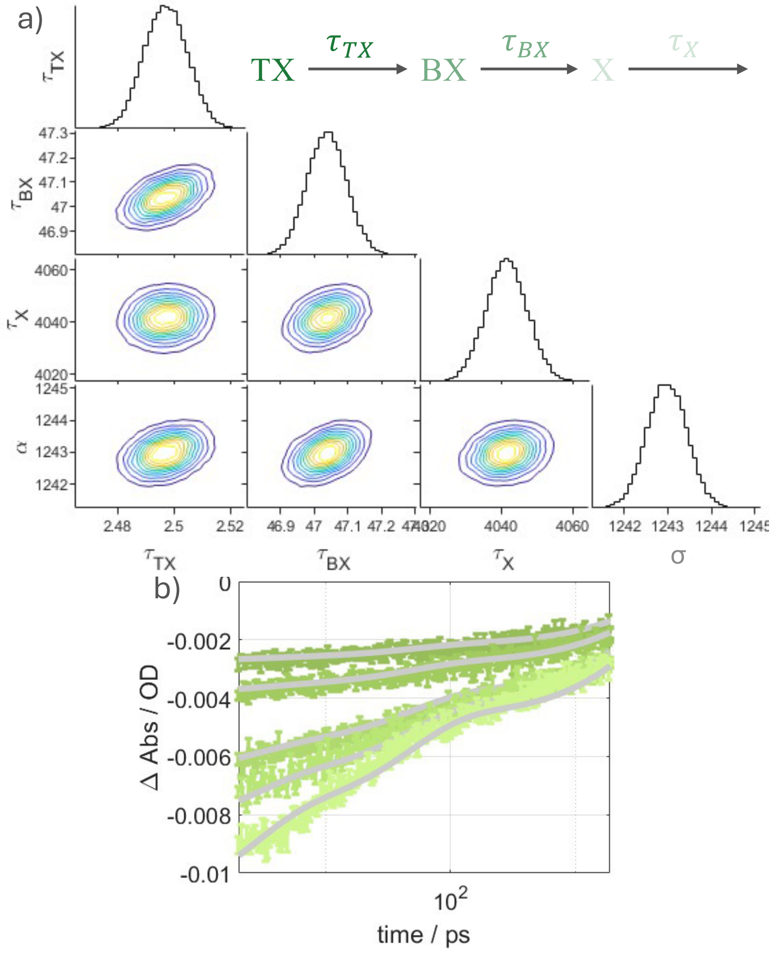

Figure A 25: *TX model was used for MCMC fitting of 3.4 nm TOPO capped QD in thin film. (a) Contour plot representing the fit parameters obtained from MCMC. (b) Intensity dependent kinetics of B_1 bleach with the fit (grey lines).*

Table A 11: *Intensities used for MCMC fitting of TOPO capped 3.4 nm QD thin film and < N >, σ and, α obtained from MCMC fitting.*

Intensity **$\mu W \mu m^{-2}$**	**< *N* >**	***σ*** **$\mu W^{-1} \mu m^{2}$**	***α*** **cm^{2}**
0.0005	0.4	1242.8	3.1×10^{-15}
0.0007	0.6		
0.0014	1.2		
0.0020	1.7		
0.0037	3.2		

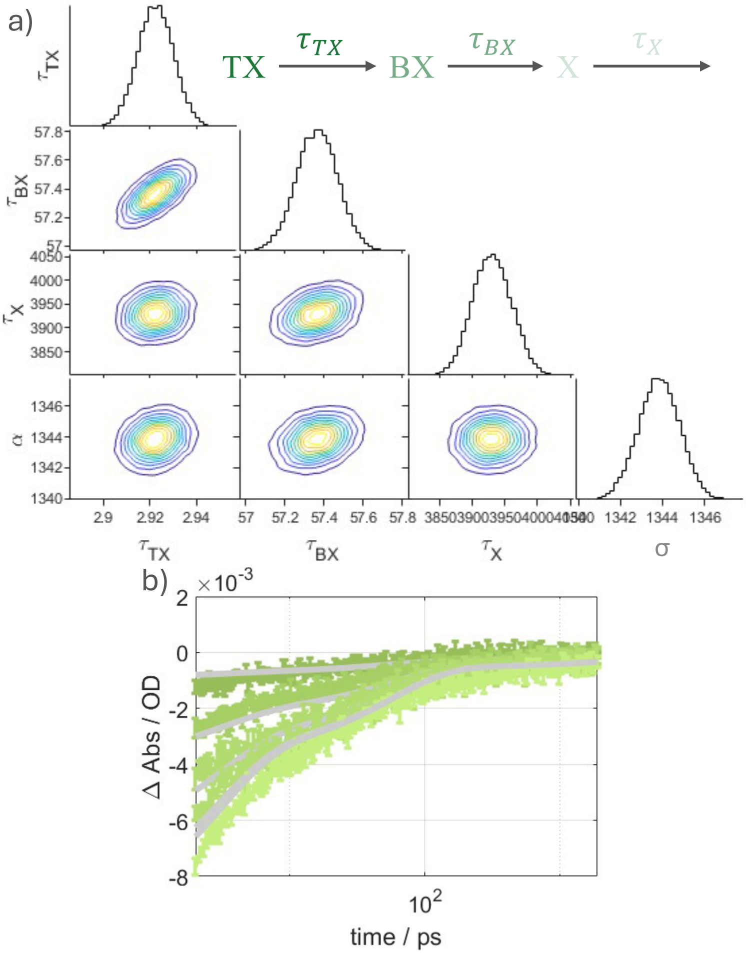

Figure A 26: *TX model was used for MCMC fitting of 3.4 nm S^{2-} capped QD in thin film. (a) Contour plot representing the fit parameters obtained from MCMC. (b) Intensity dependent kinetics of B_1 bleach with the fit (grey lines).*

Table A 12: *Intensities used for MCMC fitting of S^{2-} capped 3.4 nm QD thin film and $< N >$, σ and, α obtained from MCMC fitting.*

Intensity $\mu W \mu m^{-2}$	$< N >$	**σ** $\mu W^{-1} \mu m^{2}$	**α** cm^2
0.0005	0.5	1343.7	3.3×10^{-15}
0.00141	1.2		
0.00244	2.1		
0.00421	3.7		
0.01097	9.6		

List of Publications

Publications included in the thesis:

R. Baruah, M. Dilshad, A. Undisz, M. Diegel, J. Dellith, J. Plentz, A. Szeghalmi, M. Wächtler, "Deposition of CdSe nanocrystals in highly nanoporous SiO2 matrices - in-situ growth vs. infiltration methods" *Materials* 2024, 17, 4379.

R. Baruah, K. Kumar, M. Wächtler, "Probing high order multiexcitons in CdSe quantum dots via transient absorption spectroscopy" (under preparation).

Additional publications:

H. N. Gopalakrishna, **R. Baruah**, C. Hünecke, V. Korolev, M. Thümmler, A. Croy, M. Richter, F. Yahyaei, R. Hollinger, V. Shumakova, I. Uschmann, H. Marschner, M. Zürch, C. Reichardt, A. Undisz, J. Dellith, A. Pugžlys, A. Baltuška, C. Spielmann, U. Peschel, S. Gräfe, M. Wächtler, and D. Kartashov, "Tracing spatial confinement in semiconductor quantum dots by high-order harmonic generation", *Phys. Rev. Research*, 5, 013128 (2023).

M. Micheel, **R. Baruah**, K. Kumar, M. Wächtler, "Assembly. Properties, and Application of Ordered Group II-VI and IV-VI Colloidal Semiconductor Nanoparticle Films", *Adv. Mater. Interfaces* 2022, 9, 2201039.

S. Benndorf, A. Schleusener, R. Müller, M. Micheel, **R. Baruah**, J. Dellith, A. Undisz, C. Neumann, A. Turchanin, K. Leopold, W. Weigand, M. Wächtler, "Covalent Functionalization of CdSe Quantum Dot Films with Molecular [FeFe] Hydrogenase Mimics for Light-Driven Hydrogen Evolution", *ACS Appl. Mater. Interfaces*, 15 (2023), 18889-18897.

K. Kumar, J. Uhlig, **R. Baruah**, S. Yadav, M. Wächtler, "Multiexciton absorption cross-sections of CdSe@CdS nanorods studied using Pump-rePump-Probe Spectroscopy", ChemRxiv. 2024; doi:10.26434/chemrxiv-2024-xtmjk.

List of Conference Contributions

Bunsen-Tagung 2024	**Poster presentation:** Markov Chain Monte Carlo methods to model multiexciton dynamics in CdSe quantum dots
Bunsen-Tagung 2022	**Poster presentation:** Colloidal CdSe nanocrystals deposited into thin films and infiltrated into nanoporous matrices for nonlinear optical applications
WE Heraus Seminar, 2022	**Poster presentation:** Thin films via deposition of colloidal nanocrystals for high-order harmonic generation
nanoGe spring meeting, 2022	**Poster presentation:** Colloidal nanocrystals deposited into thin films and infiltrated into nanoporous matrices for nonlinear optical applications
Bunsen-Tagung 2021	**Poster presentation:** Quantum dots layers for high-order harmonic generation
nanoGe spring meeting, 2021	**Poster presentation:** Strong to weak confinement regime post-synthetic modification of colloidal quantum dots
Internet Conference for Quantum Dots, 2021	listener
nanoGe Fall meeting, 2019	listener

Curriculum Vitae

PERSONAL INFORMATION

Name	**RAKTIM BARUAH**
Date of Birth	June 1, 1996
Nationality	Indian
Current designation	PhD Student
Address	Department of Chemistry, RPTU Kaiserslautern-Landau, Erwin-Schrödinger-str. 52, 67665, Germany
Contact	raktim.baruah@rptu.de

EDUCATIONAL BACKGROUND

Doctor of Philosophy	Chemistry, Leibniz Institute of Photonic Technology, Jena (Oct 2019 -June 2023), RPTU Kaiserslautern-Landau (July 2023 – December 2024) Supervisor: Prof. Maria Wächtler
Master of Science	Chemistry, Rajiv Gandhi University, Itanagr, INDIA (2017 - 2019)
Bachelor of Science	Chemistry, Sibsagar College, Joysagar, Dibrugarh University, Assam, INDIA (2014 - 2017)

RESEARCH EXPERIENCE

Doctoral Thesis	Exciton- and Multiple Exciton Dynamics in Colloidal Nanocrystals
Master Thesis	Synthesis and Characterization of Luminescent 3D Metallacages
Summer Internship	Synthesis and Characterization of ZnS: Mn and Cu based Nanoparticles for Electroluminescence Applications
Bachelor of Thesis	Green synthesis of TiO_2 nanoparticles

INSTRUMENTATION SKILL

Spectroscopy	Steady-state absorption and photoluminescence spectroscopy, FT-IR ATR spectroscopy, time-resolved photoluminescence spectroscopy (TCSPC, streak camera), pump-probe transient absorption spectroscopy, pump-pump-probe transient absorption spectroscopy, Raman spectroscopy
Others	Schlenk line, Glove box, spin coating, liquid-air interface method (dip coating), Langmuir-Blodgett, Helium cryostat

DIGITAL SKILL

OriginLab, Python, Matlab, MS-Office, Chemdraw, imageJ, Inkscape, Blender

LANGUAGE SKILL

English (fluent and high proficiency), Hindi (fluent) and Assamese (mother tongue)